A PRODUCTION CHARACTERIZATION OF THE EAGLE FORD SHALE, TEXAS – A BAYESIAN ANALYSIS APPROACH

A Thesis

by

NEFELI GEORGE MORIDIS

Submitted to the Office of Graduate and Professional Studies of
Texas A&M University
in partial fulfillment of the requirements for the degree of

MASTER OF SCIENCE

Chair of Committee,	Thomas A. Blasingame
Co-Chair of Committee,	Zenon Medina-Cetina
Committee Members,	Walter Ayers
Head of Department,	A. Daniel Hill

May 2015

Major Subject: Petroleum Engineering

ABSTRACT

We begin this research by asking "can we better estimate reserves in unconventional reservoirs using Bayes' theorem?" To attempt to answer this question, we obtained data for 68 wells in the Greater Core of the Eagle Ford Shale, Texas. As process, we eliminated the wells that did not have enough data, that did not show a production decline and/or wells that had too much data noise (this left us with 8 wells for analysis).
We next performed decline curve analysis (DCA) using the Modified Hyperbolic (MH) and Power-Law Exponential (PLE) models (the two most common DCA models), consisting in user-guided analysis software. Then, the Bayesian paradigm was implemented to calibrate the same two models on the same set of wells.

The primary focus of the research was the implementation of the Bayesian paradigm on the 8 well data set. We first performed a "best fit" parameter estimation using least squares optimization, which provided an optimized set of parameters for the two decline curve models. This was followed by using the Markov Chain Monte Carlo (MCMC) integration of the Bayesian posterior function for each model, which provided a full probabilistic description of its parameters. This allowed for the simulation of a number of likely realizations of the decline curves, from which first order statistics were computed to provide a confidence metric on the calibration of each model as applied to the production data of each well.

Results showed variation on the calibration of the MH and PLE models. The forward models (MH and PLE) either over- or underestimate the reserves compared with the Bayesian calibrations, proving that the Bayesian paradigm was able to capture a more accurate trend of the data and thus able to determine more accurate estimates of reserves. In industry, the same decline curve models are used for unconventional wells as for conventional wells, even though we know that the same models may not apply. Based on the proposed results, we believe that Bayesian inference yields more accurate estimates of

reserves for unconventional reservoirs than deterministic DCA methods. Moreover, it provides a measure of confidence on the prediction of production as as function of varying data and varying decline curve models.

DEDICATION

To life.

I am excited to see where you will take me from here.

ACKNOWLEDGEMENTS

I would like to thank my committee chair, Dr. Thomas A. Blasingame, my committee co-chair, Dr. Zenon Medina-Cetina, and my committee member, Dr. Walter Ayers, for their guidance and support throughout the course of this research.

I would also like to extend a big thank you to the people responsible for making this research happen by providing the data necessary. Due to confidentiality requirements, I cannot thank this company publicly, but your participation has been crucial in completing my research.

Thanks also go to my friends and colleagues and the Department faculty and staff for making my time at Texas A&M University a great experience. I would like to thank Dr. Sam Noynaert, who was the first to give me a TA assignment and to whom I have had to graciously decline his offer to become his Ph.D. student. Thank you for all your help these last few years. I would also like to thank Ms. Mary-Lu Epps, Dr. Ted Seidel, Ms. Betty Robbins and Mr. Stuart White. You all helped me through this process, whether it be a TA problem or a research problem, and I do appreciate it.

I also want to extend my gratitude to Mr. Farbod Soltanpour of the Civil Engineering Department, for his invaluable help with the coding required for this study.

I would like to thank my parents, Vivi Fissekidou and George Moridis, who have supported me throughout my academic career and have never stopped pushing me; to my siblings, Iris-Eleni Moridis and Julius-Maximos "small fry" Moridis, who have been there to remind me how old I am getting and that I need to graduate. The comic relief was greatly appreciated.

Finally, I would like to thank all my friends who have supported me, listened to me through the hard times, and celebrated with me through the good ones. They say that your

friends are the family you choose, and in my case this could not be truer. I would especially like to thank Clotilde Chen, Patricia Varela, Francisco Tovar, Sara Parsons and Stella Kritikou. To my office mates, for always encouraging me throughout my research efforts and for making sure that we have our Richardson 821 office outings. To my IFP friends, Juan Manuel Lacayo, Juan Felipe Rios Arios, Cesar Leal, Loreline Kauscar, Natalia Dernovaya and Amalia Setyawati, for all the great adventures we had when we were in France at IFP together.

A special thanks goes to Ms. Emily Blunt, perhaps one of the best people I have met and definitely one of the best roommates a girl can ask for. Thank you for taking care of me during two knee surgeries, both of which occurred within months of defending this thesis. I truly would not have been able to finish without your help.

NOMENCLATURE

a	=	Intercept constant for Duong's model
b	=	Arp's dimensionless hyperbolic constant
BOE	=	Barrels of Oil Equivalent (BOE)
BOE/D	=	Barrels of Oil Equivalent per Day (BOE/d)
D_i	=	Initial decline (1/day)
D_∞	=	Decline parameter for the Power-Law Exponential DCA model (1/day)
D_{lim}	=	Limit below which D cannot decline (1/day)
EUR	=	Estimated Ultimate Recovery (BOE)
K	=	EUR parameter for the Logistic Growth Curve DCA model (BOE)
LSQ	=	Least Squares
m	=	Dimensionless slope parameter for Duong DCA model
MCMC	=	Markov Chain Monte Carlo
MH	=	Modified Hyperbolic DCA model
n	=	Time exponent parameter for the Power-Law Exponential DCA model
PLE	=	Power Law Exponential DCA model
$P(\theta\|D)$	=	Posterior
$P(\theta)$	=	Prior
$P(D\|\theta)$	=	Likelihood
q_i	=	Initial flowrate (BOE/D)
$q(t)$	=	Flowrate (BOE/D)
t	=	Time (days)
x	=	Observed data
α	=	Parameter for the Logistic Growth Curve DCA model
η	=	Time exponent parameter for the Stretched Exponential DCA model
θ	=	Set of known parameters
μ	=	Mean of parameters
σ	=	Standard deviation
τ	=	Time parameter of the Stretched Exponential DCA model (days)

TABLE OF CONTENTS

Page

LIST OF FIGURES

Page

LIST OF TABLES

Page

1. INTRODUCTION

The petroleum industry in the U.S. has shifted its focus to unconventional plays due to the enormous amount of estimated reserves and its ability to revolutionize the oil and gas industry, notably with new technology. The majority of proved oil reserves are located in the Middle East as of January 2011, as is the majority of the world's natural gas reserves. The United States has 322.7 trillion cubic feet of gas reserves and 33.4 billion barrels of oil (EIA, 2012-13.) This being said, there is an irreversible shift to gas both in exploration and production, as seen in **Fig. 1**.

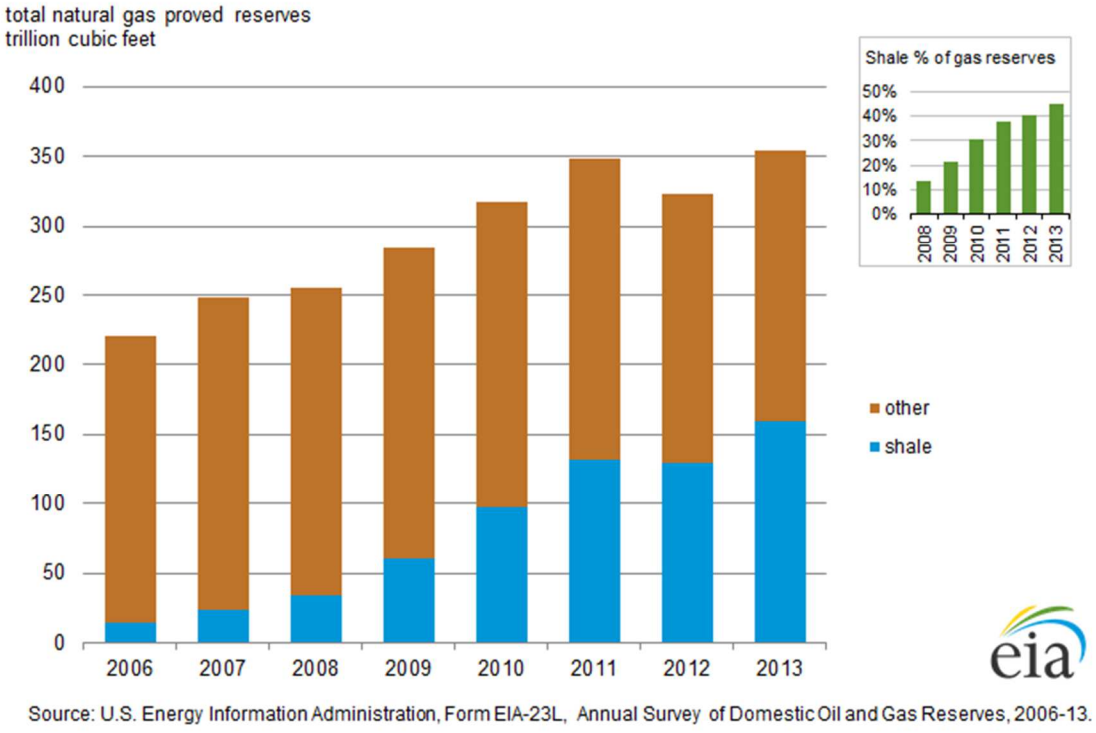

Fig. 1— U.S. total natural gas proved reserves shows an increase in shale gas reserves, where in 2008 it was approximately 12% of the gas reserves, and in 2013 it was nearly 50% of gas reserves (U.S. EIA, 2013)

As seen in **Fig. 2**, the majority of the energy production today is natural gas, and is forecasted to continue being the main source of energy through 2040.

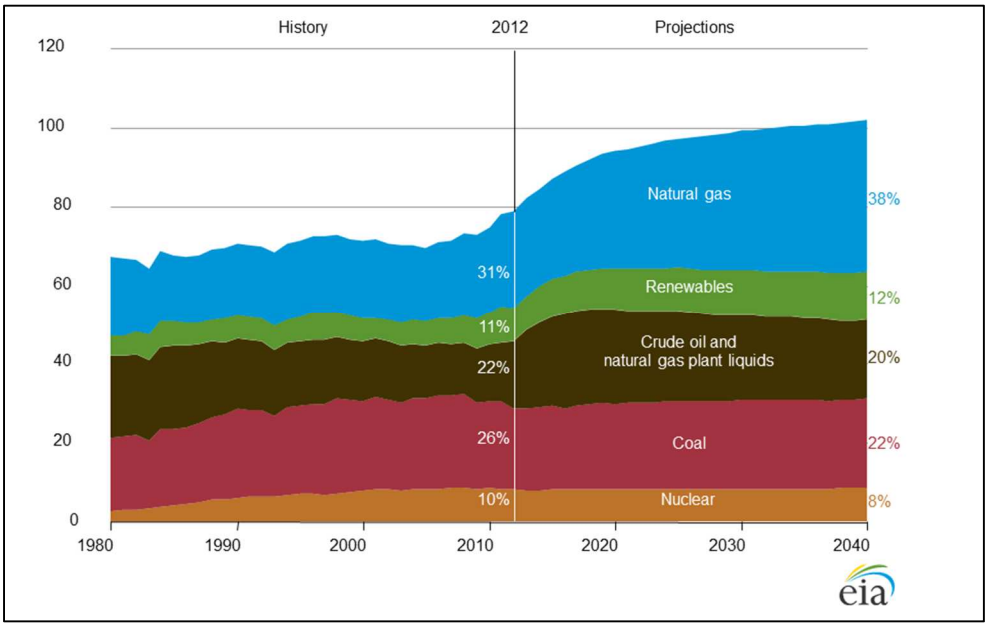

Fig. 2 — U.S. energy production by fuel, 1980-2040, quadrillion BTU (U.S. DOE EIA 2012)

Natural gas is produced from shale gas, tight gas and coalbed methane reservoirs. Due to the extremely low permeability of such reservoirs, horizontal drilling and hydraulic fracturing are used to produce them economically. According to the "resource triangle" (Holditch, 2011) shown in **Fig. 3** below, conventional reservoirs are of high to medium quality, are difficult to find but easy to produce, and thus less expensive. However, as we shift to unconventional reservoirs, the reservoir quality is low, and although the location of unconventional reservoirs are relative well-known (as source rocks), these are difficult to exploit and new technologies are required to extract the hydrocarbons, leading to increased prices for drilling and completions, which ultimate requires high oil and gas prices to achieve profitability.

In the "resource triangle, the apex of the triangle is where the conventional reservoirs are located, and "are difficult to find but easy to extract," and we progress lower into the resource triangle, the resources are easier to find — however harder to extract due to the

necessity of improved technologies, and are thus more expensive to extract (Holditch, 2011).

This study will focus on the Eagle Ford Shale, and in particular, on oil wells in the Greater Core Eagle Ford Area. Our stated goal is to develop a method based on a probabilistic approach to identify, characterize, and better model well production based on standard decline curve models.

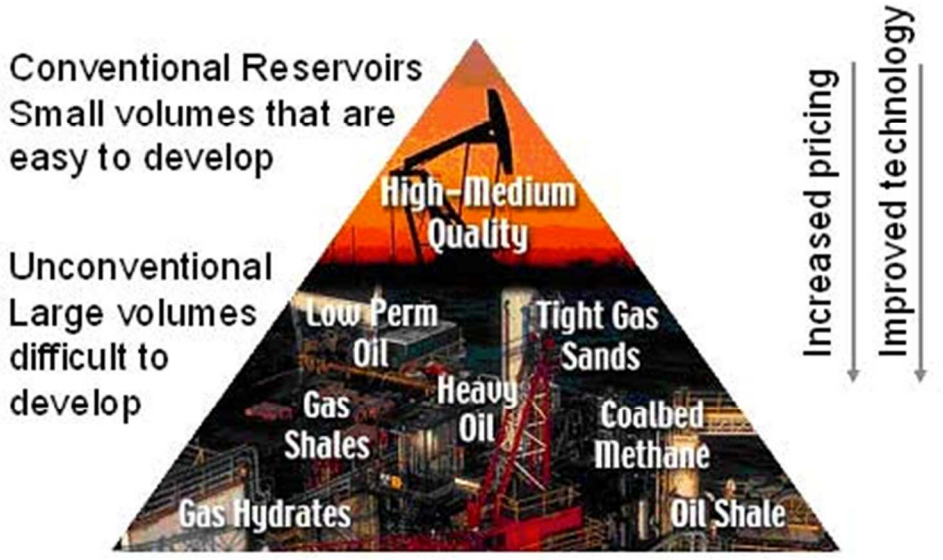

Fig. 3 — The resource triangle (Holditch, 2011).

The Eagle Ford Shale is located in Texas and is 50 miles wide and 400 miles long, covering 23 counties in South Central Texas (Gong et al, 2013). The Eagle Ford Shale is the source rock for the Austin Chalk and is now being developed as its own self-sourcing reservoir (Tian, et al, 2013). This play is composed of Cretaceous mudstone and

carbonates which are especially brittle due to the high carbonate and low clay content, meaning that hydraulic fracturing is especially effective. The productive portion of the Eagle Ford shale ranges from 2,500 to 14,000 ft; and the thickness ranges from 120 to 350 ft (Gong et al). The geology of the Eagle Ford shale is quite complex and the calcareous makeup of the rock leads to the "condensate rich environment of this play" which presents "unique fracture design challenges" (Bazan et al., 2012).

The Eagle Ford Shale has been in development since 2008 and is being exploited using horizontal wells with multi-stage hydraulic fracture treatments. The estimated resources in the Eagle Ford Shale are 21 trillion cubic feet (TCF) of gas and 3.35 billion barrels of oil (BBO), however the estimation of resources has high uncertainty (Gong et al., 2013).

According to Ayers, et al., the Greater Core of the Eagle Ford is the region of highest oil production, and this is where the focus of this thesis will lie. In the first month of production a well will generally produce more than 5,000 bbl. The regions of highest gas production are between the Stuart City and Sligo Shelf Margins, where the first month of the wells' production exceeds 60 MMcf (Tian et al., 2013).

Although the production differs throughout the play, the most productive wells "are located south of the Stuart City Shelf Margin, where production commonly exceeds 80 MMcf/month/well" while oil production is highest in Karnes and Gonzalez counties, typically exceeding 16 Mbbl/month/well (Tian et al., 2013).

2. LITERATURE REVIEW

2.1 Geology of the Eagle Ford Shale

The Eagle Ford Shale is the source rock for the Austin Chalk, however is now being developed as its own self-sourcing reservoir (Tian et al., 2013). The lower part of the reservoir is shale-rich, and the upper part is carbonate-rich, and the whole Eagle Ford lies over the Buda Limestone, which is overlain by Austin Chalk (Tian et al., 2013). This being said, the Eagle Ford Shale is an unconventional reservoir, which "consists of a wide variety of liquid sources including oil sands, extra heavy oil, gas to liquids and other liquids." (IEA 2013). Furthermore, unconventional reservoirs are more difficult to produce because they require advanced technology. With regards to the shale plays, they are self-sourcing reservoirs, therefore the hydrocarbon does not migrate, but stays in place. These shale reservoirs have also been the source rocks for many of the conventional reservoirs, before it was determined that we could economically produce these unconventional reservoirs. A conventional reservoirs is defined as "a petroleum system is a dynamic hydrocarbon generating system, functioning in a geologic space and time scale" that requires "the timely convergence of geologic elements and events essential to the formation of petroleum deposits that include mature source rock, expulsion, secondary migration to reservoir rock, accumulation in a trap and retention." (Ayers, 2011).

The characteristics of a source rock are that they are made up of fine grained clastics, most organics are deposited on ocean or lake bottoms, they have a low matrix porosity and permeability and are also brittle, indicating that they may be naturally fractured.
The Eagle Ford Shale is an Upper Cretaceous shale, where the regional source rock has Kerogen Types 1, 2 and possibly Type 3, and where the hydrocarbon fluid composition greatly varies with thermal maturity.

Kerogen is defined as "the organic material in sedimentary rocks that is insoluble in organic solves, under microscopic examination, kerogen appear as disseminated organic fragments within sedimentary rocks and some kerogen is structured and recognizable as

plant fragments, spores, algae, and other pieces with definite biological origins." (Ayers, 2011).

Kerogen types are defined by the Van Krevelen Diagram, shown below in **Fig. 4**, which indicates the Atomic Hydrogen (H) to Carbon (C) ratio versus the Atomic Oxygen (O) to Carbon (C) Ratio. Kerogen Types 1 and 2 are indicative of a higher H:C ratio, and are indicative of oil whereas Type 3 kerogen has a lower H:C ratio, and higher O:C ratio, more indicative of gas. Since the Eagle Ford Shale has predominantly Types 1 and 2 of Kerogen, this means that there is oil present in the field.

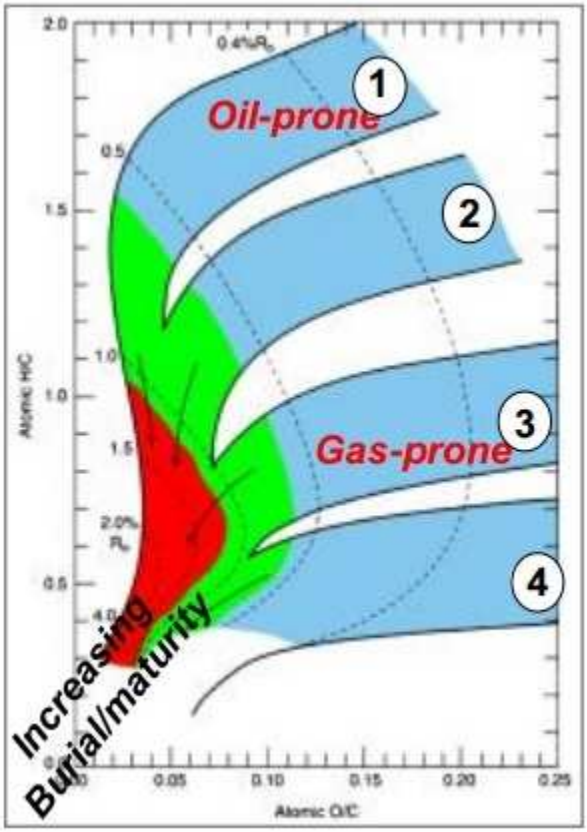

Fig. 4 — Van Krevelen diagram, defining the four types of Kerogen, where Types 1 and 2 are indicative of oil, and Types 3 and 4 are indicative of gas (Ayers, 2011)

The permeability of the Eagle Ford Shale ranges from 10^{-8} and 1 md. Furthermore, the permeability decreases and the depth of the formation increases. The permeability

decreases with depth because of compaction, where the deeper layers are more compacted therefore get "crushed" and thus, decreasing the permeability.

Through the work that Mullen (2010) performed, it was discovered that the mineralogy of the Eagle Ford changes going from west to east; the "more western well is more quartz rich" while the other two wells he investigated are more carbonate and clay rich. This difference in mineralogy is explained by the geology of the Eagle Ford Shale. "In the Cretaceous period, the eastern side of play subsided less than the western side; consequently, the upper Cretaceous rocks in the eastern side of the play contain more shale and carbonates and less sandstone in comparison with time-equivalent rocks in the western part of the play" (Mullen, 2010).

2.2 Producing the Eagle Ford Shale

Hydraulic fracturing has been used since the 1940s and is now a "key element" in developing unconventional reservoirs worldwide (Fazelipour, 2011(a)). Hydraulic fracturing provides an economical way to recover the hydrocarbons present in unconventional reservoirs – such as the Eagle Ford Shale. To optimize these hydraulic fractures, it is common to increase the length of the well, along with implementing an increased multi-stage hydraulic fracturing treatment, both of which lead to the maximum of the reservoir exposed, hence producing the maximum amount of hydrocarbons (Fazelipour, 2011(a)).

Since 2009, the Eagle Ford Shale has grown significantly, greatly due to the use of hydraulic fractures to acquire the hydrocarbon from the play, and the strong performance of the wells. This paper focuses primarily on the gas, condensate and oil windows of the Eagle Ford Shale, whose acreage has over 200 rigs as of February 2012 (Bazan et al., 2012).

Shale-gas formations (such as the Eagle Ford Shale) have natural fractures present, which increase the complexity of the "growth patterns of hydraulic fractures." Furthermore, when multistage hydraulic-fracturing treatments are implemented, it creates "conductive networks that could be considered as stimulated reservoir volumes which have been effectively contacted and contribute to economically viable production profiles." (Fazelipour, 2011(b)).

When designing the hydraulic fracture, several factors must be considered. The space between the hydraulic fractures and the amount of proppant to be injected are two important parameters. Furthermore, the orientation of the well and the conductivity of the fractures are "fundamental design parameters that must be rigorously evaluated when designing horizontal wells." When determining the proppant to use, five main parameters are considered:

- The fracture fluid selection
- Proppant cost
- Availability
- Resulting fracture conductivity
- Economics

The fluid used in the hydraulic fracture has a huge impact on the type of proppant that will be used. Since the Eagle Ford Shale has very low permeability, "often the need for fracture conductivity is regarded as unimportant, and instead fracture designs focus on increasing reservoir contact."

In unconventional reservoirs, one of the primary goals when designing the completion, is to contact as much of the reservoir as possible. This makes these reservoirs economical for development, however leads to limited connectivity between the hydraulic fractures and the wellbore (Bazan et al., 2012).

When designing the hydraulic fracture treatments for the Eagle Ford Shale, a large volume of water is pumped to displace the proppant from the wellbore. This is the standard

practice used for all unconventional reservoirs. However, this method was unsuccessful in the Eagle Ford because of the calcareous makeup and complex geology of the reservoir, which poses significant completion design challenges. The hydraulic fracture design currently used in the Eagle Ford is composed to use "7500-9000 bbl of a hybrid fracturing fluid (slickwater and linear gel) with 40/80 lightweight ceramic proppant." (Bazan et al., 2012). This design has proved successful in the Eagle Ford, increases the conductivity of the fractures and uses remarkably less water per stage than the original design that was first mentioned (Bazan et al., 2012).

2.3 Fluids Present in the Eagle Ford Shale

There are three different fluid types present in the Eagle Ford Shale due to the three maturation windows, ranging from black oil to dry gas (Ilk et al., 2012), as seen in **Fig. 5**. Tian, et al. (2013) determined the type of hydrocarbon present by analyzing the GOR of the first three months of production. As seen in the map below, The Greater Core Eagle Ford (circled in red) ranges from black oil to dry gas wells (Tian et al., 2013), and the hydrocarbon fluid composition greatly varies with thermal maturity, as previously stated. It is seen in the figure below, which indicated different degrees of thermal maturation. Higher thermal maturation leads to gas, and lower thermal maturation leads to oil. This study will focus on certain oil wells in the Karnes region.

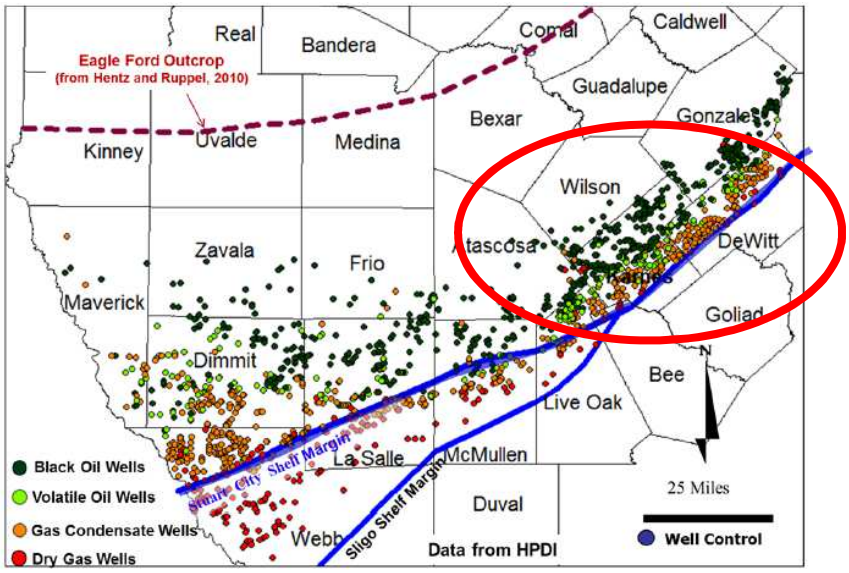

Fig. 5 — Different hydrocarbon types present in the Eagle Ford Shale (Tian et al., 2013)

The majority of the dry gas wells are located on the Stuart City Shelf Margin, which, as seen in Fig. 5 runs though The Greater Core Eagle Ford. The oil wells are located above the Stuart City Shelf Margin, and range from volatile oil to black oil wells as you move upward into the county.

2.4 Flow Regimes of the Eagle Ford Shale

Three flow regimes are present in the Eagle Ford shale gas regions. The three regimes are bilinear flow, boundary dominated flow and matrix linear flow, and are present only in the gas-bearing zones of the Eagle Ford. These three regimes are seen in a log-log plot of the production of a well over time, where early time is indicative of bilinear flow due to the negative ¼ slope, late time is where the boundary effect is seen and in between is the matrix linear flow, shown by the negative half-slope, as indicated in **Fig. 6** below (Xu et al., 2012)

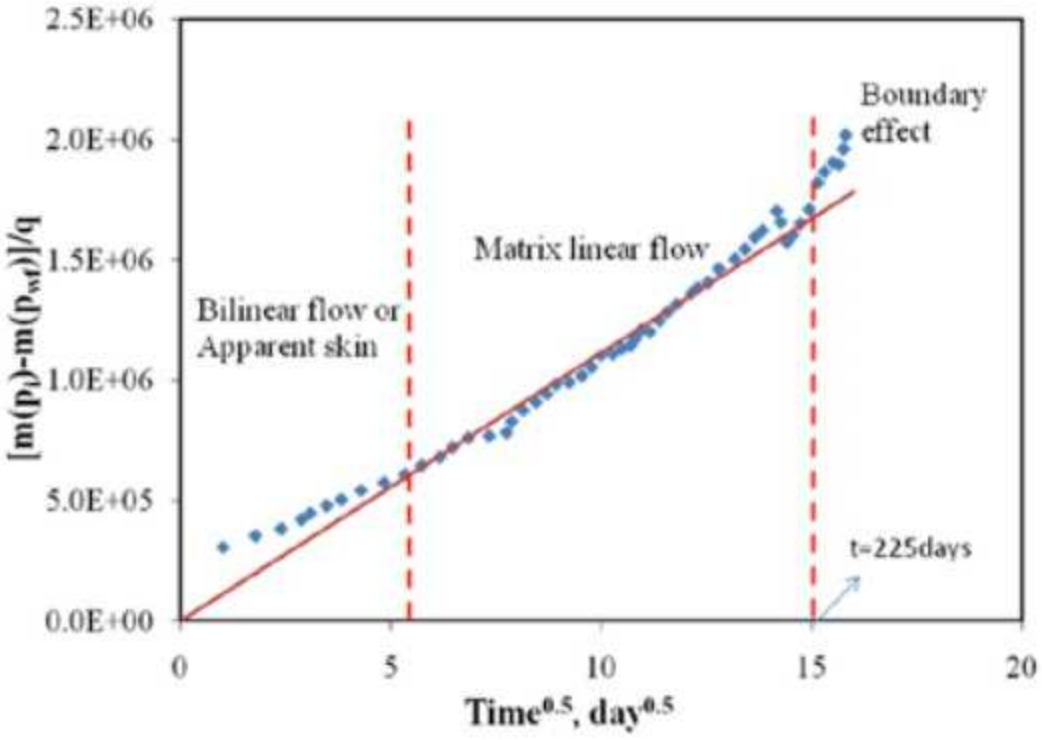

Fig. 6 — Identification of the three flow regimes in the gas reservoir of the Eagle Ford (Xu et al., 2012)

When producing these different regions, different hydraulic fracture treatments are used, "depending on the fluid type – for example, slickwater fluid system is pumped for gas rich areas, whereas hybrid or crosslink fluid system with higher proppant concentrations are pumped for the liquid-rich areas (Bazan, et al., 2012)

Bilinear flow is "resulting from combined simultaneous linear flow in perpendicular directions. This flow regime is seen most commonly in tests of hydraulically fractured wells and occurs for finite-conductivity fracture where linear flow exists both in the fracture and to the fracture plane." (Schlumberger Glossary, 2014).

2.5 Models Already Created to Forecast and Determine Reserves

Reservoir simulation, type-curve and decline-curve analysis were considered the most useful methods for estimating reserves (Gong et al.). Several methods have been used to to estimate and forecast the production of the Eagle Ford. Monte Carlo simulation was performed along with reservoir simulation was performed by Dong et al. on dry gas wells to forecast production and determine the reserves. Arps' decline curve analysis has often been used in unconventional reservoirs to determine reserves and forecast production, however is inaccurate due to the low permeability of the reservoir (Gong et al., 2013).

Decline curve models have been created to estimate reserves. The power-law decline model was introduced by Ilk et al. The stretched-exponential-production-decline (SEPD) model was introduced by Valko and Lee, and has been adapted to determine resources and reserves, however tends to underestimate total reserves (Gong et al., 2013).

Bootstrap methods were created by Jochen and Spivey, and Cheng et al. that generate probabilistic decline-curve forecasts for wells based on producing wells. A Bayesian method has been developed by Gong et al. which, again, uses a probabilistic approach and data from producing wells. These methods also determine reserves and resources, and it is the method that was used in Gong et al. (2012) paper.

In this study, we will apply only the Modified Hyperbolic and the Power Law Exponential Models to our data set, however will present a variety of different equations that can be used to perform decline curve analysis.

2.5.1 Deterministic Decline Curve Models

In this section, I will present the different deterministic decline curve models that are used for decline curve analysis.

Eq. 2.1 and Eq. 2.2 are Arps' equations, where Eq. 2.2 is the exponential decline and Eq. 2.1 follows a harmonic decline when $b = 1$ and a hyperbolic decline when $b \neq 1$. These two equations are standard equations used when performing decline curve analysis, and are ideal for the conventional reservoirs cases.

$$q(t) = \frac{q_i}{(1 + bD_i t)^{1/b}}; b \neq 0 \quad \text{..... (2.1)}$$

$$q(t) = q_i \exp(-Dt); b = 0 \quad \text{..... (2.1)}$$

In the two equations above, *b* is Arp's dimensionless hyperbolic decline constant. In conventional reservoirs, the exponent b is between 0 and 1 and the producing well is in boundary-dominated flow. However, in unconventional reservoirs, the flow is not boundary-dominated, therefore *b* is greater than 1. Though this is an incorrect use of Arp's equation, it is often used to estimate reserves (Gong et al.).

Eq. 2.3 is the Power Law Exponential (PLE) equation.

$$q(t) = q_i \exp(-D_\infty t - D_i t^n) \quad \text{..... (2.2)}$$

where $-D_\infty$ is the power law decline rate at infinite time constant, n is the dimensionless time exponent, typically between 0 and 1, and D_i is the power law decline constant, however is determined by determining D_1, which is the instantaneous decline at t=1, therefore

$$D_i = \frac{D_1}{n} \quad \text{.....(2.4)}$$

D_i, in this model, is not the initial instantaneous decline but the instantaneous decline at t=1 divided by n when D_∞ is equal to one. Also, the D_∞ term can fit many different values in early-time, however it affects late-time rates therefore the "forecasts become sensitive to D_∞" (Mattar et al., 2008)

Eq. 2.5 is the Modified Hyperbolic (MH) equation.

$$q(t)=\begin{cases}\dfrac{q_i}{[1+bD_it]^{1/b}}; & t<t^*\\ q_{i\exp}\exp[-D_{\lim}t]; & t>t^*\end{cases}\quad\ldots\ldots\ldots\ldots\ldots\ldots\ldots\ldots\ldots\ldots\ldots\ldots(2.5)$$

$$D=\frac{1}{\frac{1}{D_i}+bt}\quad\ldots\ldots\ldots\ldots\ldots\ldots\ldots\ldots\ldots\ldots\ldots\ldots\ldots\ldots\ldots\ldots\ldots\ldots\ldots\ldots\ldots\ldots(2.6)$$

The decline rate, D, is not a constant but decreases continuously, as seen in Eq. 2.6. "When D becomes too small, the gas rate no longer declines significantly, and the reserves can be over-predicted. To circumvent the problem of D becoming too small, Robertson (1988) introduced the Modified Hyperbolic Decline method, that imposes a limit below which D is not allowed to decline ($D_{\lim}$)." (Mattar et al., 2008)

Eq. 2.7 is the Stretched Exponential Production Decline Model equation.

$$q(t)=q_i\exp[-(\frac{t}{\tau})^{\eta}]\ldots\ldots\ldots\ldots\ldots\ldots\ldots\ldots\ldots\ldots\ldots\ldots\ldots\ldots\ldots\ldots\ldots\ldots\ldots\ldots\ldots\ldots(2.7)$$

where τ is the characteristic time parameter and η is the dimensionless exponent parameter. This model was introduced by Valko and Lee in 2010, and is used to quantify the uncertainty in field production forecasts. However, it does not quantify the uncertainty the reserves based on the production of a single well (Gong et al., 2012)

Eq. 2.8 is the Rate-Decline Analysis for Fractured-Dominated Shale Reservoir equation.

$$q(t)=q_it^{-m}\exp[\frac{a}{1-m}(t^{1-m}-1)]\ldots\ldots\ldots\ldots\ldots\ldots\ldots\ldots\ldots\ldots\ldots\ldots\ldots\ldots\ldots\ldots\ldots\ldots\ldots\ldots\ldots\ldots(2.8)$$

where a is the intercept constant for Duong's model (1/time) and m is the dimensionless slope for Duong's model (Gonzalez, 2013).

Eq. 2.9 is the Logistic growth curve equation.

$$q(t) = \frac{Knat^{n-1}}{(a+t^n)^2} \quad \text{.....(2.9)}$$

where K is the EUR in Mcf, a is a constant, n is a hyperbolic exponent that controls the steepness of the decline, and where

$$t^n = \frac{K}{2} \quad \text{.....(2.10)}$$

Clark et al presented this method in 2011 (Gonzalez et al., 2013).

None of the above DCA models quantify the uncertainty in production forecasts and reserves estimates by themselves (they need to be combined with other models to properly quantify these uncertainties - Gong et al., 2012) .

2.5.2 Probabilistic Decline Curve Models Proposed for Decline Curve Analysis

The Bootstrap Method (JSM) was presented by Jochen and Spivey in 1996. This model generates synthetic realizations of production data, however is not well calibrated for conventional reservoirs. This model can generate probabilistic decline curve forecasts and quantify reserves uncertainty for single wells based on the existing production. The P90-P10 range for reserves using this method estimated 40% of the "true reserves". This method modifies the historical production to generate different realizations to match, which should be avoided because we want the production data to be untouched. The work done was done on 100 conventional wells (Gong et al., 2012).

The Modified Bootstrap Method (MBM) was presented by Cheng et al. (2010). This method generates synthetic realizations of production data, and has been well calibrated for a limited number of test cases. This model also generates probabilistic decline curve forecasts and quantifies uncertainty for single wells based on existing production. However, the P90-P10 range for reserves is estimated at 80% of the true reserves, which

is expected because this method is calibrated probabilistically. This method, again, alters the original production data which is avoided when possible (Gong et al.)

The Markov Chain Monte Carlo (MCMC) was presented by Dong et al. (2011). It does not modify the actual production data, and has been well calibrated for a limited number of test cases. This method is faster and generates a smaller confidence interval than the MBM. MCMC has been combined with Bayes' theorem by Liu and McVay in 2009 and Xie et al. in 2011, to quantify uncertainty in reservoir simulation (Gong et al., 2012).

These three methods were all developed based on Arp's method, and there is limited work published on the use of these methods (particularly in unconventional reservoirs) (Gonzalez, 2013). The methods presented above were all done on Barnett Shale wells.

3. SITE CHARACTERIZATION OF THE EAGLE FORD SHALE

3.1 Specific Geology of the Greater Core of the Eagle Ford Shale

The Greater Core Eagle Ford has an interesting geology because of the plethora of geological features present. Firstly, the Karnes trough runs through the county. Furthermore, the Stuart Shelf line runs through the county as well. As seen in Fig. 4, the majority of the dry gas wells fall along this line.

The Karnes Trough is a thick, organic-rich part of the Eagle Ford Shale that is a "sediment trap for shelf-derived Eagle Ford siltsone" and is a "fault-controlled graben system with expected higher natural fracture intensity" (Corbett, 2010). The trough was created by the Person-Dubose Edwards shelf edge, which separates the Eagle Ford Shale into an "up-dip oil play and a down-dip gas play." This also helps control the fluid migration by using the faults as barriers. This all explains the reason there are several fluid types within the same county, and can be seen in the figure below.

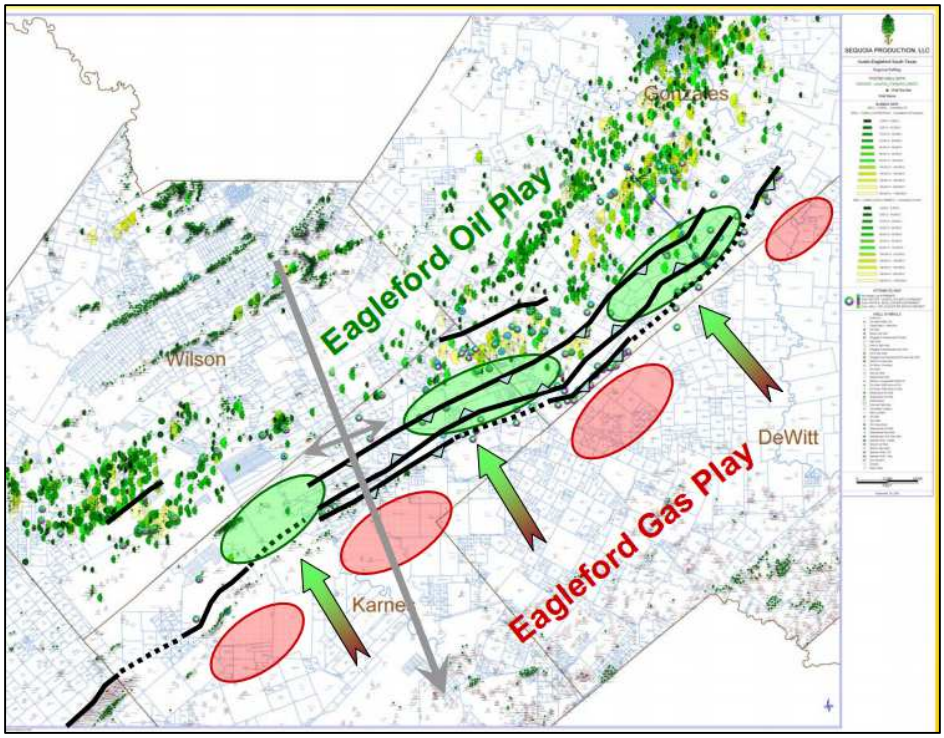

Fig. 7 — The Eagle Ford Play Distribution where we can see the difference between the oil and gas plays due to the Karnes Trough and the Stuart City Edwards reef (Corbett, 2010)

These two plays found in the same region (and specifically, the Greater Core Eagle Ford) create two environments. As previously seen, up-dip of the reef margin is oil-rich, however it is also normally pressured, with a "significant lateral variability in organic-rich shale abundance and reservoir quality related to reef margin controlled depocenters." (Corbett, 2010). Down-dip of the reef margin is the gas play, and is an area of the field that is significantly over-pressured, with a high lateral variation of the reservoir "and primary permeability controlled by the location of distal turbidite deposition." (Corbett, 2010).

The northwestern part of The Greater Core Eagle Ford, where the oil play is located, shows deposits of the Early Cretaceous, which are also seen in the outcrops, located 75 miles northwest of the county. This region is not affected by any significant facies changes, however they are observed in different areas of the Eagle Ford.

There are three different geological groups in the northwestern part of The Greater Core Eagle Ford. The deepest, named Trinity, consists of five formations. The deepest formation is Sligo, with a lithology of limestone. Above is Hammet, with a lithology of shale, followed by Cow Creek with a lithology of shaly limestone. Above is Bexar with a lithology of shale and finally, the upper Trinity's formation is the Glen Rose, with a lithology of shale, limestone and dolomitic limestone. Above Trinity is the Fredericksburg group which consists of two formations. The Walnut formation has a lithology of shaly limestone and the lower Edwards has a lithology of dolomitic limestone. Finally the Washita group consists of five formations. The middle Edwards with a lithology of shale and limestone, the upper Edwards with a lithology of dolomitic limestone, the Georgetown with a lithology of shaly limestone dolomitic limestone, the Del Rio with a lithology of calcareous clay, and finally, the Buda with a lithology of shaly limestone. As previously discussed, the oil play of The Greater Core Eagle Ford is primarily shale-based, which is proven by this break down of the different formations.

3.2 Specific Production of the Greater Core Eagle Ford

Based on **Fig. 8** below, it is evident that the oil production of The Greater Core Eagle Ford is higher than the majority of the Eagle Ford. The maximum oil production reaches around 80,000 barrels on the northwest side of the county which is where the majority of the oil wells are located. It is evident from the same figure that the oil production decreases as we go to the southeast side of the county. This is where the Stuart City Shelf Margin intercepts the county, indicating that this region is filled with dry gas wells, as seen in Fig. 8. Hence, the decrease in oil production in this area of the county is expected due to the nature of the wells.

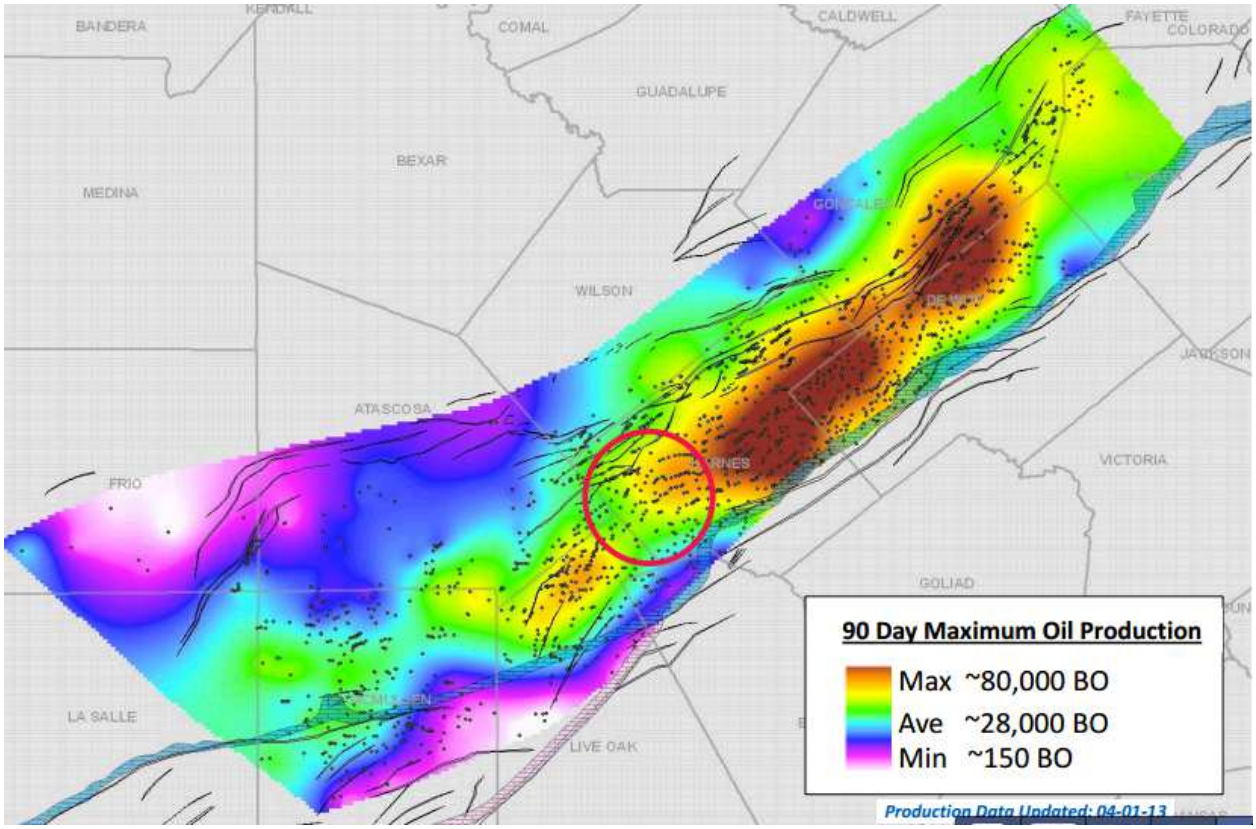

Fig. 8 — Hydrocarbon production window. The Greater Core Eagle Ford has one of the regions of maximum oil production of the region indicated on the map. The red circled area of The Greater Core Eagle Ford indicates the gas condensate and dry gas wells (Breyer et al., 2013)

According to Tian et al. (2013), it can also be noted that there are fewer gas wells and the gas production of The Greater Core Eagle Ford is significantly lower than the oil production.

3.3 Specific Fluid Types of the Greater Core Eagle Ford

As previously stated, The Greater Core Eagle Ford has three different hydrocarbon types being produced. The fluid types range from oil to dry gas. The Greater Core Eagle Ford is especially interesting because all three of types of fluids are produced, which is a trend not seen in other counties, as seen in **Fig. 9** below.

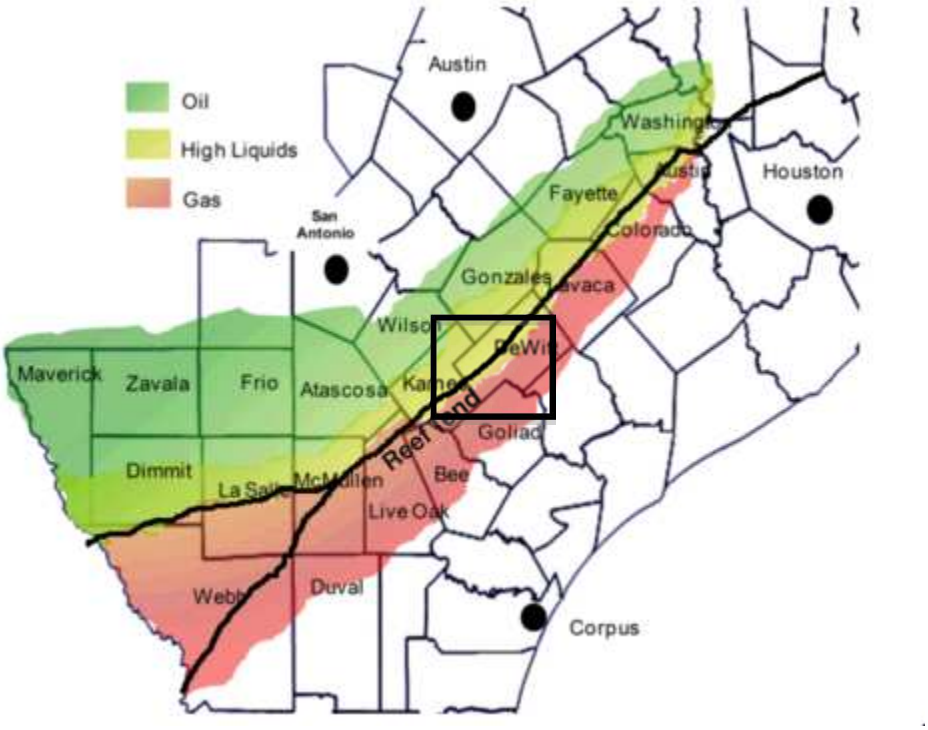

Fig. 9 — Fluid phases of the Eagle Ford Shale, specifically focusing on the Greater Core Eagle Ford and the three phases present (Mullen, 2010)

Mullen (2010) performed a case study on three different wells in three different hydrocarbon zones - a dry-gas window, a gas condensate window and an oil window. The author has not disclosed the location of the three wells thus we will assume that the fluid types are the same throughout the play. Well 1 (gas-condensate) is located in the Eastern part of the field, and Well 3 (oil) is located in the Western part of the field, with Well 2 (dry-gas) in between the two, as seen below in **Fig. 10**.

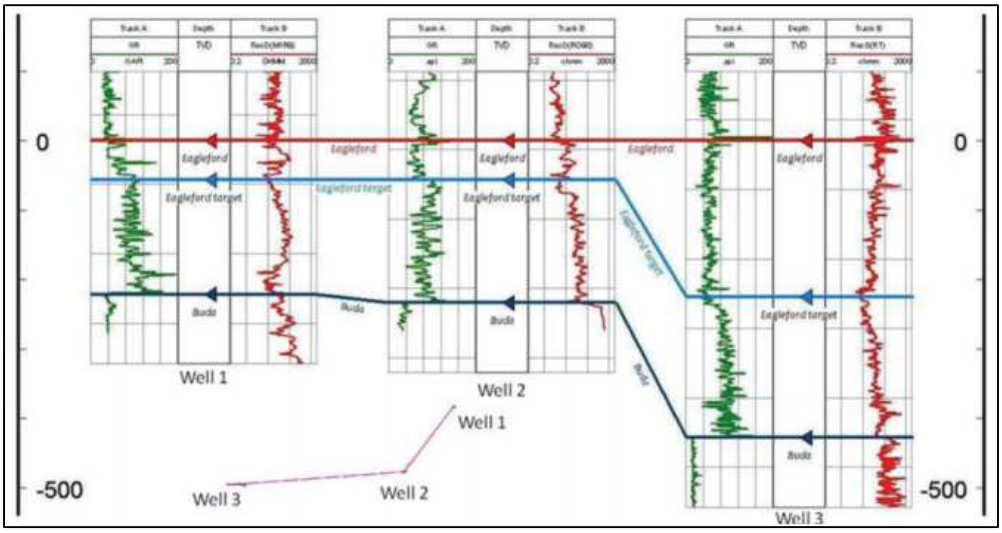

Fig. 10 — Relative locations of the three wells, along with their thicknesses and the basic log response across the Eagle Ford Shale (Mullen, 2010)

Each of the three fluid windows has different properties, and the three will be explored below. The gas-condensate window, where Well 1 of Mullen's analysis is located, is in the eastern part of the field. The rock in this part of the field is soft due to the high clay content, and thus the proppant used when hydraulically fracturing this part of the reservoir can become embedded in the fractures, and also can lead to high closure pressures. Both of these characteristics need to be taken into consideration when finalizing the completions design of this part of the reservoir. From Mullen's analysis, it was also determine that the porosity of this area ranges from 8% to 18%, the permeability from 1 to 800 nD, and has a total organics content (TOC) ranging from 2% to 8%. It was also determined that the "sweet spot" is between 12,860 and 12,880 feet, therefore future drilling in this area should be targeted to this interval.

Well 2 is located in the dry-gas window. This area has a different geological composition than seen in Well 1. It is more clay-rich, making the reservoir rock is much "softer", thus swelling is a potential problem and the completion should be designed accordingly. The porosity was determined to be 8%, and the permeability was tested using core data, however could not be identified due to the limitations of the NMR tool and the extremely

low permeability. This area of the Eagle Ford is kerogen-rich, meaning that the reservoir rock in the lower Eagle Ford is of better quality than the rock in the higher Eagle Ford. Well 3 is located in the oil window. This area of the Eagle Ford is much more clay-rich than seen previously, with "~70% swelling clays making up about 7% of the total rock composition" meaning that when fracturing the reservoir, clay control will be necessary to minimize "swelling clays on the pore throats in the reservoir." (Mullen, 2010). The total porosity of this area of the Eagle Ford is between 5% and 14%, averaging around 10%. It is evident from Fig. 10 that the thickness of the reservoir in Well 3 is much larger compared to the other two wells.

4 METHODOLOGY

4.1 Overview of the Research

Production and completion data of 68 wells in the Greater Eagle Ford Core was used to perform this study. The first step of this process was to determine what type of fluid we wanted to work with. It was decided to work with Barrels of Oil Equivalent (BOE) to incorporate both the oil and gas production of these wells. Therefore, we converted the gas production to oil production, using the conversion shown below in Eq. 4.1, and added it to the oil production.

$$bbl = \frac{Mscf}{6} \quad \text{.....(4.1)}$$

After this was done, we plotted all of the production data against time to determine which wells were good candidates to perform decline curve analysis. From these 68 wells, we determined that 16 had a good set of data, with a good decline and an adequate amount of data to perform the study. The production data is presented below in **Fig. 11**.

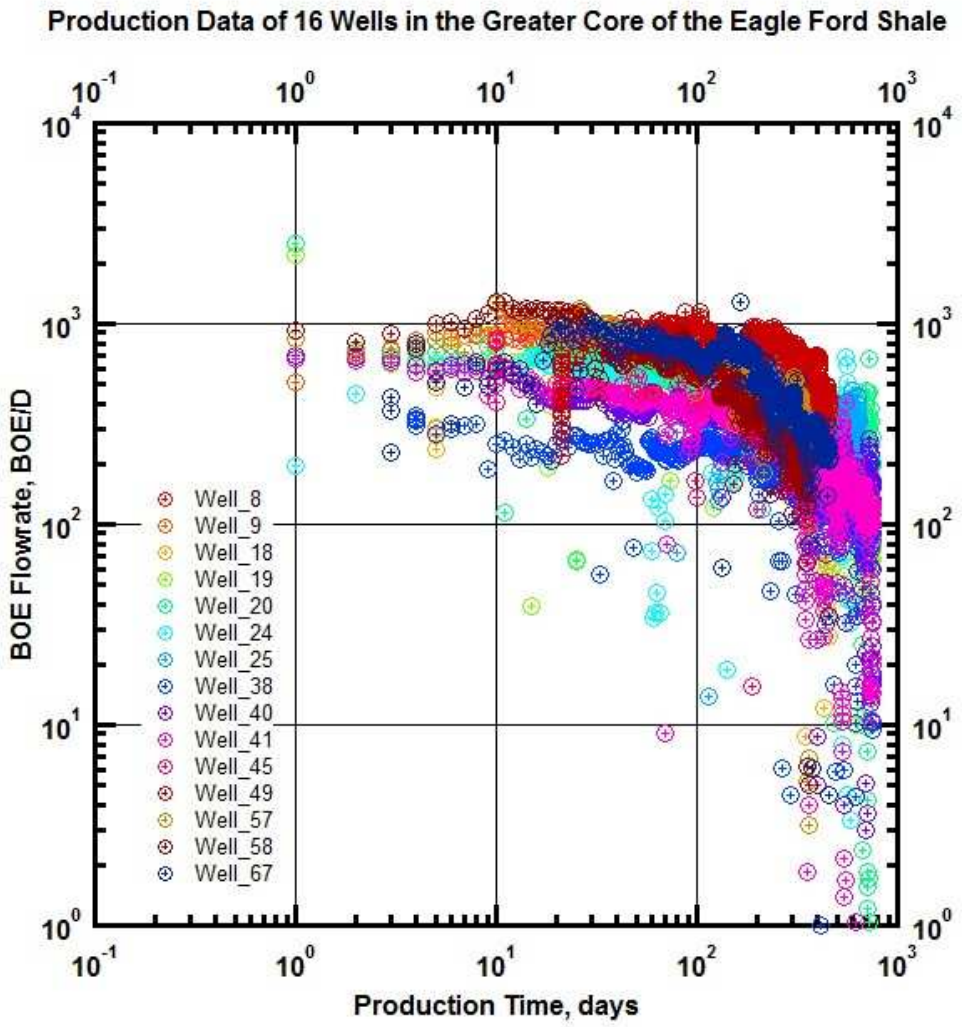

Fig. 11 — Data Production of the initial 16 wells to be used in this study, located in the Greater Eagle Ford

We performed the decline curve analysis on these 16 wells using the Modified Hyperbolic (MH) and Power Law Exponential (PLE) models, where we retrieved the Estimated Ultimate Recovery (EUR), and different parameters used in each model.

We looked at these 16 wells, and decided to set up two sets of wells. The first set was for five wells producing more than 700 days, and the second set was for three wells producing more than 450 days. Set 1 data set was then truncated to 700 days, and the set 2 data was

truncated to 450 days. This was done to be able to compare the results of the wells in each set to each other, which provides a good comparison of the results.

The next step was to perform the Bayesian forecasting using the Bayesian paradigm on the wells in the two different sets. We began this step by performing a least-squares optimization to obtain the optimized values of the different parameters of the two different models. After this was done, we performed a Markov Chain Monte Carlo (MCMC) using both the MH and PLE models. The MCMC was run between 2 and 50 million iterations, depending on how long it took for the parameters to converge. This gave the most accurate value of each of the parameters of the two models.

With the values of MCMC, we ran the prediction using the Bayesian paradigm. The prediction was run for the number of truncated days in the two sets, meaning 700 days for Set 1 and 450 days for Set 2, and then it was run for 30 years, the industry set time for abandonment. Therefore, each well has two sets of results – one using the MH model to run the Bayesian Forecasting, and one using the PLE model to run the Bayesian paradigm.

Finally, the results of the Bayesian approach were compared to the results of the decline curve analysis. This research was to determine whether or not the decline curve analysis performed in industry is an appropriate analysis of the reserves in unconventional reservoirs.

4.2 Deterministic Decline Models

4.2.1 Decline Curve Analysis using the Modified Hyperbolic and Power Law Exponential Models

We plotted the production data of the 68 wells and determined that 16 of the 68 had a good set of data to perform decline curve analysis. The 16 wells chosen had enough production

data to show the trend of the data, and showed a decline, which is necessary when performing decline curve analysis.

The two models used in this study are the Modified Hyperbolic and the Power Law Exponential, shown below in Eq. 4.2 and Eq. 4.5, respectively.

$$q(t) = \begin{cases} \dfrac{q_i}{[1+bD_i t]^{1/b}}; & t < t^* \\ q_{i\,\exp} \exp[-D_{\lim} t]; & t > t^* \end{cases} \quad \text{.....(4.2)}$$

where:

$$D_{\lim} = -\frac{\ln[1-p]}{365} \quad \text{.....(4.3)}$$

$$t^* = \frac{(\frac{D_i}{D_{\lim}} - 1)}{bD_i} \quad \text{.....(4.4)}$$

For the Modified Hyperbolic method, we set the decline limit (*p)* to 10%, which is a conservative decline limit. "When D becomes too small, the gas rate no longer declines significantly, and the reserves can be over-predicted. To circumvent the problem of D, Robertson (1988) introduced the Modified Decline method that imposes a limit below which D is not allowed to decline (D_{lim}). Once the decline reaches D_{lim}, the equation switches to Exponential Decline" (Mattar et al., 2008)

$$q(t) = q_i \exp(-D_\infty t - D_i t^n) \quad \text{.....(4.5)}$$

In the Power Law Exponential, we will set D_∞ to 0 and *n* to 1, which makes the power law change to an exponential decline. "As *n* trends to 0, the power law's decline rates start off large, but become smaller over time, similar to how tight reservoirs behave. The reason for D_∞ in the Power Law is that it places a limit on how low the decline can become to avoid reserve over-prediction". (Mattar et al., 2008)

After we ran the two models, we obtained a set of results of the parameters of each equation, as well as a value of Estimated Ultimate Recovery (EUR). **Tables 1** and **2** show the results for each of the models.

Table 1 — Parameters of the Modified Hyperbolic method, along with the EUR

	Modified Hyperbolic				
	D-parameter			t=30 years	qboe=5 BOE/d
Well	Intercept (Di)	qboie	b	EUR (BOE)	EUR (BOE)
1	0.00373	1115.386	0.5	643454	632495
8	0.00898	789.355	1	394789	387327
9	0.00628	824.935	0.48	247315	235310
18	0.00277	1020.636	0.3	505779	495450
19	0.0036	714.131	0.21	252692	247766
20	0.00219	723.808	0.46	552483	543715
24	0.0019	626.8	0.87	807015	817654
25	0.00227	713.334	1	909052	924353
38	0.00157	286.153	0.21	215717	207021
40	0.00191	435.649	0.18	267903	260995
41	0.00347	525.846	0.73	380685	372341
45	0.00463	996.807	0.6	480552	470083
49	0.00135	986.275	0.51	1267115	1282834
57	0.00356	968.403	0.06	285287	283237
58	0.00779	1091.106	0.32	215884	210765
67	0.00425	1063.378	0.3	353379	345636

We notice that the D_i is very low, which differs from what is used in industry. This is because these results are initial decline per day, not per year. However, it can also be noted that there are several results that are unrealistic. Wells 25 and 49 both show reserves around 1 million BOE, which are unlikely.

Table 2 — Parameters of the Power Law Exponential method, along with the EUR

	Power-Law Exponential					
					t=30 years	qboe=5 BOE/d
Well	Slope (n)	Intercept (Di hat)	D infinity	qboie	EUR (BOE)	EUR (BOE)
1	0.6965	0.0187	0	1232.802	551036	546140
8	0.6647	0.0323	1E-14	827.781	208848	205579
9	0.817	0.0147	1E-14	939.062	178914	177303
18	0.0435	1.34	0.0017121	4425.02	454454	451574
19	0.0285	2.59	0.0024472	12780.193	241667	239657
20	0.0075	11.23	0.0012364	72724314	436232	432252
24	0.7955	0.00519	1E-14	635.131	504359	497220
25	0.3675	0.123	5.102E-05	1125.896	950851	1014745
38	0.0075	1.6	0.0015799	1484.943	169108	165952
40	0.0125	6.69	0.0012804	468183.01	262772	258939
41	0.6505	0.021	1E-14	577.211	289908	282623
45	0.8965	0.00654	1E-14	1030.316	292684	290799
49	0.8965	0.00191	1.2E-14	972.7	1081871	1074957
57	0.0105	1.87	0.0034623	6919.812	272443	271004
58	0.0285	1.43	0.0050045	4947.388	192747	191755
67	0.024	2.16	0.0029534	10663.469	306097	304421

As previously stated, D_{inf} should be approximately 0. It is evident from these results that many of the values are, in fact, very close to 0 however others are not. We also see that there are several initial rates (q_{boi}) that are unrealistic, such as in wells 19, 20, 40, 57 and 67. It can also be seen that in the wells where q_{boi} is unrealistic, so is D_i. This is most likely due to the data not following the PLE model, therefore we are forcing the data to fit this model and we obtain unrealistic results.

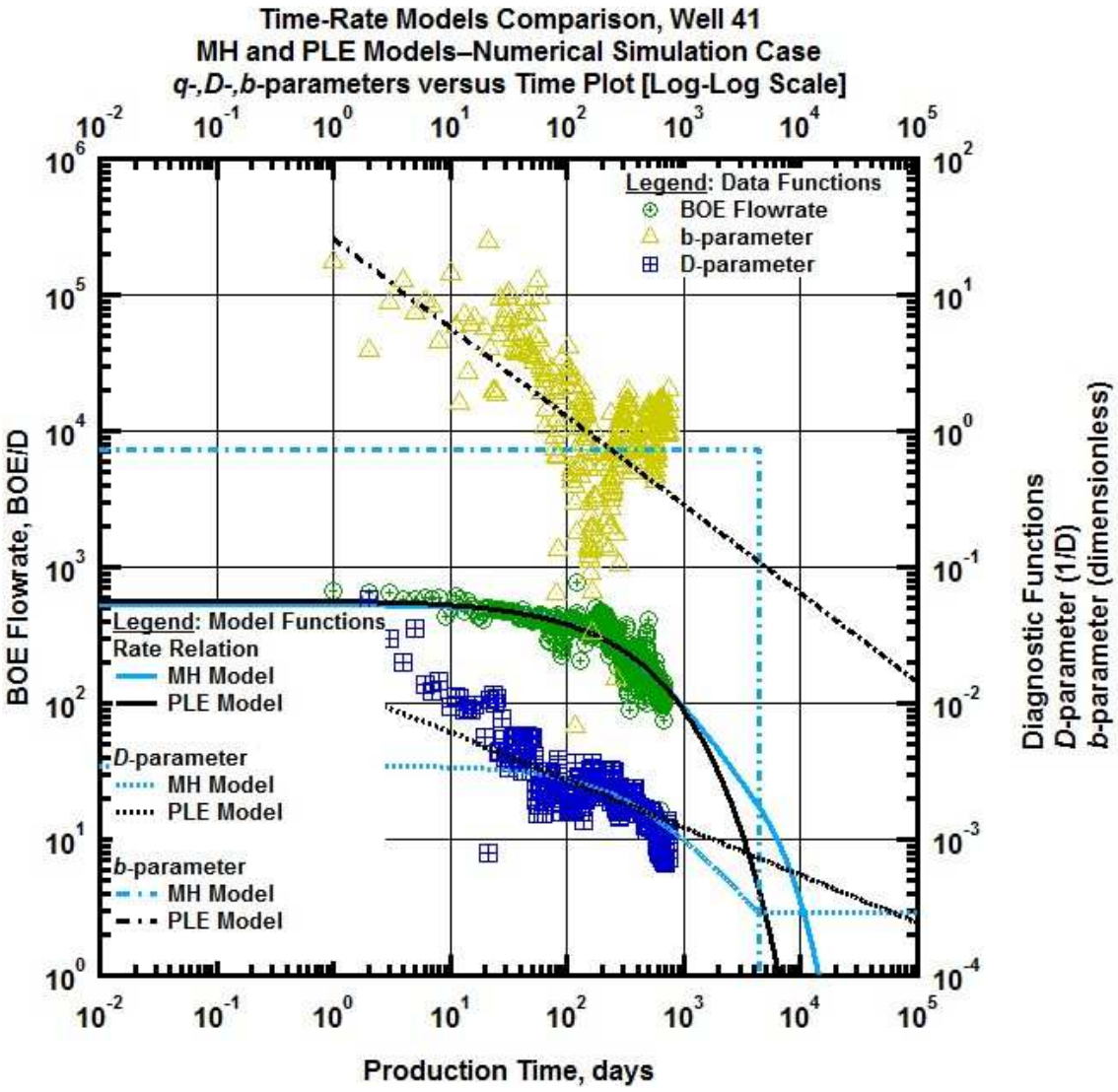

Fig. 12 — qDb plot of Well 41: The solid lines represent the two decline curve models.

4.2.2 Parametric Analysis of the Three Parameters in each DCA Model

There are several parameters in these two equations. In the Modified Hyperbolic, the three variable parameters are the *b*-factor, D_i and q_i, and in the Power Law Exponential, the three variable parameters are n, D_i and q_i, while time (t) is considered constant in both. To better understand how these three parameters affect the two decline curve models, we performed a parametric analysis. The results of this analysis are presented in **Fig. 13-18**.

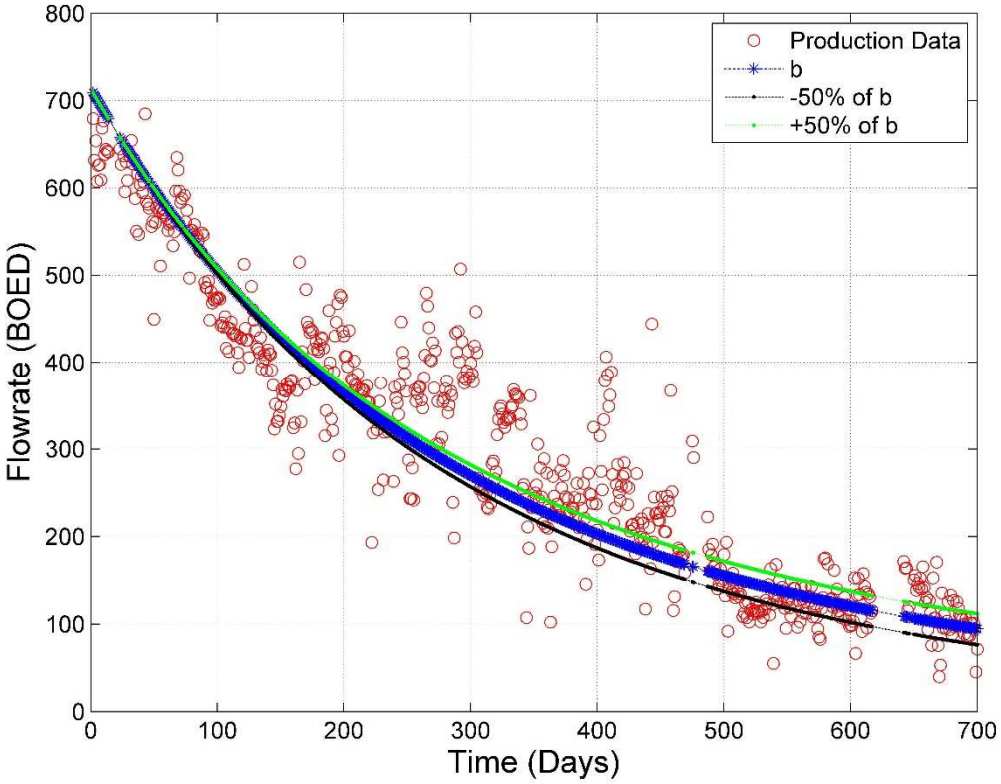

Fig. 13 — Parametric Analysis of the b-factor of the Modified Hyperbolic model

For the parametric analysis of the *b*-factor, we can see from the graph above that when the b-factor is increased, the curve slightly rises above the initial curve, but only in late time. We see the opposite with a decrease in the b-factor. It is also very interesting to see that the curves do not begin to diverge until around 200 days, so the b-factor has more of an influence in the later times of the wells' production.

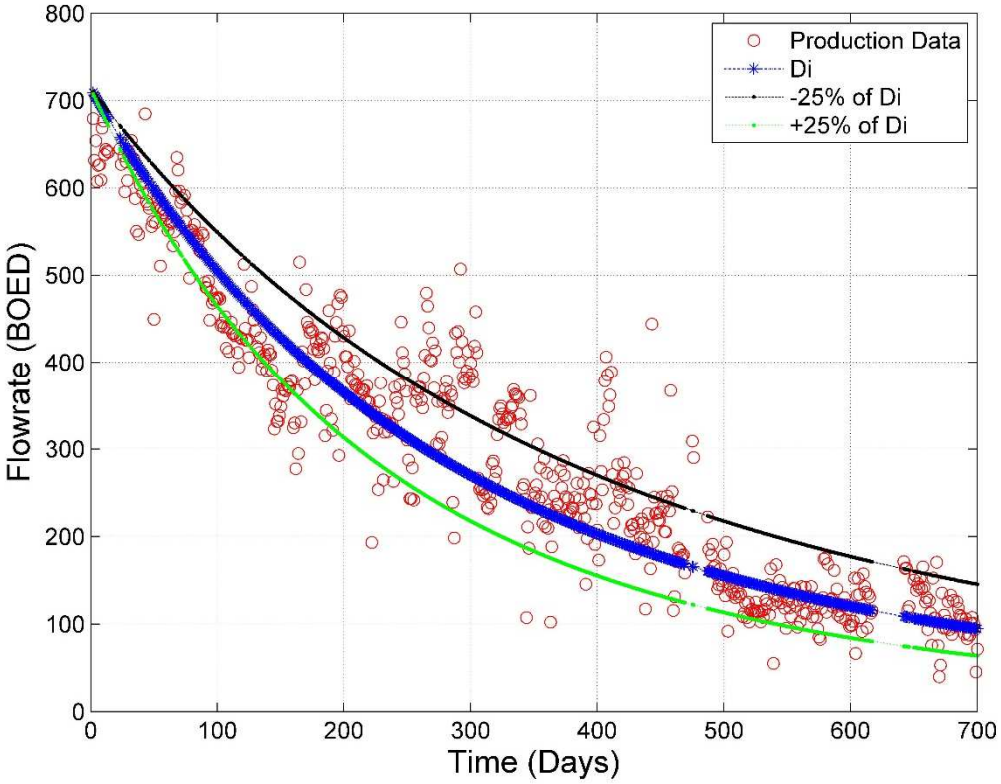

Fig. 14 — Parametric Analysis of D_i for the Modified Hyperbolic model

For the parametric analysis of D_i, we can see from the graph above that when D_i is increased, the curve falls below the initial curve instantaneously. We see the opposite with a decrease in D_i. It is also very interesting to see that the curves begin to depart from time 0, therefore the initial decline plays an important role in the trend that the decline curve will take.

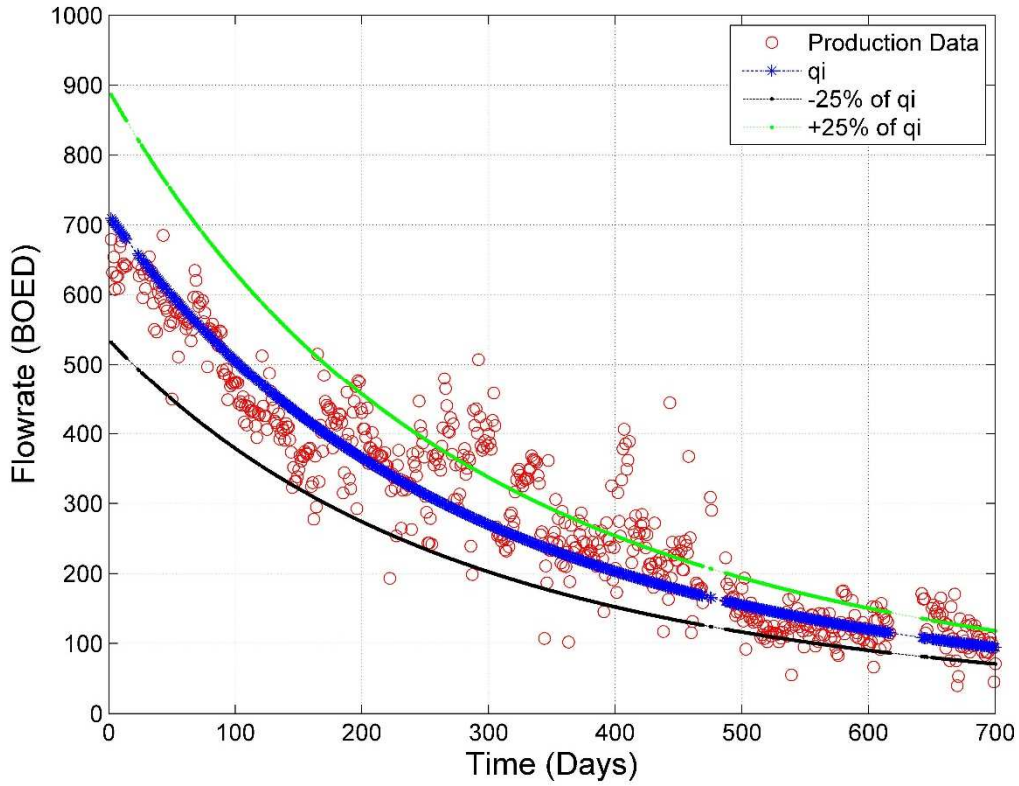

Fig. 15 — Parametric Analysis of q_i for the Modified Hyperbolic Model

For the parametric analysis of q_i, we can see from the graph above that when q_i is increased, the starting point of the decline curve is higher. We see the opposite with a decrease in q_i. These results are expected because the initial rate is changing. It is also interesting to see that the decline curve does not fit the production data when the q_i is incorrect, however the three curves converge in late time. This indicates that initial rate's primary influence is on the early time of the decline curve, however it is also evident that if the value is too high, we will overestimate the reserves, and if the initial rate is too low, we will underestimate the reserves.

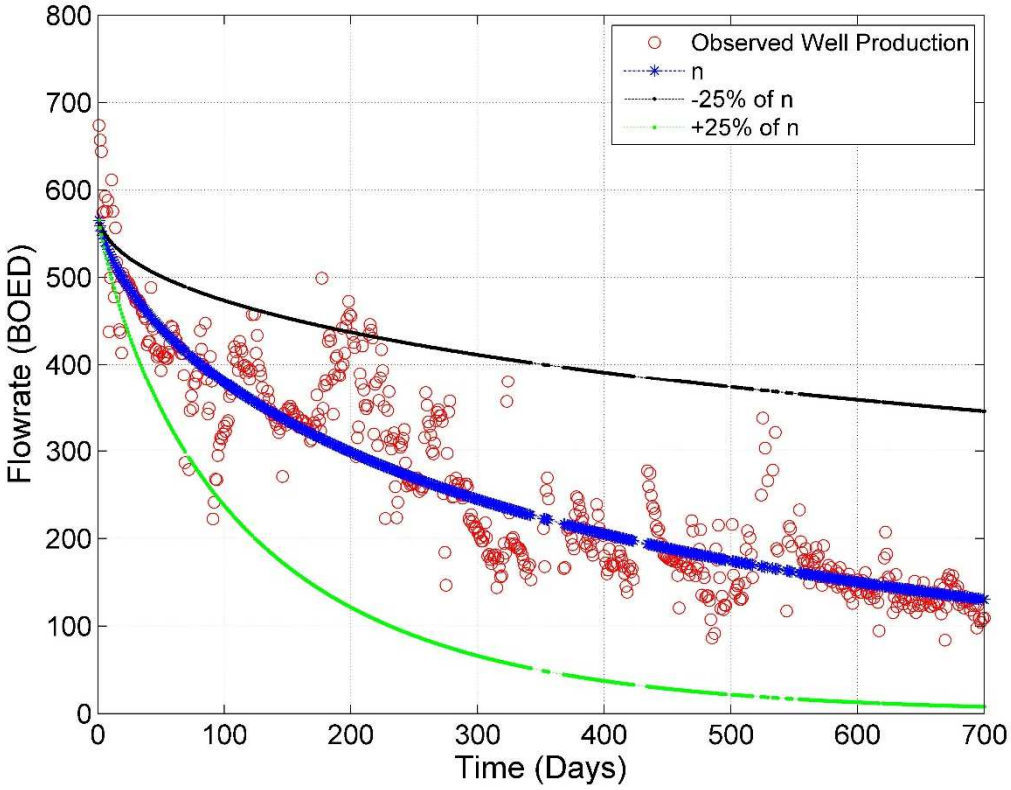

Fig. 16 — Parametric Analysis of the time exponent (n) of the Power Law Exponential model

For the parametric analysis of the time exponent (*n*), when *n* is increased, we see that the decline curve begins at the same rate as the original *n* value, however we see that the slope is decreased. Furthermore, we see that when we increase the *n*, the initial point remains the same (as seen when the *n* is decreased), however that the slope of the curve increases. This is consistent with the definition, because the time exponent is, in fact, a slope.

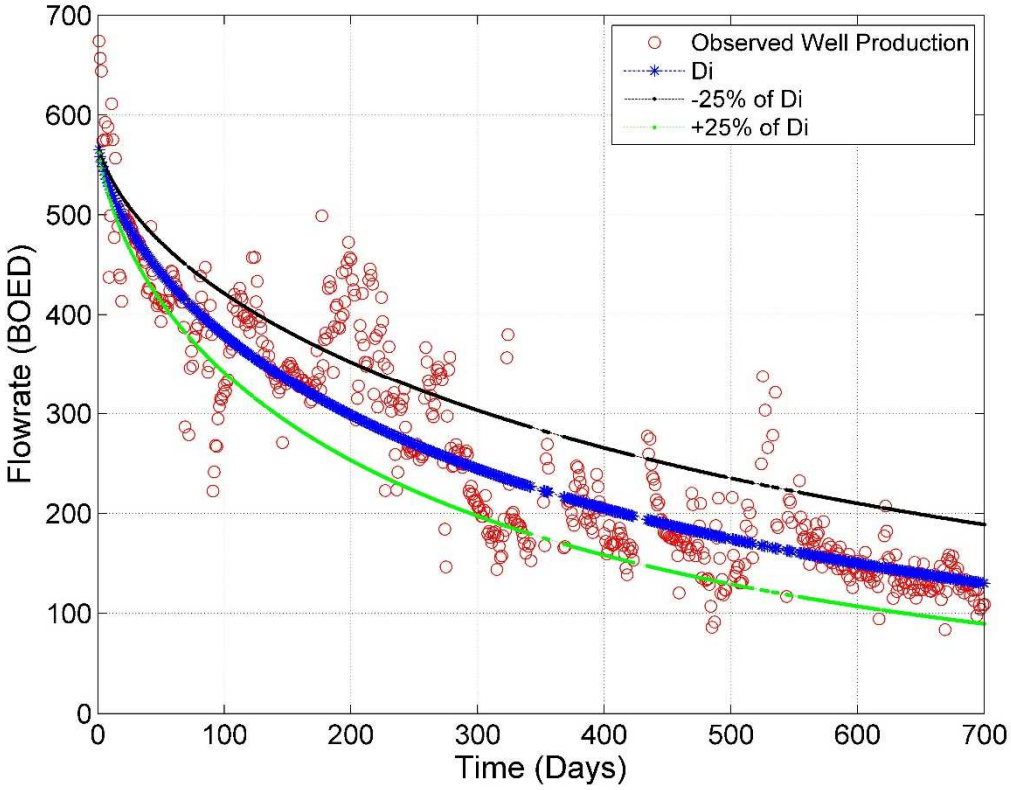

Fig. 17— Parametric Analysis of D_i for the Power Law Exponential Model.

For the parametric analysis of D_i, the three curves share the same initial point. However, when D_i is increased, we see that the decline curve falls below the original curve and that the decline curve is underestimating the reserves. When D_i is decreased, we see that the curve is significantly higher than when using the correct D_i. Furthermore, we can see that using a low D_i will greatly overestimate the reserves, while using a higher value of D_i will underestimate the reserves. It is also interesting to note that the behavior of D_i in the PLE model is the same as the behavior of the D_i in the MH model.

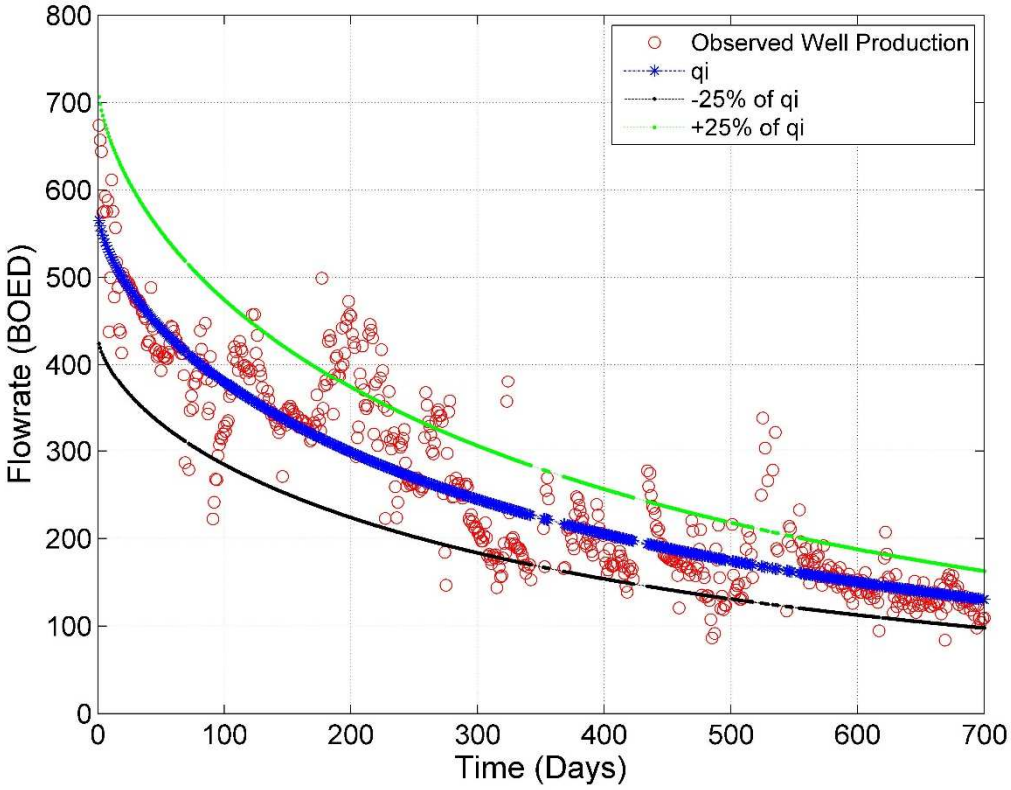

Fig. 18 — Parametric Analysis of q_i for the Power Law Exponential Model

For the parametric analysis of q_i, we can see from the graph above that when q_i is increased, the starting point of the decline curve is higher. We see the opposite with a decrease in q_i. These results are expected because the initial rate is changing. It is also interesting to see that the decline curve does not fit the production data when the q_i is incorrect, however the three curves converge in late time. This indicates that initial rate's primary influence is on the early time of the decline curve, however it is also evident that if the value is too high, we will overestimate the reserves, and if the initial rate is too low, we will underestimate the reserves. This is the same behavior seen in the MH model.

4.3 Data Truncation

Once we performed the decline curve analysis using the Modified Hyperbolic and the Power Law Exponential on the 16 wells, we looked at the production days of these wells. We then decided to truncate the data based on the number of production days each well has. Several wells only produce for a short period of time, therefore we decided to discard them for this study. The desired wells for this study have been producing for over one year.

We identified two sets of wells. One set that has production of over 700 days and another set that has production over 450 days. We then truncated each well's production data to 700 and 450 days, respectively. This was done to be able to perform the Bayesian forecasting on both sets of wells, and then to be able to compare the results to each other, while having a consistent data set of all the wells in each set. Set 1 is the data set that is truncated at 700 days and consists of five wells; Set 2 is truncated to 450 days and consists of three wells. **Table 3** below identifies both data sets.

Table 3 — Identification of two sets of truncated wells. The wells in red font are Set 1, truncated to 700 days, the wells in purple font are Set 2, truncated to 450 days

Well Name	Production Days
Well_8	266
Well_9	268
Well_18	489
Well_19	727
Well_20	738
Well_24	560
Well_25	644
Well_38	705
Well_40	721
Well_41	740
Well_45	274
Well_57	360
Well_58	359
Well_67	459

Once these two data sets were identified, we implemented the Bayesian paradigm on only the eight identified wells. The table shows the number of production days of all 16 wells that we had initially identified, and we can see that Wells 8, 9, 45, 57 and 58 do not have sufficient data, therefore the trend of the production data is not as prevalent as in the wells that have been on production longer. This is why we decided to use 700 days and 450 days to truncate the wells. Furthermore, we did not want to truncate the wells of Set 1 to 450 days because we would have lost the trend of the production data, and would not be able to capture the decline correctly.

4.4 Solving the Inverse Problem using Bayes' Theorem

There are several steps needed to implement Bayes' Theorem. First, we apply an optimization to obtain an optimized set of parameters for each model. It was determined that the least squares optimization was suitable for this study.

After we obtained the optimized set of parameters, we implemented the Markov Chain Monte Carlo. Using the optimized values of parameters, we begin the MCMC using these optimized results. Then, the MCMC runs between two and 50 million iterations, until the parameters converge, which is seen when the results of the MCMC are graphed. From the graphed results, we determine the burn-in point. The burn-in point identifies the point where the parameter has converged, and needs to be the same for each of the three parameters of the two models. After it has been set, we run the Bayesian paradigm. We obtained 1,000 realizations of 1,000 different possibilities of decline curves, then took the mean of these realizations and plotted them against the forward model (either the MH or the PLE). We extended the forecast to 30 years, and compared the forward model with the Bayesian forecast.

4.4.1 Least Squares Optimization

We chose the least squares optimization (LSQ), which is a type of regression analysis, where "the most important applications is "data fitting"(Wikipedia). The objective of the least squares optimization is to obtain the best fit of the model by changing the parameters. For this study, we applied the nonlinear least squares optimization, where we defined the initial values of the parameters (b, D_i, q_i for the MH and n, D_i, q_i for the PLE). When we completed this optimization, we obtain an optimized set of values for the parameters. For this study, we used the least squares optimization function in Matlab. The flowchart for the optimization is shown below in **Fig. 16**, which shows the specific progression of the code.

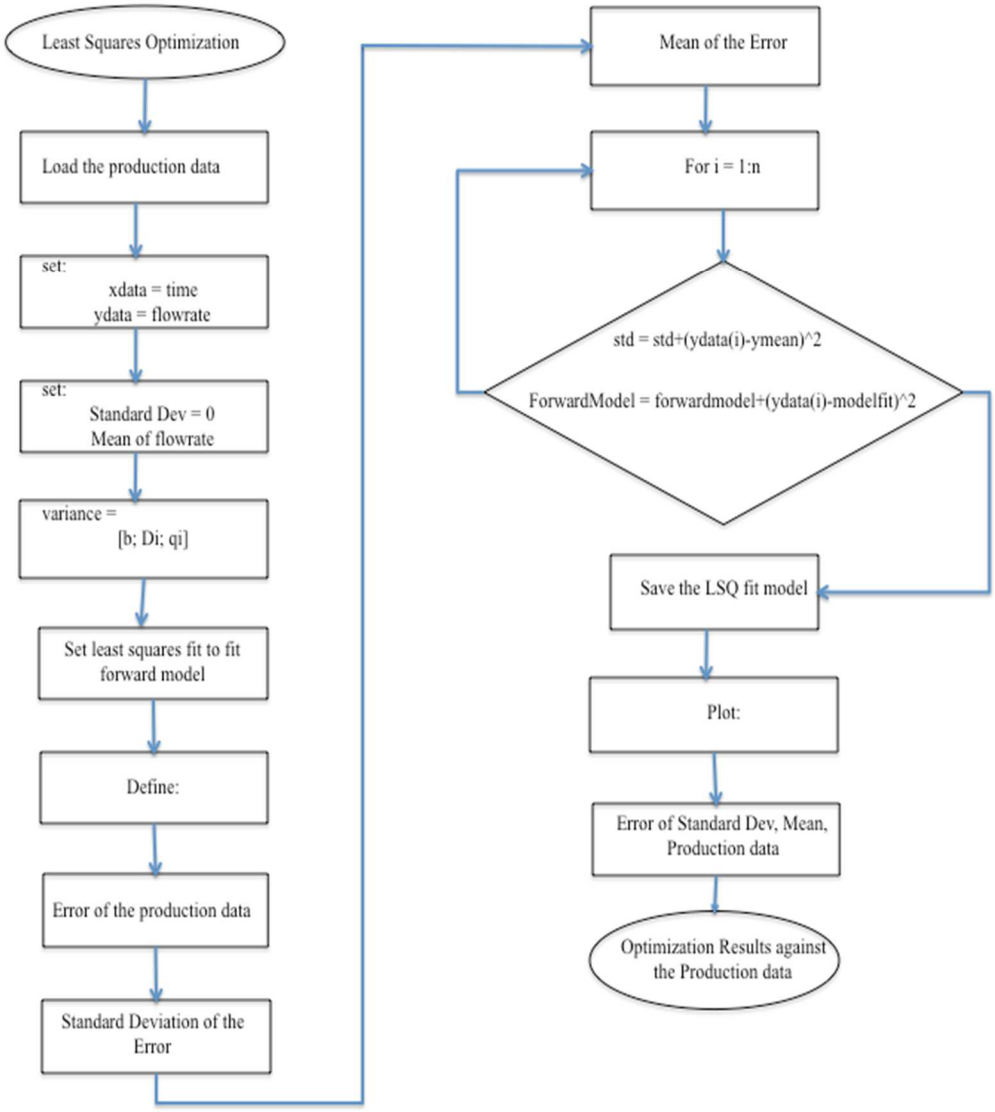

Fig. 19 — Flowchart of the Least Squares Optimization

We plotted the results of the optimized results versus the forward model results, shown below in **Fig. 20**.

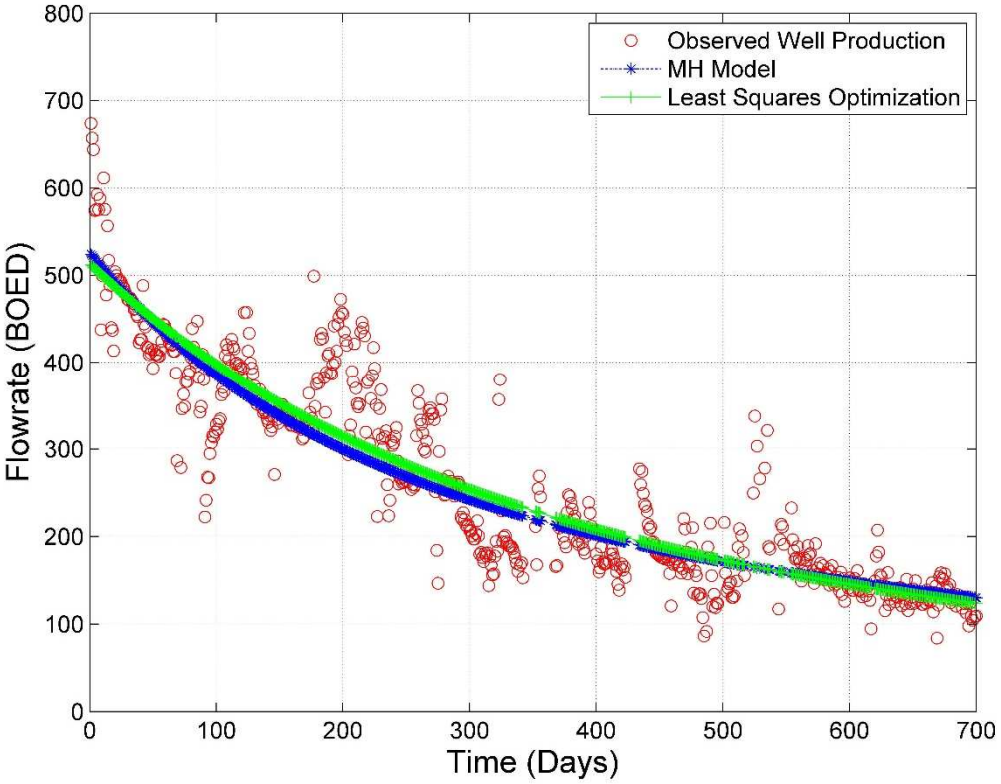

Fig. 20 — The MH model compared with the Least Squares Optimization results. It is visible that the LSQ results show a different starting point, and furthermore we see that the MH model begins higher than the LSQ results, however around day 100 moves beneath the optimized curve, until they converge at 700 days

Since we see a lower initial rate with the optimized results than with the results found when performing the MH model, this means that the optimized q_i is lower than the actual q_i. Furthermore, we see that the *b*-factor and the initial decline are both a bit lower than the initial MH results, which is why there is a slight discrepancy between the two curves. The same analysis was performed on each of the wells for both the MH and the PLE models, and the results are presented in Appendix I at the end.

4.4.2 The Bayesian Paradigm

It is known that none of decline curve equations will accurately forecast the amount of hydrocarbon in shale reservoirs or the length of time that it will produce economically. This is due to the fact that Arp's equations are based on Darcy's law, which are meant for conventional reservoirs with high permeability. Shale reservoirs have a negligible permeability therefore this set of equations will not provide an accurate representation of the well's behavior. The inverse problem does not take into consideration Darcy's equation, and will be solved using Bayes' Theorem and MCMC.

To perform the inverse problem, we will use Bayes theorem that states:

$$P(\boldsymbol{\theta}|\mathbf{D}) \propto P(\boldsymbol{\theta})P(\mathbf{D}|\boldsymbol{\theta}) \quad \text{.....(4.6)}$$

Meaning that the posterior, $P(\theta|D)$, is proportional to the prior, $P(\theta)$, times the likelihood, $P(D|\theta)$. The θ is the set of known parameters, and the likelihood function indicates the likelihood of the event to occur. In this study, the priors are the initial rate (q_i), the initial decline (D_i), the *b*-factor and the time exponent (n), and we will assume that they are non-informative priors, meaning that they will all follow a uniform distribution.

We can obtain the posterior distribution using Bayes' Theorem with Eq. 4.7 and Eq. 4.8 below.

$$P(\boldsymbol{\theta}|\mathbf{d}) = \frac{P(\boldsymbol{\theta})P(\mathbf{d}|\boldsymbol{\theta})}{\int P(\boldsymbol{\theta})P(\mathbf{d}|\boldsymbol{\theta})d\boldsymbol{\theta}} \quad \text{.....(4.7)}$$

$$E[f(\boldsymbol{\theta})\Big|\mathbf{d}] = \frac{\int f(\boldsymbol{\theta})P(\boldsymbol{\theta})P(\mathbf{d}|\boldsymbol{\theta})d\boldsymbol{\theta}}{\int P(\boldsymbol{\theta})P(\mathbf{d}|\boldsymbol{\theta})d\boldsymbol{\theta}} \quad \text{.....(4.8)}$$

We can re-write the above equations to find the following equation:

$$E[f(X)] = \frac{\int f(x)\pi(x)dx}{\int \pi(x)dx} \quad \text{.....(4.9)}$$

where $\pi(x)$ is the likelihood.

We then move to apply the MCMC, which is "a class of algorithms for sampling from a probability distribution based on constructing a Markov chain that has the desired distribution as its equilibrium distribution. The state of the chain after a number of steps is then used as a sample of the desired distribution." (Wikipedia). We used the Metropolis-Hasting algorithm, which is a "MCMC method for obtaining a sequence of random samples from a probability distribution for which direct sampling is difficult"(Wikipedia). The Metropolis-Hastings criteria follows Eq. 4.10 below.

$$\alpha(\mathrm{x}_t, y) = \min\left\{1, \frac{\pi(y)q(x_t|y)}{\pi(x_t)q(y|x_t)}\right\} \quad \text{.....(4.10)}$$

where $q(x_t|y)$ is the proposed distribution. In this research, we will assume that the priors will follow a uniform distribution. The constant values in in Eq. 4.10 will cancel from the numerator and the denominator.

We will assume that the likelihood is normally distributed, and will be determined using Eq. 4.11 below.

$$P(D|\boldsymbol{\theta}) = (2\pi)^{\frac{-n}{2}} |\boldsymbol{\sigma}|^{-0.5} e^{-0.5(\mathbf{d}-\boldsymbol{\theta})'\boldsymbol{\sigma}^{-1}(\mathbf{d}-\boldsymbol{\theta})} \quad \text{.....(4.11)}$$

where $\boldsymbol{\sigma}$ is the standard deviation, $\boldsymbol{d}$ is the observed data and that $\boldsymbol{\theta}$ is the forward model, so in this research, either the MH or the PLE models.

The first step in beginning this research is to determine the random and the constant variables of the two decline curve analysis models. For the MH model, we will set q_i, D_i and the *b*-factor as the set of random variables, and they are all greater than 0, and will keep *t* and D_{lim} as a constant variable. For the PLE model, we will set q_i, D_i, and n as the random variables, and keep *t* and D_∞ as the constant variables.

The next step was to perform the least squares optimization on the initial values of the forward model parameters. A set of results was presented in Fig. 17 for Well 19. After this, we determine the standard deviation as a constant for the likelihood definition. **Fig. 21** below shows the least square model results against the production data. From here, we will determine the error of the LSQ versus the actual data, shown in a histogram in **Fig. 22** and the cumulative distribution of the error, shown in **Fig. 23**, and finally the total error is presented in **Fig. 24**. Fig. 21-24 are the MH results of Well 41.

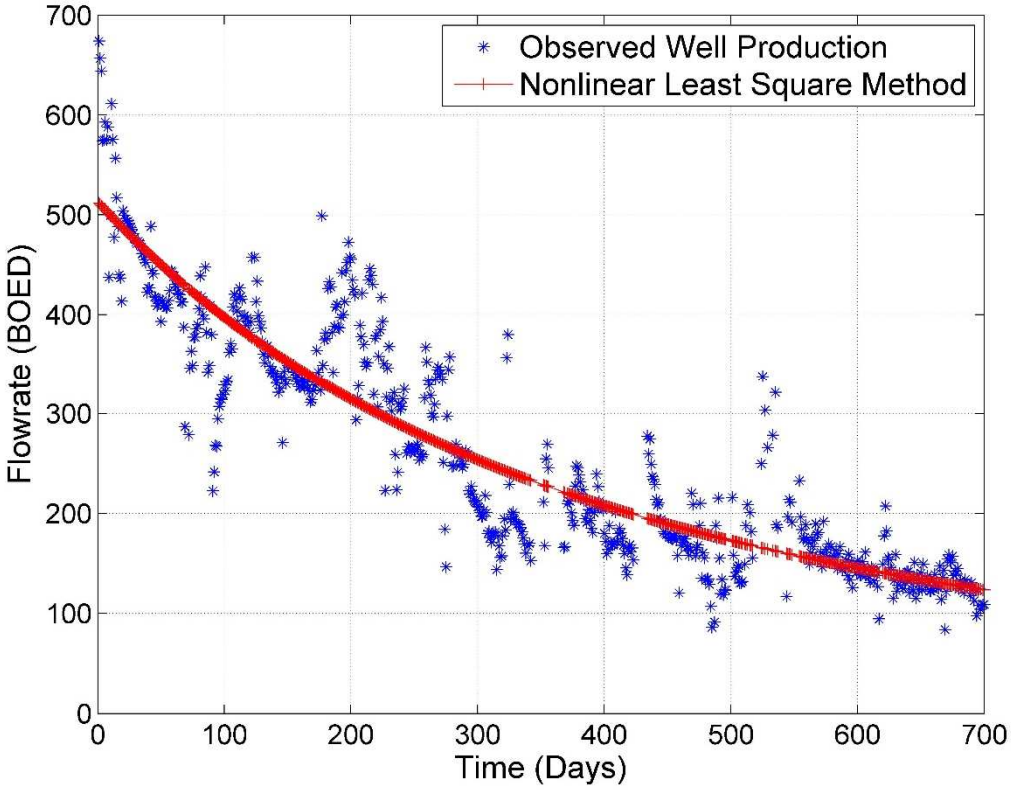

Fig. 21 — Results of the least squares optimization against the production data

The figure above shows the decline curve using the optimized parameters for the MH model of Well 41. This was performed using the LSQ method, as previously described. We used the least squares optimization function in Matlab to obtain these results.

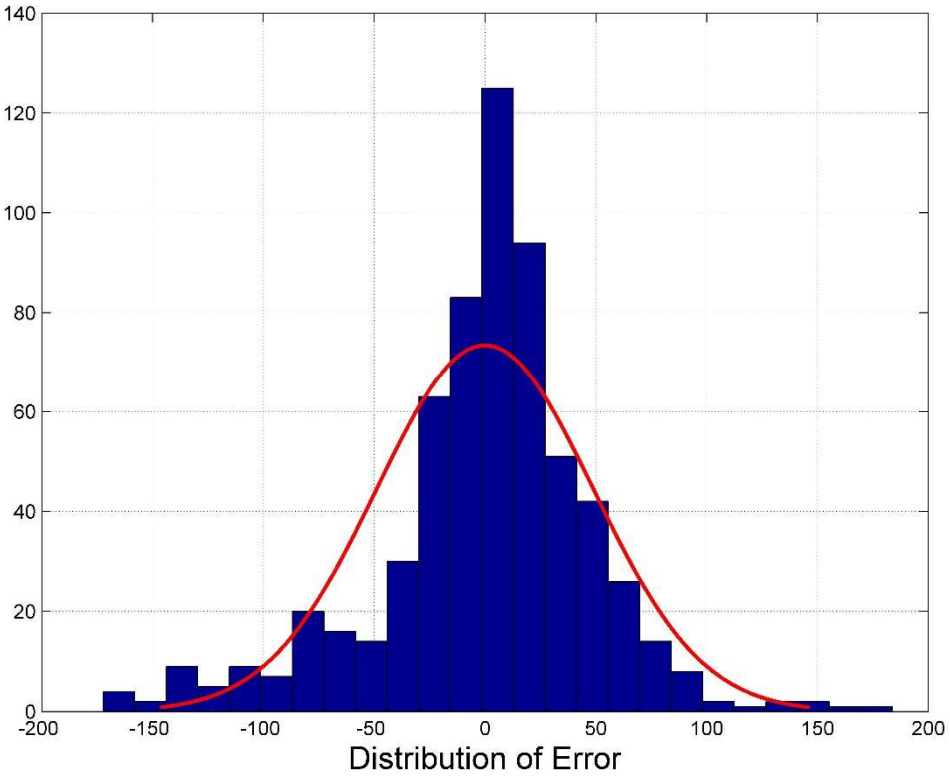

Fig. 22 — The distribution of error between the production data and the LSQ results

Fig. 22 shows that the distribution of error between the optimized results and the actual production data is a Gaussian distribution.

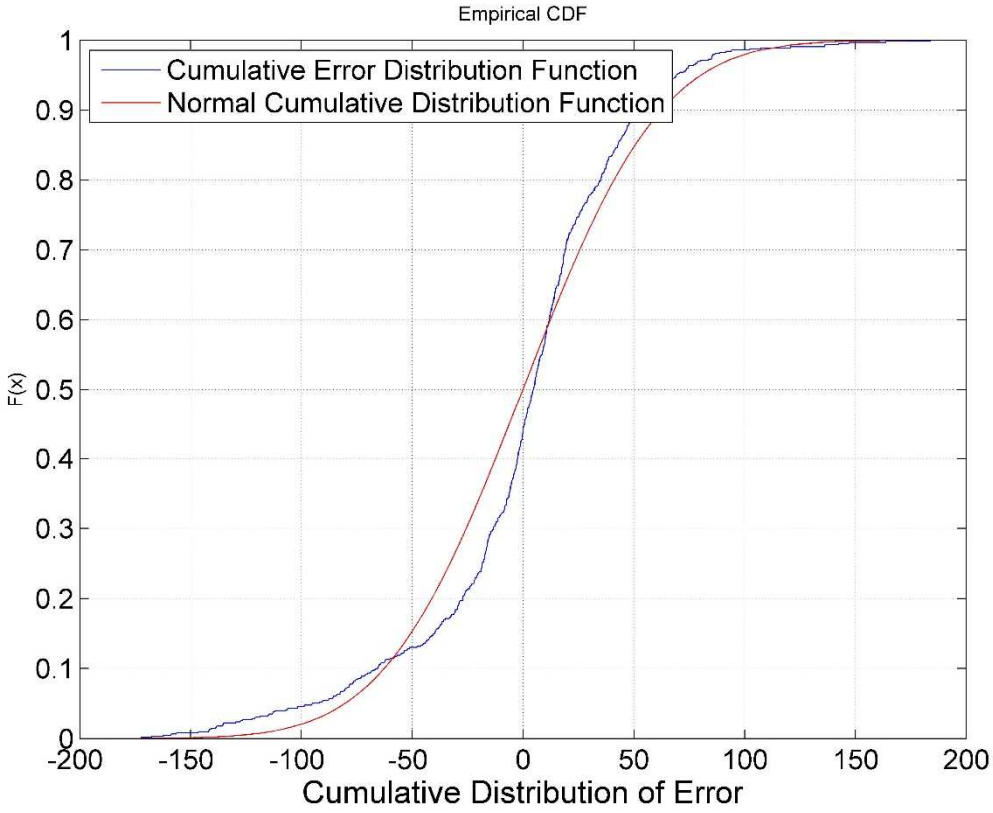

Fig. 23 — The cumulative distribution of error is plotted against the normal cumulative distribution function

The figure above shows the cumulative error distribution function (blue curve) against the normal cumulative distribution function (red curve). This graphs shows the error of the LSQ optimization against the actual normal distribution. From this graph, it can be deduced that the optimization performed yielded accurate results because the two curves are very close to each other. However, it would be ideal if the two curves overlapped.

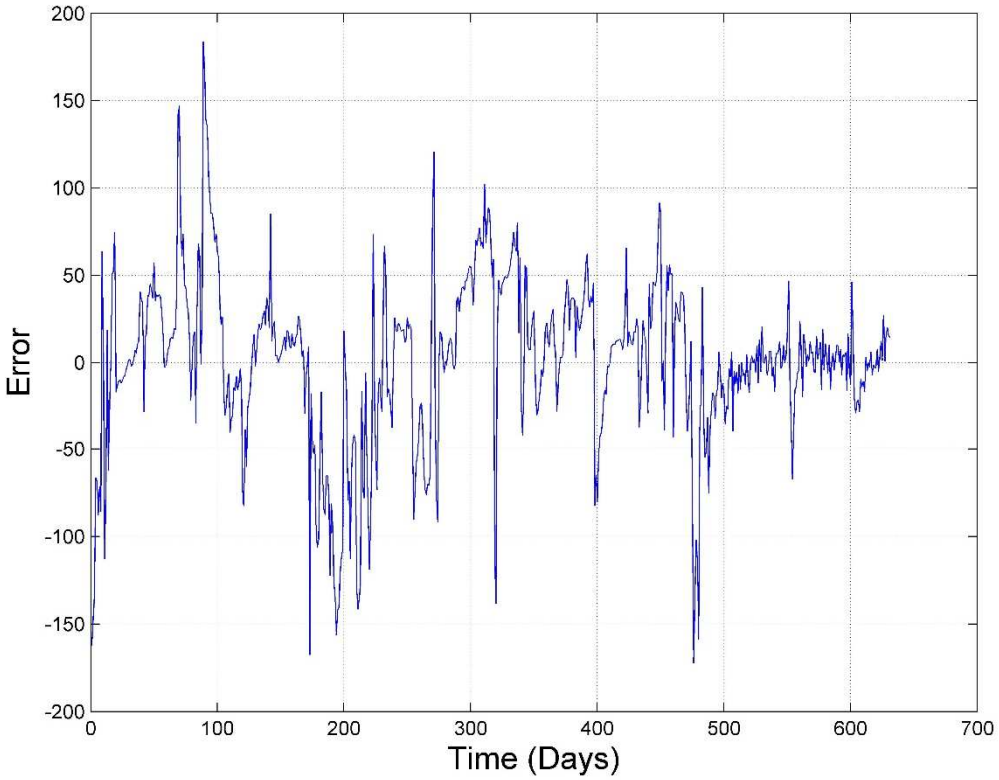

Fig. 24 — The error of the least squares optimization against the number of production days

Fig. 24 shows the error between the least squares optimization and the production data. It is visible from the graph that the error decreases with an increasing number of production days. This is expected when applying the LSQ optimization, and it is also ideal for the study. This graph indicates that as we increase the amount of information, the more accurate our optimized results will become, which is what we see in the graph above.

4.5 Analysis and Discussion of the Results

Three methods were used in this study to forecast the eight wells in the Greater Core Eagle Ford. The first was the forward model, using the MH and the PLE models, as would be used in industry. Secondly, was the LSQ optimization, where we used the MH and PLE, but optimized the parameters of the two equations to provide a more accurate set of

parameters than those determined visually when fitting the decline curve of the MH and PLE models. Finally, we applied the Bayesian paradigm. This included performing the MCMC on the three parameters to obtain the most accurate value, and then implement Bayesian forecasting, which works by learning the trend of the production data and better estimating the following point. These three approaches have their pros and cons, which is what will be discussed in this section, along with a comparison of the DCA results.

The MH and PLE models were implemented by using proprietary software. To perform this initial part of the study, we input the production data of the wells into the software. After this was completed, we chose which models we wanted to implement in this study, and decided on the MH and the PLE models. To fit the data, we manually moved the curves using the cursor and when it was visually determined that there was a fit, saved the parameters and the data of the set decline curve. This practice is done in industry on unconventional wells, and it also gave us values of the three different parameters of the two equations. We created qDb plots of the results of each well using Igor, all of which are included in Appendix I.

Once we obtained the initial results using the DCA models, we applied the LSQ optimization. This method used the parameters determined when using the conventional forward models and optimized them to create a more accurate result. After this was done, we applied the MCMC on the three parameters of the two forward equations. This method used millions of iterations to determine the most accurate value of each parameter, which was then used when applying the Bayesian paradigm. The Bayesian paradigm works by "learning" about the trend of the data and thus estimating where the next point will be based on the knowledge it has acquired from the previous data points. Since there are several possibilities, we plotted 1,000 possible realizations and took the mean of these realizations.

4.5.1 Analysis of the Bayesian Paradigm Results when Implementing the Modified Hyperbolic of Well 41

As previously stated, we will also assume that the priors are all non-informative, meaning that they follow a uniform distribution. The next step is to set the coefficient of variation to fix the step size of the proposed distribution. We decided the set the coefficient of variation to 0.1 for all of the wells and all the models.

From this step, we generated the MCMC iterations, which generated the cumulative mean and standard deviation of each random variable, along with a graph of the iterations of each parameter. Fig. 25 through 30 show these results, and are the results of the MH model of Well 41.

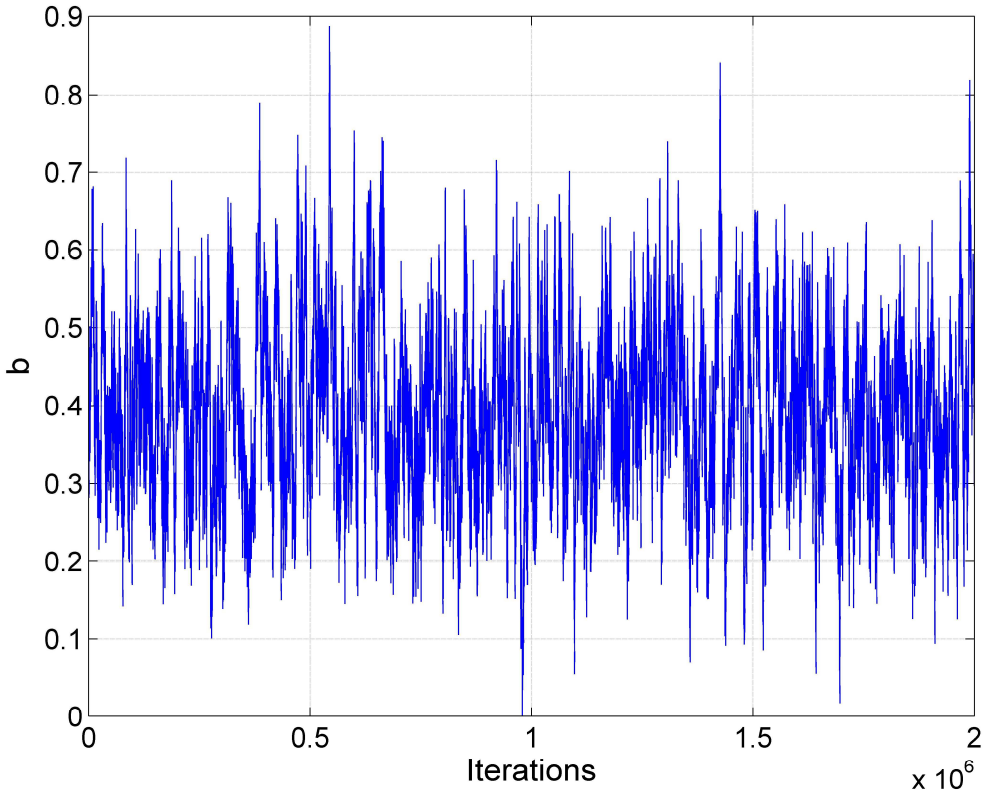

Fig. 25 — MCMC results of the *b*-factor for the MH model

The figure above shows the *b*-factor of the MH model converges immediately. It is also clear that the mean value of *b* is approximately 0.4, which is confirmed in Fig. 26, below.

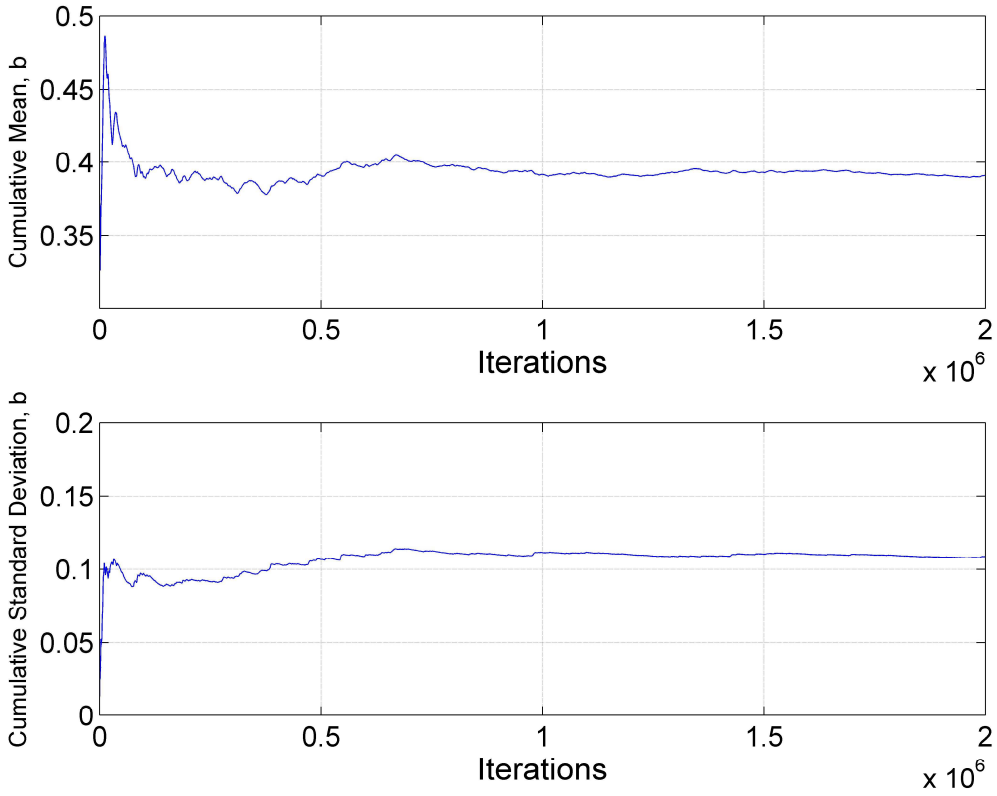

Fig. 26 — Cumulative mean and standard deviation of the *b*-factor

It is evident from the graph above that the *b*-factor for Well 41 converges after one million iterations. It is evident that there is no more noise in the data and that the MCMC has determined the true value of the *b*-factor. Furthermore, the standard deviation of *b* is 0.11 from the figure above.

We performed the same analysis on D_i and q_i, and the results are presented below.

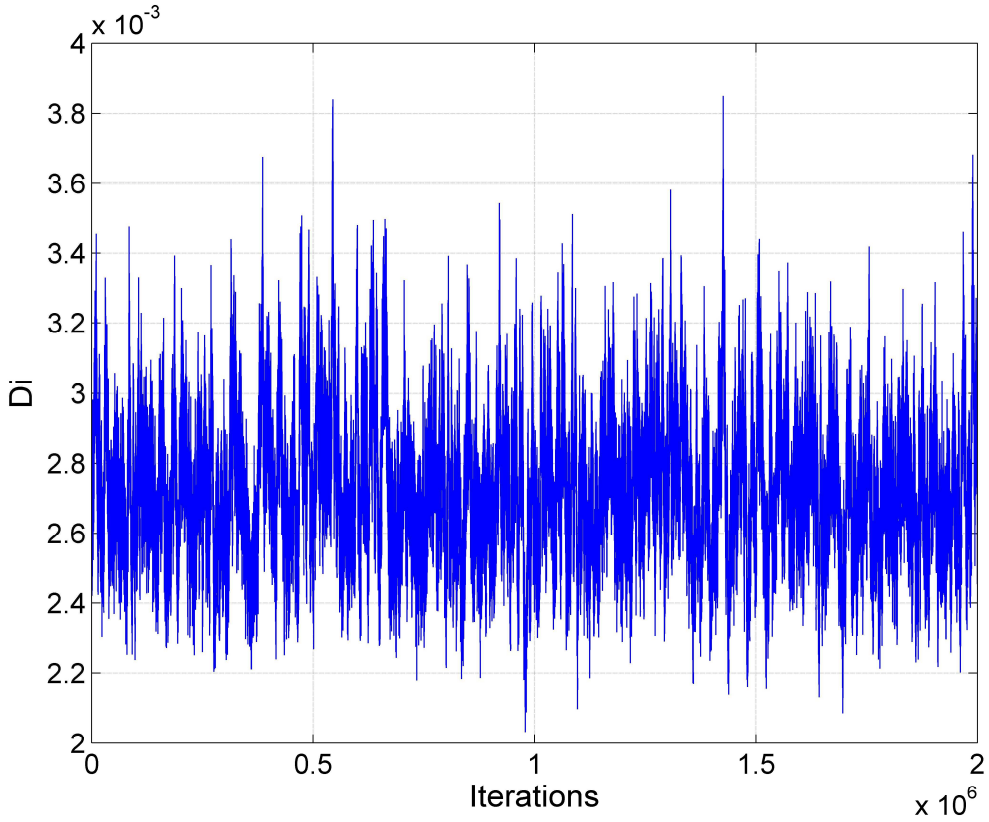

Fig. 27 — MCMC results of D_i for the MH model

The figure above shows the D_i of the MH model converges immediately. It is also clear that the mean value of D_i is approximately 2.8E-03, which is confirmed in Fig. 28, below.

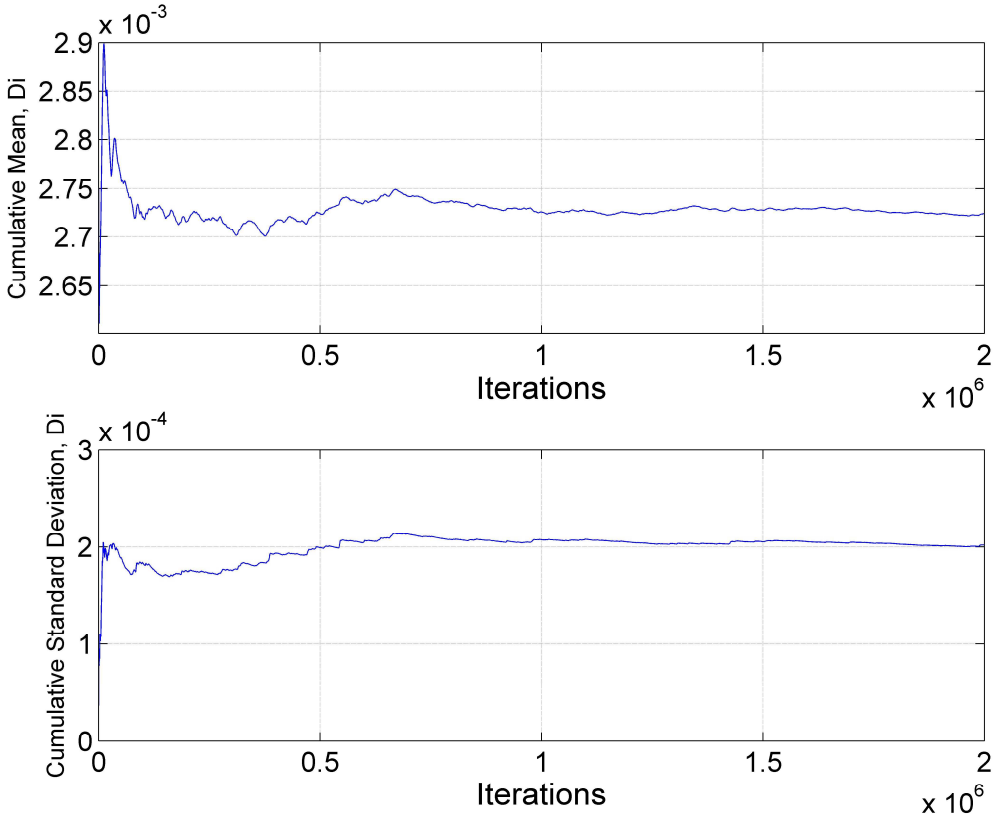

Fig. 28 — Cumulative mean and standard deviation of D_i

It is evident from the graph above that D_i for Well 41 converges almost immediately. After one million iterations, it is obvious that there is no more noise in the data and that the MCMC has determined the true value of the D_i.

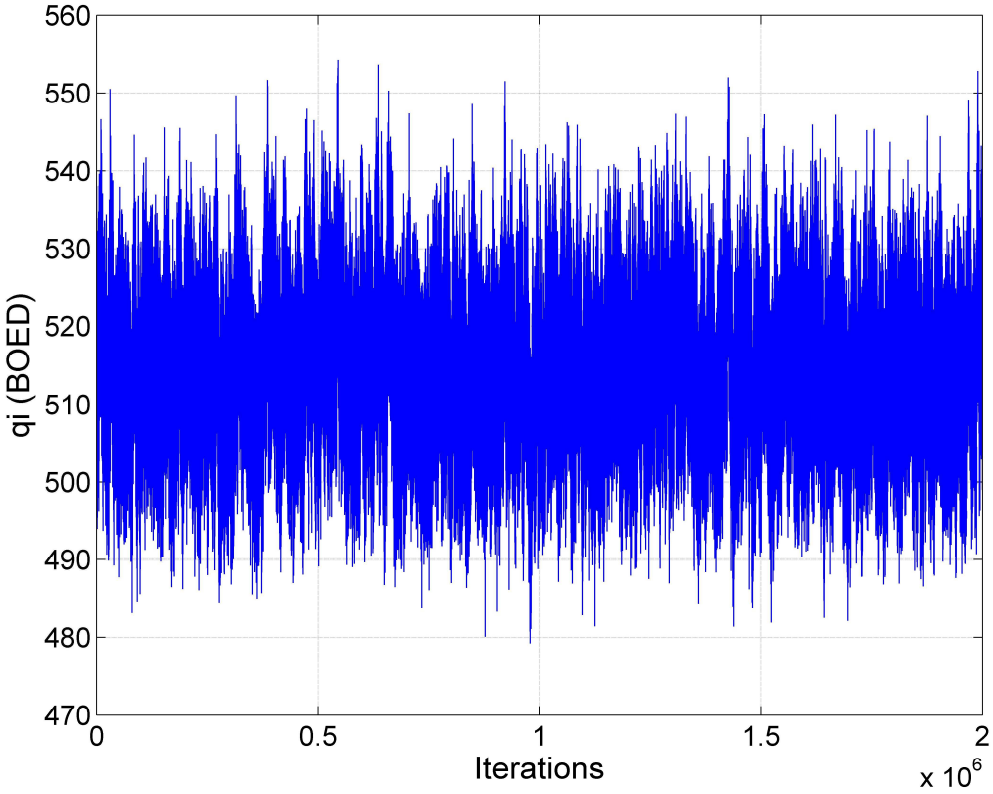

Fig. 29 — MCMC results of q_i for the MH model

The figure above shows the q_i of the MH model converges immediately. It is also clear that the mean value of q_i is approximately 515 BOED, which is confirmed in Fig. 30, below.

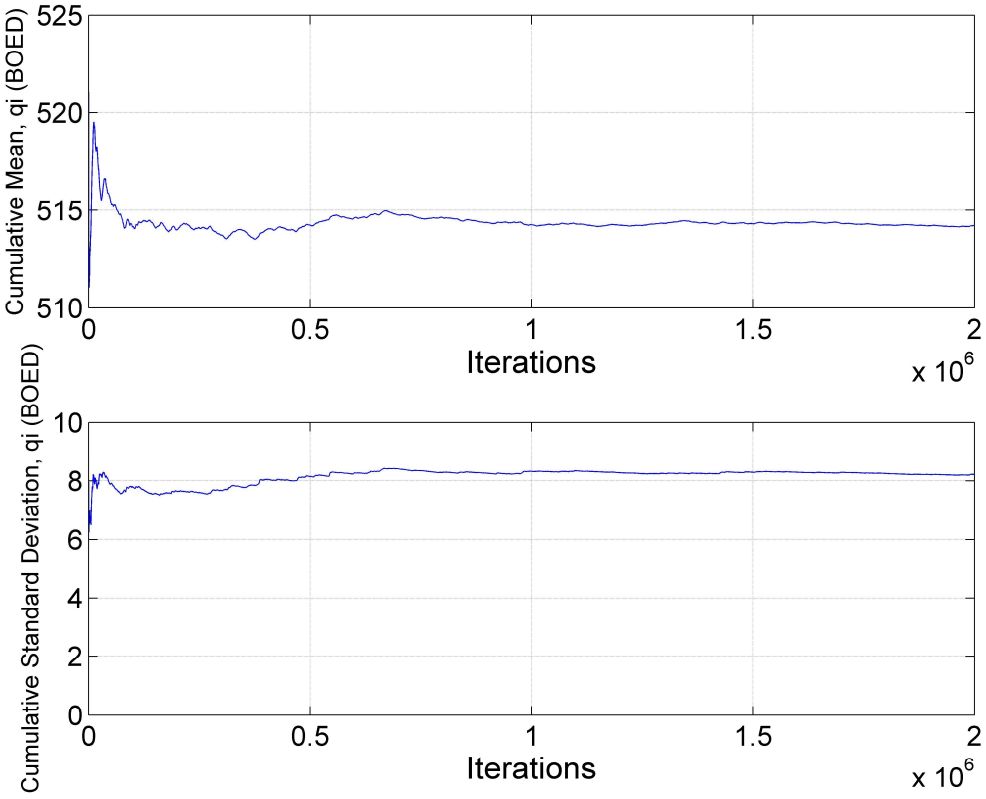

Fig. 30 — Cumulative mean and standard deviation of q_i

It is evident from the graph above that q_i for Well 41 converges almost immediately. After one million iterations, it is obvious that there is no more noise in the data and that the MCMC has determined the true value of the q_i.

Overall, the MH model for Well 41 is a very successful run. All three parameters converged after only two million iterations. The results for the remainder wells vary depending on the model used when the Bayesian paradigm was implemented.

From the cumulative means and standard deviations of each parameter (presented in Fig. 26, 28 and 30), we set the burn-in point, which is the point where the iterations reach a stationary condition. This burn-in point was determined visually, as some cases converged

very quickly with only 2 million iterations, and others did not converge after 50 million iteration. For the case presented above, we set the burn-in point at one million iterations. After the burn-in point was determined, it only took into consideration the values after the set point; meaning that if we set the burn-in point at one million iterations and we had a total of 2 million iterations, the model will only take into account the last million values and not the first million, where there is noise in the data.

From the results of using the burn-in point, we obtain the descriptive statistics of our models; the random variable histograms, the relative frequency histograms, and the cumulative distribution of the parameters. This gives a visual representation of the behavior of the parameters of the different models. Fig. 31 through 39 below show the results.

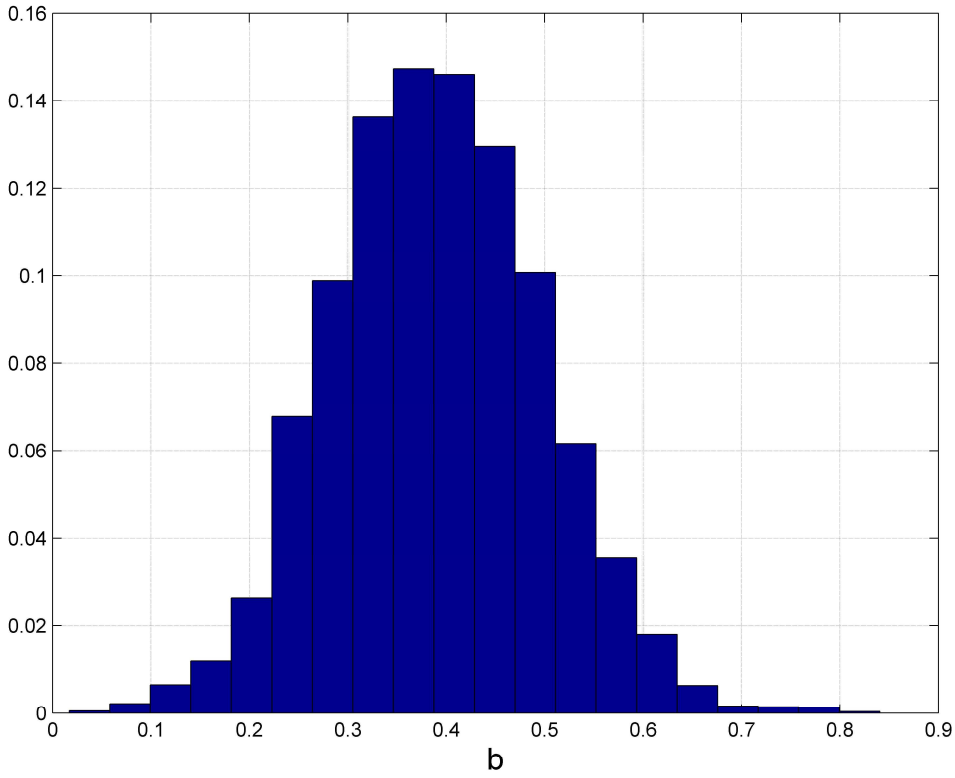

Fig. 31 — Posterior relative frequency histogram of *b*

The posterior relative frequency histogram of *b* shows the distribution of the *b*-factor after the burn-in point has been set. This graph indicates that the *b*-factor has a Gaussian distribution after the initial million data points were discarded.

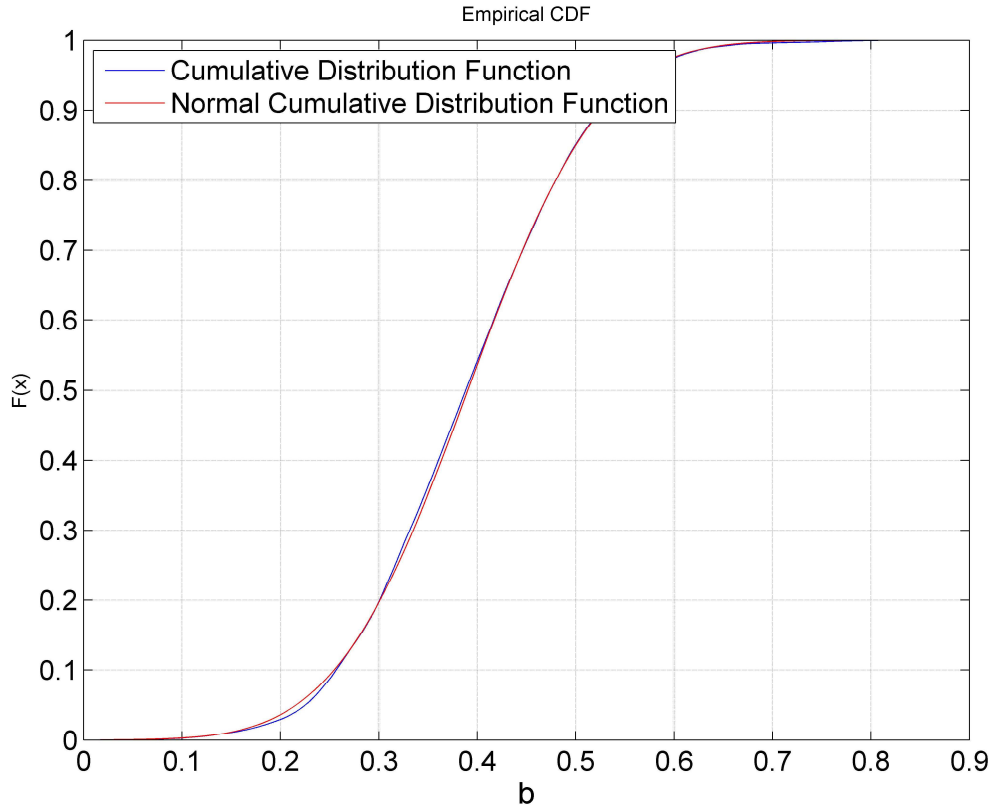

Fig. 32 — Cumulative posterior relative frequency histogram of the *b*-factor

The cumulative posterior relative frequency histogram of the *b*-factor shows the error between the value of the MCMC after the burn-in point was set, with respect to the normal cumulative distribution function. The two curves are superposed, indicating that the results we have determined do not have any error attributed to them, and this is the correct value of the *b*-factor to use for this data set, while using the MH model.

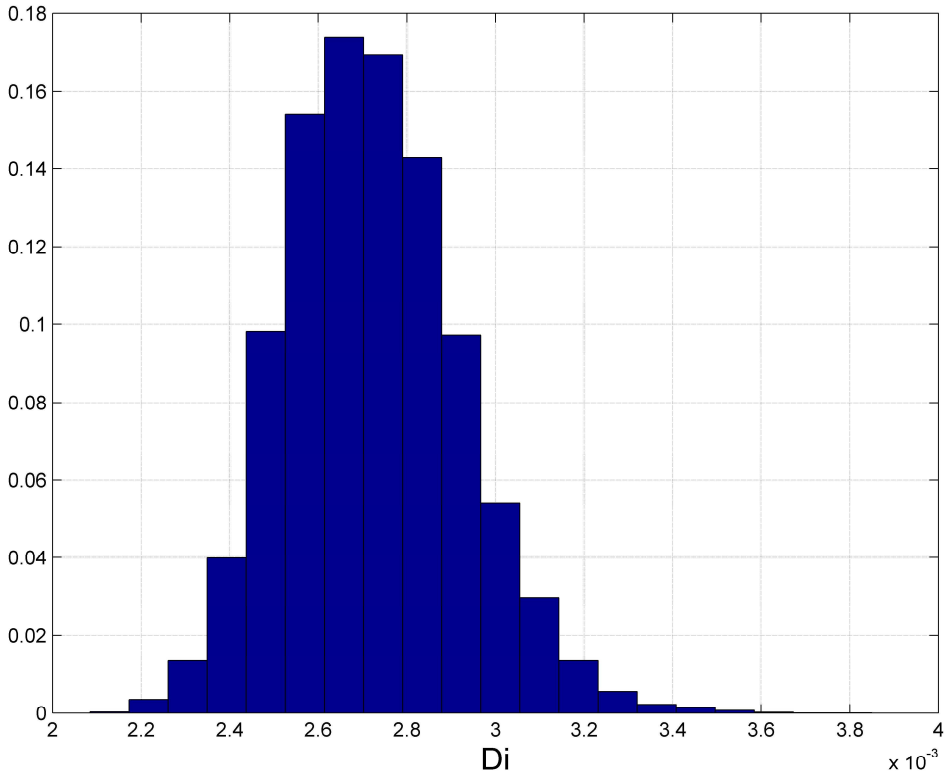

Fig. 33 — Posterior relative frequency histogram of D_i

The posterior relative frequency histogram of D_i shows a lognormal distribution, as opposed to the Gaussian distribution seen for the *b*-factor.

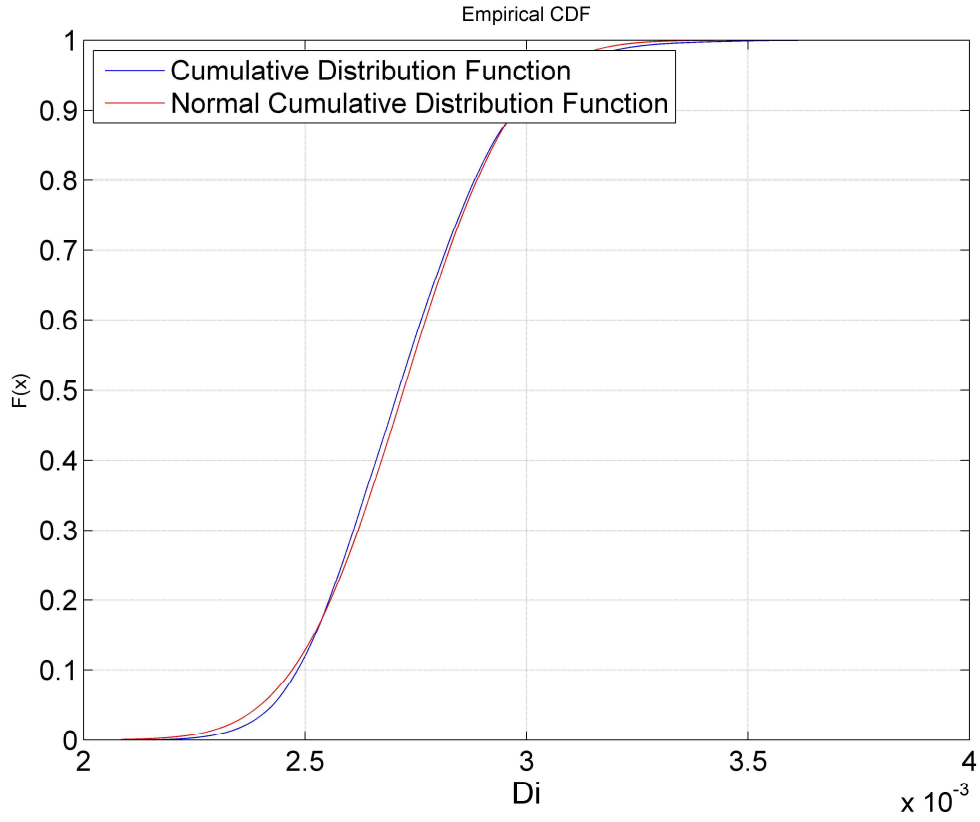

Fig. 34 — Cumulative posterior relative frequency histogram of D_i

The cumulative posterior relative frequency histogram of D_i shows the error between the value of the MCMC after the burn-in point was set, with respect to the normal cumulative distribution function. The two curves are superposed, indicating that the results we have determined do not have any error attributed to them, and this is the correct value of D_i to use for this data set, while using the MH model.

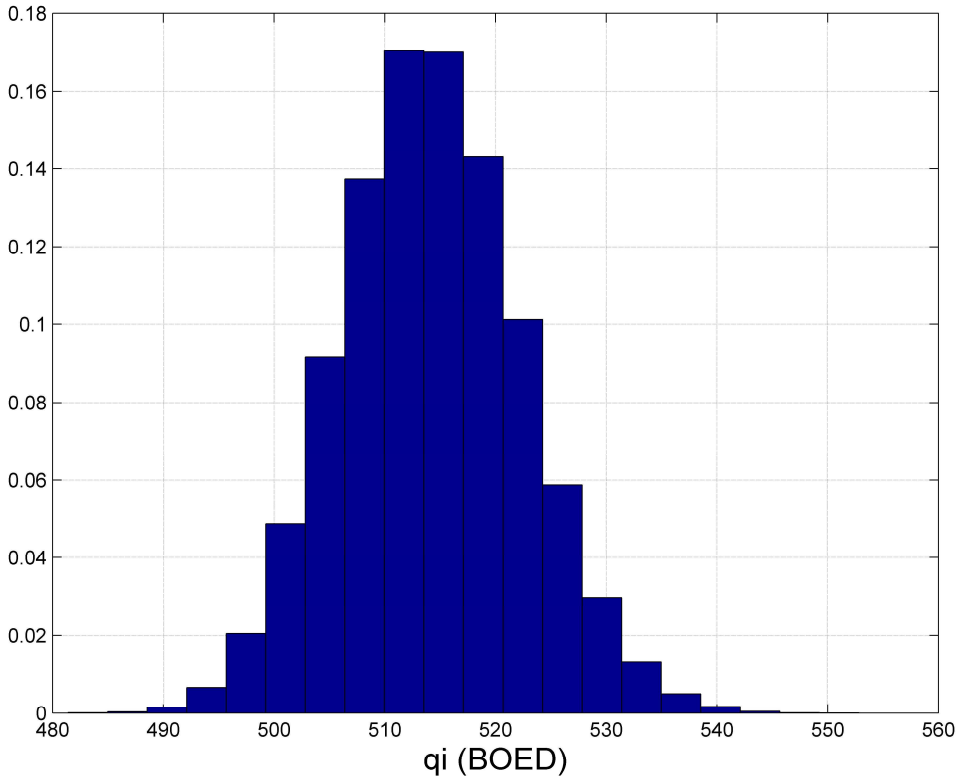

Fig. 35 — Posterior relative frequency histogram of q_i

The posterior relative frequency histogram of q_i shows the distribution of q_i after the burn-in point has been set. This graph indicates that the q_i has a Gaussian distribution after the initial million data points were discarded.

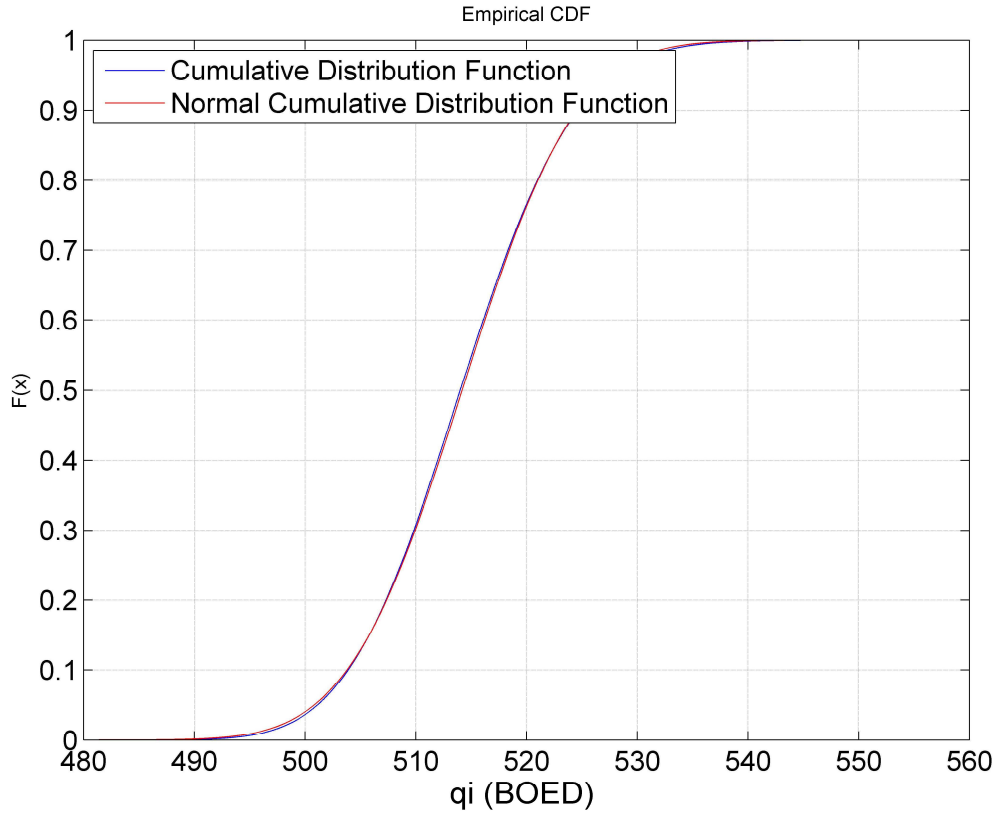

Fig. 36 — Cumulative posterior relative frequency histogram of q_i

The cumulative posterior relative frequency histogram of q_i shows the error between the value of the MCMC after the burn-in point was set, with respect to the normal cumulative distribution function. The two curves are superposed, indicating that the results we have determined do not have any error attributed to them, and this is the correct value of q_i to use for this data set, while using the MH model.

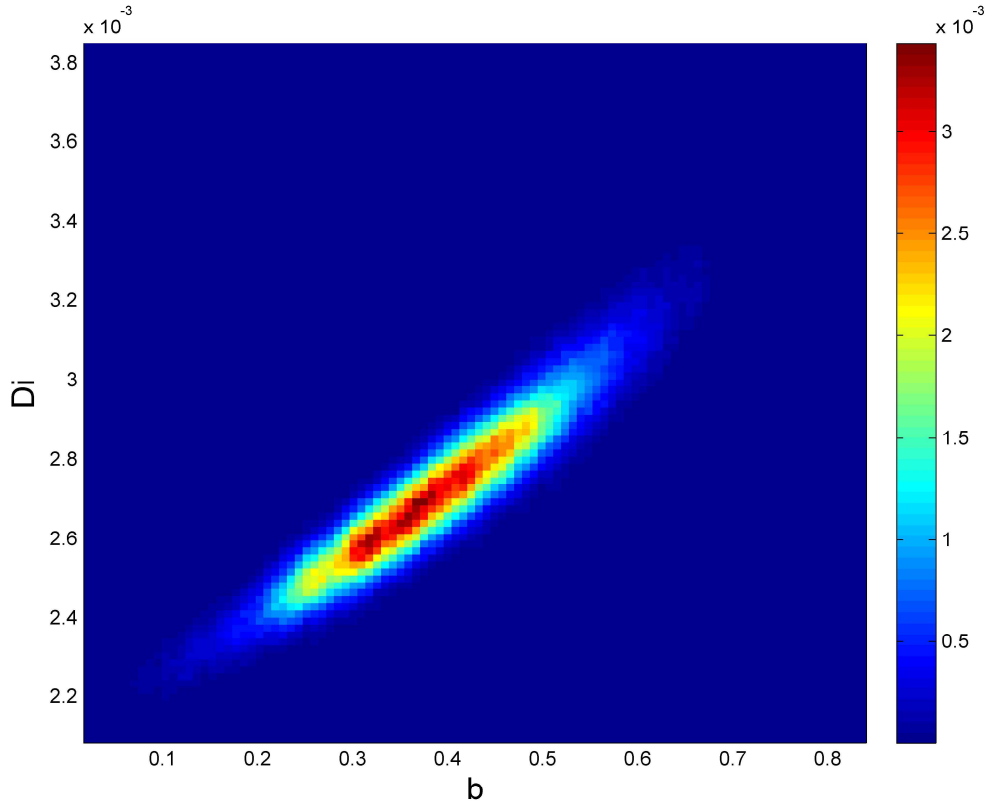

Fig. 37 — Relative frequency diagram between D_i and b

The relative frequency diagram between D_i and b shows the relationship between these two parameters for the MH model. The red region in the center of the curvature in the graph indicates the ideal combination of these two parameters for this specific set of data points and model. Though there should not be any relationship between these parameters, it is evident from the graph above that there is a relationship.

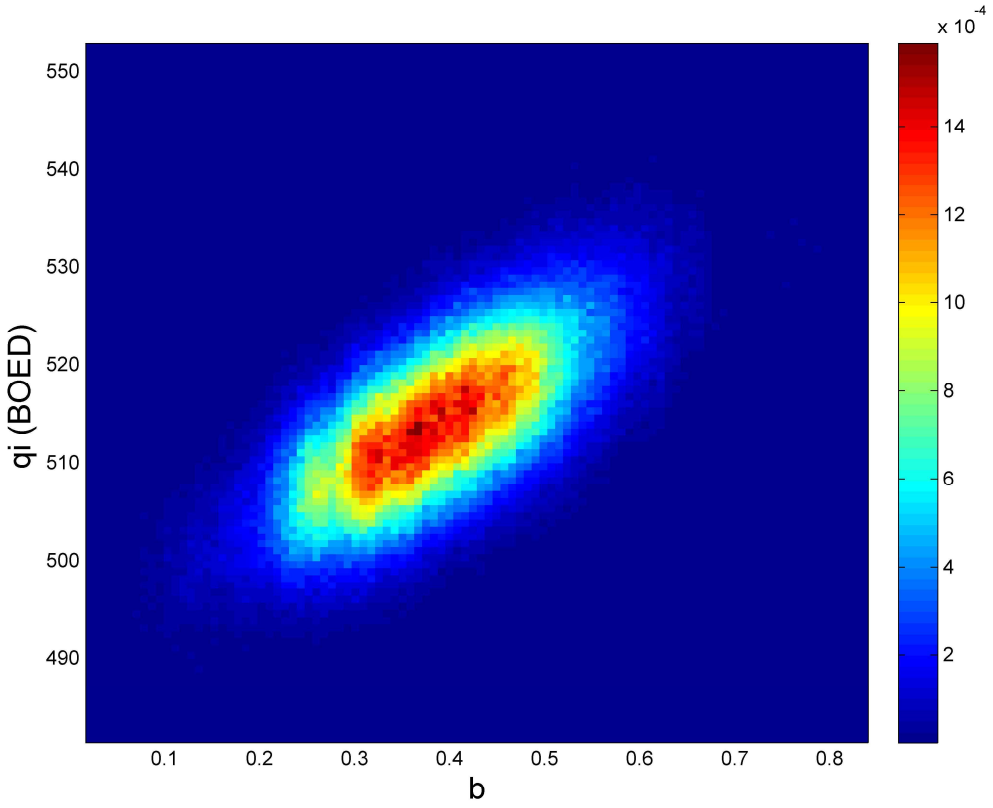

Fig. 38 — Relative frequency diagram between q_i and b

The relative frequency diagram between q_i and b shows the relationship between these two parameters for the MH model. The red region in the center of the curvature in the graph indicates the ideal combination of these two parameters for this specific set of data points and model. Though there should not be any relationship between these parameters, it is evident from the graph above that there is a linear relationship.

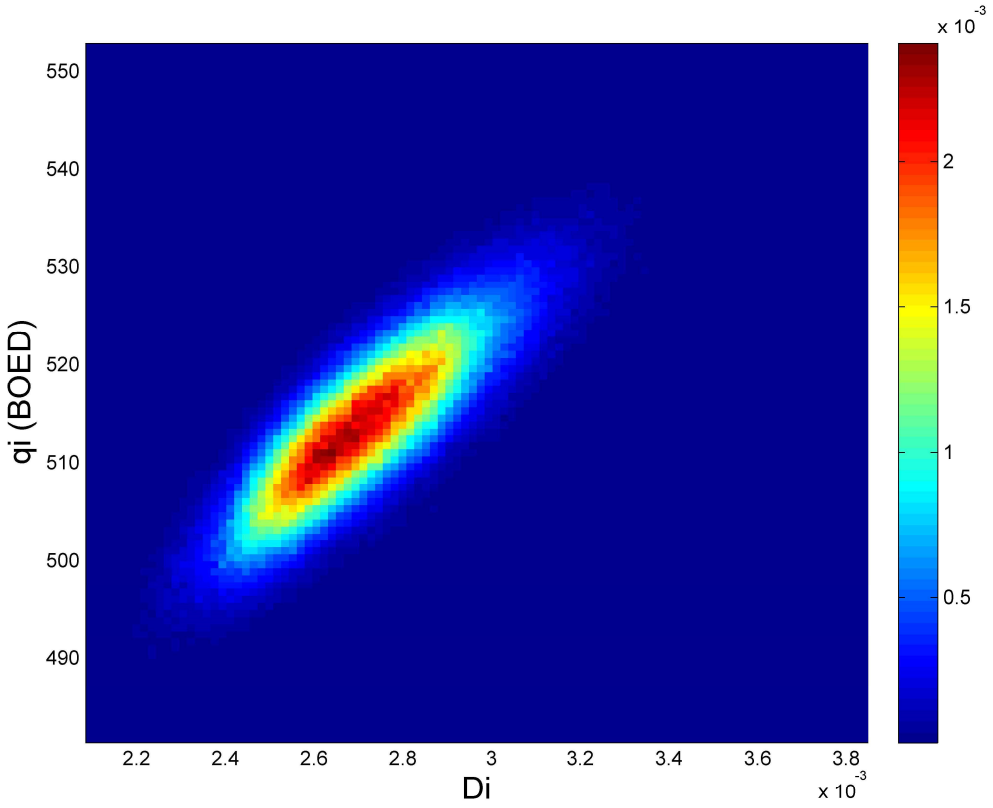

Fig. 39 — Relative frequency diagram between q_i and D_i

The relative frequency diagram between q_i and D_i shows the relationship between these two parameters for the MH model. The red region in the center of the curvature in the graph indicates the ideal combination of these two parameters for this specific set of data points and model. Though there should not be any relationship between these parameters, it is evident from the graph above that there is a relationship.

The results presented in Fig. 31-39 validate that our model is working properly and that the set burn-in point was accurate.

Using the spatial statistics and the results of the parameters, we generated 1,000 realizations of the model predictions from the determined posterior distribution. It is possible to generate as many realizations are desired, however it was determined that

1,000 gave an accurate range of results. From there, we determine the mean of these realizations and the standard deviation, which indicates the uncertainty of our Bayesian model. This was done for the 700 and 450 days, and then was extended to 30 years. Below are the results in Fig. 40 through 45 for Well 41 using the MH model.

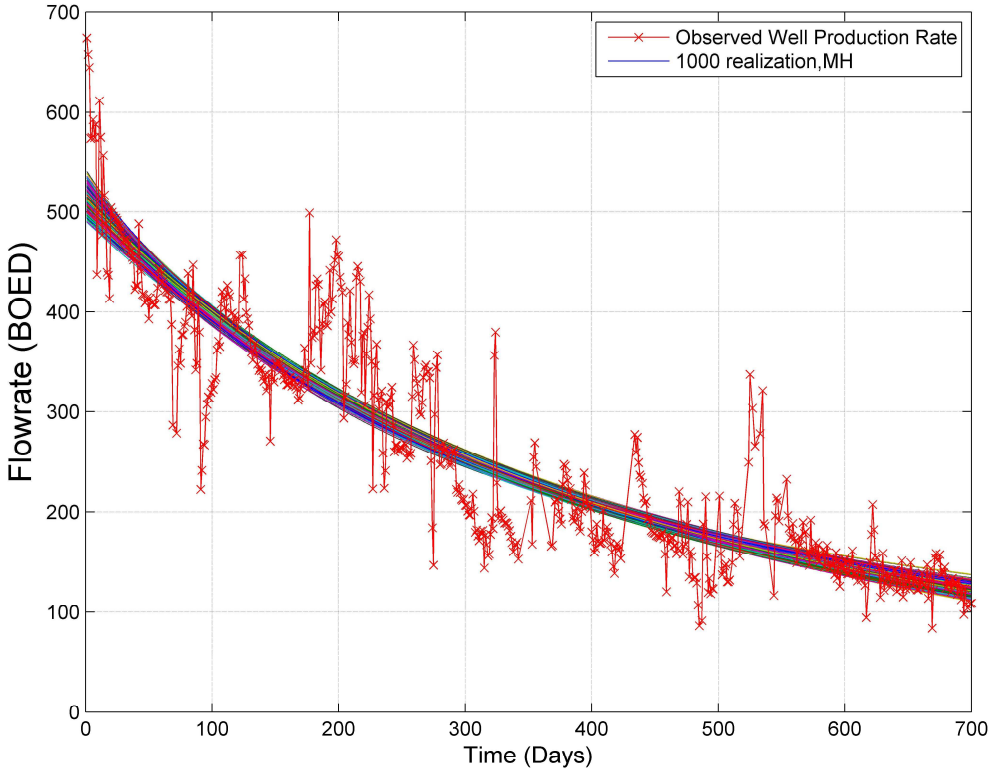

Fig. 40 — The 1,000 realizations of the model predictions using the Bayesian paradigm

Fig. 40 shows the 1,000 realizations that were created using the parameters that were determined with the MCMC. By looking at the graph, we can see that all the results fall in a similar range. This graph shows 1,000 possible combinations of results. The next step is to take the mean of these results, and compare it to the optimized values and the forward model values.

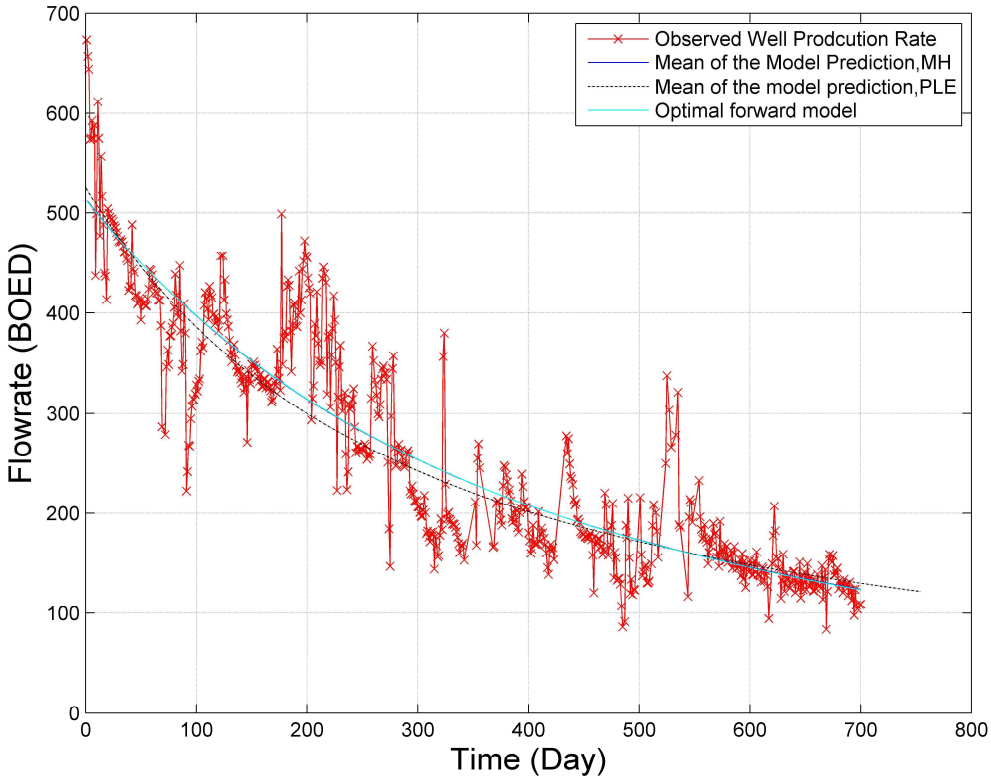

Fig. 41 — The production data with the mean of the realizations, the optimal forward model and the expert forward model

The graph above shows the three methods used in this study against the production data. In this case, the black curve is the optimal forward model, that was determined by the applying the least squares optimization, the blue curve is the mean of the 1,000 realizations and finally, the turquoise curve is the expert forward model, which in this case is the MH model. It is evident that in this case, the MH model and the mean of the model predictions are superposed; therefore the two returned the same result. This is unexpected, however it means that the MH was the correct model to use initially, and it means that the Bayesian model produced the same results, therefore it agrees with the original forward model.

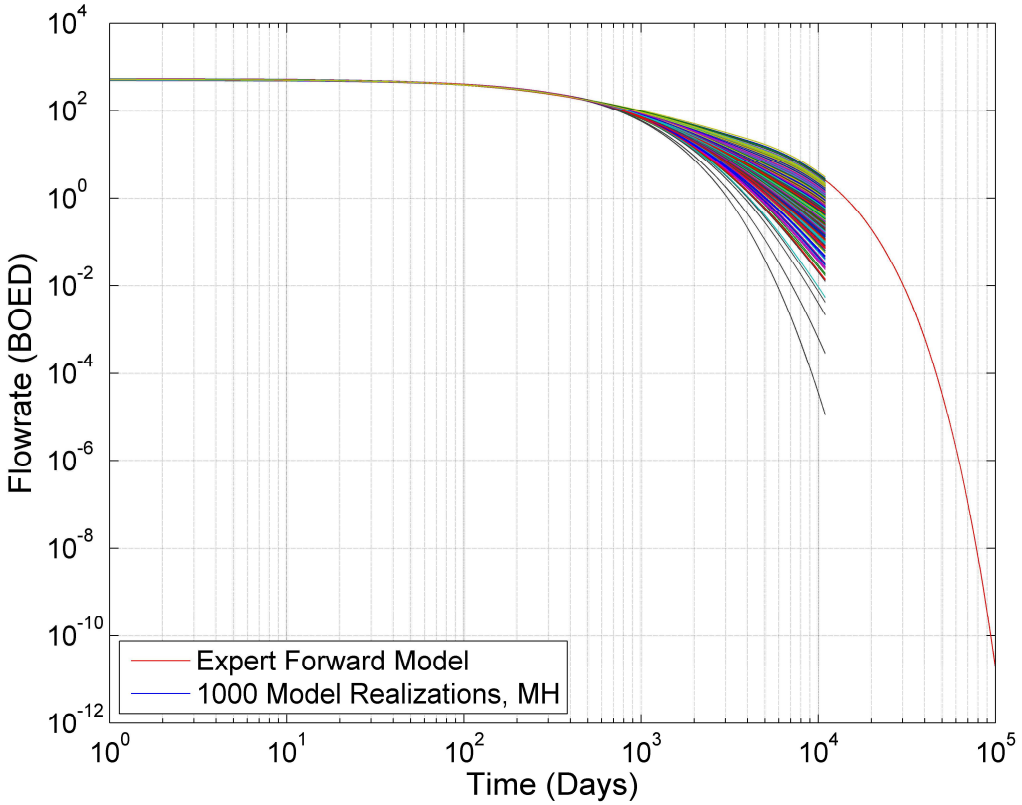

Fig. 42 — The 1,000 realizations of the model predictions using the Bayesian paradigm for 30 years

Fig. 42 shows the realizations of the model predictions for 30 years. We produced this result because in industry, the economic limit of the DCA practice is 30 years. In the graph above, the red curve is the expert forward model, therefore in this case, the MH model, and the remaining curves are the realizations. It is interesting to note that the forward model underestimates the reserves, which is noticeable because the curve is so far below the remaining curves.

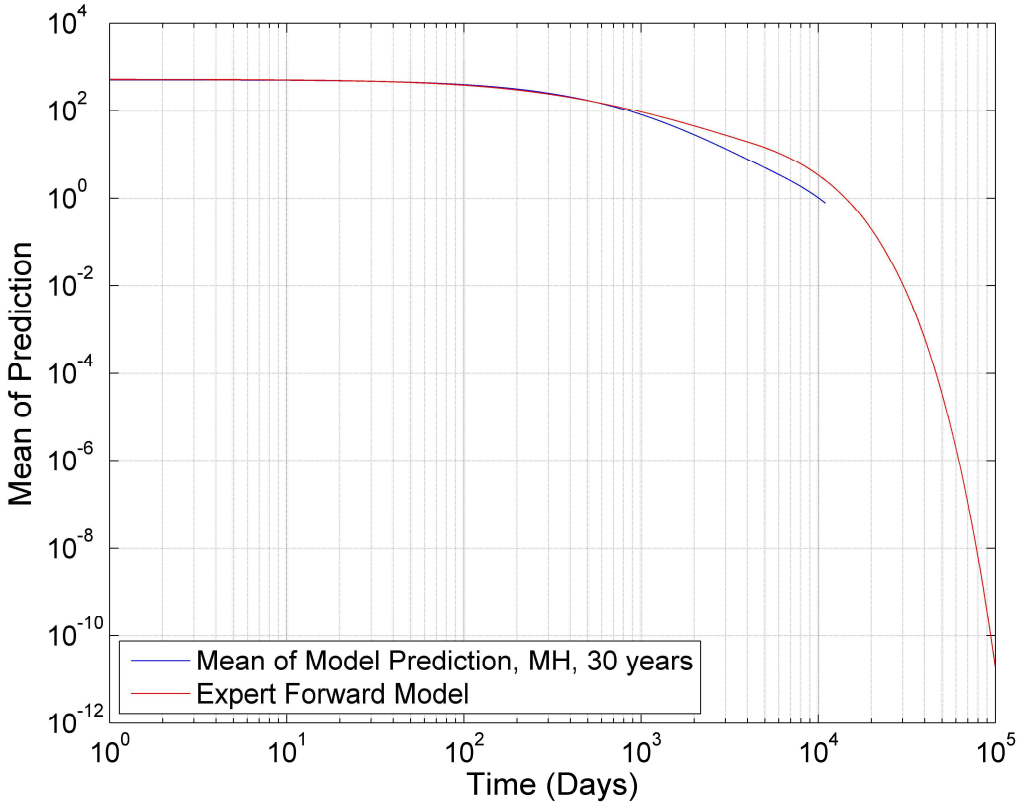

Fig. 43 — The mean of the realizations and the expert forward model, plotted for 30 years

Like the previous figure, Fig. 43 is plotted for 30 years because of the economic limit set by the industry. This graph is similar to the previous graph, however shows the mean of the 1,000 realizations, therefore gives a clearer view of the behavior of the model predictions. In this graph, it is evident that the expert model (the MH model) is underestimating the results. We can see that in early time, the two graphs seem to be overlapped, which is also evident in Fig. 41, however it is evident from Fig. 43 that the forward model and the Bayesian model do not yield the same results. This is interesting to see, and an important conclusion to draw, because it shows that the forecast is necessary for a longer period of time to see how the two models act. We can see again that the forward model is significantly underestimating the reserves compared to the Bayesian model.

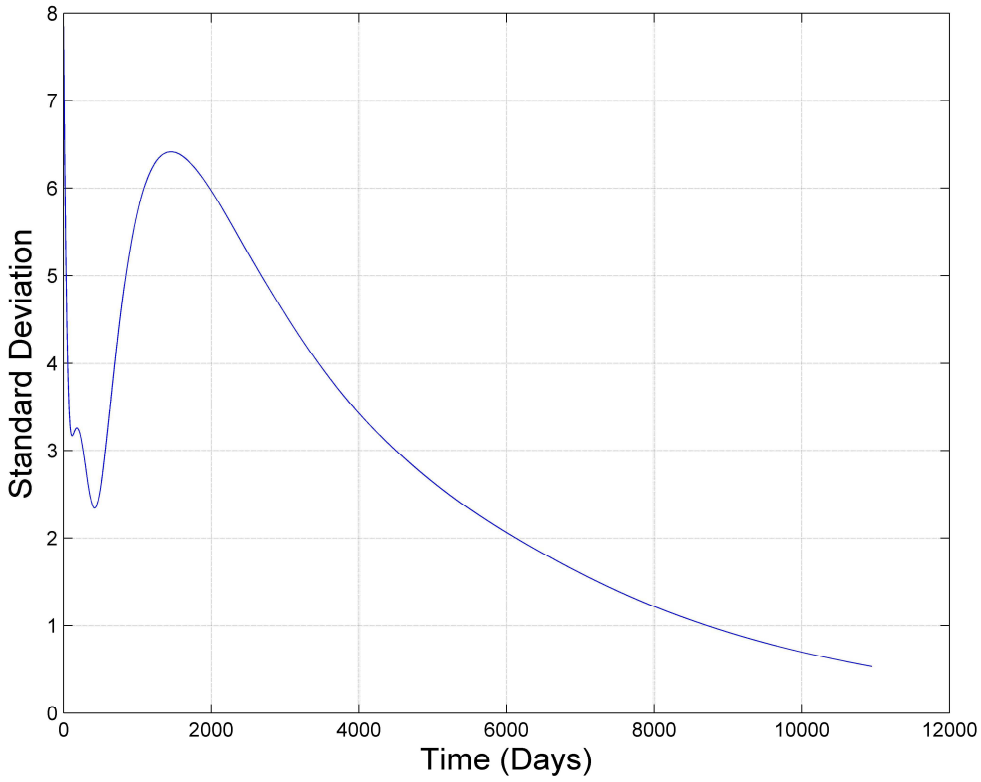

Fig. 44 — The standard deviation of the Bayesian model

Fig. 44 shows the standard deviation of the Bayesian model, however it is representing the uncertainty of the model. This graph is interesting because it shows that the uncertainty quickly decreases in early time, which is where we have the production data, and then begins to increase again. However, we can also see that as we continue to run the forecast, the uncertainty decreases once more.

4.5.2 Analysis of the Bayesian Paradigm Results when Implementing the Power Law Exponential of Well 41

The same process was used when the PLE model was applied to Bayesian paradigm. The coefficient of variation was set to 0.1 for all of the wells and all the models, just as before. This is constant for all the models for all the wells.

From this step, we generated the MCMC iterations, which generated the cumulative mean and standard deviation of each random variable, along with a graph of the iterations of each parameter. Fig. 45 through 50 show these results, and are the results of the PLE model of Well 41.

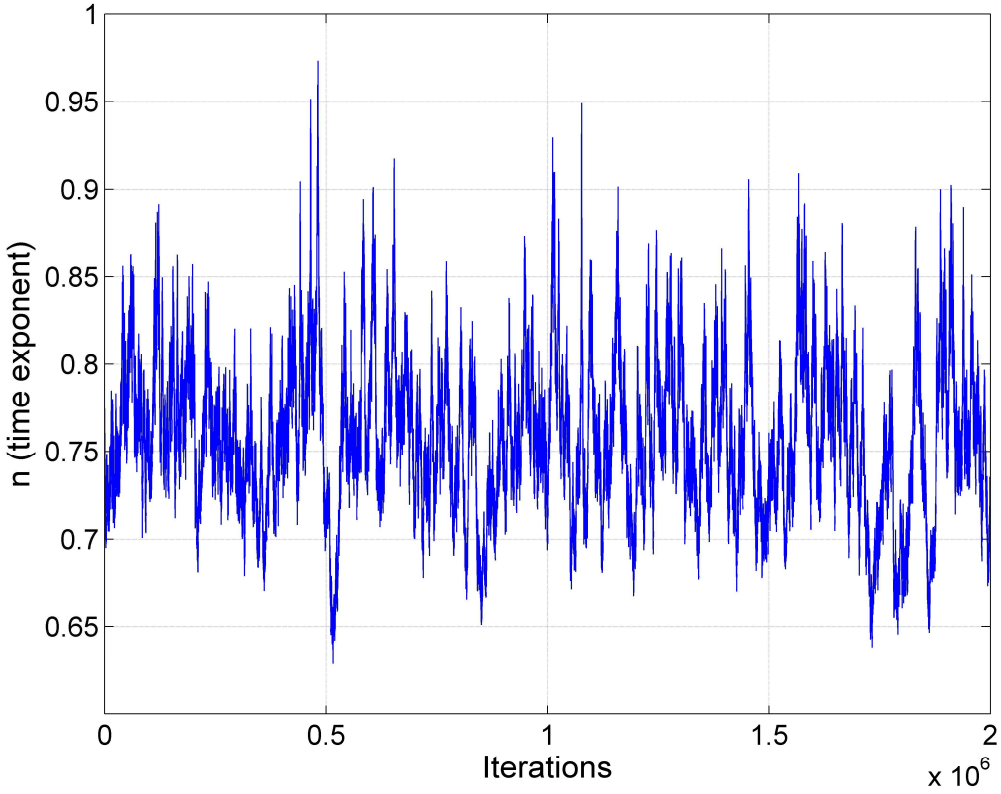

Fig. 45 — MCMC results of *n* for the PLE model

The figure above shows *n* of the PLE model converges immediately. It is also clear that the mean value of *n* is approximately 0.76, which is confirmed in Fig. 46, below.

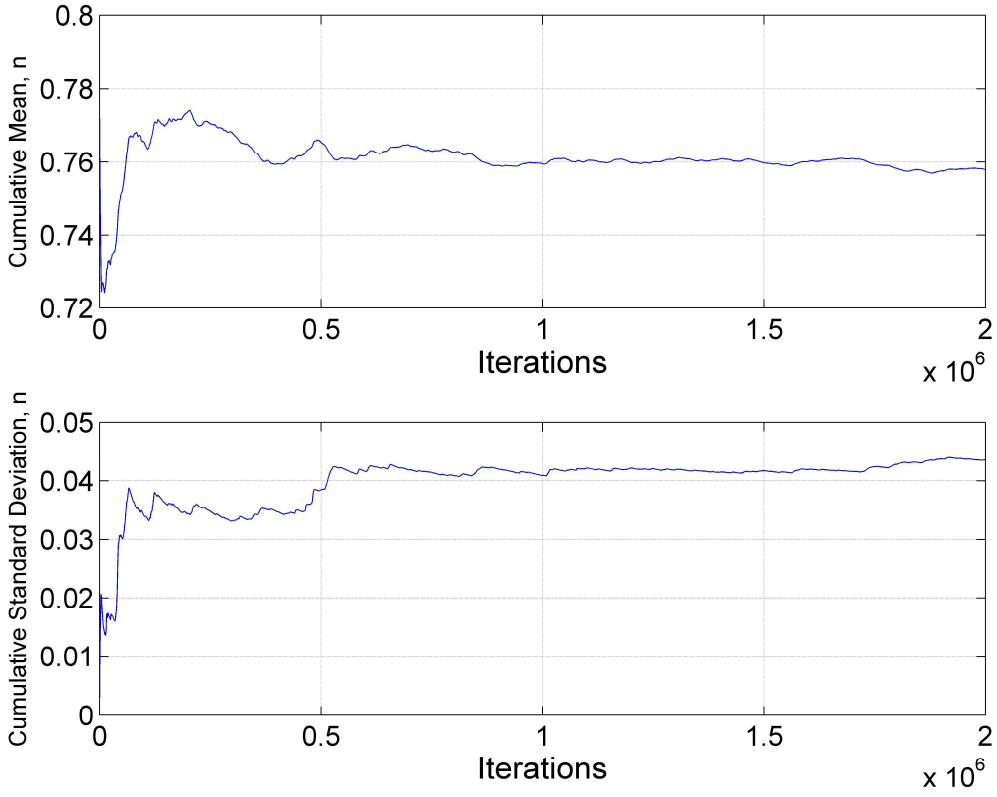

Fig. 46 — Cumulative mean and standard deviation of the *b*-factor

It is evident from the graph above that *n* for Well 41 converges after one million iterations. It is evident that there is no more noise in the data and that the MCMC has determined the true value of the *b*-factor. Furthermore, the standard deviation of *n* is 0.04 from the figure above.

We performed the same analysis on D_i and q_i, and the results are presented below.

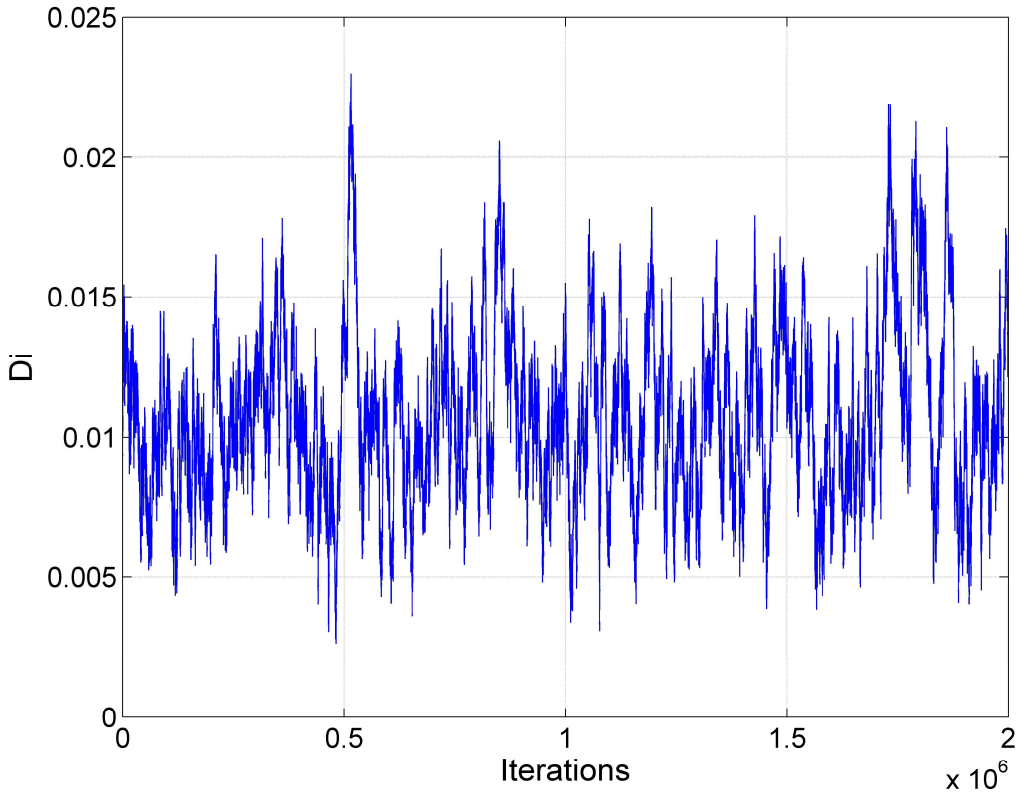

Fig. 47 — MCMC results of D_i for the PLE model

The figure above shows the D_i of the PLE model converges immediately. It is also clear that the mean value of D_i is approximately 0.01, which is confirmed in Fig. 48, below.

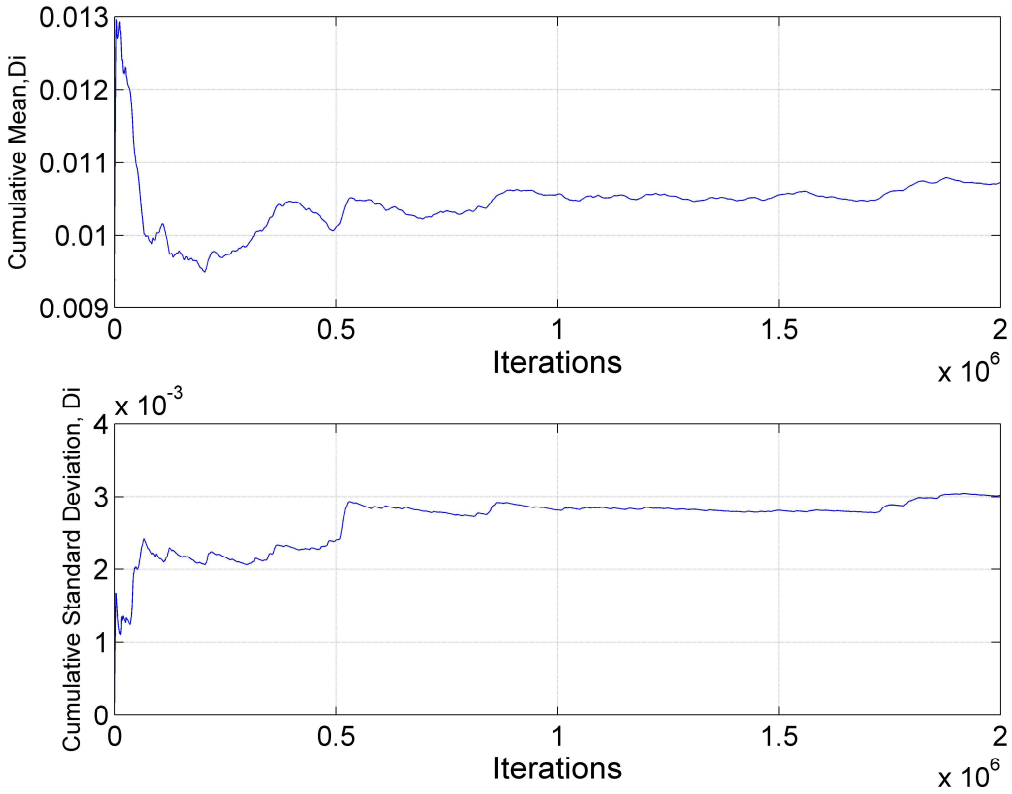

Fig. 48 — Cumulative mean and standard deviation of D_i

It is evident from the graph above that D_i for Well 41 converges almost immediately. After one million iterations, it is obvious that there is no more noise in the data and that the MCMC has determined the true value of the D_i.

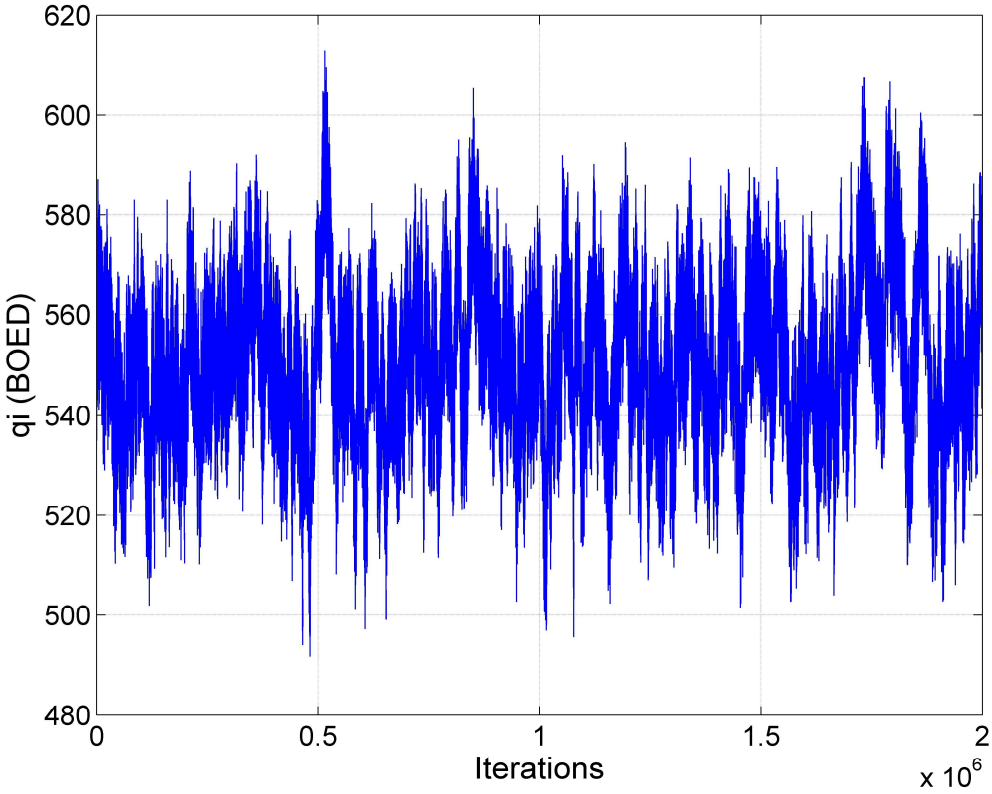

Fig. 49 — MCMC results of q_i for the PLE model

The figure above shows the q_i of the PLE model converges immediately. It is also clear that the mean value of q_i is approximately 550 BOED, which is confirmed in Fig. 50, below.

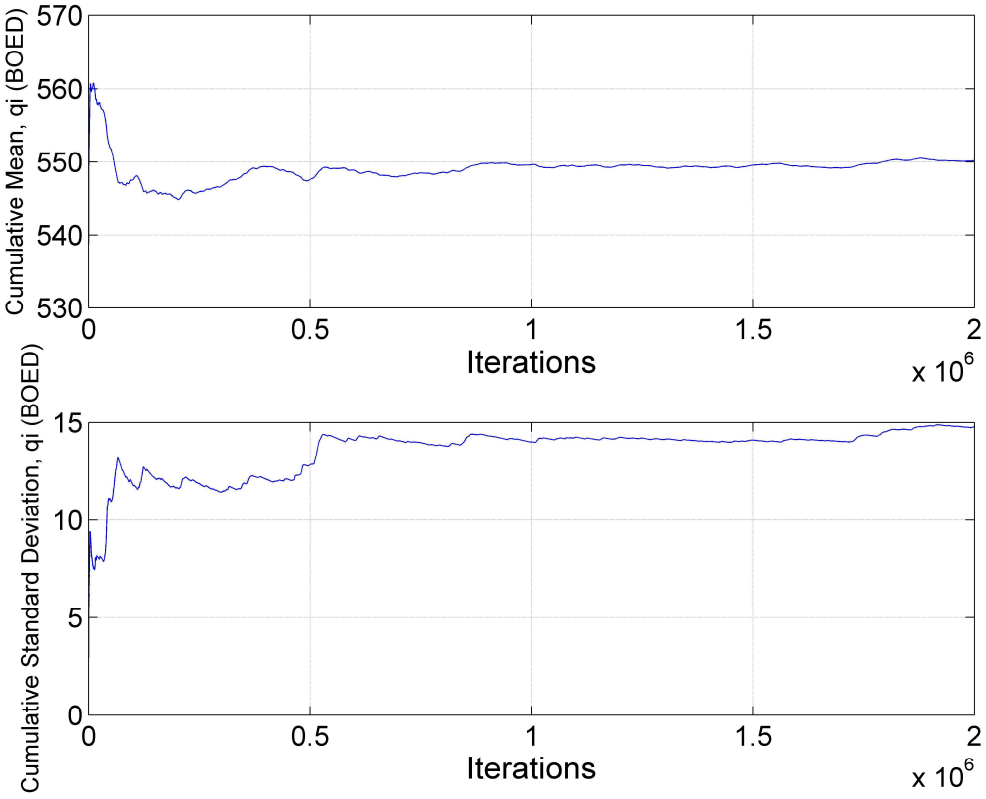

Fig. 50 — Cumulative mean and standard deviation of q_i

It is evident from the graph above that q_i for Well 41 converges almost immediately. After one million iterations, it is obvious that there is no more noise in the data and that the MCMC has determined the true value of the q_i.

Overall, the PLE model for Well 41 is a very successful run. All three parameters converged after only two million iterations.

From the cumulative means and standard deviations of each parameter (presented in Fig. 46, 48 and 50), we set the burn-in point to one million iterations.

From the results of using the burn-in point, we obtain the descriptive statistics of our models. Fig. 51 through 59 below show the results.

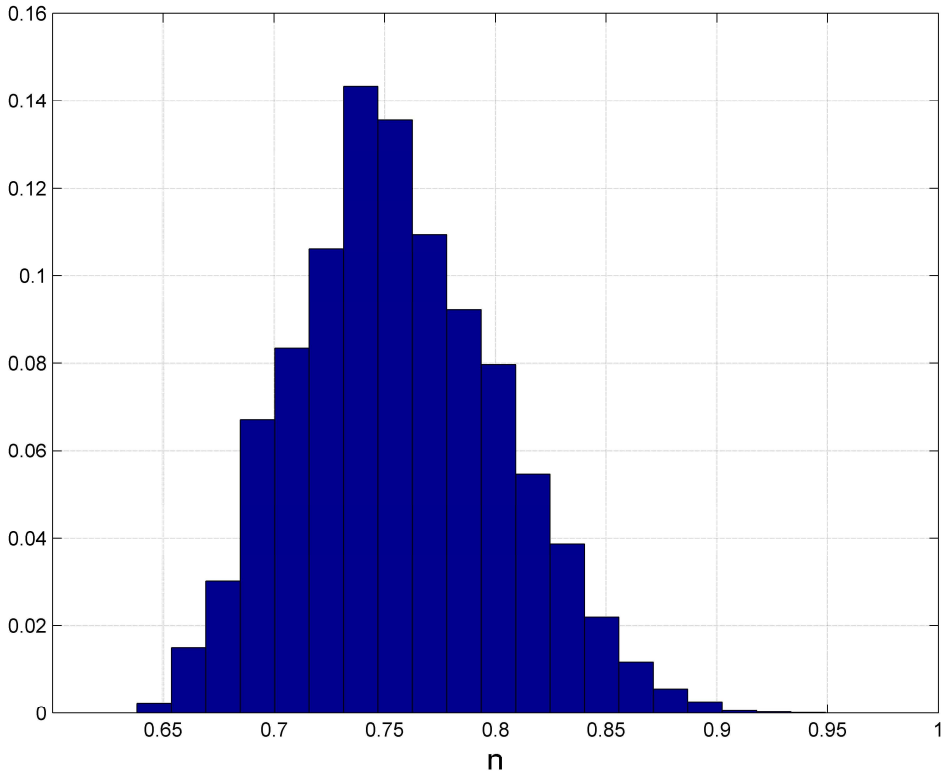

Fig. 51 — Posterior relative frequency histogram of *n*

The posterior relative frequency histogram of *n* shows a Gaussian distribution after the initial million data points were discarded. This result is expected and is seen in other cases.

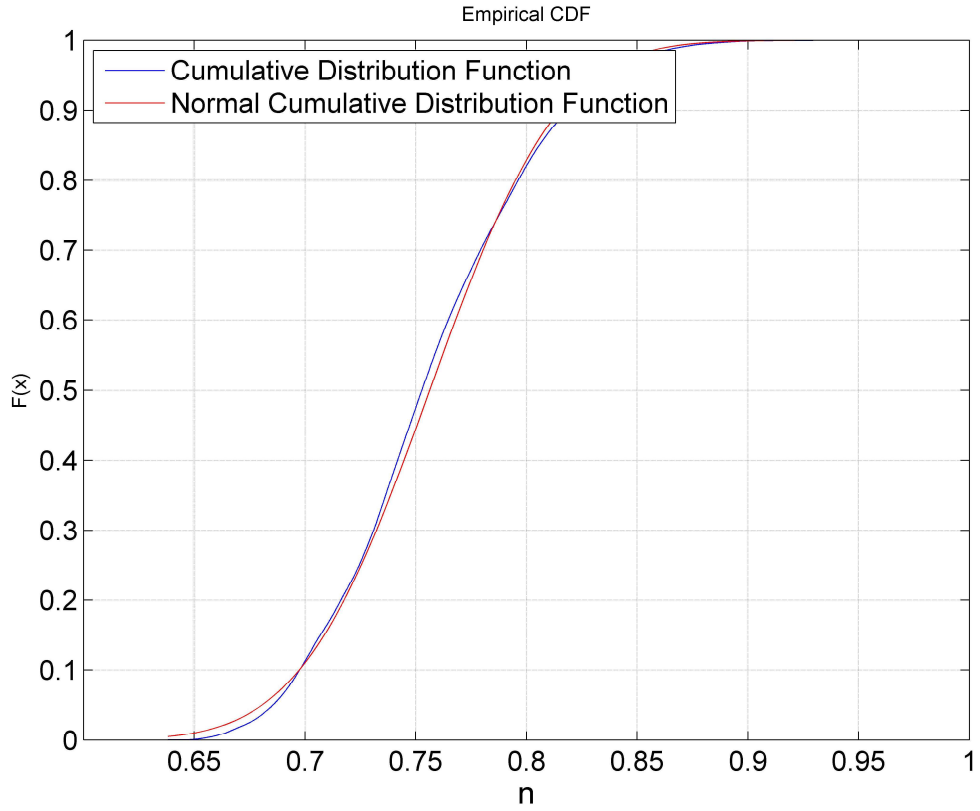

Fig. 52 — Cumulative posterior relative frequency histogram of *n*

The cumulative posterior relative frequency histogram of *n* shows the error between the value of the MCMC after the burn-in point was set, with respect to the normal cumulative distribution function. The two curves have a slight different, indicating that the results we have determined have a slight error attributed to them.

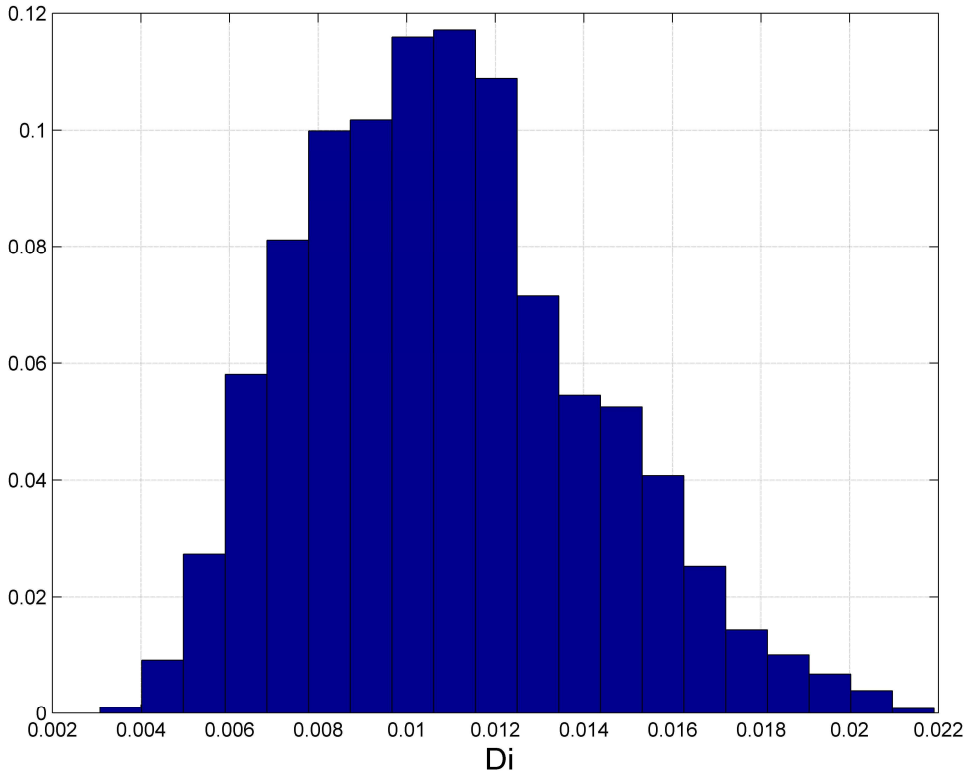

Fig. 53 — Posterior relative frequency histogram of D_i

The posterior relative frequency histogram of D_i shows a lognormal distribution, as opposed to the Gaussian distribution seen for *n*. This result is consistent through this study.

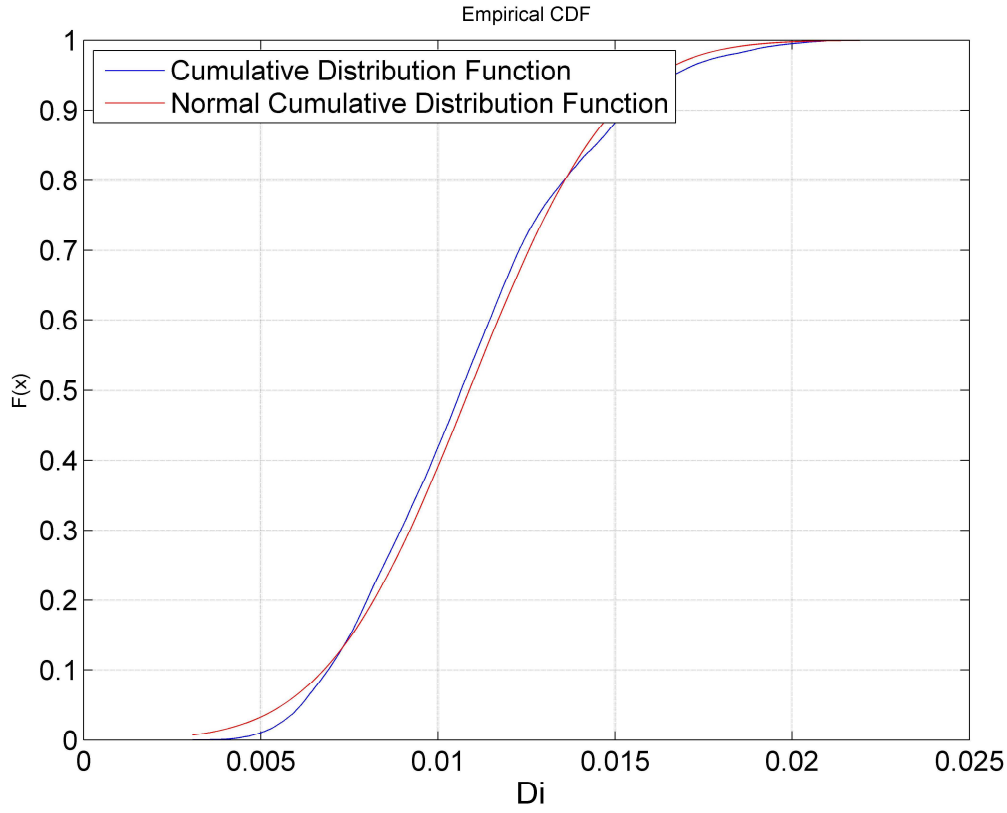

Fig. 54 — Cumulative posterior relative frequency histogram of D_i

The cumulative posterior relative frequency histogram of D_i shows the error between the value of the MCMC after the burn-in point was set, with respect to the normal cumulative distribution function. The two curves are not entirely superposed, indicating a slight error, and therefore we can assume that this is the correct value of D_i to use for this data set, while using the PLE model.

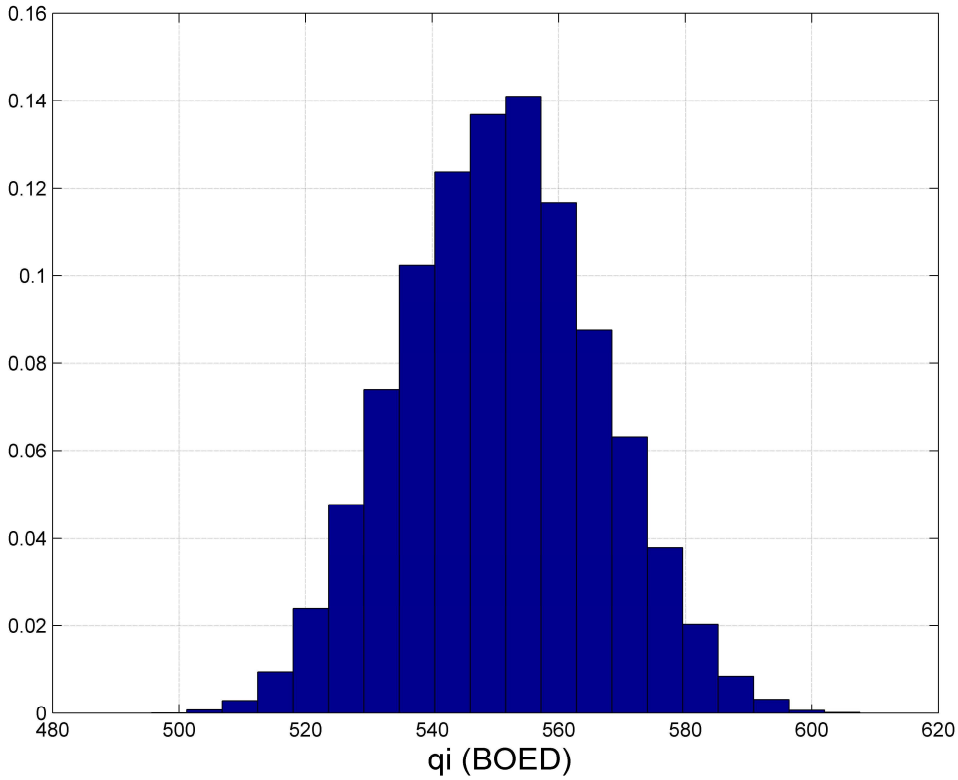

Fig. 55 — Posterior relative frequency histogram of q_i

The posterior relative frequency histogram of q_i shows the distribution of q_i after the burn-in point has been set. This graph indicates that the q_i has a Gaussian distribution after the initial million data points were discarded.

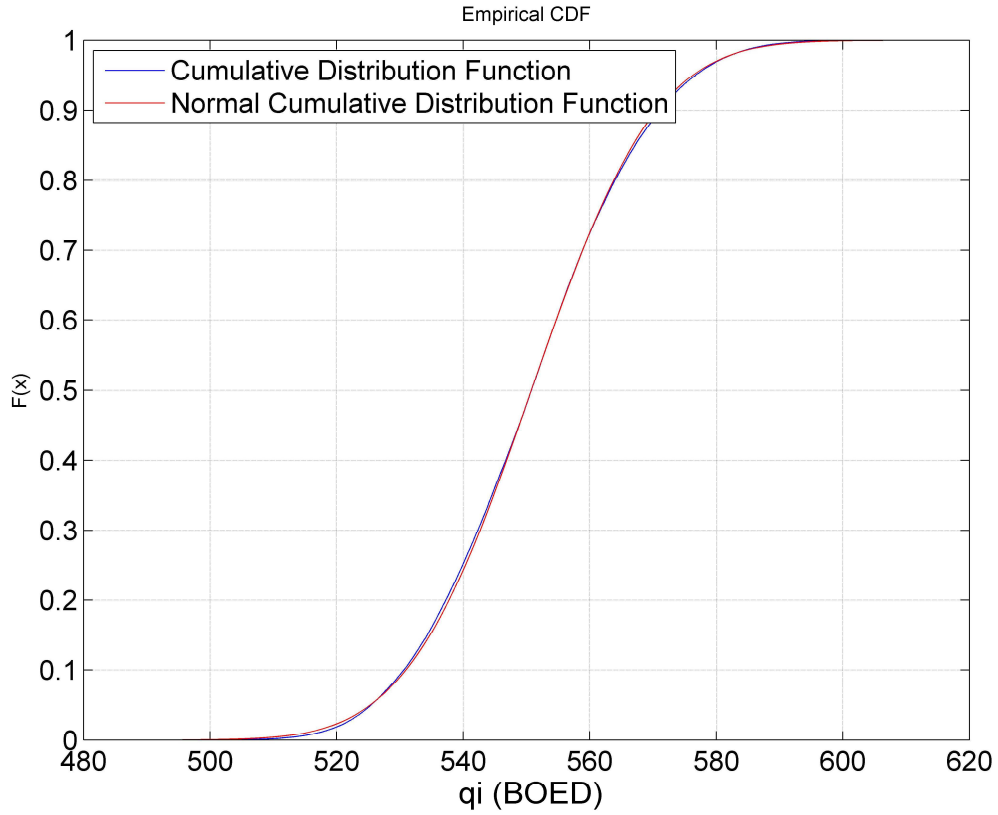

Fig. 56 — Cumulative posterior relative frequency histogram of q_i

The cumulative posterior relative frequency histogram of q_i shows the error between the value of the MCMC after the burn-in point was set, with respect to the normal cumulative distribution function. The two curves are superposed, indicating that the results we have determined do not have any error attributed to them, and this is the correct value of q_i to use for this data set, while using the PLE model.

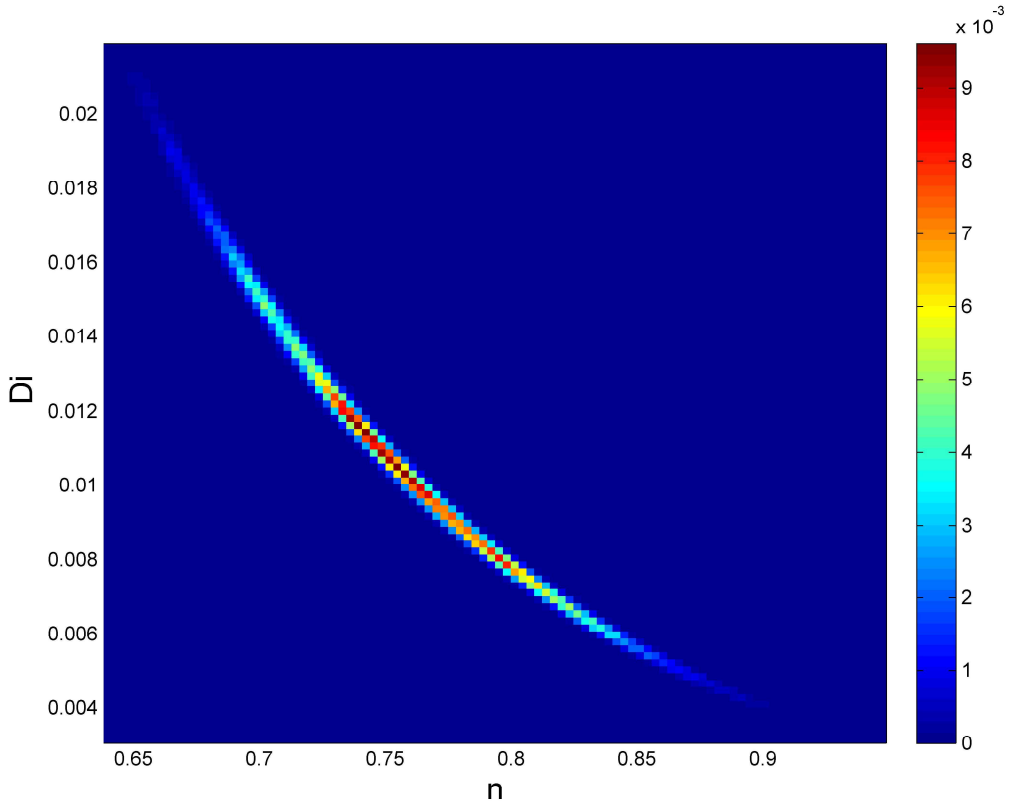

Fig. 57 — Relative frequency diagram between D_i and n

The relative frequency diagram between D_i and n shows the relationship between these two parameters for the PLE model. There is no distinct relationship between these two parameters, though the red center of the curve in the graph above indicates the most accurate set of parameters for the given data set.

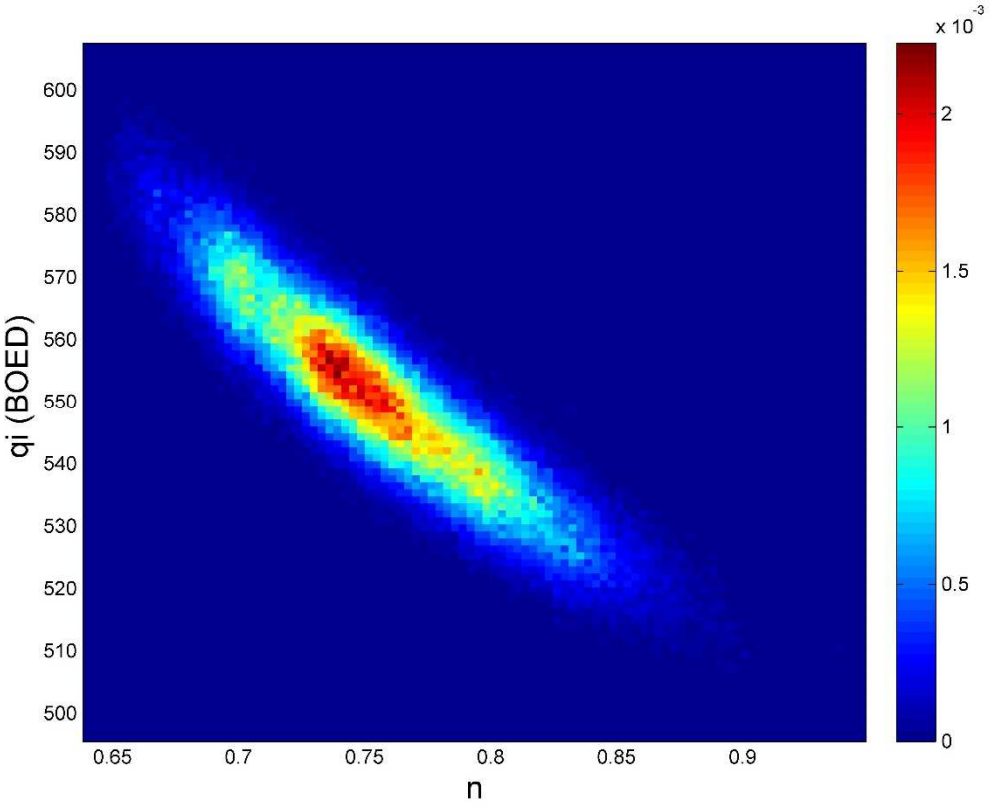

Fig. 58 — Relative frequency diagram between q_i and n

The relative frequency diagram between q_i and n shows the relationship between these two parameters for the PLE model. The red region in the center of the curvature in the graph indicates the ideal combination of these two parameters for this specific set of data points and model. Though there should not be any relationship between these parameters, it is evident from the graph above that there is a negative linear relationship.

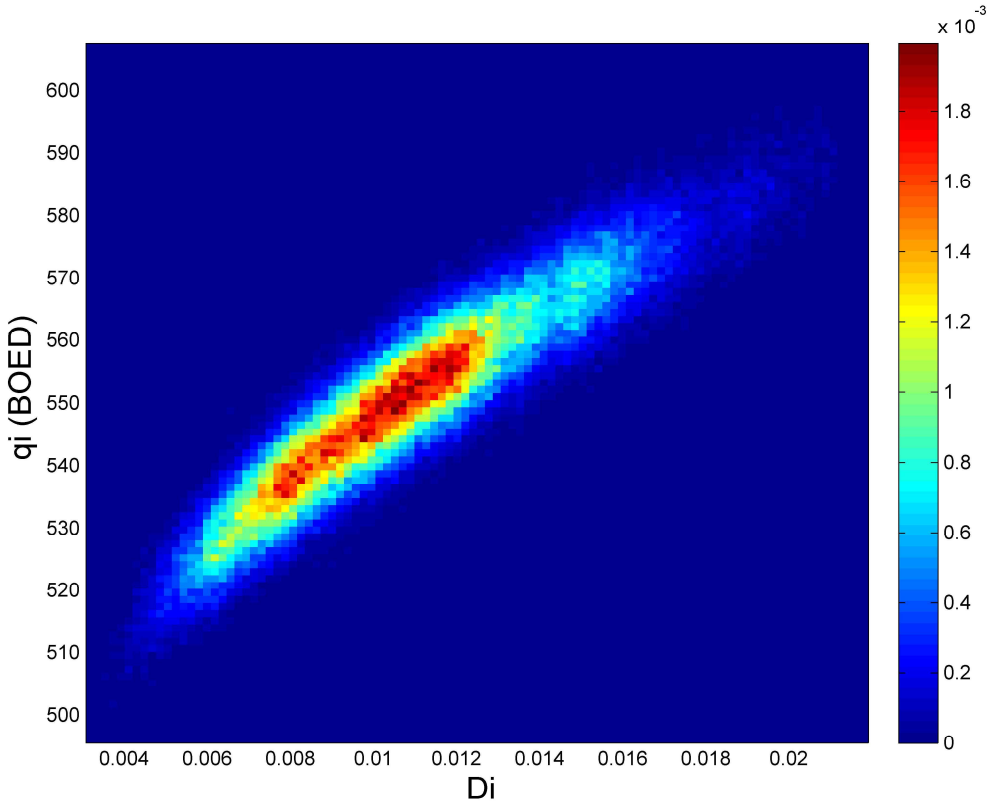

Fig. 59 — Relative frequency diagram between q_i and D_i

The relative frequency diagram between q_i and D_i shows the relationship between these two parameters for the MH model. The red region in the center of the curvature in the graph indicates the ideal combination of these two parameters for this specific set of data points and model.

The results presented in Fig. 51-59 validate that our model is working properly and that the set burn-in point was accurate.

Using the spatial statistics and the results of the parameters, we generated 1,000 realizations of the model predictions from the determined posterior distribution. It is possible to generate as many realizations are desired, however it was determined that 1,000 gave an accurate range of results. From there, we determine the mean of these

realizations and the standard deviation, which indicates the uncertainty of our Bayesian model. This was done for the 700 and 450 days, and then was extended to 30 years. Below are the results in Fig. 60 through 65 for Well 41 using the PLE model.

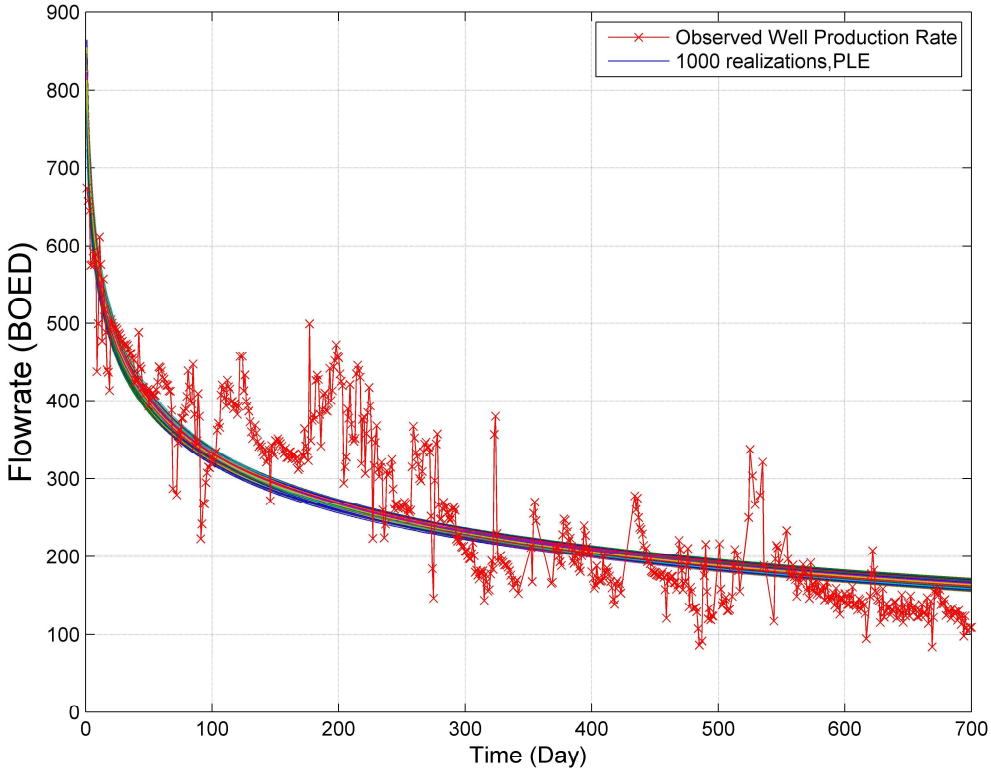

Fig. 60 — The 1,000 realizations of the model predictions using the Bayesian paradigm

Fig. 60 shows the 1,000 realizations that were created using the parameters that were determined with the MCMC. By looking at the graph, we can see that all the results fall in a similar range. This graph shows 1,000 possible combinations of results. The next step is to take the mean of these results, and compare it to the optimized values and the forward model values.

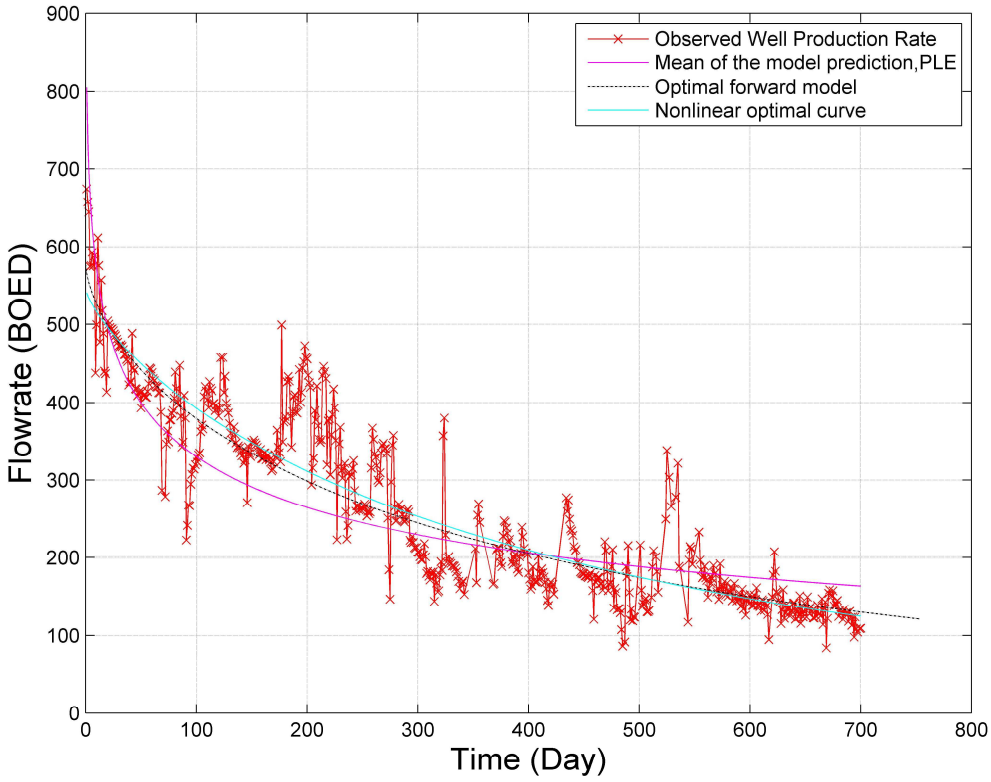

Fig. 61 — The production data with the mean of the realizations, the optimal forward model and the expert forward model

The graph above shows the three methods used in this study against the production data. In this case, the black curve is the optimal forward model, that was determined by the applying the least squares optimization, the blue curve is the mean of the 1,000 realizations and finally, the turquoise curve is the expert forward model, which in this case is the PLE model. It is evident that in this case, the PLE model and the mean of the model predictions are superposed; therefore the two returned the same result. This is unexpected, however it means that the PLE was the correct model to use initially, and it means that the Bayesian model produced the same results, therefore it agrees with the original forward model.

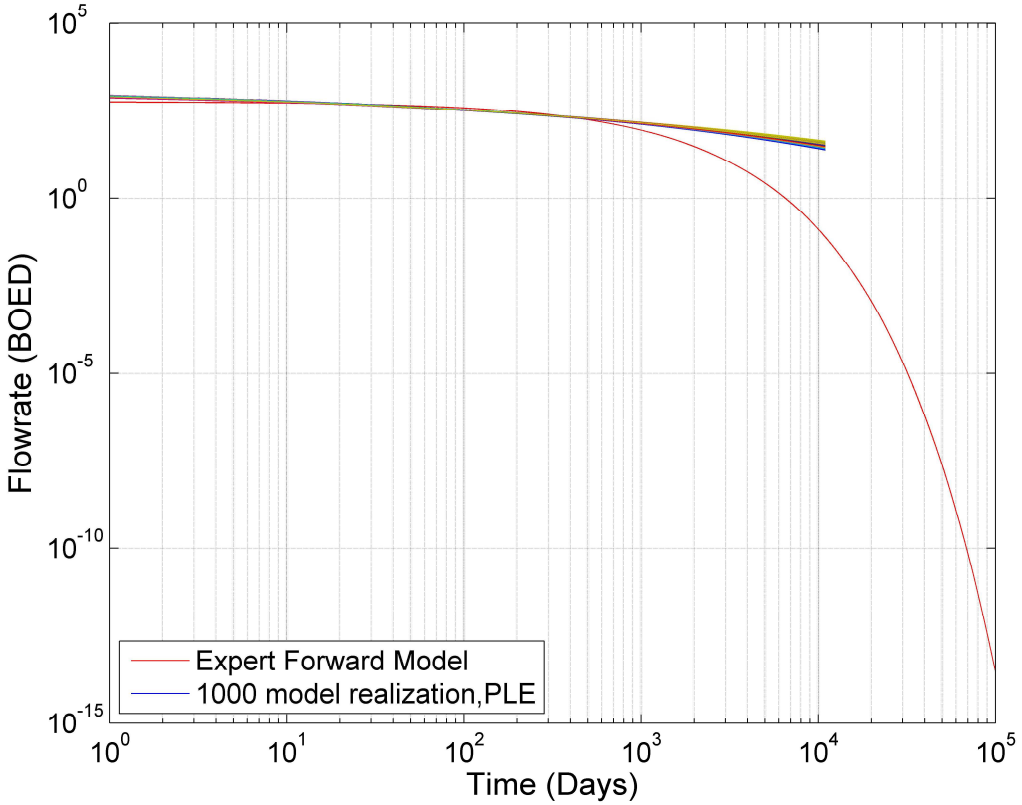

Fig. 62 — The 1,000 realizations of the model predictions using the Bayesian paradigm for 30 years

Fig. 62 shows the realizations of the model predictions for 30 years. In the graph above, the red curve is the expert forward model, therefore in this case, the MH model, and the remaining curves are the realizations. It is interesting to note that the forward model underestimates the reserves, which is noticeable because the curve is so far below the remaining curves.

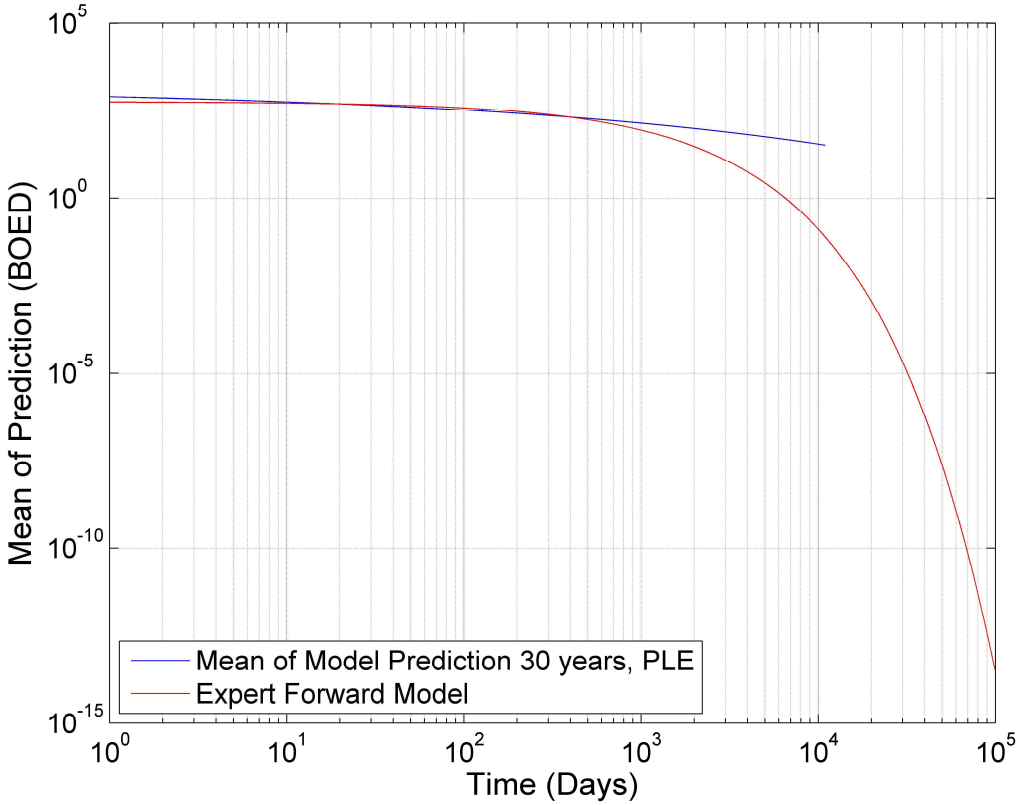

Fig. 63 — The mean of the realizations and the expert forward model, plotted for 30 years

Like the previous figure, Fig. 63 is plotted for 30 years. This graph is similar to the previous graph, however shows the mean of the 1,000 realizations, therefore gives a clearer view of the behavior of the model predictions. In this graph, it is evident that the expert model (the PLE model) is underestimating the results. We can see that in early time, the two graphs seem to be overlapped, which is also evident in Fig. 61, however it is evident from Fig. 63 that the forward model and the Bayesian model do not yield the same results. This is interesting to see, and an important conclusion to draw, because it shows that the forecast is necessary for a longer period of time to see how the two models act. We can see again that the forward model is significantly underestimating the reserves compared to the Bayesian model.

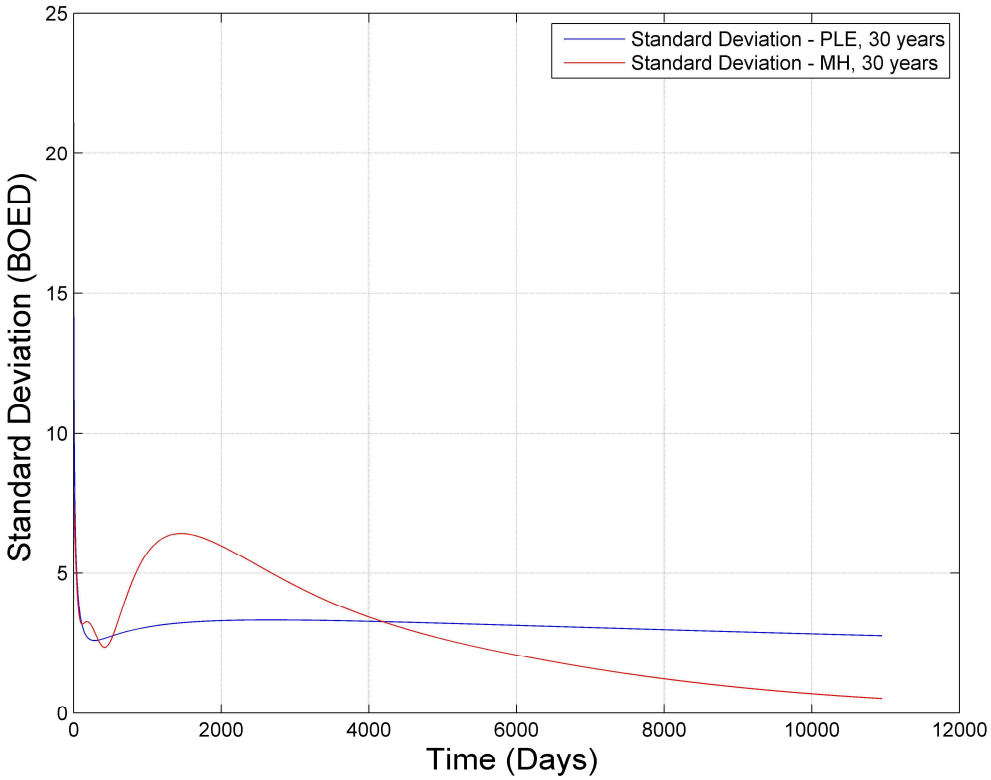

Fig. 64 — The comparison of the standard deviations of the two Bayesian models

Fig. 64 shows the two standard deviations of the two Bayesian models. It compares the uncertainty of the two models. From the graph, it is evident that the uncertainty of Bayesian paradigm when used with the MH model decreases over time, whereas that of the PLE model remains constant. From this, it is evident that the MH model would be more desirable for this specific case because the objective, when implementing the Bayesian paradigm, is to decrease uncertainty over time.

The results of the other seven wells are included in Appendix I through VIII.

4.5.3 Discussion of the Results

Well 41 shows a beautiful convergence of the MCMC results for all three parameter of the MH model and of the PLE model. The posterior distributions for the MH model when implemented the Bayesian paradigm are also as expected – Gaussian for the *b*-factor and for q_i, and lognormal for D_i, which has been a trend in this study. We see the same trends for the PLE posterior results; a Gaussian distribution for *n* and q_i, and a lognormal distribution of D_i. This is a truly excellent example of what we were trying to show with this study. The parameters of the two different models have the same distributions, even though they are not related. This does tell us that the two D_i values may somehow be related, since we see the same behavior.

Based on the posterior distributions of the three parameters, we created the relative frequency histograms that show the relationship between two different parameters -- D_i vs. *b*, q_i vs. *b* and q_i vs D_i for the MH model and D_i vs. *n*, q_i vs. *n* and q_i vs D_i for the PLE model.

The PLE results of the relative frequency histograms are also very clear, and follow the same trend as seen in Well 19 (Appendix III). It is important to show that both models for all the wells are showing the same trends.

Finally we reach the realizations of the Bayesian paradigm using the MH and PLE models. We notice when we plot the mean of the realizations versus the optimal forward model (the results from the LSQ optimization), and the expert forward model (either MH or PLE), the mean of the model prediction and the expert forward model often times have close values for the 700 production days plotted. However, when we extend the results to 30 years that there is a divergence between two sets of results. In this case, the MH model, when applied to the Bayesian paradigm overestimates reserves. However in this case, the PLE model does not follow the same trend as the MH model, and is underestimating the

reserves. This is the first time that we see this result. It is interesting to see that the same well and same set of production data can lead to such different results.

The graph that compares the standard deviations of the two sets of Bayesian results identifies the uncertainty of the two models. From the results, we see a similar trend in the uncertainty as we did for Well 41. This is interesting because this well's cases both yielded excellent results, however from these results, we can see that the MH model is decreasing uncertainty with time but the PLE model is not.

5 CONCLUSIONS AND FUTURE WORK

5.1 Conclusions

The conclusions of based on our detailed analysis of Well 41 are:

- The Bayesian paradigm implemented with the MH model overestimates reserves.
- The Bayesian paradigm implemented with the PLE model underestimates reserves.

Furthermore, the *uncertainty* of the two models:

- Decreases when the MH model is applied to the Bayesian paradigm.
- Remains constant when the PLE model is applied to the Bayesian paradigm.

An indicator of a successful model in the Bayesian paradigm is that it's uncertainty decreases with time — as such, this work suggests that the MH model should yield the most reliable results when the Bayesian paradigm is applied. We note for completeness that these results and conclusions are only valid for this well (Well 41), and may not necessarily apply for the other two wells.

The data diagnostics and analyses for the remainder of the wells are shown in the Appendices. Overall, Set 1, the set of five wells truncated at 700 days, has more accurate results than Set 2, the set of three wells truncated at 450 days. This is most likely because there are more production data available in Set 1 and therefore the Bayesian model can more effectively isolate the model based on the underlying trend in the data. However, there are certain results of Set 2 that show a good convergence of the three parameters of the model (e.g., the Bayesian forecast using the PLE model for Well 67). Overall, it is better to have more production history. Due to the lesser production history, it is probable that the decline behavior of the wells in Set 2 will change as more data is collected.

The majority of the wells exhibit behavior that favor the MH model (in particular, Wells 18, 20, 24, 38, 40 and 41), all of which yield their best results when we apply the Bayesian paradigm using the MH model. Wells 19 and 67 are the two "best cases" for when the PLE model is applied to the Bayesian paradigm.

We see that the MH and PLE forward models and the mean of the realizations are often juxtaposed at early times and the difference between the models is seen at later times. When the forecast was extended to 30 years, we can observe whether or not the forward model over- or underestimates the reserves. As comment, it is interesting that the majority of the wells evaluated follow the MH model rather than the PLE model.

Well 38 has poor results for both models, however when the MH model was applied to the Bayesian forecast, only one of the three parameters did not converge. The same behavior was observed for Well 24. However as previously discussed, Well 24 does not exhibit a good production trend and the lack of a strong data trend does not aid in obtaining accurate DCA or statistical results. Well 41 does exhibit a good match when the PLE model was applied to the Bayesian forecast although the standard deviation for the MH model is lower, which is our target criteria.

The goal of this study is to show the discrepancy (or error) obtained when using traditional decline curve methods compared to the application of the (Bayesian) statistical model. As process, the DCA approach using the two forward models (Modified-Hyperbolic (MH) and Power-Law Exponential (PLE)) was performed visually, where the best fit of the data was obtained using a proprietary software. After this process was performed for each of the wells, the resulting values of the different parameters for each DCA relation were documented, along with the EUR results. This part of the study was not very time consuming, and as is the convention, we would expect such results to tend towards the median of the Bayesian paradigm (at least that is the expectation).

When applying the Bayesian paradigm using the MH or PLE models, there are multiple steps involved, and significant computational time is required. Initially, we apply the LSQ optimization, then apply the MCMC methodology on the different parameters for each decline model, and finally we forecast the results for the historical data, and then for 30 years. When the MCMC methodology is implemented, the simulation takes hours to run for the case of two million iterations — however, for the case of 50 million iterations,

models took several days to run. This process, being time consuming, can be seen as a drawback. However; once the results are presented, we can visually see that the Bayesian paradigm produces results that are statistically more accurate, and clearly shows when the forward model is over- or under-estimating results for a given case.

5.2 Future Work

The next step in this study is to perform a comparison of the 30-year forecasted cumulative production as a surrogate for EUR. This action was not provided in this work due to constraints in the modeling approach. This would have to be performed "externally" to the Bayesian approach in the current solution configuration. After this has been done, it would be ideal to change the prior estimate. Instead of assuming that the prior estimate is unknown, we can begin to update this value using the different stages of information. This will show that the more information we have, the more accurate the Bayesian forecast will be. Using these results we could show directly that uncertainty decreases over time, indicating that the more information known in the model, the less uncertain the model will be. Such a process will also indicate if there is a point where no more information is needed in the prior estimations, and that having information on a certain (minimum) number of data points will not affect the result of the forecast. We can assume that the model will be more accurate as more information is provided — however; we would like to prove this conjecture.

Finally, we would like to plot surfaces of the different parameters of the two forward equations to have a 3D representation of how the parameters change in 3D space. Initially, we will plot the values of the eight wells that have been used in this study. Then, we will eliminate one well and see if the estimated values at that point are the same, or approximately the same as the actual values. If we find that the two values correspond, we can remove another well, to see how well the model will estimate the values at that point. After this has been completed, we can increase the area of investigation and begin to estimate values at different parts of the play that do not have producing wells. The

results may also indicate if a particular well is worth drilling or not, and there would be a visual representation production potential of the play.

REFERENCES

Al-Attar, Hazim Hassan, and Sulaiman Al-Zuhair: "A General Approach for Deliverability Calculations of Gas Wells", paper SPE 111380 presented at the 2008 SPE North Africa Technical Conference and Exhibition, Marrakech, Morrocco, March 12-14

Arps, J. J.: "Analysis of Decline Curves", *Trans.* AIME (1944), paper SPE 945228, vol 160, issue 01, pp 228-247

Aster, Richard C., Borchers, Brian, and Thurber, Clifford H.: *Parameter Estimation and Inverse Problems* in Elsevier, Amsterdam, The Netherlands (2013)

Ayers, Walter B.: "PETE 612 - Unconventional Oil and Gas Reservoirs", Course Notes, Texas A&M University (2011)

Bahadori, Alireza, and Hari Vuthaluru: "A simple decline-curve analysis approach for evaluating gas reserves and predicting future production in gas reservoirs", paper SPE 139057 presented at the 2010 SPE Eastern Regional Meeting, Morgantown, West Virginia, USA, October 12-14

Bazan, Lucas W., Lattibeaudiere, Michael G., and Palisch, Terry: "Hydraulic Fracture Design and Well Production Results in the Eagle Ford Shale: One Operator's Perspective", paper SPE 155779 presented at the 2012 Americas Unconventional Resources Conference, Pittsburgh, Pennsylvania, USA, June 5-7

Benedict, Jon: "The Mathematics Of Decline Curves", paper SPE 10537 (1981)

Benjamin, Jack R. , and C. Allin Cornell: *Probability, Statistics, and Decision for Civil Engineers*, McGraw-Hill Book Company (1970)

Bhattacharya, Srimoyee, and Nikolaou, Michael: "Using Data From Existing Wells To Plan New Wells in Unconventional Gas Field Development", paper CSUG/SPE 147658 presented at the 2011 Canadian Unconventional Resources Conferences, Alberta, Canada, November 15-17

Breyer, John A., et al.: "Stratigraphy and Sedimentary Facies of the Eagle Ford Shale (Cretaceous) between the Maverick Basin and the San Marcos Arch, Texas, USA," Search and Discovery Article #50899 presented at the 2013 AAPG Annual Convention and Exhibition, Pittsburgh, Pennsylvania, USA, May 19-22

Chen, G., D. H. Tehrani, and J. M. Peden: "Calculation of Well Productivity in a Reservoir Simulator (II)" , paper SPE 29932 presented at the 1995 International Meeting on Petroleum Engineering, Beijing, China, November 14-17

Corbett, Kevin: "Eagleford Shale Exploration Models: Depositional Controls on Reservoir Properties," Search and Discovery Article #10242 presented at the 2010 AAPG Annual Convention and Exhibition, Denver, Colorado, USA, June 7-10

Cuesta, J. F.: "Reservoir Parameter Calculations From D.S.T. Pressure Analysis," Paper No. 80-31-40 presented at the 1980 Petroleum Society of CIM, Calgary, May 25-28

Fazelipour, W.: "Development of Technicques to Integrate Hydraulic Fracturing Design and Reservoir Simulation Technologies - Application to Forecast Production of Stimulated Wells in Unconventional Gas Reservoirs", paper SPE 142337 presented at the 2011(a) SPE Middle East Unconventional Gas Conference and Exhibition, Muscat, Oman, January 31- February 2

Fazelipour, W.: "Innovative Reservoir Modeling and Simulation of Unconventional Shale Gas Reservoirs Powered by Microseismic Data", paper SPE 141877 presented at the 2011(b) SPE Middle East Unconventional Gas Conference and Exhibition, Muscat, Oman, January 31- February 2

Fetkovich, M. J.: "Decline Curve Analysis Using Type Curves", paper SPE 4629 presented at the 1973 SPE 48th Fall Meeting, Las Vegas, Nevada, USA , September 30-October 3

Gentry, Robert W.: "Decline-Curve Analysis", paper SPE 3356, *Journal of Petroleum Technology* (1972), vol 24, issue 01, pp 38-41

Gong, Xinglai, et al.: "Assessment of Eagle Ford Shale Oil and Gas Resources," paper SPE 167241 presented in the 2013 SPE Unconventional Resources Conference Canada, Calgary, Alberta, Canada, November 5-7

Gonzalez, R., Gong, X. and McVay, D.A..: "Prior Information Enhances Uncertainty Quantification in Shale Gas Decline Curve Forecasts," paper SPE 167150 presented in the 2013 SPE Unconventional Resources Conference Canada, Calgary, Alberta, Canada, November 5-7

Gross, Henry Emmett: "Decline-curve Analysis", *Trans.* AIME, SPE 939101 (1939), vol 132, issue 01, pp 101-102

Guo, Boyun, and Xiance Yu: "A Simple and Accurate Mathematical Model for Predicting Productivity of Multifractured Horizontal Wells", paper SPE 114452 presented at the 2008 CIPC/SPE Gas Techonology Symposium Joint Conference, Calgeary, Alberta, Canada, June 16-19

Hao, Mingqiang, et al.: "Establishment and Application of the Multi-Peak Forecasting Model", paper IPTC 16897 presented at the 2013 International Petroleum Technology Conference, Beijing, China, March 26-28

Holditch, S.: "Unconventional Oil and Gas Go For the Source", Lecture at Texas A&M University, slide 6, 2011

Ilk, D., and T. A. Blasingame: "Decline Curve Analysis for Unconventional Reservoir Systems -- Variable Pressure Drop Case", paper SPE 167253 presented at the 2013 SPE Unconventional Resources Conference-Canada, Calgary, Alberta, Canada, November 5-7

Ilk, Dilhan, Neal J. Broussard, and Thomas Alwin Blasingame: "Production Analysis in the Eagle Ford Shale -- Best Practices for Diagnostic Interpretations, Analysis, and Modeling", paper SPE 160076 presented at the 2012 SPE Annula Technical Conference and Exhibition, San Antonio, Texas, USA, October 8-10

Ilk, Dilhan, et al.: "Hybrid Rate-Decline Models for the Analysis of Production Performance in Unconventional Reservoirs", paper SPE 135616 presented at the 2010 SPE Annual Technical Conference and Exhibition, Florence, Italy, September 19-22

Ilk, Dilhan, Creties David Jenkins, and Thomas Alwin Blasingame: "Production Analysis in Unconventional Reservoirs - Diagnostics, Challenges, and Methodologies", paper SPE 144376 presented at the 2011 North American Unconventional Gas Conference and Exhibition, the Woodlands, Texas, USA, June 14-16

Ilk, Dilhan, Jay Alan Rushing, and Thomas Alwin Blasingame: "Decline-Curve Analysis for HP/HT Gas Wells: Theory and Applications", paper SPE 125031 presented at the 2009 SPE Annual Technical Conference and Exhibition, New Orleans, Louisiana, USA, October 4-7

Ilk, Dilhan, Jay Alan Rushing, and Thomas Alwin Blasingame: "Integration of Production Analysis and Rate-Time Analysis via Parametric Correlations -- Theoretical Considerations and Practical Applications", paper SPE 140556 presented at the 2011 SPE Hydraulic Fracturing Technology Conference, The Woodlands, Texas, USA, January 24-26

International Energy Agency. http://www.iea.org/ (2014)

Jensen, Jerry L., et al.: *Statistics for Petroleum Engineers and Geoscientists*, *Handbook of Petroleum Exploration and Production* in Elsevier, Amsterdam, The Netherlands (2000)

Johnson, Nathalie Louise, et al.: "A Simple Methodology for Direct Estimation of Gas-in-place and Reserves Using Rate-Time Data", paper SPE 123298 presented at the 2009 SPE Rocky Mountain Petroleum Technology Conference, Denver, Colorado, April 14-16

Jordan, C. L., M. J. Fetkovich, and L. R. Sibbald: "Simple, Accurate Gas Production Analysis for Forecasting and Reserves," paper PETSOC-2005-030 presented at the 2005 Canadian International Petroleum Conference, Calgary, Alberta, Canada, June 7-9

Klins, M. A., and M. B. Biterge: "A Semianalytical Approach to Pseudopressure Calculations", paper SPE 15914, *Journal of Petroleum Technology* (1987), vol 39, issue 4, pp 468-472

Larsen, Leif: "Productivity Computations for Multilateral, Branched and Other Generalized and Extended Well Concepts", paper SPE 36754 presented at the 1996 SPE Annual Technical Conference & Exhibition, Denver, Colorado, USA, October 6-9

Ling, Kegang, and Jun He: "Theoretical Bases of Arps Empirical Decline Curves," paper SPE 161767 presented at the 2012 Abu Dhabi International Petroleum Conference and Exhibition, Abu Dhabi, UAE, November 11-14

Lolon, Elyezer, et al.: "New Semianalytical Solutions for Multilayer Reservoirs", paper SPE 114946 presented at the 2008 CIPC/SPE Gas Technology Symposium Joint Conference, Calgary, Alberta, Canada, June 16-19

Mannon, Robert W.: "Oil Production Forecasting By Decline Curve Analysis," paper SPE 1254 presented in the 1965 Fall Meeting of the Society of Petroleum Engineers of AIME, Denver, Colorado, USA, October 3-6

Martinez, Wendy L., and Angel R. Martinez: *Computational Statistics Handbook with Matlab* in Chapman & Hall/CRC, Boca Raton, Florida, USA, (2008)

Mattar, Louis: "Production Analysis and Forecasting of Shale Gas Reservoirs: Case History-Based Approach", paper SPE 119897 presented in the 2008 SPE Shale Gas Production Conference, Fort Worth, Texas, USA, November 16-18

McNulty, Robert R., and Roy M. Knapp: "Statistical Decline Curve Analysis", paper SPE 10279 presented in the 1981 SPE Annual Technical Conference and Exhibition, San Antonio, Texas, USA, October 4-7

Mead, Homer N.: "Modifications to Decline Curve Analysis", paper SPE 464, original copyright American Institute of Mining, Mettalurgical and Petroleum Engineering (1956)

Medina-Cetina, Zenon: "Probabilistic Calibration of a Soil Model", Ph.D. Dissertation, Johns Hopkins University (2006)

Miller, Bradley M., and David L. Ranum: *Python Programming in Context* in Jones and Bartlett Publishers, Sudbury, MA, USA, (2009)

Mullen, J.: "Petrophysical Characterization of the Eagle Ford Shale in South Texas", paper CSUG/SPE 138145 presented at the 2010 Canadian Unconventional Resrources & International Petroleum Conference, Calgary, Alberta Canada, October 19-21

Okouma Mangha, Viannet, et al.: "Practical Considerations for Decline Curve Analysis in Unconventional Reservoirs - Application of Recently Developed Rate-Time Relations", paper SPE 162910 presented at the 2012 SPE Hydrocarbon Economics and Evaluation Symposium, Calgary, Alberta, Canada, September 24-25

Redden, Jim: "Eagle Ford Rig count down; operators cautiously bullish as permits, new wells soar", *World Oil Online* (2010), vol 233, issue 7, pp 1-13

Richardson, J. G., and R. J. Blackwell: "Use of Simple Mathematical Models for Predicting Reservoir Behavior", paper SPE 2928, *Journal of Petroleum Technology* (1971), vol 23, issue 9, pp 1145-1154

Schlumberger, Oilfied Glossary. *In* http://glossary.oilfield.slb.com/ (2014)

Seshadri, Jagan Nathan, and Louis Mattar: "Comparison of Power Law and Modified Hyperbolic Decline Methods", paper SPE 137320 presented at the 2010 Canadian Unconventional Resources and International Petroleum Conference, Calgary, Alberta, Canada, October 19-21

Solhjell, Ida K.: "Bayesian Forecasting and Dynamic Models Applied to Strain Data from the Gota River Bridge" *in* M.Sc. Thesis, Department of Mathematics, University of Oslo (2009)

Tarantola, Albert: *Inverse Problem Theory and Methods for Model Parameter Estimation*, in The Society for Industrial and Applied Mathematics, Philadelphia, Pennsylvania, USA (2005)

Tian, Yao, Walter Barton Ayers, and William D. McCain: "The Eagle Ford Shale Play, South Texas: Regional Variations in Fluid Types, Hydrocarbon Production and Reservoir Properties", paper IPTC 16808 presented at the 2013 International Petroleum Technology Conference, Beijing, China, March 26-28

Tucker, Delos R.: "Lower Cretaceous Geology, Northwestern Karnes County, Texas", *The American Association of Petroleum Geologists* (1968), vol 52, issue 5, pp 820-851

U.S. Energy Information Administration, Independent Statistics & Analysis http://www.eia.gov/ (2013)

Wang, Lei, et al.: "A Semianalytical Solution for Multifractured Horizontal Wells in Box-Shaped Reservoirs," *Mathematical Problems in Engineering* (2014), vol 2014, Article ID 716390, pp 12

West, Mike, and Jeff Harrison: *Bayesian Forecasting and Dynamic Models*, in Springer, New York, New York (1997)

Wikipedia: Least squares. http://en.wikipedia.org/wiki/Least_squares (2015)

Wikipedia: Markov chain Monte Carlo, http://en.wikipedia.org/wiki/Markov_chain_Monte_Carlo. (2015)

Xu, Bingxiang, et al.: "Production Data Analysis in Eagle Ford Shale Gas Reservoir", paper SPE 153072 presented at the 2012 SPE/EAGE European Unconventional Resources Conference and Exhibition, Vienna, Austria, March 20-22

Yao Tian, Walter B. Ayers, William D. McCain Jr.: "Regional Analysis of Stratigraphy, Reservoir Characteristics, and Fluid Phases in the Eagle Ford Shale, South Texas", *The Gulf Coast Association of Geological Societies* (2013), vol 62, pp 471-483

APPENDIX I

QDB PLOTS OF MH AND PLE MODELS

Results of the Modified Hyperbolic and Power Law Exponential methods of the two truncated data sets. Set 1 includes wells 19, 20, 38, 40, 41 and Set 2 includes wells 18, 24 and 67.

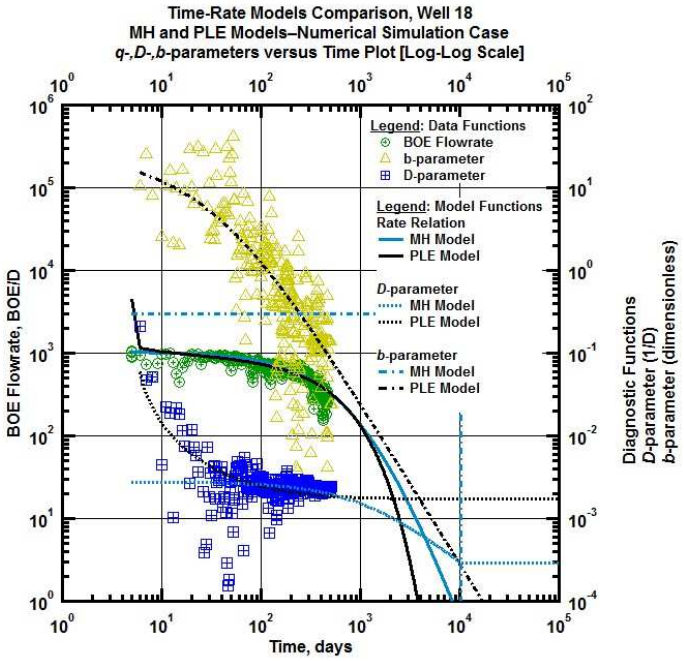

Fig. 65 — qDb plot of Well 18 using the MH and PLE models

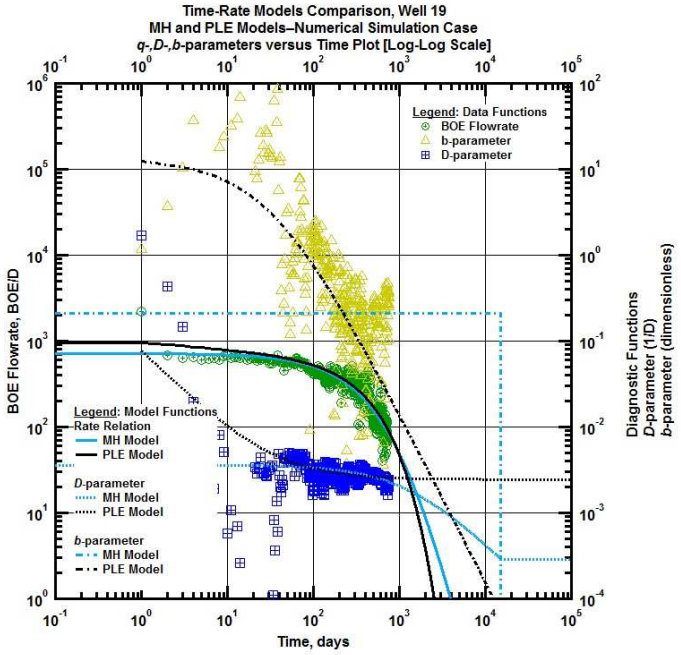

Fig. 66 — qDb plot of Well 19 using the MH and PLE models

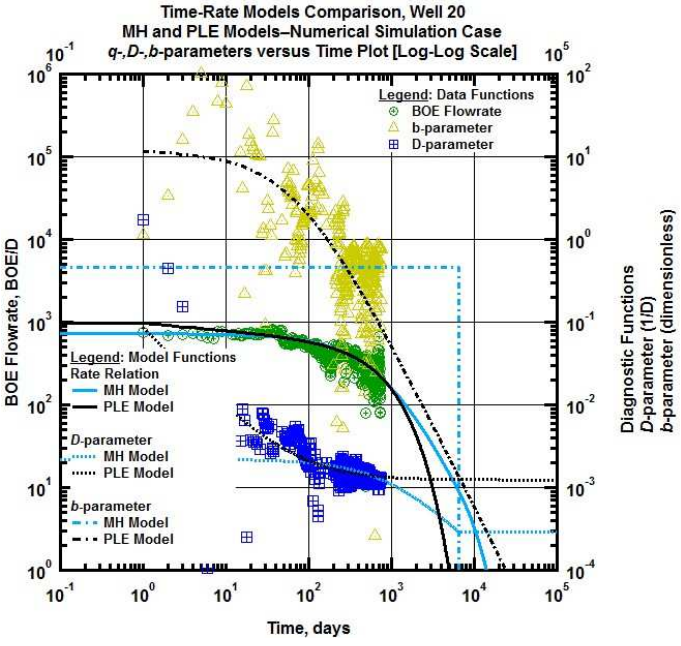

Fig. 67 — qDb plot of Well 20 using the MH and PLE models

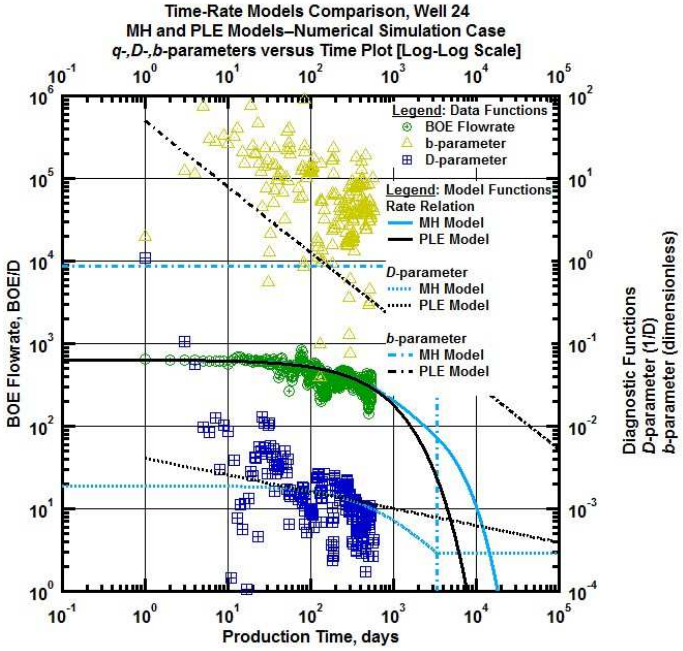

Fig. 68 — qDb plot of Well 24 using the MH and PLE models

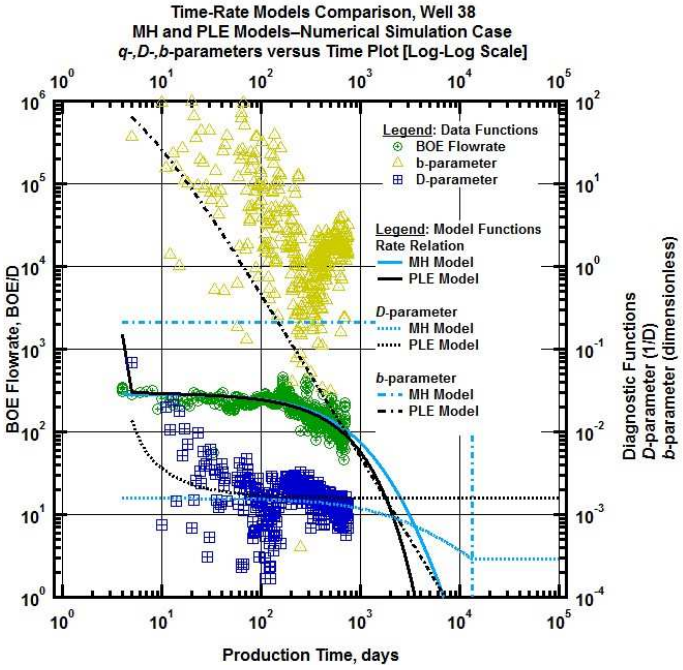

Fig. 69 — qDb plot of Well 38 using the MH and PLE models

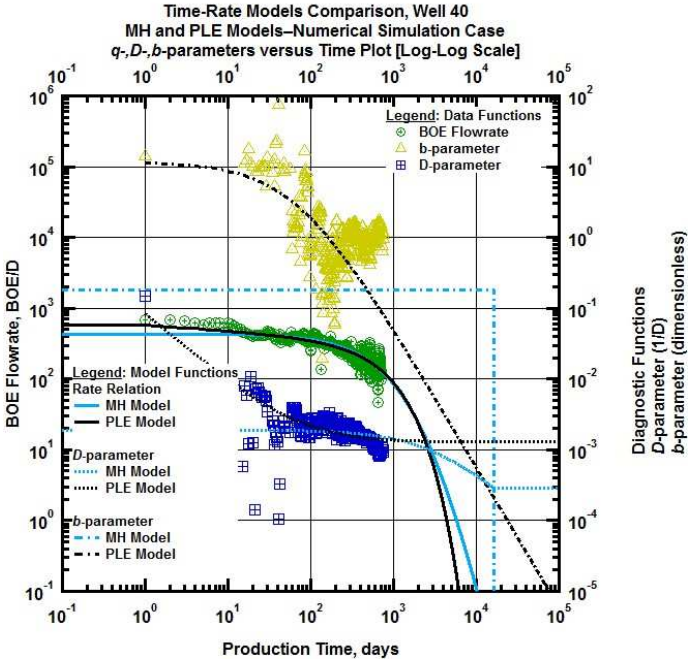

Fig. 70 — qDb plot of Well 40 using the MH and PLE models

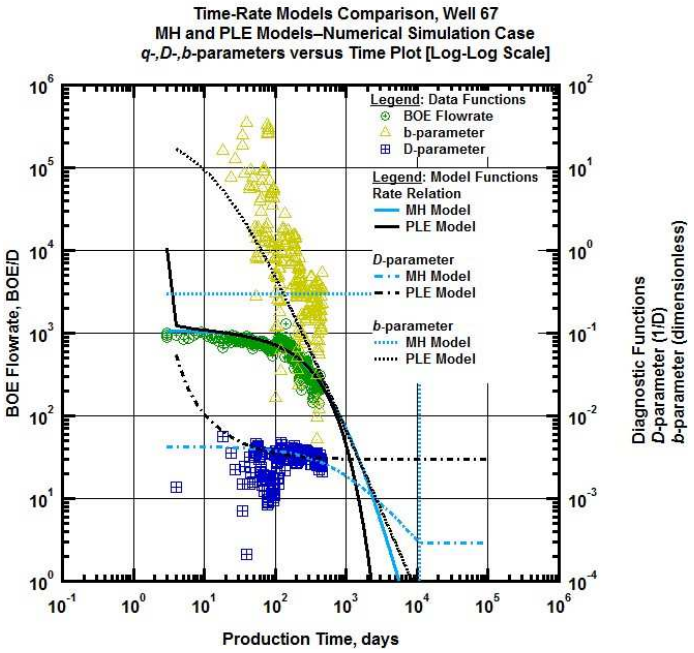

Fig. 71 — qDb plot of Well 67 using the MH and PLE models

From the eight graphs in this appendix, we can see the production trend of each well, along with the match in the *b*-factor and D_i parameters. It is from these graphs that we determined the values of these three parameters, found in Tables 1 and 2. As previously stated, we used the results to perform the LSQ optimization and when applying the Bayesian paradigm. The above graphs have both the PLE and MH results, presented in the black and blue curves, respectively. The objective when performing the DCA in these wells was the best match the production data (the green curve). This sometimes led to unrealistic results for all three parameters, however this can also be attributed to using the incorrect model to forecast the well.

From this step, we performed the LSQ optimization on all the wells, for both the MH and PLE models, and then the Bayesian paradigm will be implemented. The results of all the wells are presented below.

APPENDIX II

RESULTS AND ANALYSIS OF WELL 18

Well 18 – Modified Hyperbolic Model

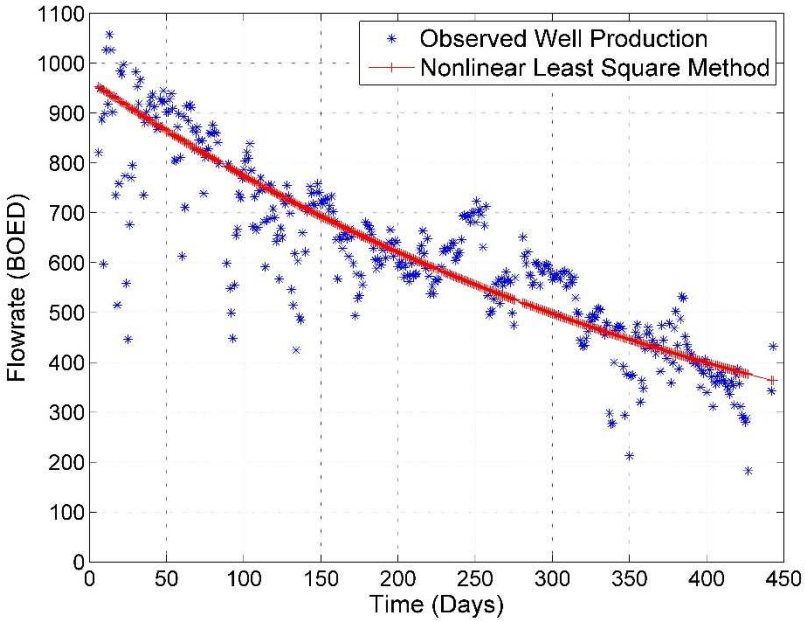

Fig. 72 — Results of the least squares optimization against the production data of Well 18 for the MH Model

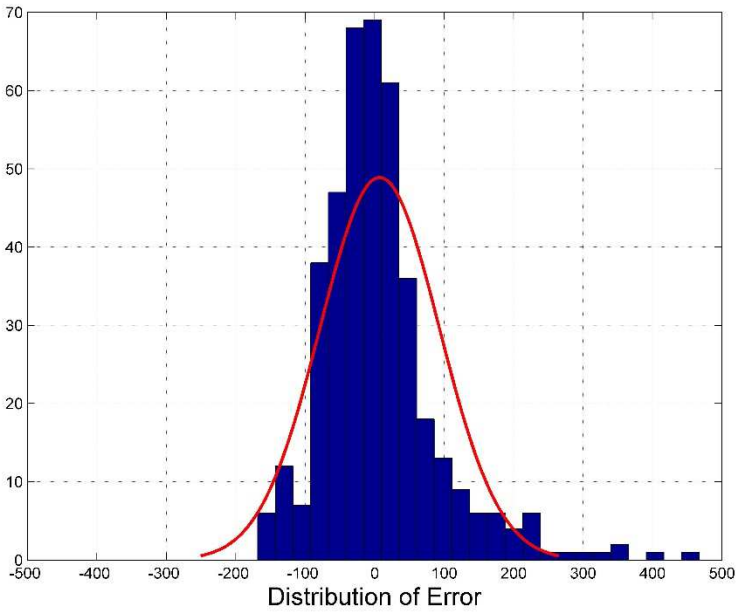

Fig. 73 — The distribution of error between the production data and the LSQ results for Well 18 for the MH Model

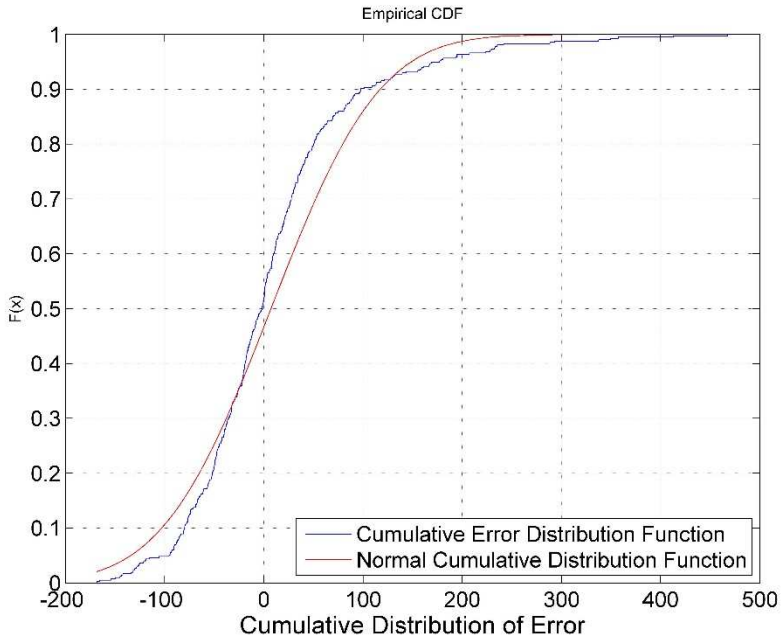

Fig. 74 — The cumulative distribution of error is plotted against the normal cumulative distribution function of Well 18 for the MH Model

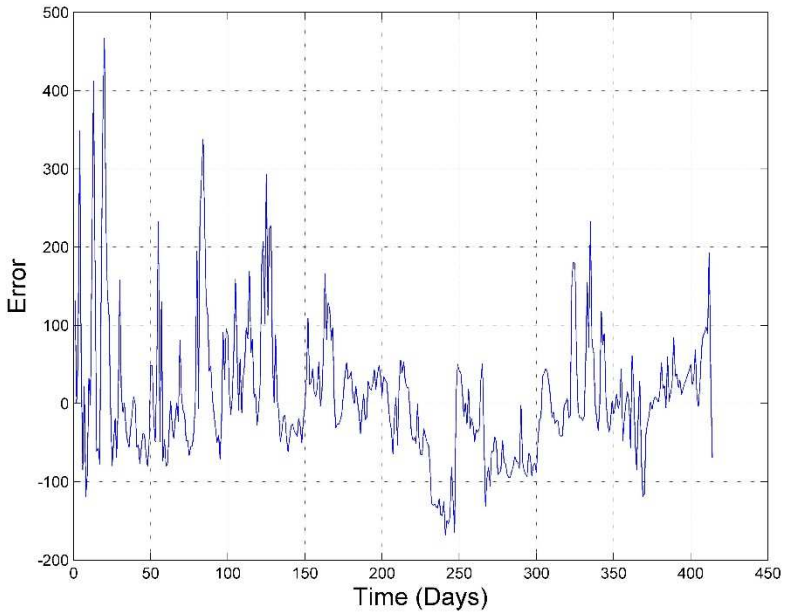

Fig. 75 — The error of the least squares optimization against the number of production days of Well 18 for the MH Model

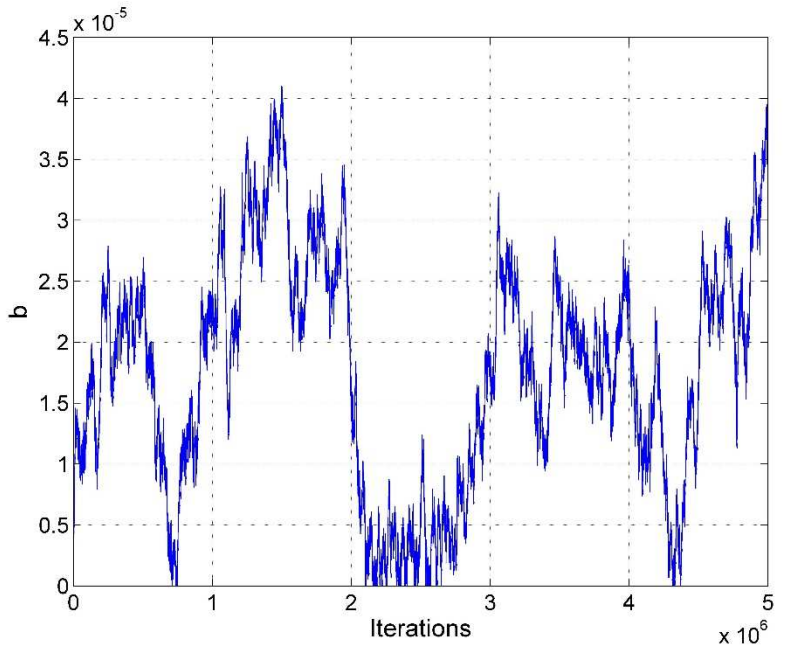

Fig. 76 — MCMC results of the *b*-factor for the MH model of Well 18 using the MH model

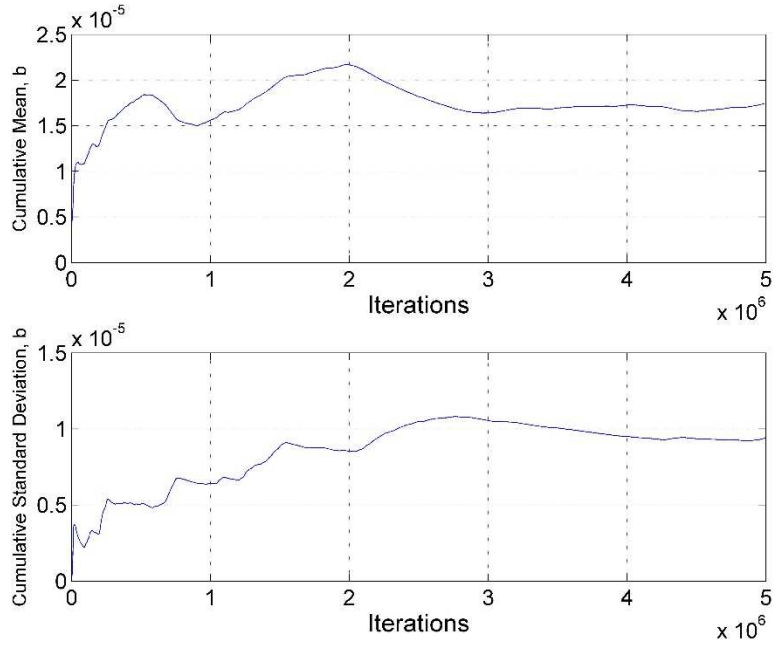

Fig. 77 — Cumulative mean and standard deviation of the *b*-factor of Well 18 using the MH model

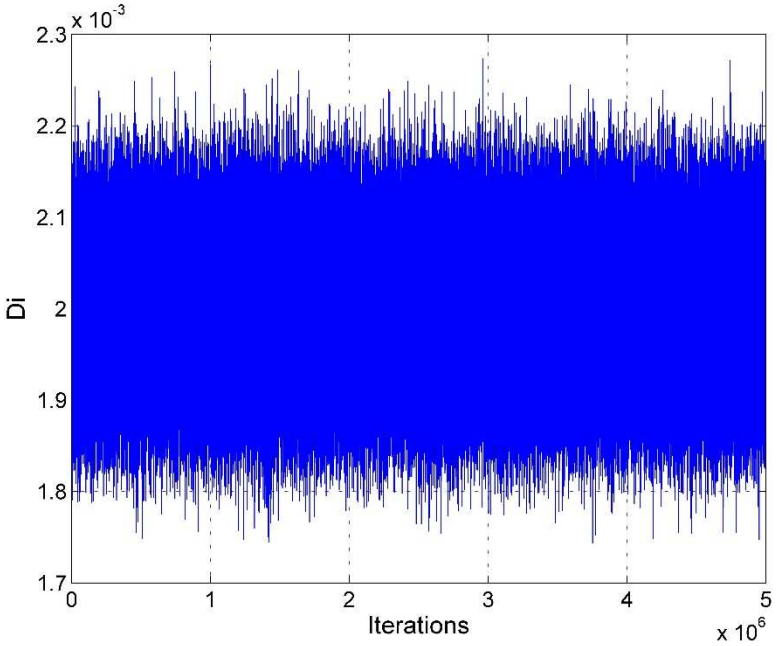

Fig. 78 —MCMC results of D_i for the MH model of Well 18 using the MH model

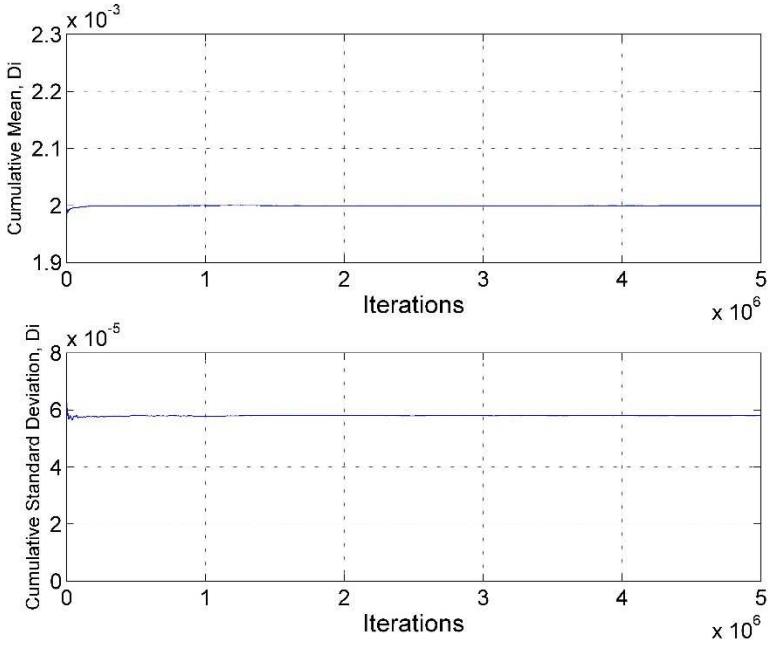

Fig. 79 — Cumulative mean and standard deviation of D_i of Well 18 using the MH model

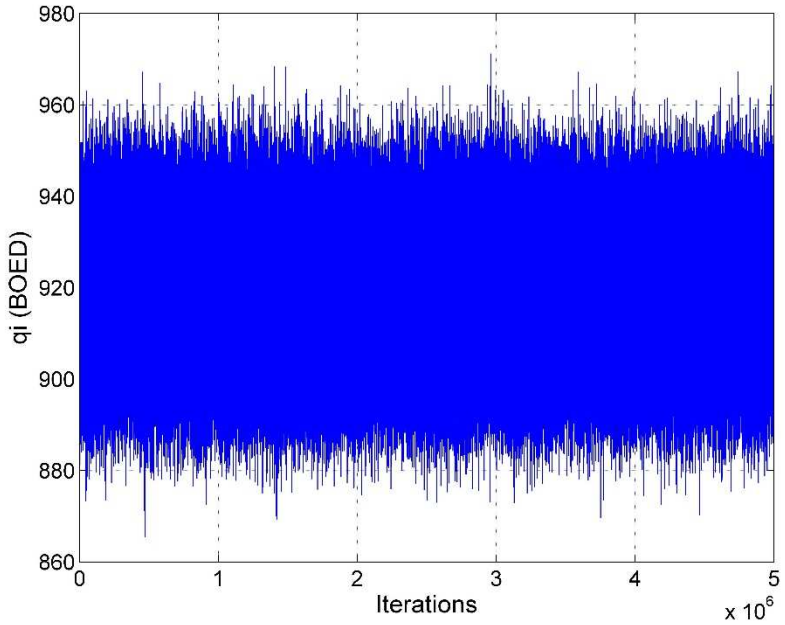

Fig. 80 — MCMC results of q_i for the MH model of Well 18 using the MH model

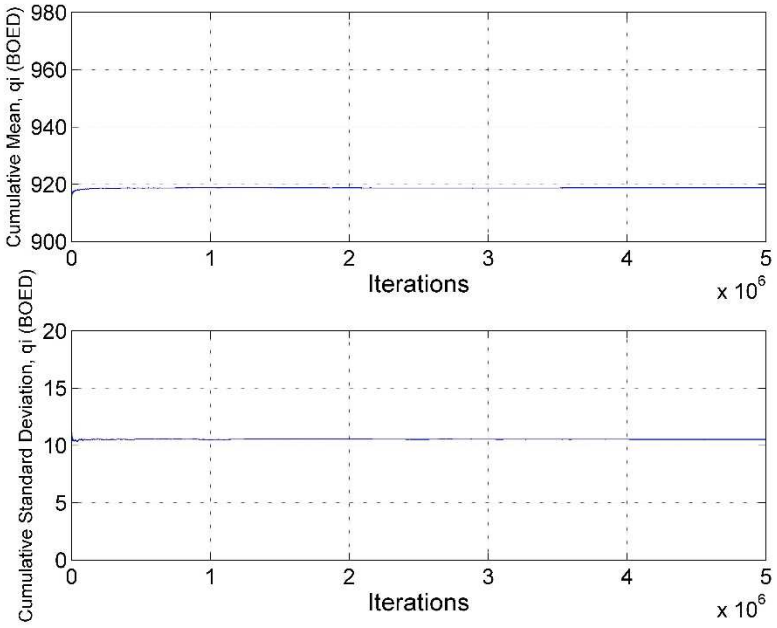

Fig. 81 — Cumulative mean and standard deviation of q_i of Well 18 using the MH model

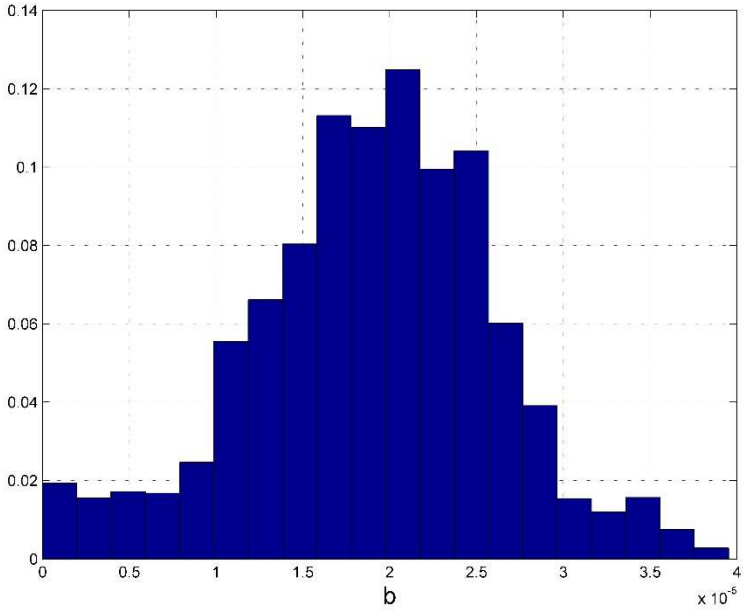

Fig. 82 — Posterior relative frequency histogram of *b* of Well 18 using the MH model

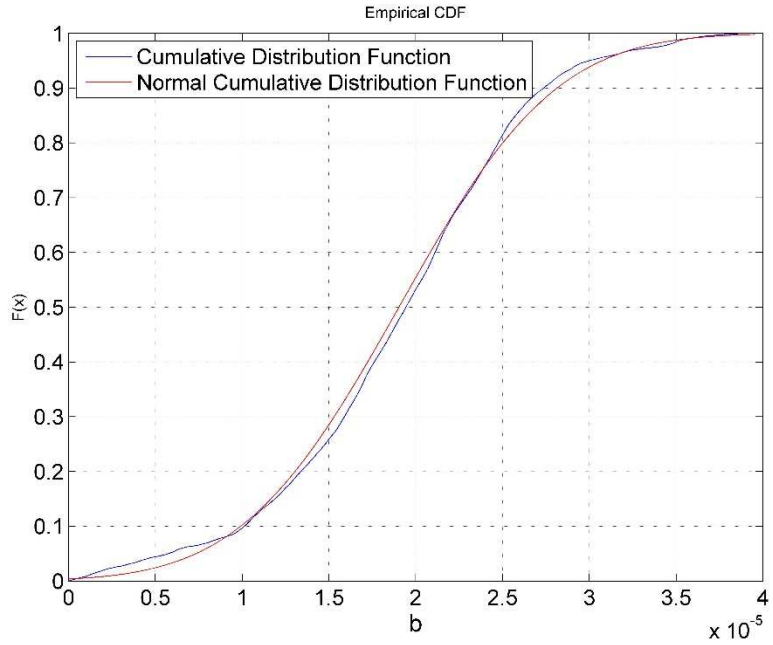

Fig. 83 — Cumulative posterior relative frequency histogram of the *b*-factor of Well 18 using the MH model

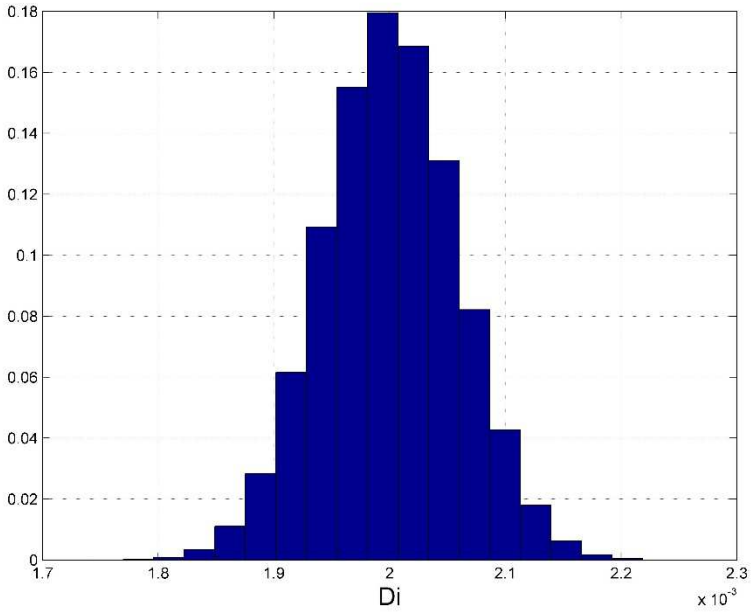

Fig. 84 — Posterior relative frequency histogram of D_i of Well 18 using the MH model

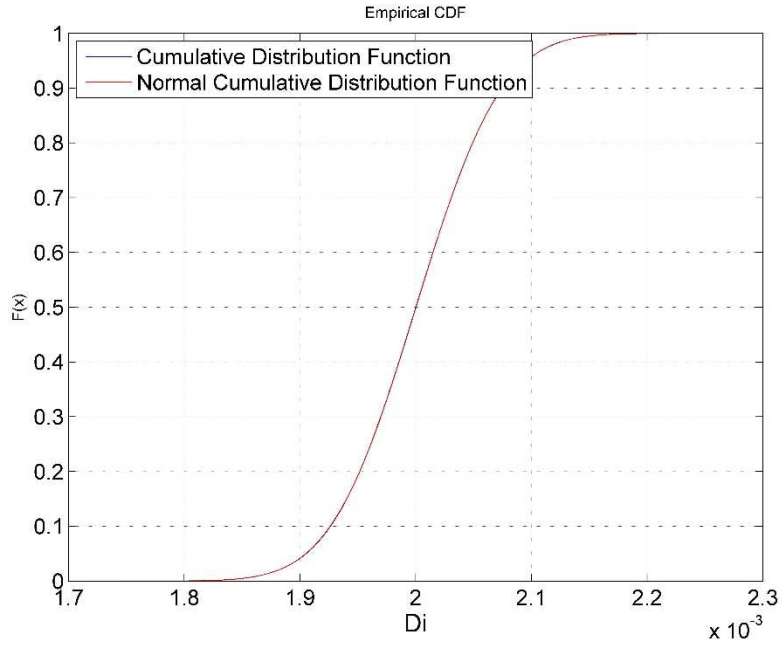

Fig. 85 — Cumulative posterior relative frequency histogram of D_i of Well 18 using the MH model

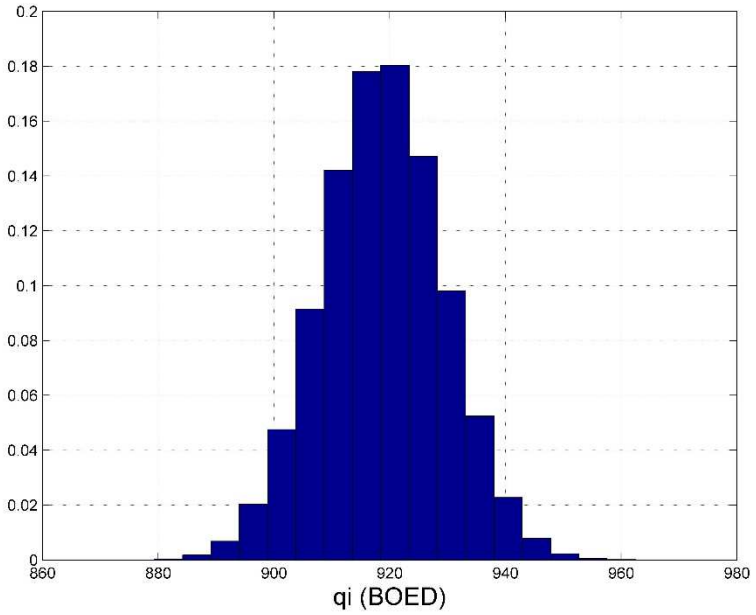

Fig. 86 — Posterior relative frequency histogram of q_i of Well 18 using the MH model

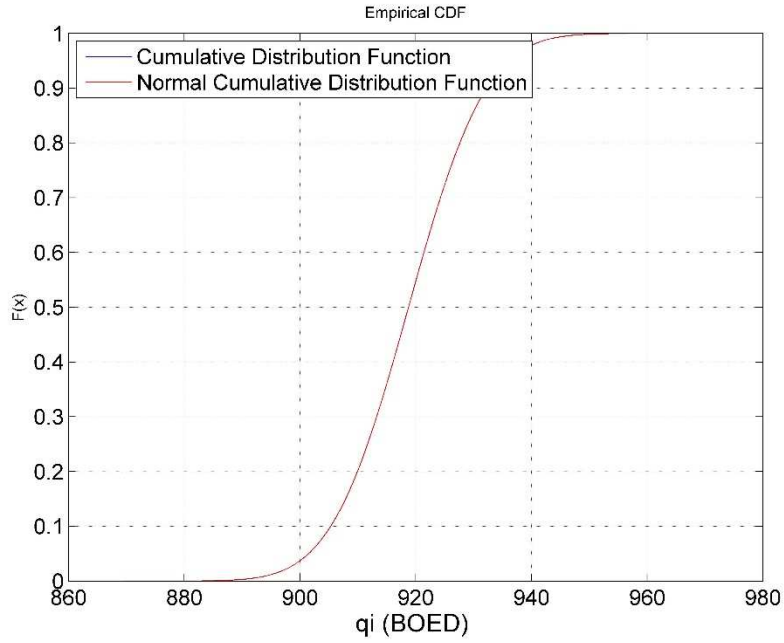

Fig. 87 — Cumulative posterior relative frequency histogram of q_i of Well 18 using the MH model

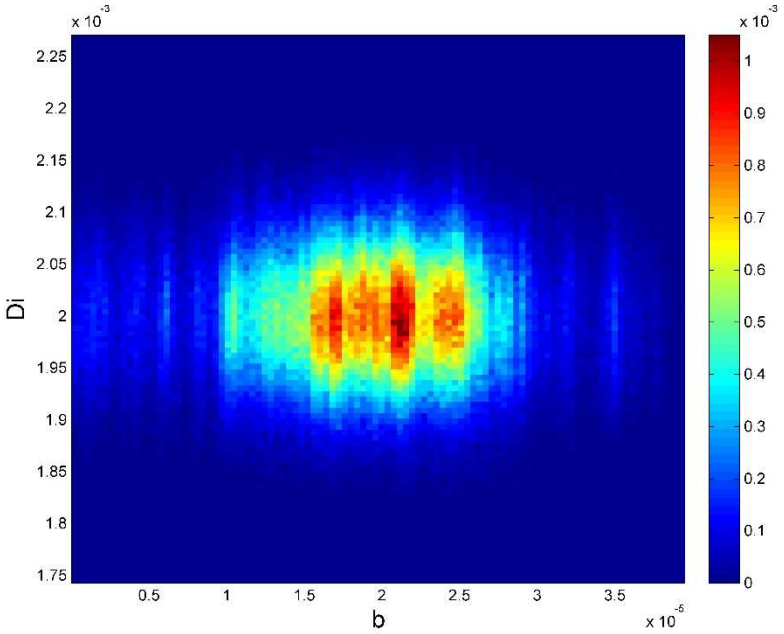

Fig. 88 — Relative frequency diagram between D_i and b of Well 18 using the MH model

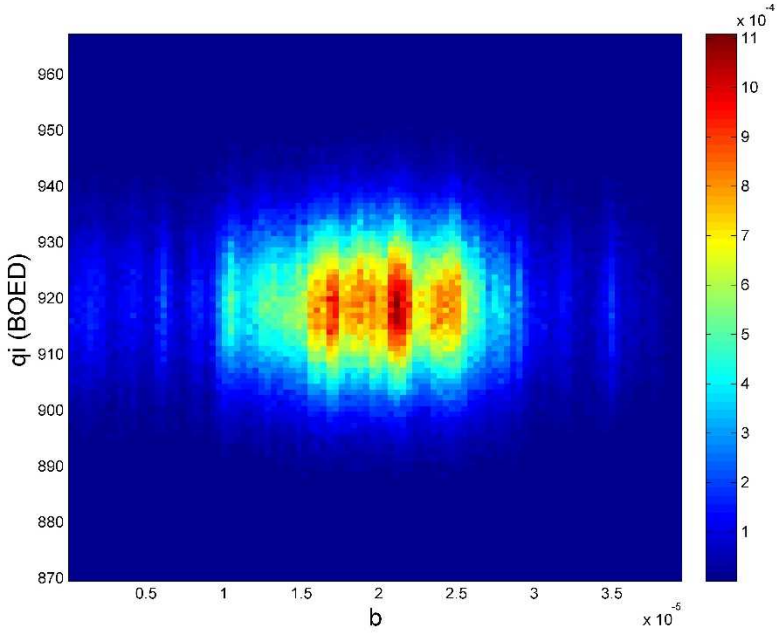

Fig. 89 — Relative frequency diagram between q_i and b of Well 18 using the MH model

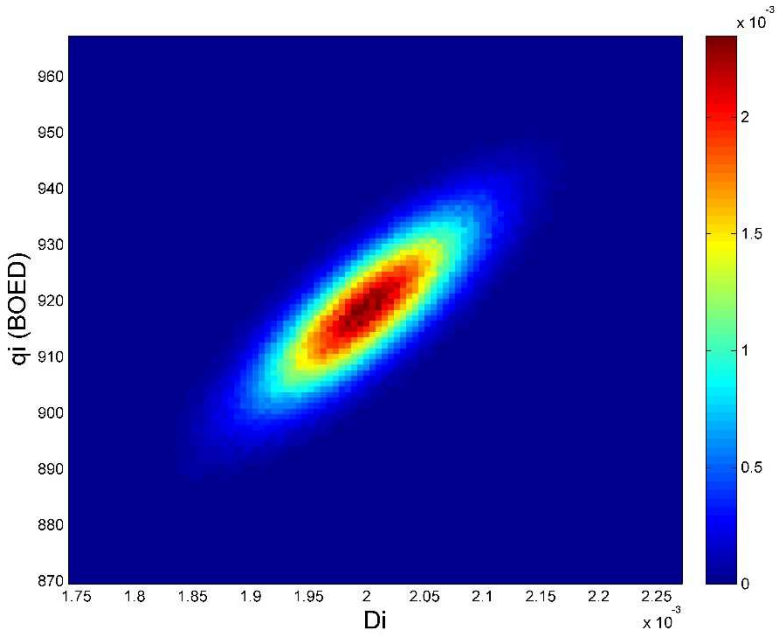

Fig. 90 — Relative frequency diagram between q_i and D_i of Well 18

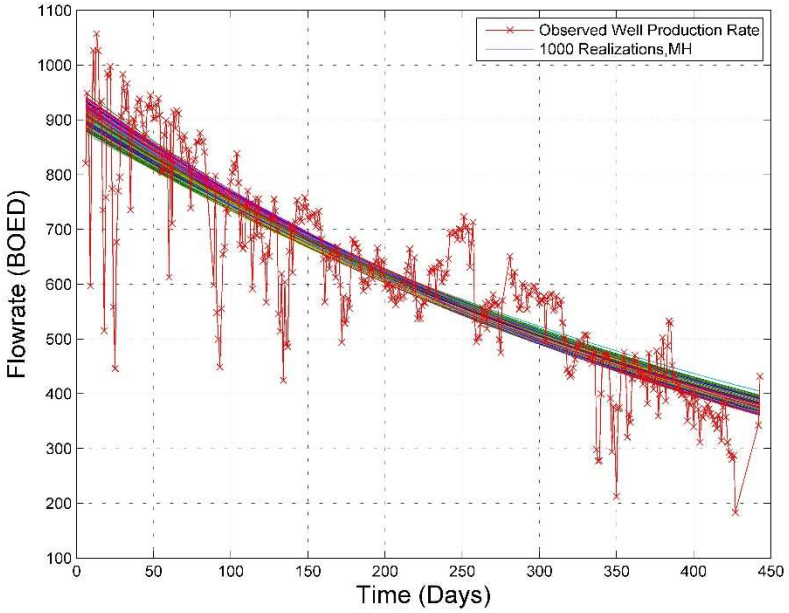

Fig. 91 — The 1,000 realizations of the model predictions using the Bayesian paradigm of Well 18 with the MH model

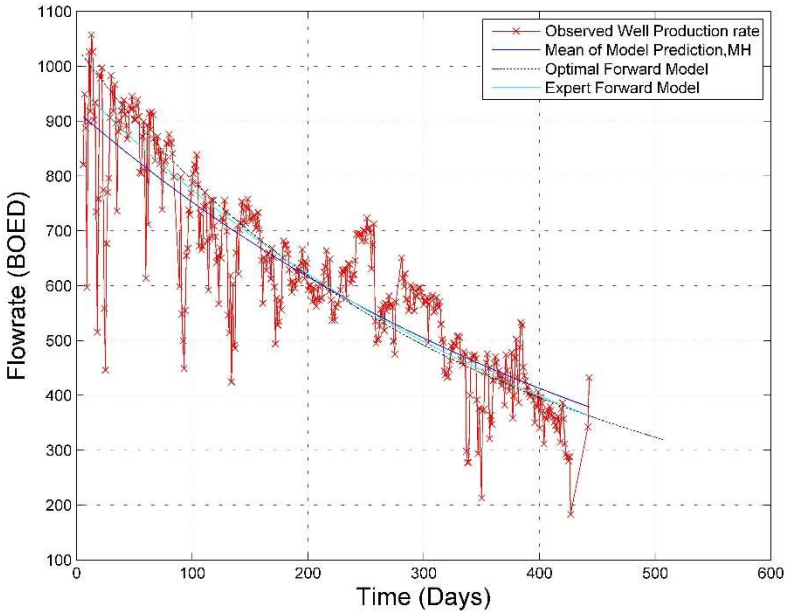

Fig. 92 — The production data with the mean of the realizations, the optimal forward model and the MH model of Well 18

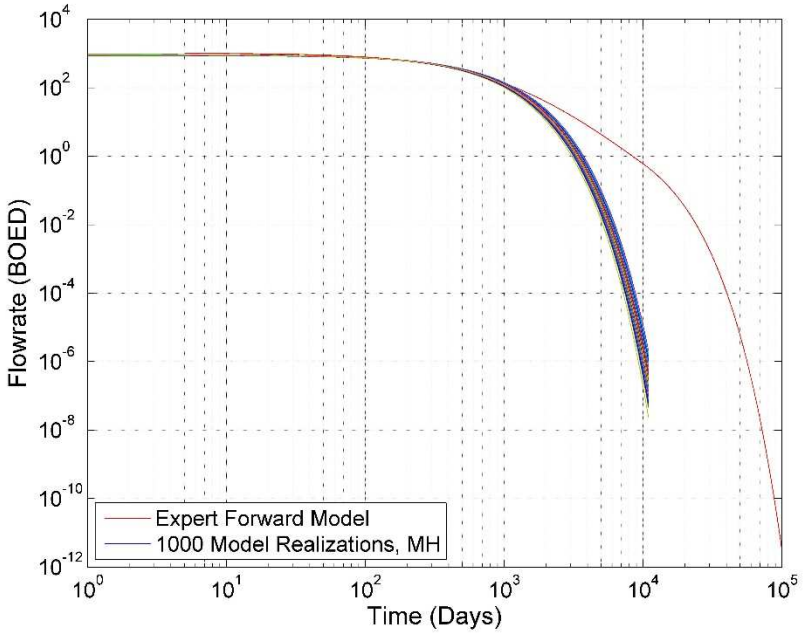

Fig. 93 — The 1,000 realizations of the model predictions using the Bayesian paradigm for 30 years of Well 18

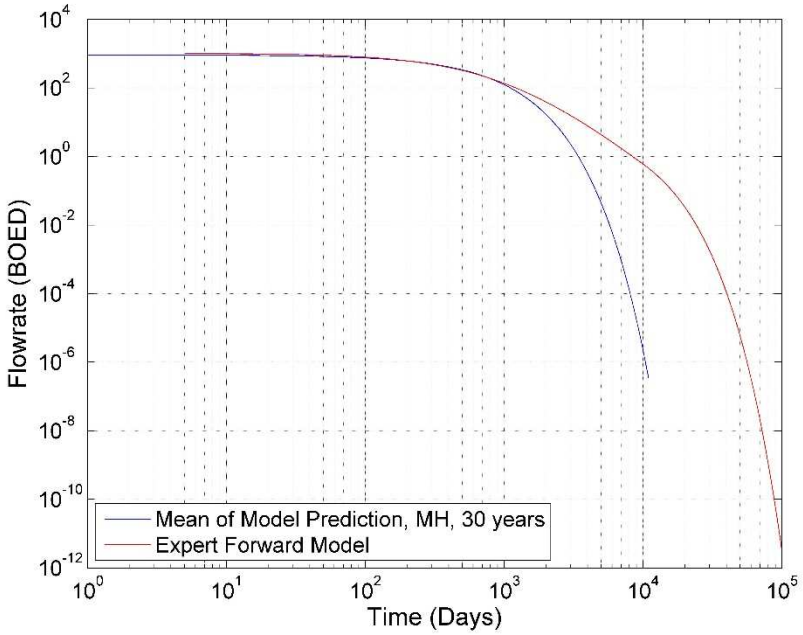

Fig. 94 — The mean of the realizations and the MH model, plotted for 30 years for Well 18

Well 18 – Power Law Exponential Model

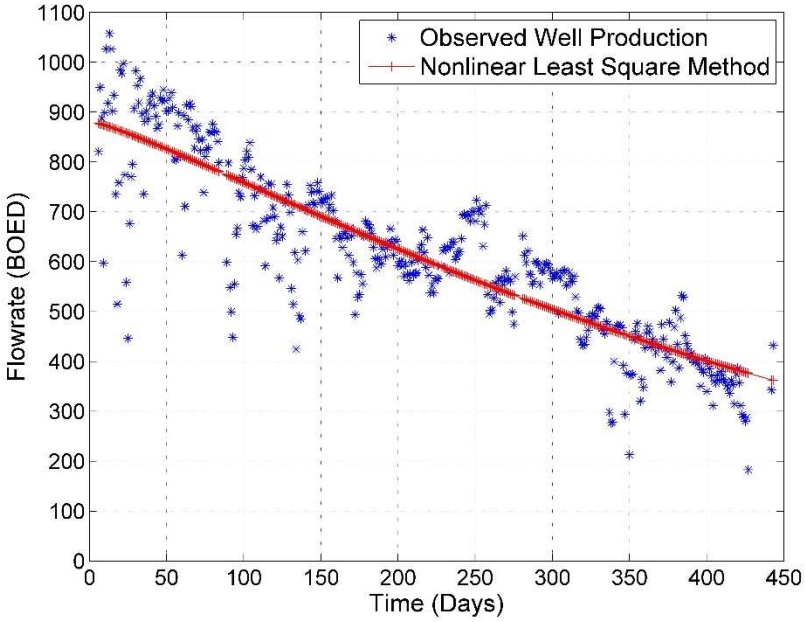

Fig. 95 — Results of the least squares optimization against the production data of Well 18 for the PLE Model

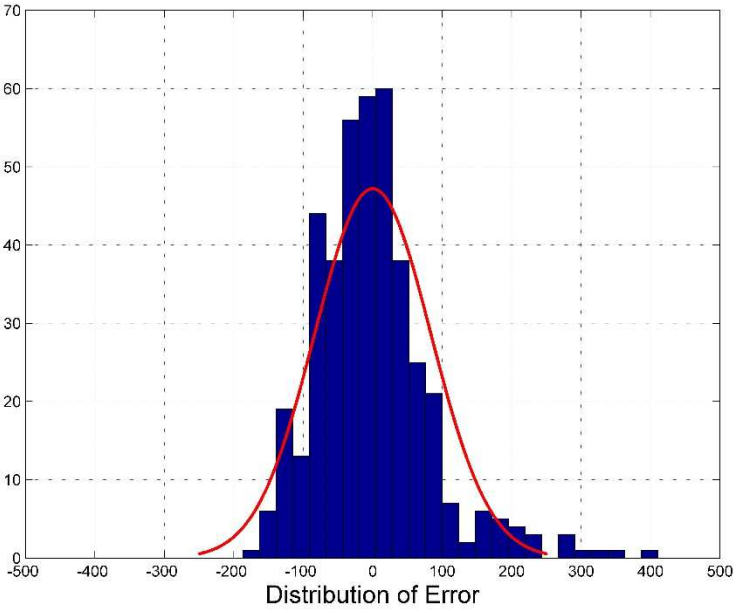

Fig. 96 — The distribution of error between the production data and the LSQ results for Well 18 for the PLE Model

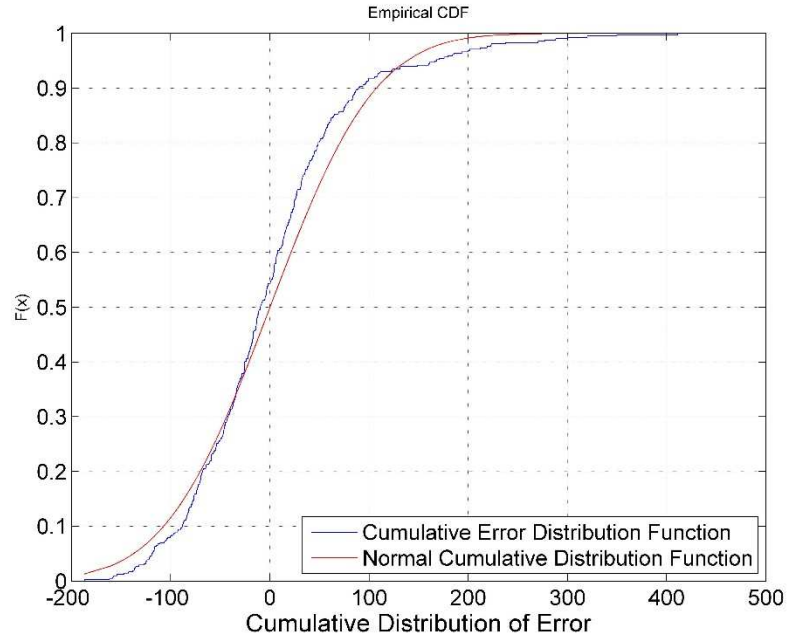

Fig. 97 — The cumulative distribution of error is plotted against the normal cumulative distribution function of Well 18 for the PLE Model

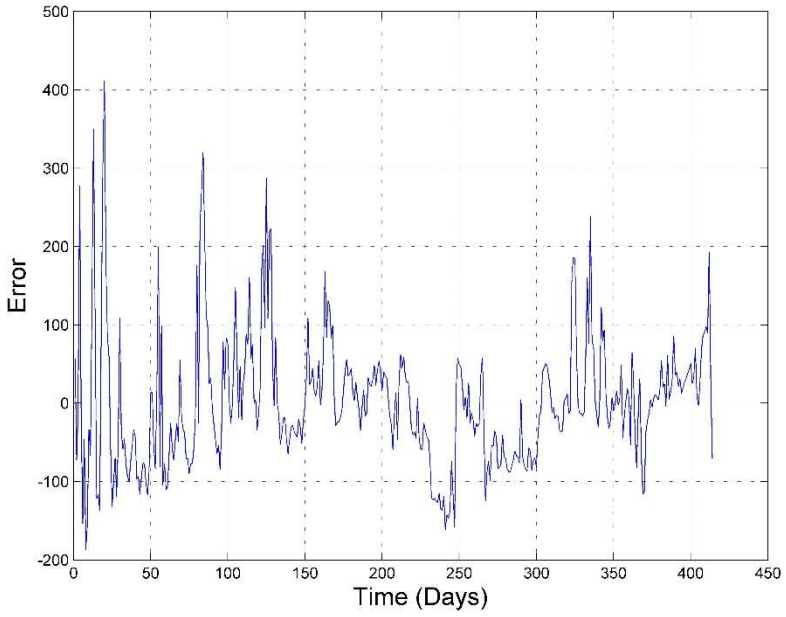

Fig. 98 — The error of the least squares optimization against the number of production days of Well 18 for the PLE Model

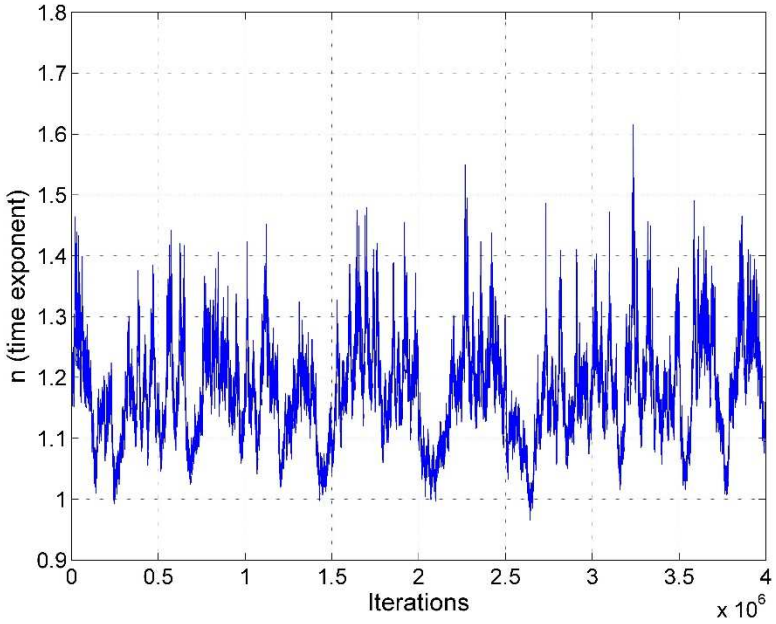

Fig. 99 — MCMC results of *n* for the PLE model of Well 18

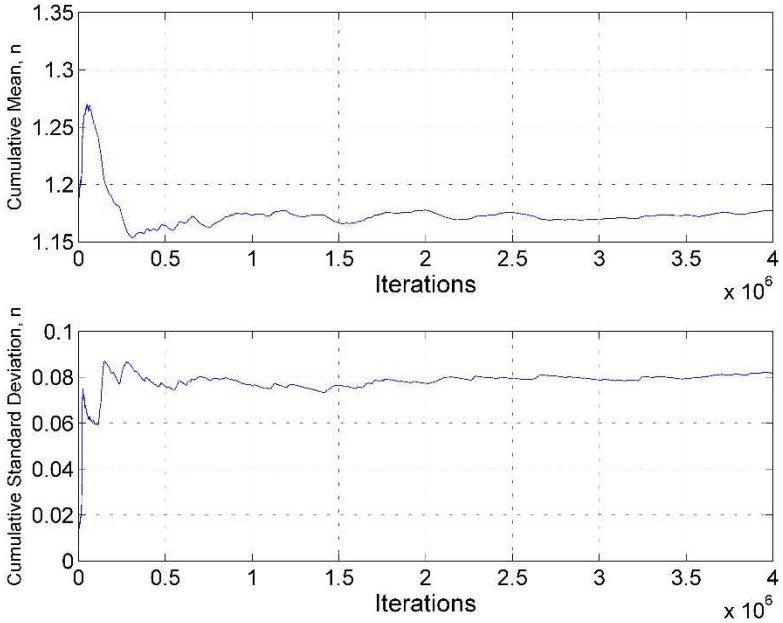

Fig. 100 — Cumulative mean and standard deviation of *n* of Well 18 using the PLE model

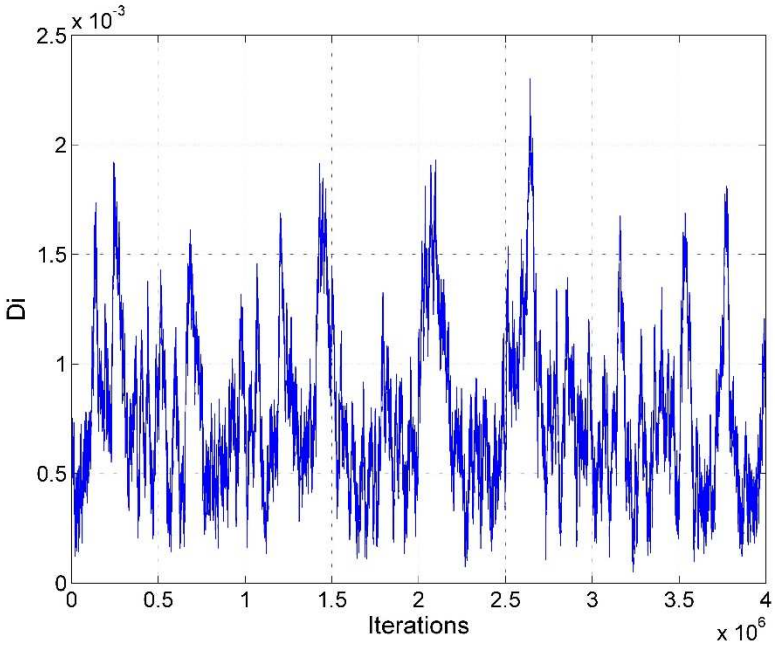

Fig. 101 — MCMC results of D_i for the MH model of Well 18 using the PLE model

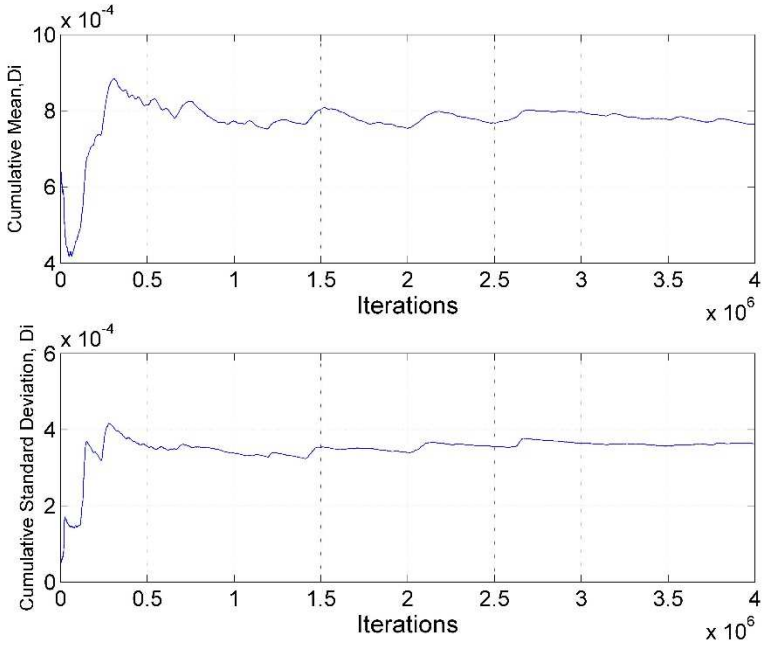

Fig. 102 — Cumulative mean and standard deviation of D_i of Well 18 using the PLE model

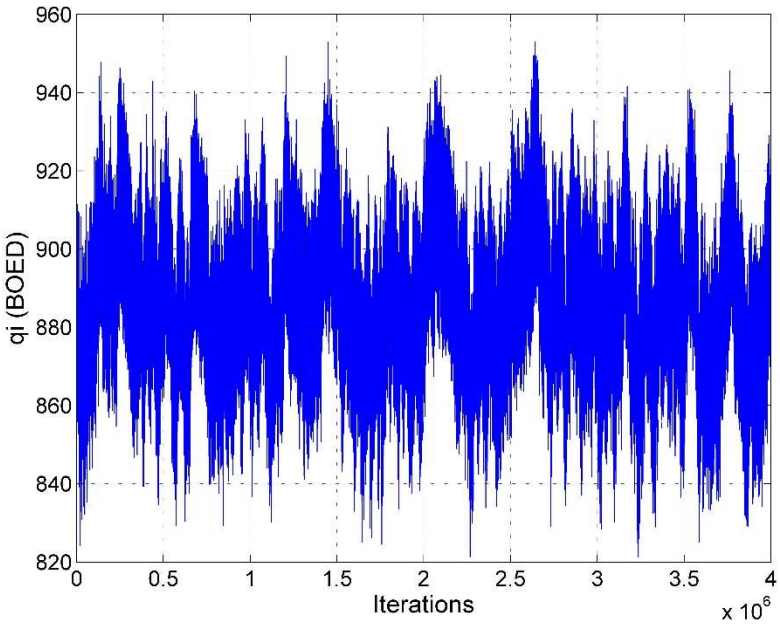

Fig. 103 — MCMC results of q_i for the MH model of Well 18 using the PLE model

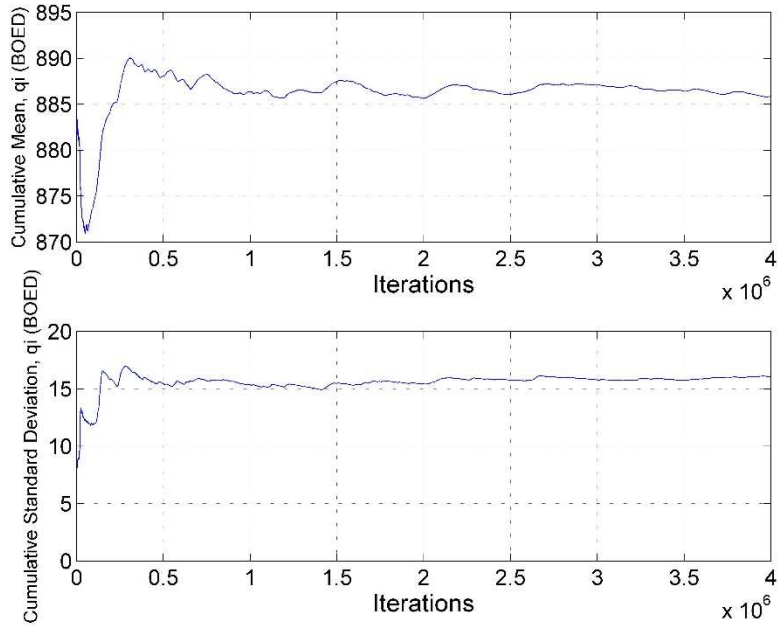

Fig. 104 — Cumulative mean and standard deviation of q_i of Well 18 using the PLE model

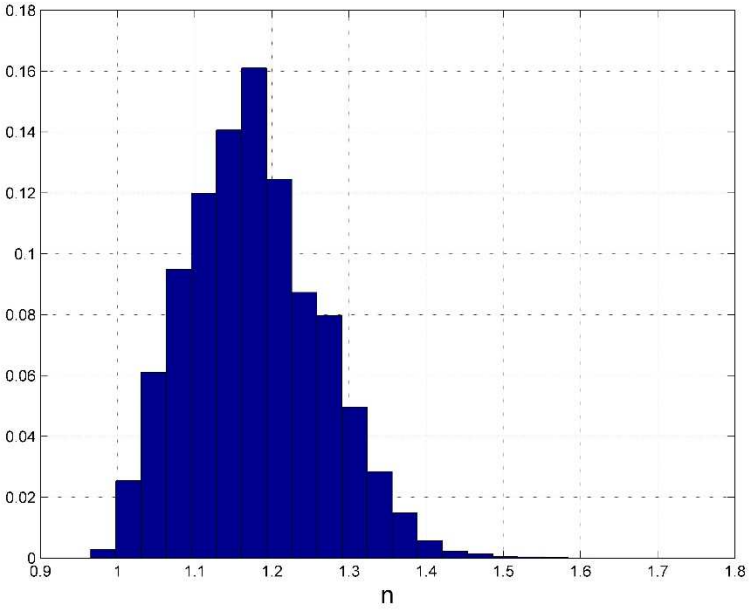

Fig. 105 — Posterior relative frequency histogram of *n* of Well 18 using the PLE model

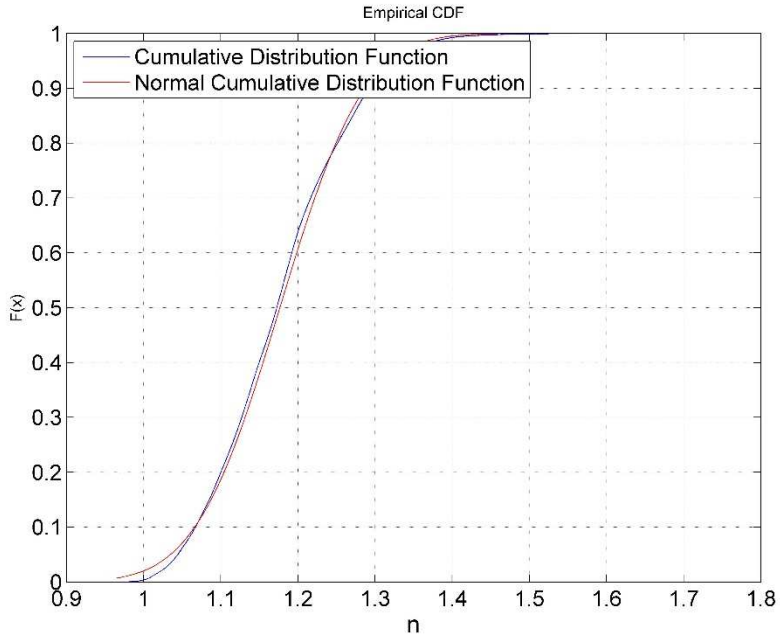

Fig. 106 — Cumulative posterior relative frequency histogram of *n* of Well 18 using the PLE model

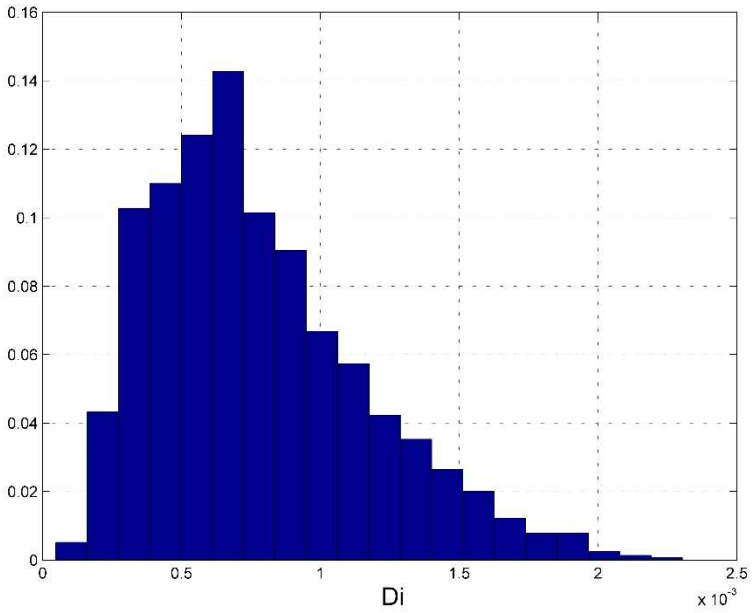

Fig. 107 — Posterior relative frequency histogram of D_i of Well 18 using the PLE model

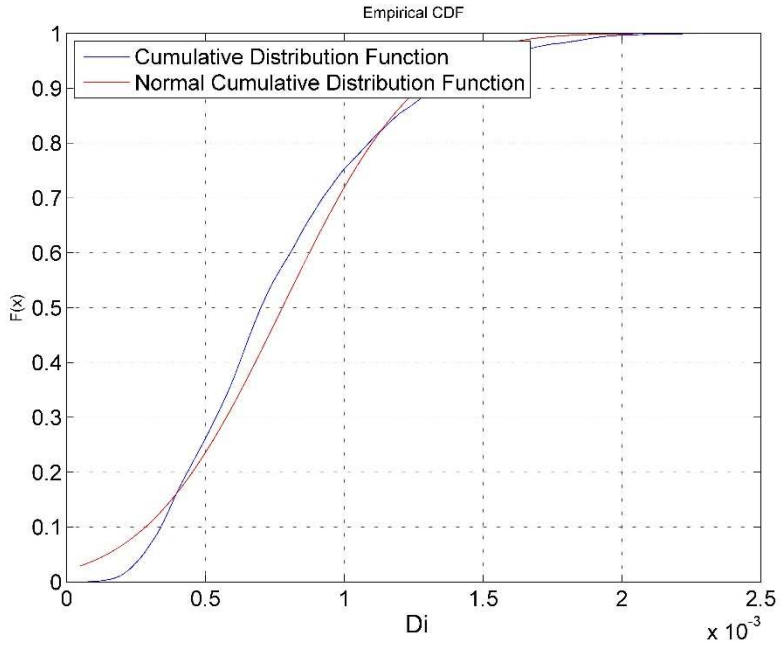

Fig. 108 — Cumulative posterior relative frequency histogram of D_i of Well 18 using the PLE model

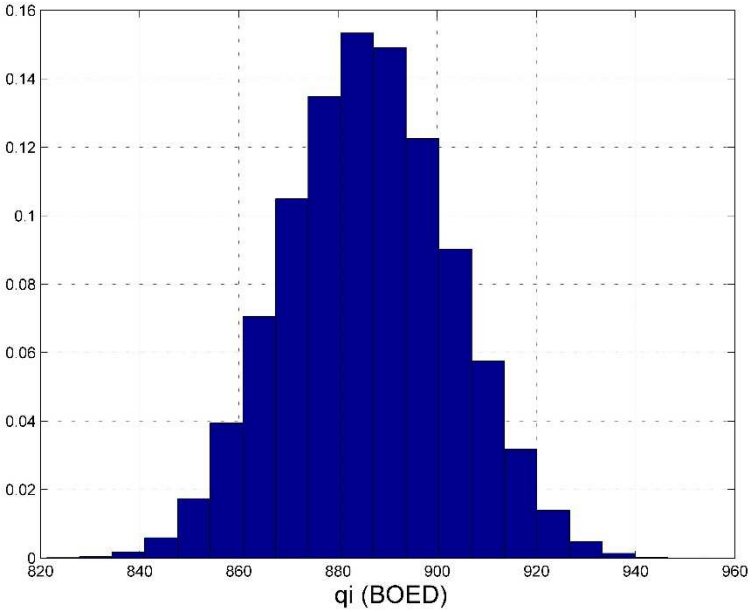

Fig. 109 — Posterior relative frequency histogram of q_i of Well 18 using the PLE model

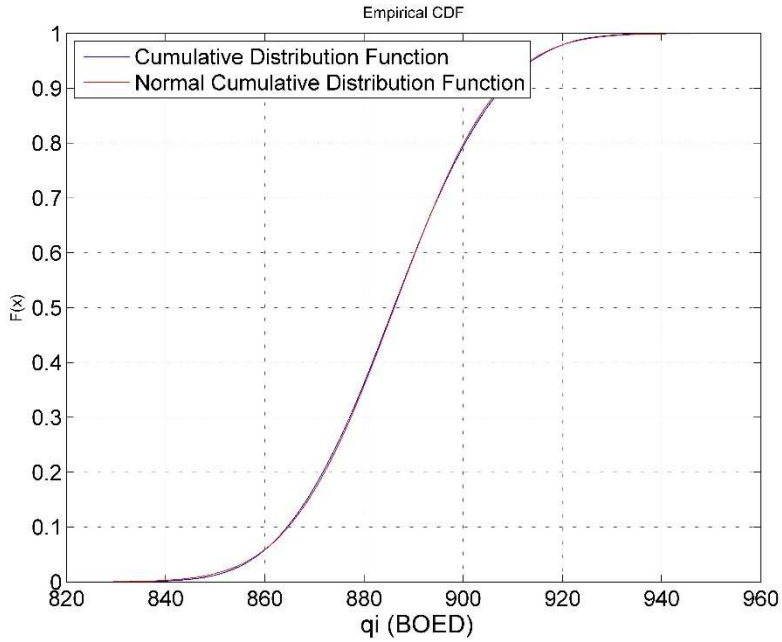

Fig. 110 — Cumulative posterior relative frequency histogram of q_i of Well 18 using the PLE model

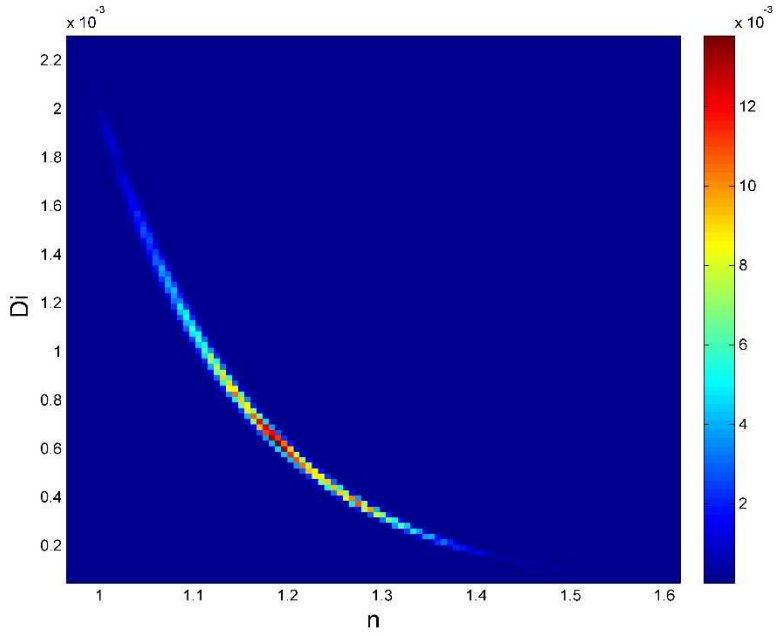

Fig. 111 — Relative frequency diagram between D_i and n of Well 18 using the PLE model

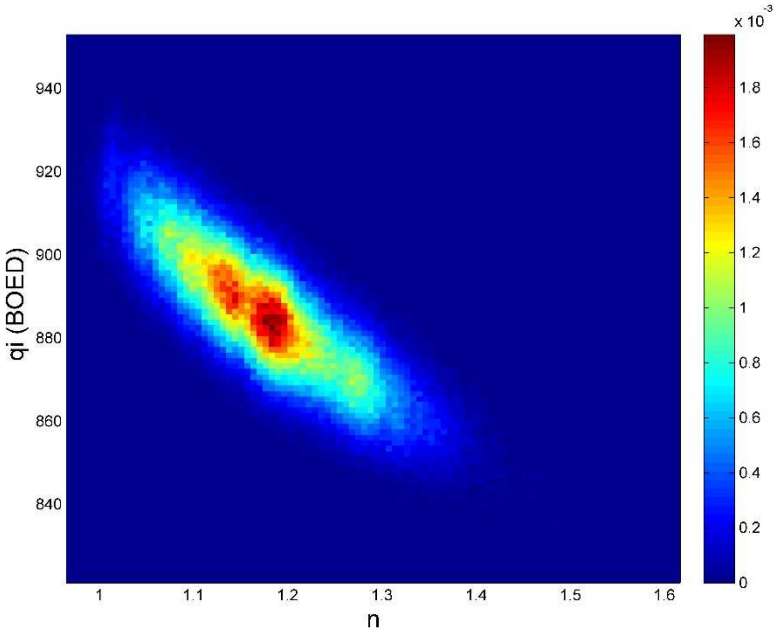

Fig. 112 — Relative frequency diagram between q_i and n of Well 18 using the PLE model

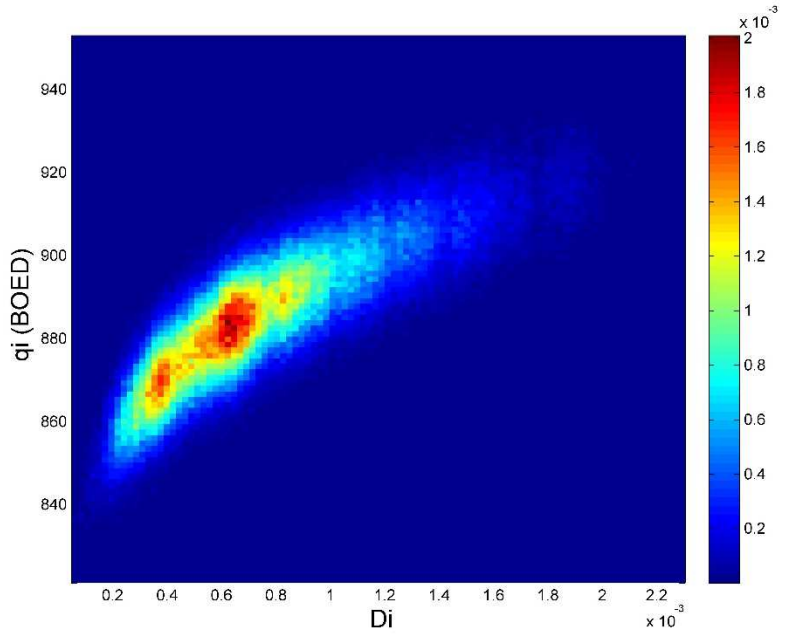

Fig. 113 — Relative frequency diagram between q_i and D_i of Well 18 using the PLE model

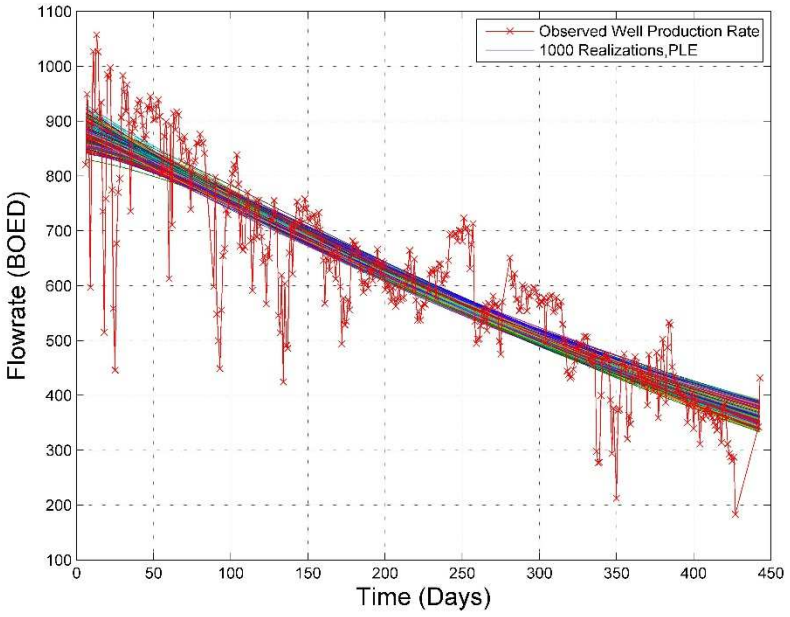

Fig. 114 — The 1,000 realizations of the model predictions using the Bayesian paradigm of Well 18 with the PLE model

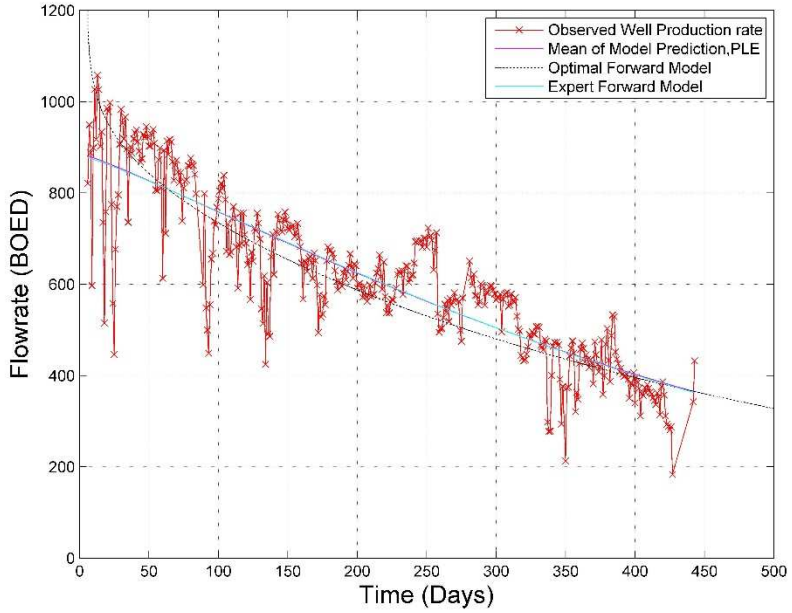

Fig. 115 — The production data with the mean of the realizations, the optimal forward model and the PLE model of Well 18

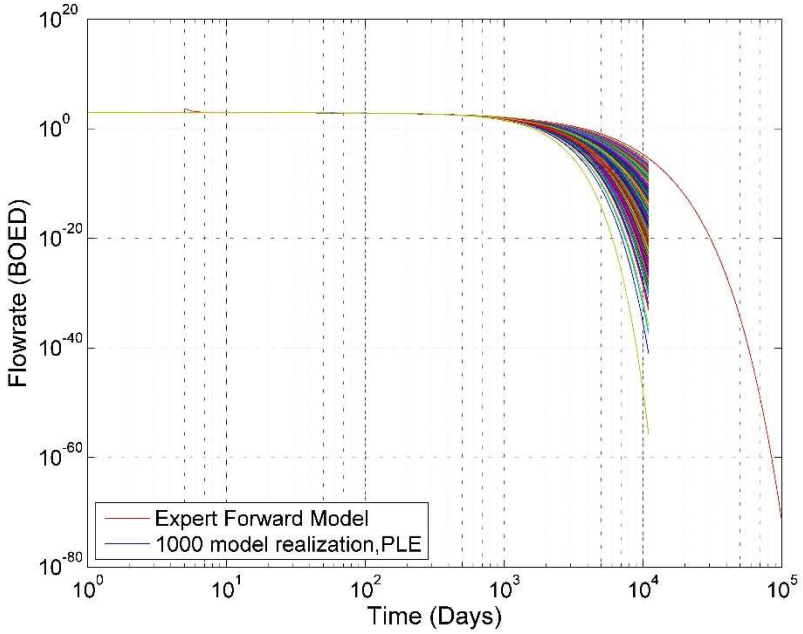

Fig. 116 — The 1,000 realizations of the model predictions using the Bayesian paradigm for 30 years of Well 18

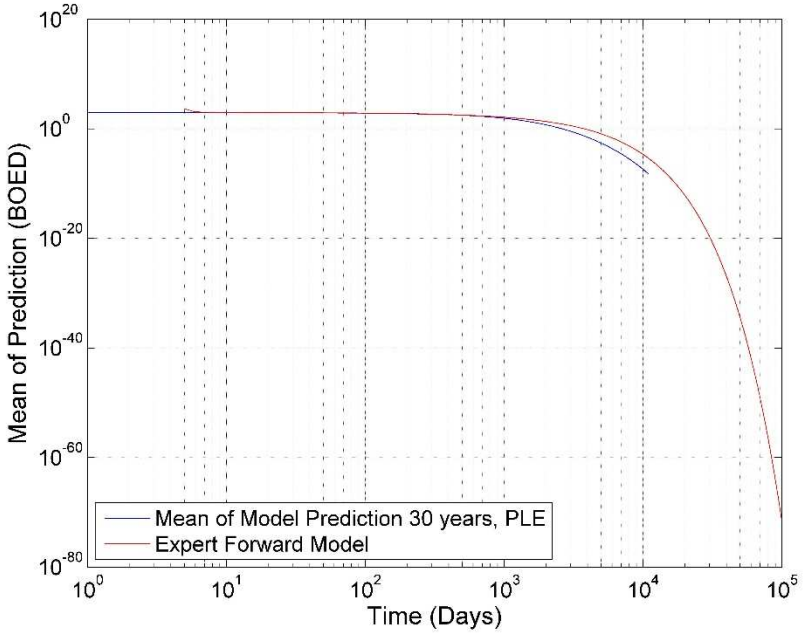

Fig. 117 — The mean of the realizations and the PLE model, plotted for 30 years for Well 18

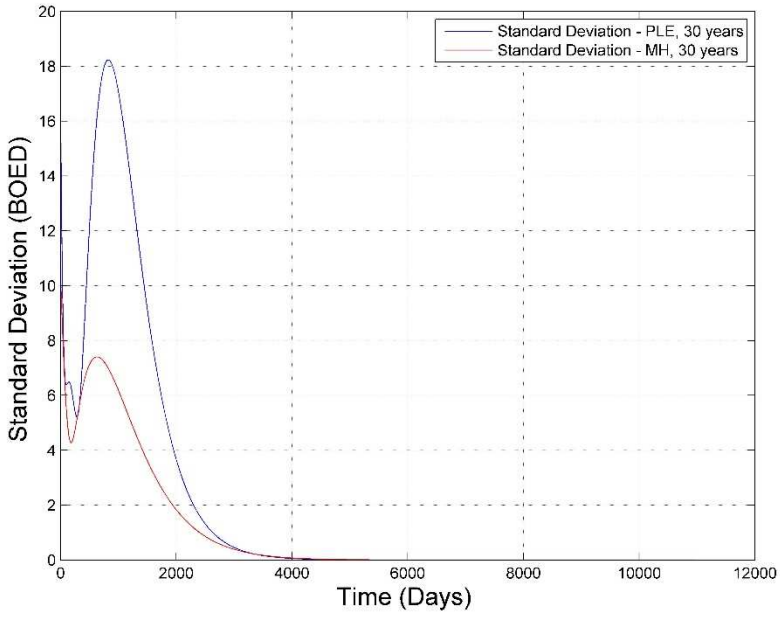

Fig. 118 — Comparison of the Standard Deviation of the two Bayesian forecasts using the MH and PLE models of Well 18

Analysis

Well 18 shows interesting results with the MCMC results, especially when determining the *b*-factor, shown in **Fig. 76**. D_i converges immediately, as does the $q_{i,}$ which can be seen in **Fig. 78** and **80**. We applied the burn-in point and notice that the posterior distribution of the three parameters is quite different. We see a Gaussian distribution for both D_i and q_i in **Fig. 84** and **86**, however see a different distribution for the *b*-factor (**Fig. 82**), which is attributed to the non-convergence of the MCMC. We expect to obtain normally distributed posteriors because this was an assumption made initially.

If we compare these MCMC results with the results produced when applying the PLE model, we notice that that model converges for *n*, the D_i and for the q_i, shown in **Fig. 99, 101** and **103**, respectively, after four million iterations. However, in this case, the only parameter that exhibits a Gaussian distribution in the posterior is q_i, shown in **Fig. 109**. Both posterior distributions for *n* and D_i are lognormal in this case. This is a different result that we have not seen from another *n*. The results may be exhibit this distribution because the conversion is not excellent, thus skewing the further results.

Based on the posterior distributions of the three parameters, we created the relative frequency histograms that show the relationship between two different parameters -- D_i vs. *b*, q_i vs. *b* and q_i vs D_i for the MH model and D_i vs. *n*, q_i vs. *n* and q_i vs D_i for the PLE model. These results can be seen in **Fig. 88, 89** and **90**, respectively, for the MH model and **Fig. 111, 112** and **113**, respectively, for the PLE model. The quality of the relative frequency histograms is based upon the quality of the posterior of the parameters, because it is just a representation of the two parameters against each other. From Fig. 88 and 89, we see that because of the poor results due to the *b*-factor that the histograms become skewed and we cannot determine the relationship of the two parameters. However, we see that in Fig. 90 that there is a linear relationship between q_i and D_i. These are same results we have seen in other wells, and have encountered the same problem due to poor

convergence of parameters. The PLE results of the relative frequency histogram show interesting results that are the same results we have seen with the other wells.

We then reach the realizations of the Bayesian paradigm using the MH and PLE models. We notice when we plot the mean of the realizations versus the optimal forward model (the results from the LSQ optimization), and the expert forward model (either MH or PLE), the mean of the model prediction and the expert forward model often times have close values for the 700 days plotted. However, when we extend the results to 30 years that there is a divergence between two sets of results. In this case, the MH forward model overestimates the reserves, as seen in **Fig. 94** for the MH model and **Fig. 117** for the PLE model. Both models show that they overestimate the reserves.

Finally, the standard deviation comparison of the two sets of Bayesian results, **Fig. 118** identifies the uncertainty of the two models. In the case of this well, it is evident that the uncertainty is much greater in the PLE model than in the MH model, in early time. However, as the model progresses, we see that the two standard deviation values converge, and are at 0. This means that there is no more uncertainty related to either of the models, which is a fascinating discovery. This being said, the uncertainty in early time is very great in the PLE model, therefore the MH model seems to provide a more accurate result when implementing the Bayesian paradigm.

APPENDIX III

RESULTS AND ANALYSIS OF WELL 19

Well 19 – Modified Hyperbolic Model

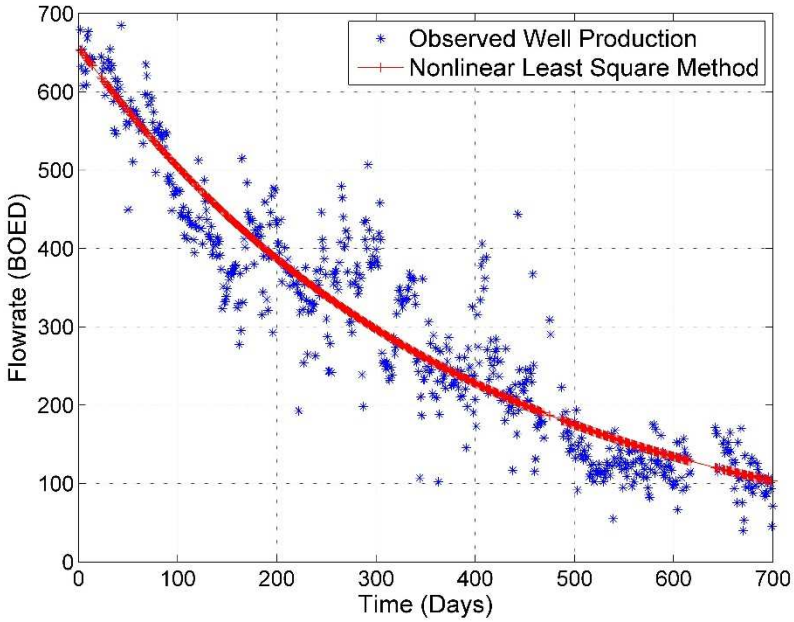

Fig. 119 — Results of the least squares optimization against the production data of Well 19 for the MH Model

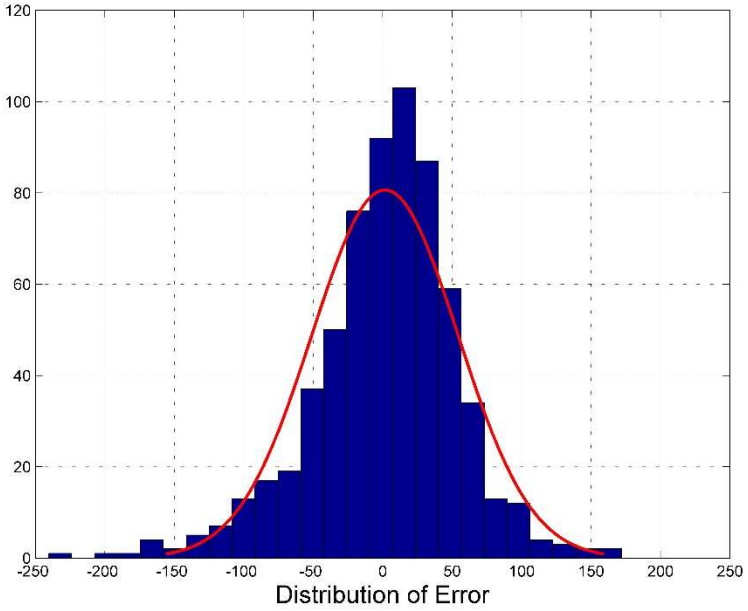

Fig. 120 — The distribution of error between the production data and the LSQ results for Well 19 for the MH Model

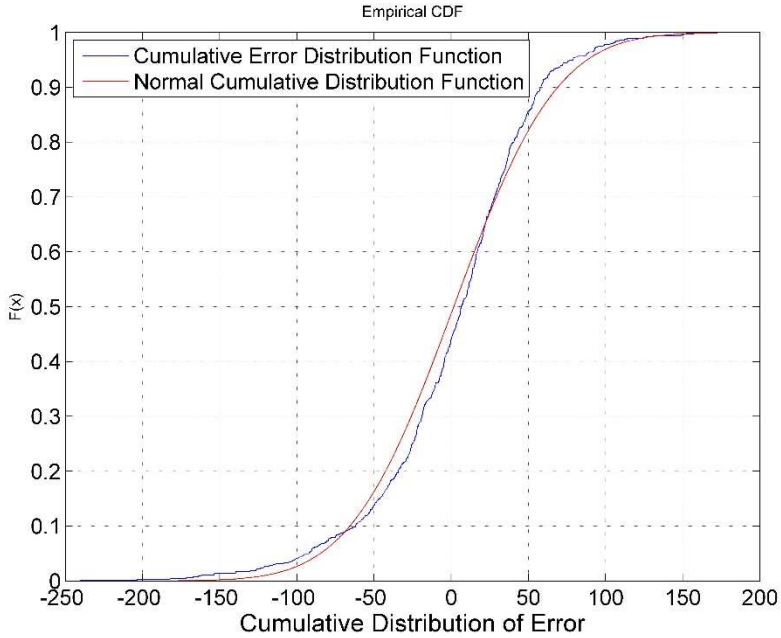

Fig. 121 — The cumulative distribution of error is plotted against the normal cumulative distribution function of Well 19 for the MH Model

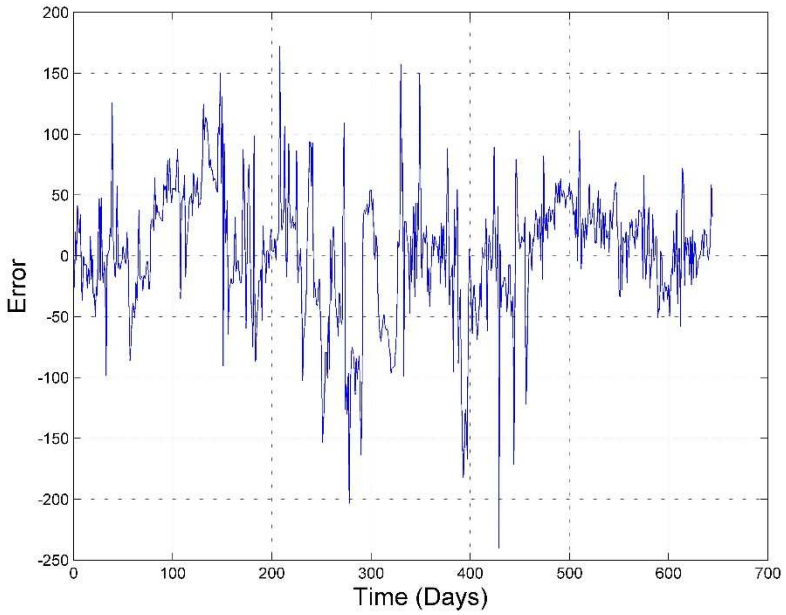

Fig. 122 — The error of the least squares optimization against the number of production days of Well 19 for the MH Model

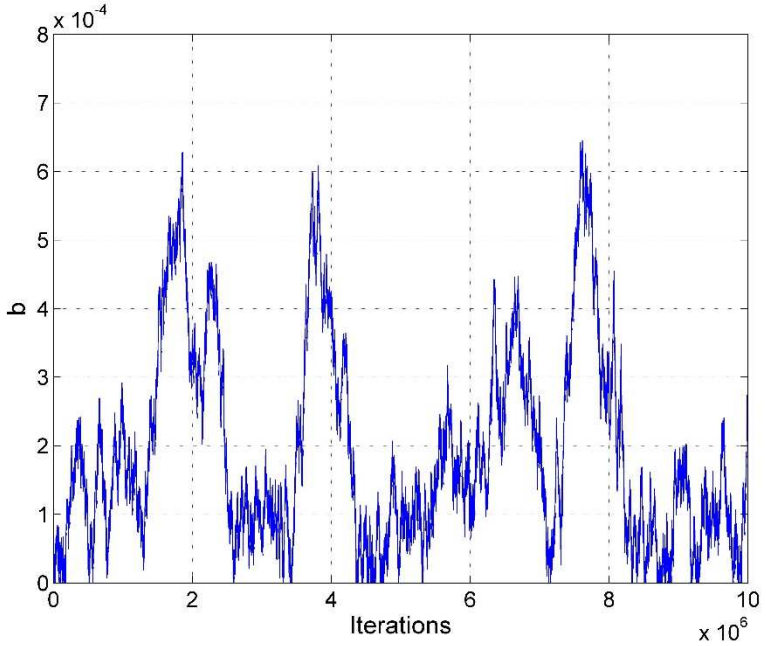

Fig. 123 — MCMC results of the *b*-factor for the MH model of Well 19 using the MH model

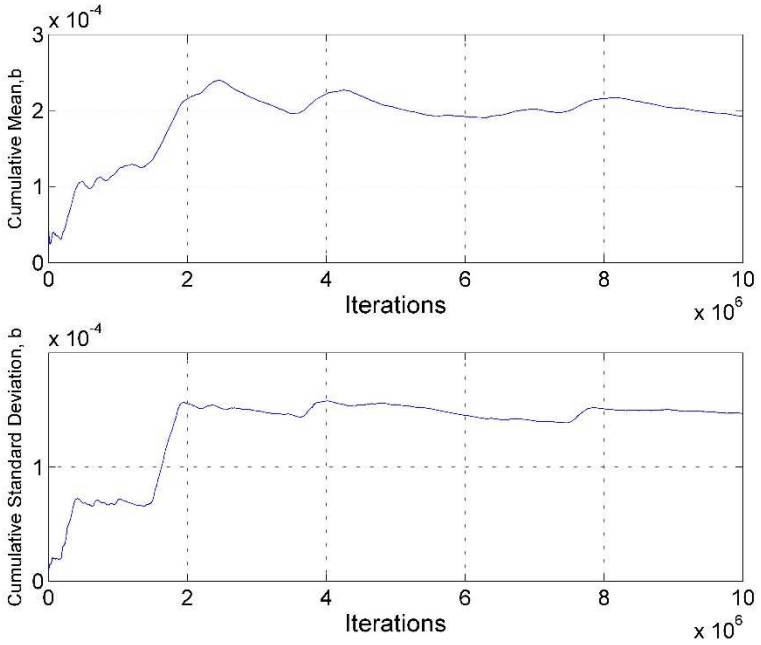

Fig. 124 — Cumulative mean and standard deviation of the *b*-factor of Well 19 using the MH model

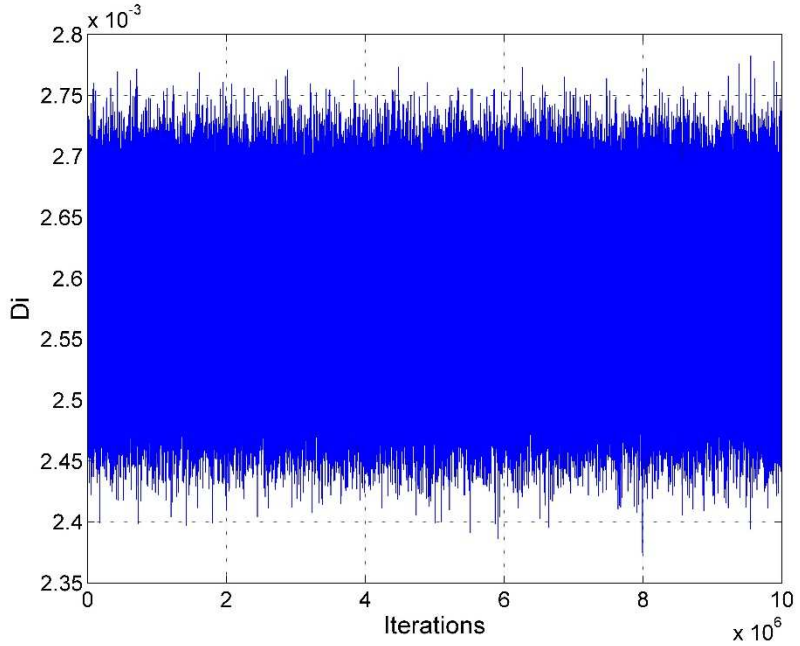

Fig. 125 — MCMC results of D_i for the MH model of Well 19 using the MH model

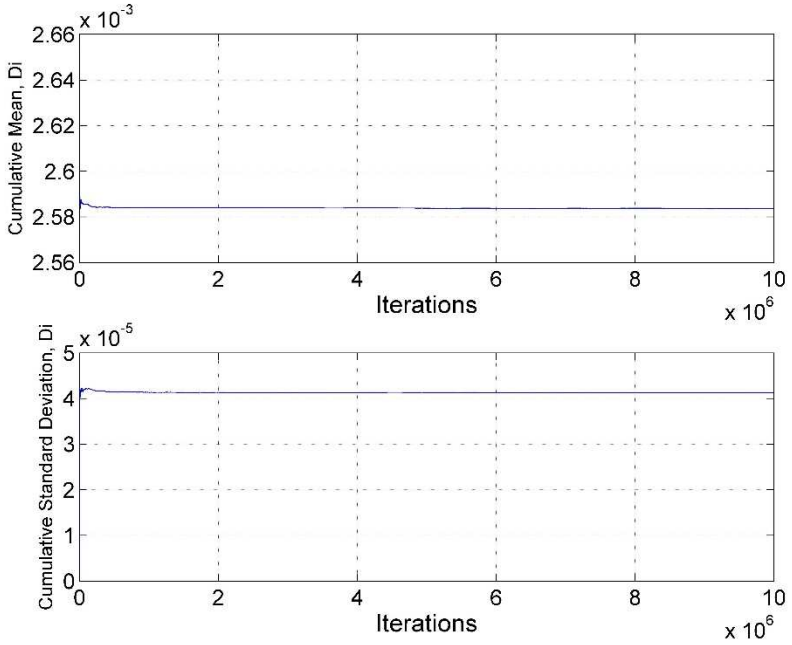

Fig. 126 — Cumulative mean and standard deviation of D_i of Well 19 using the MH model

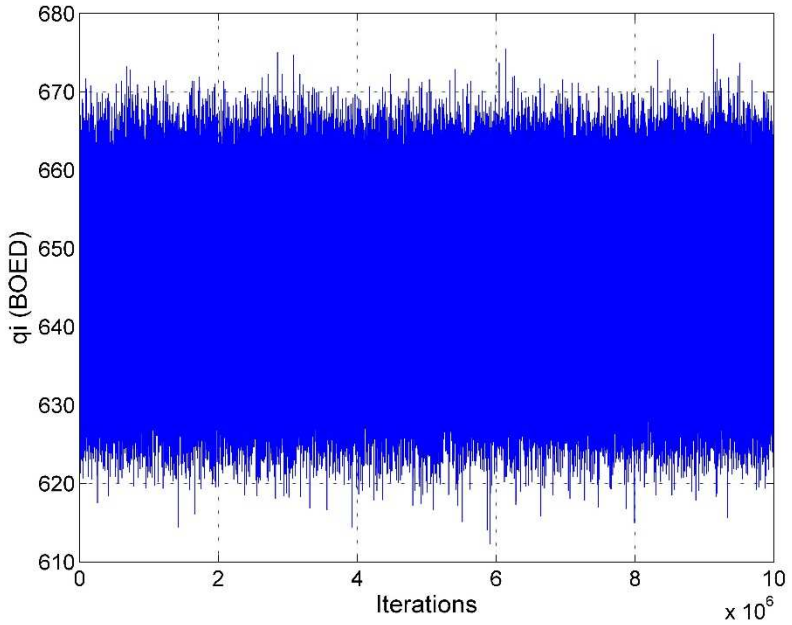

Fig. 127 — MCMC results of q_i for the MH model of Well 19 using the MH model

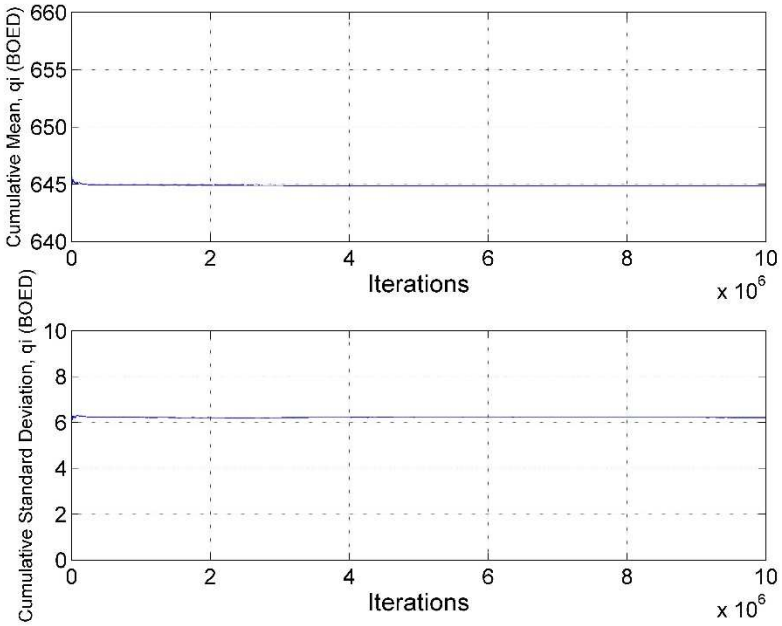

Fig. 128 — Cumulative mean and standard deviation of q_i of Well 19 using the MH model

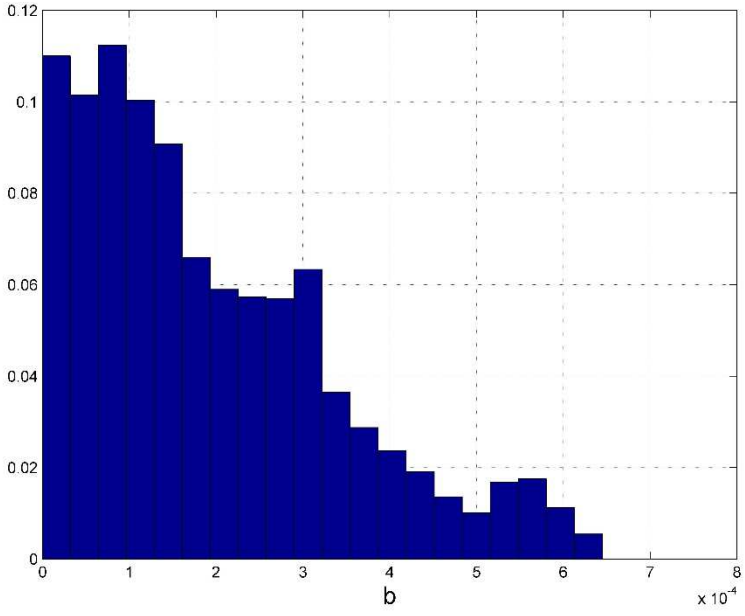

Fig. 129 — Posterior relative frequency histogram of *b* of Well 19 using the MH model

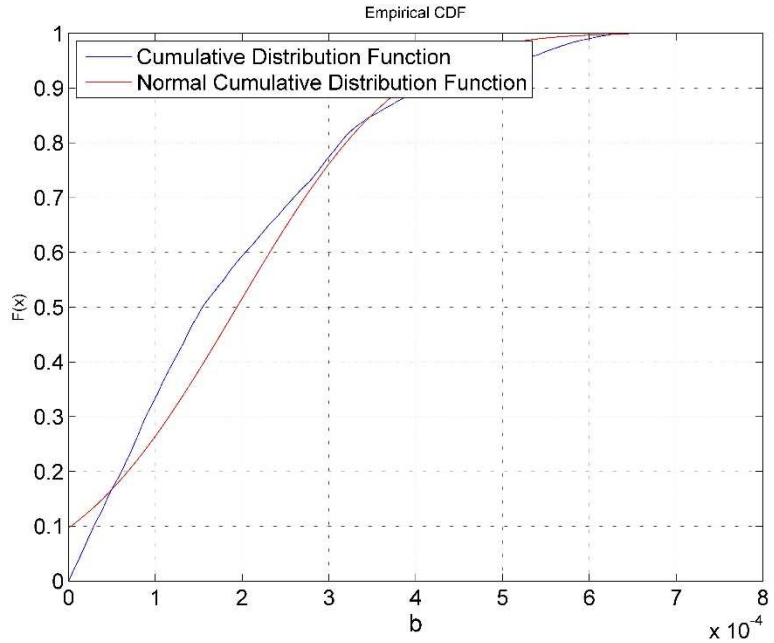

Fig. 130 — Cumulative posterior relative frequency histogram of the *b*-factor of Well 19 using the MH model

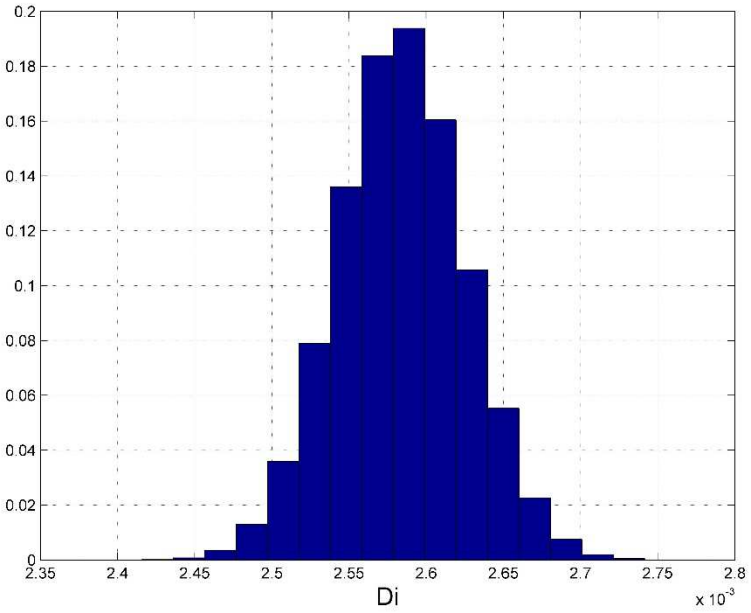

Fig. 131 — Posterior relative frequency histogram of D_i of Well 19 using the MH model

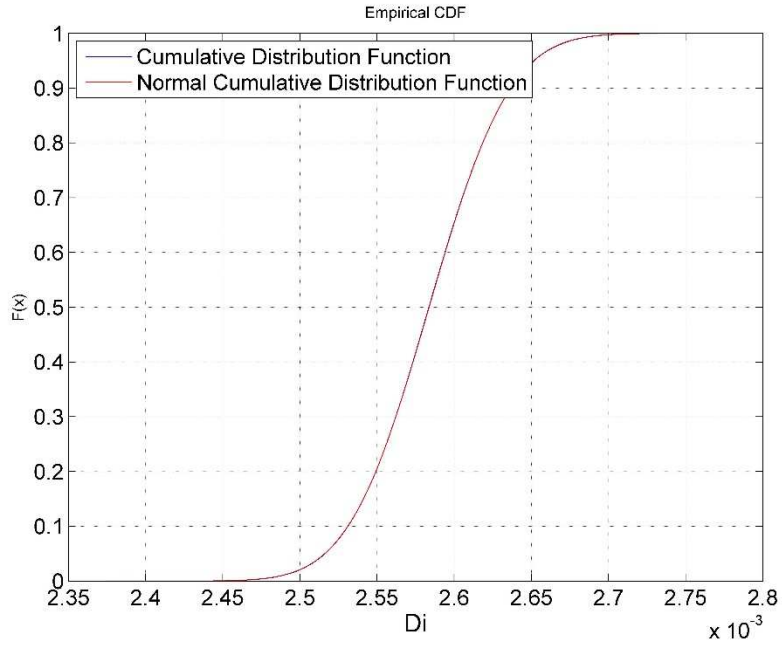

Fig. 132 — Cumulative posterior relative frequency histogram of D_i of Well 19 using the MH model

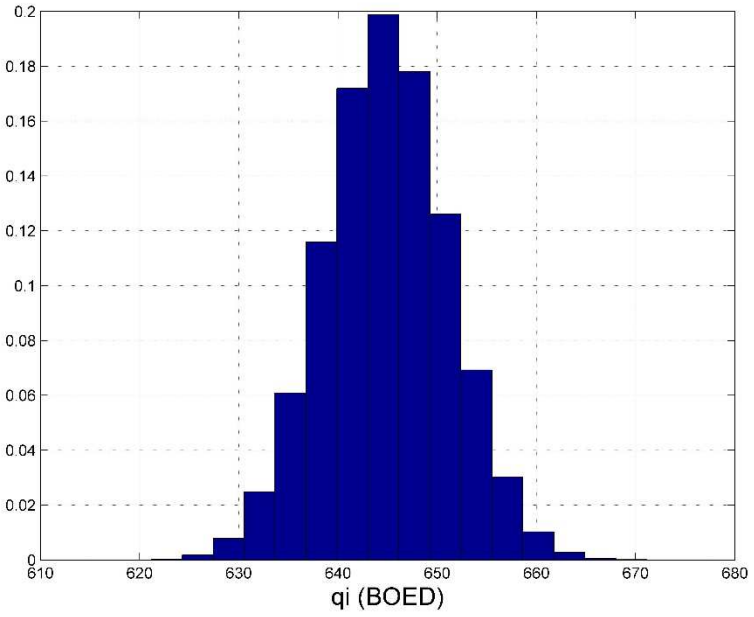

Fig. 133 — Posterior relative frequency histogram of q_i of Well 19 using the MH model

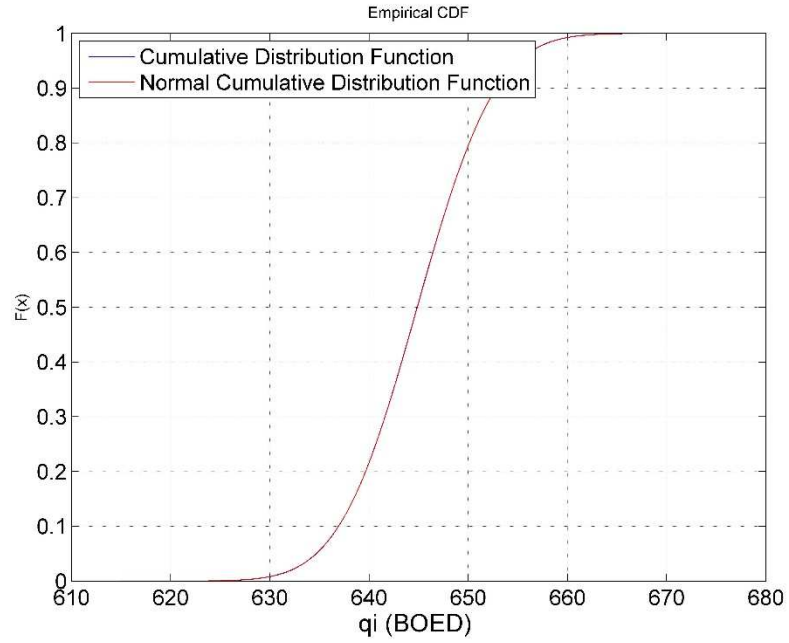

Fig. 134 — Cumulative posterior relative frequency histogram of q_i of Well 19 using the MH model

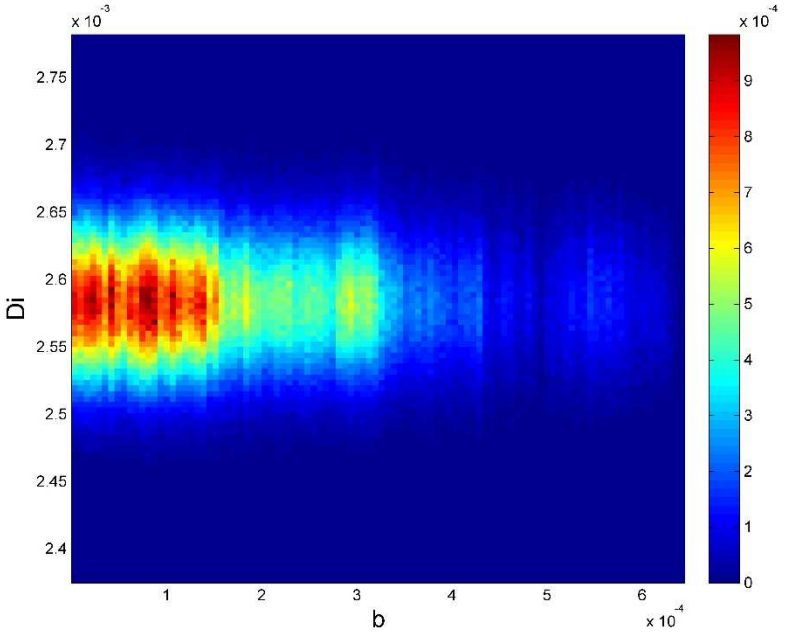

Fig. 135 — Relative frequency diagram between D_i and b of Well 19 using the MH model

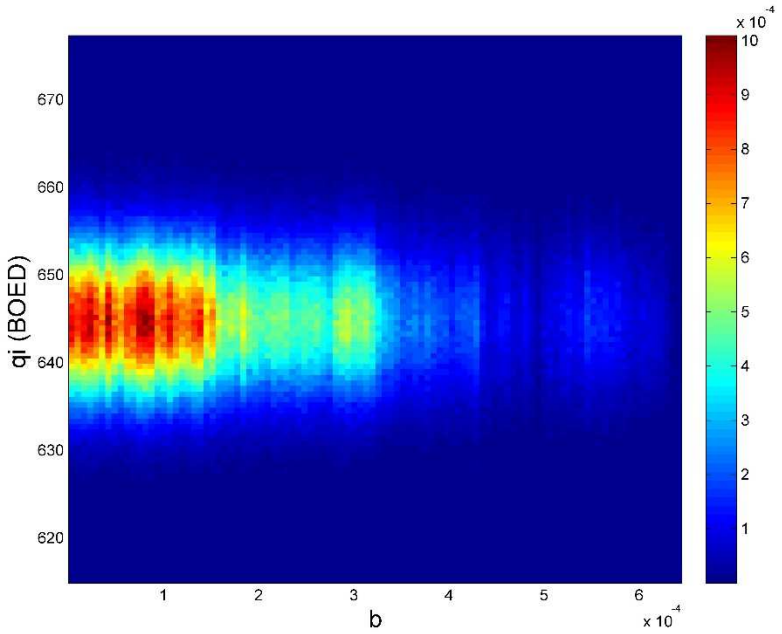

Fig. 136 — Relative frequency diagram between q_i and b of Well 19 using the MH model

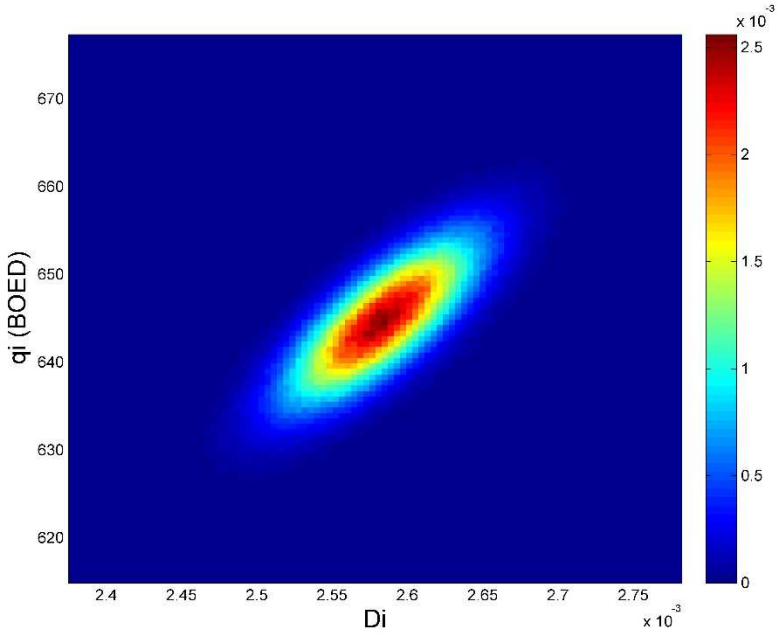

Fig. 137 — Relative frequency diagram between q_i and D_i of Well 19 using the MH model

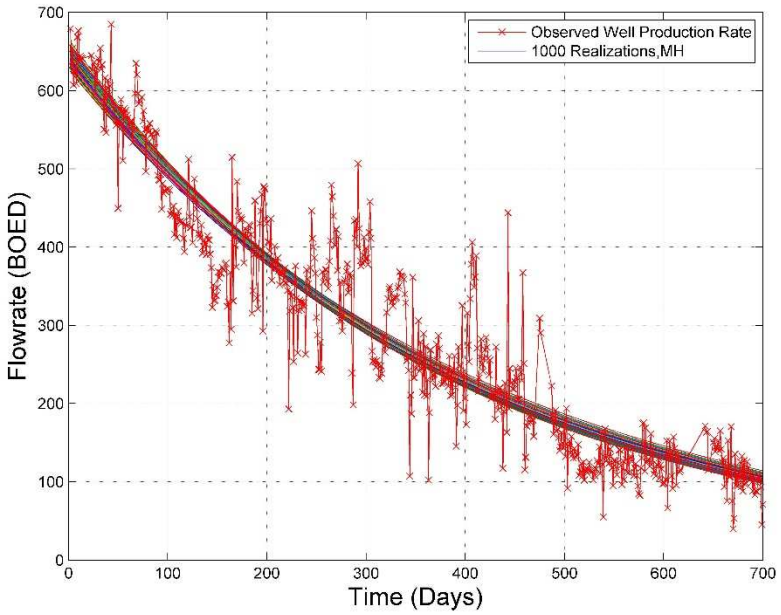

Fig. 138 — The 1,000 realizations of the model predictions using the Bayesian paradigm of Well 19 with the MH model

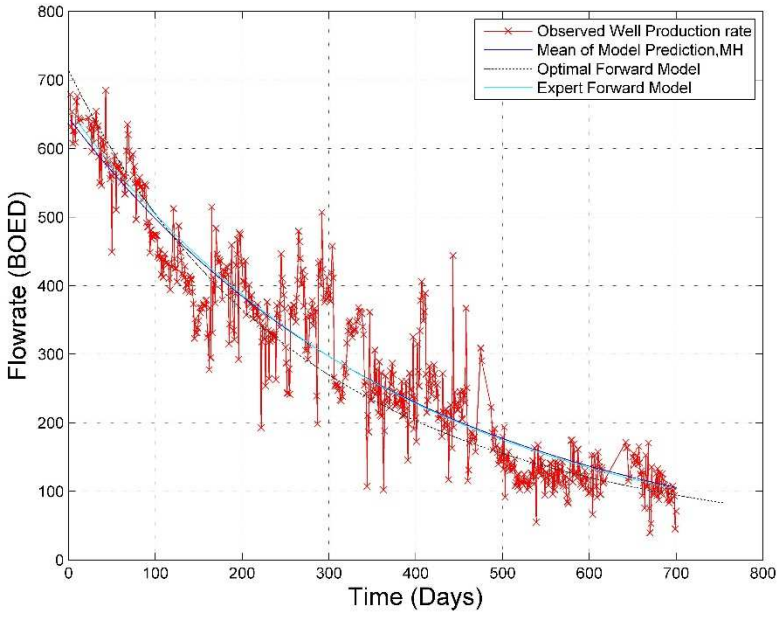

Fig. 139 — The production data with the mean of the realizations, the optimal forward model and the MH model of Well 19

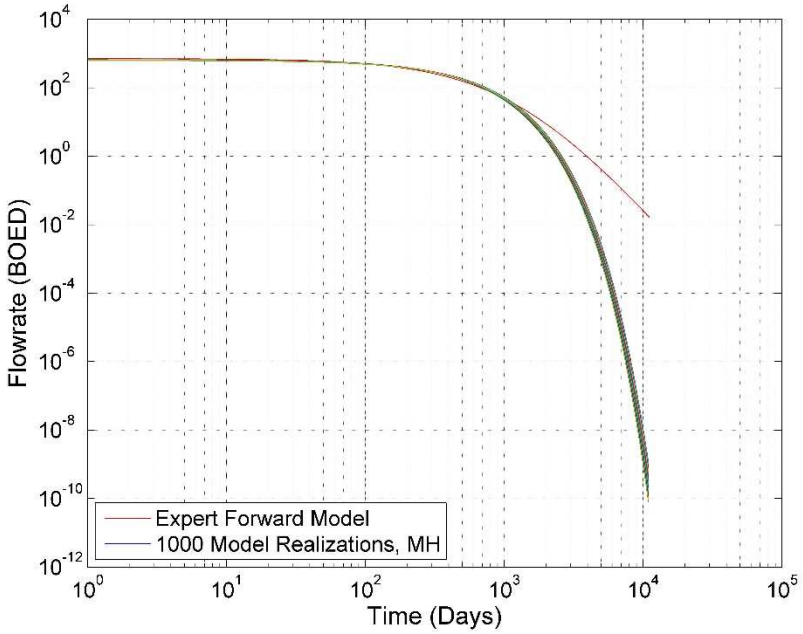

Fig. 140 — The 1,000 realizations of the model predictions using the Bayesian paradigm for 30 years of Well 19

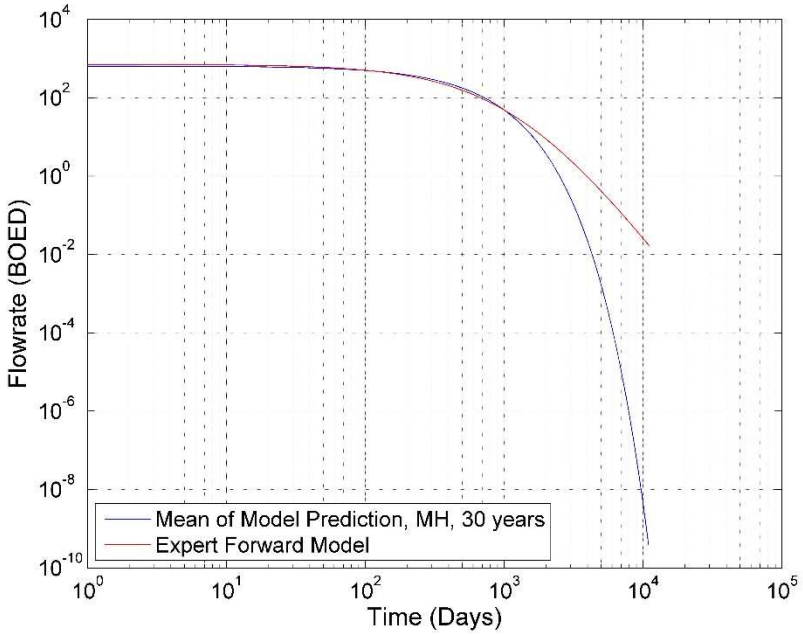

Fig. 141 — The mean of the realizations and the MH model, plotted for 30 years for Well 19

Well 19 – Power Law Exponential Model

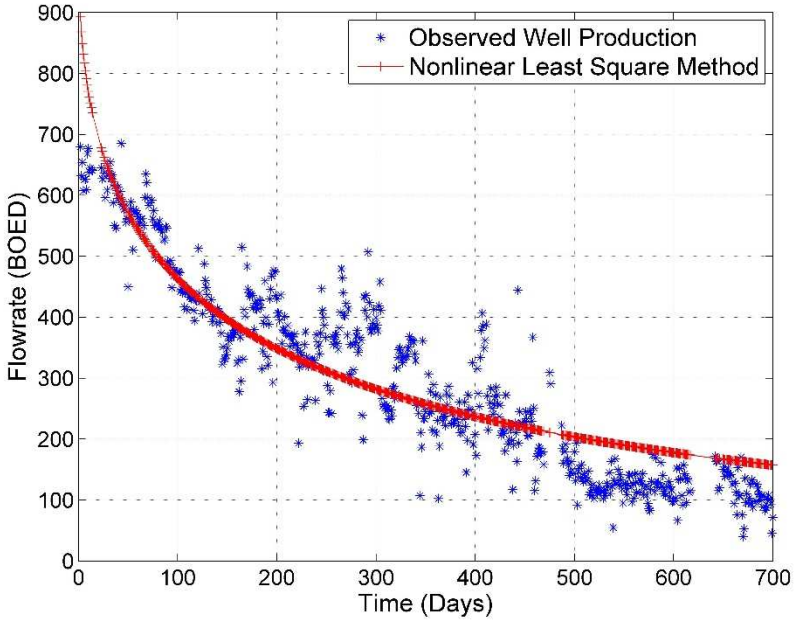

Fig. 142 — Results of the least squares optimization against the production data of Well 19 for the PLE Model

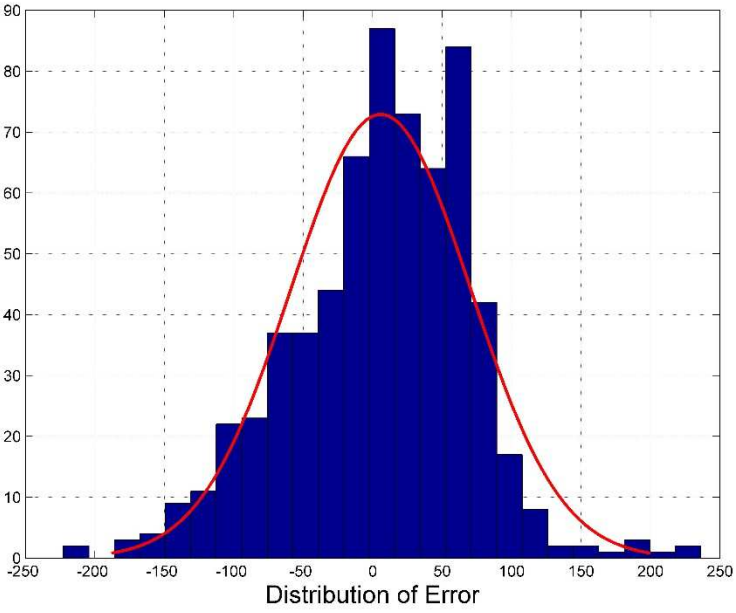

Fig. 143 — The distribution of error between the production data and the LSQ results for Well 19 for the PLE Model

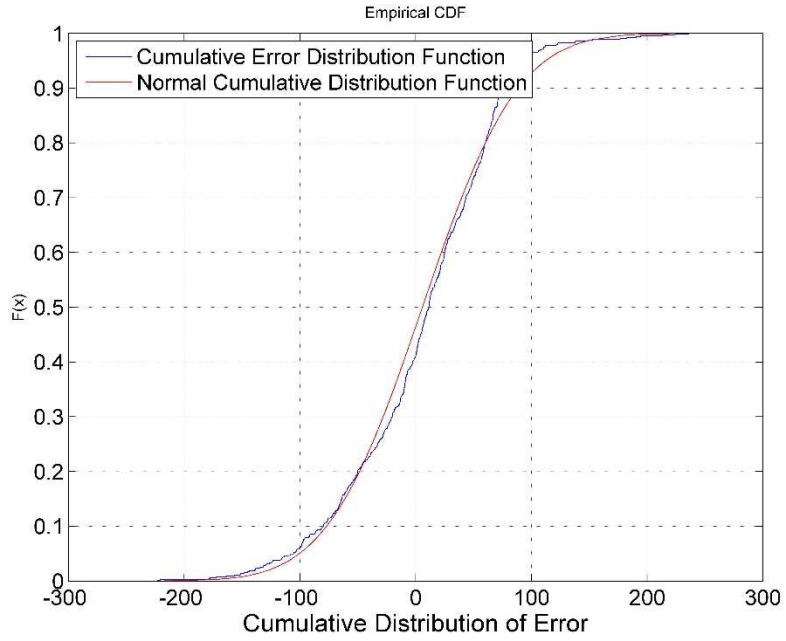

Fig. 144 — The cumulative distribution of error is plotted against the normal cumulative distribution function of Well 19 for the PLE Model

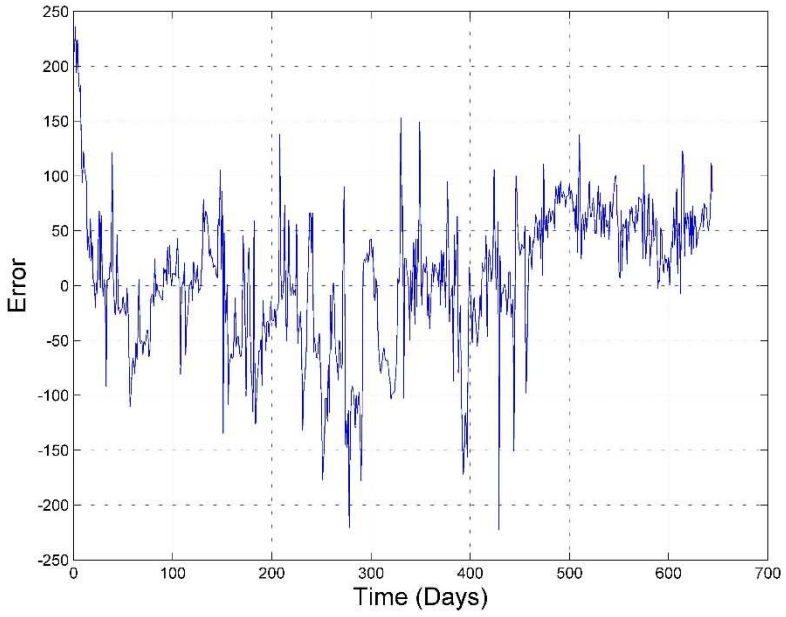

Fig. 145 — The error of the least squares optimization against the number of production days of Well 19 for the PLE Model

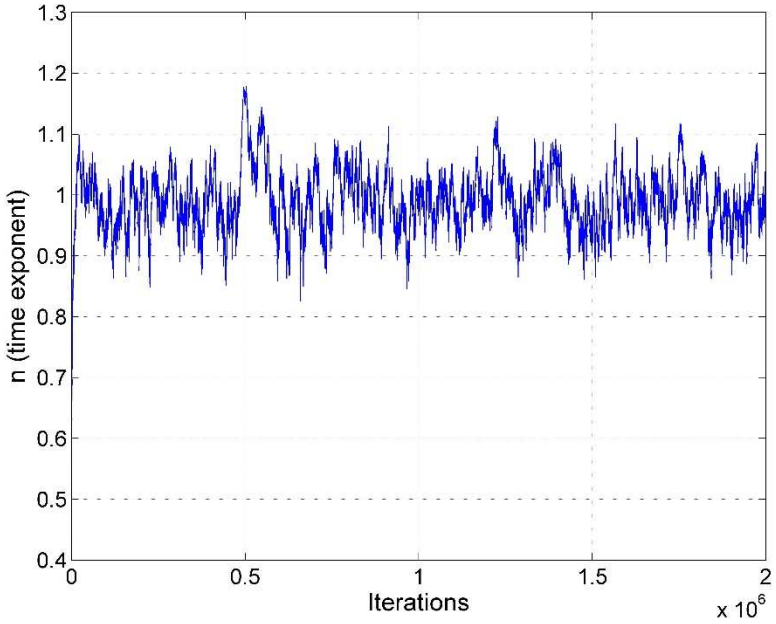

Fig. 146 — MCMC results of *n* for the PLE model of Well 19

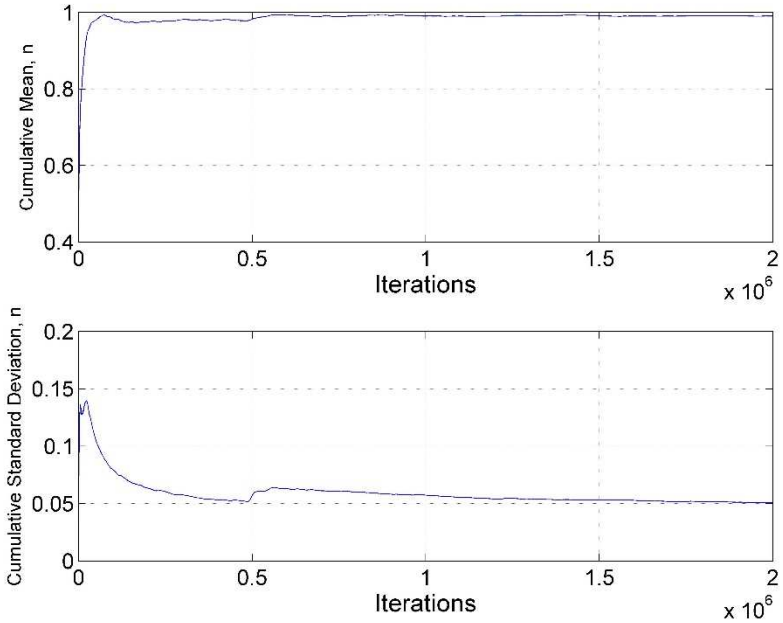

Fig. 147 — Cumulative mean and standard deviation of *n* of Well 19 using the PLE model

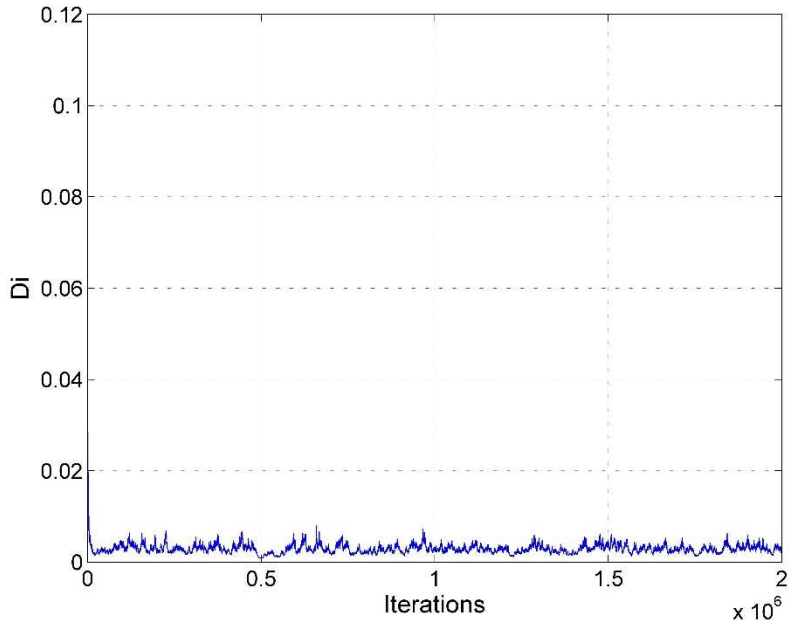

Fig. 148 — MCMC results of D_i for the MH model of Well 19 using the PLE model

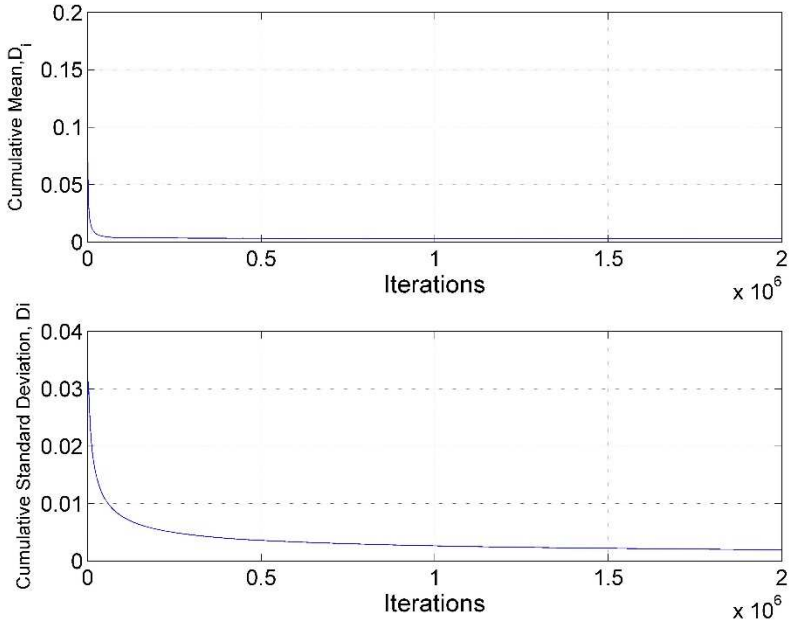

Fig. 149 — Cumulative mean and standard deviation of D_i of Well 19 using the PLE model

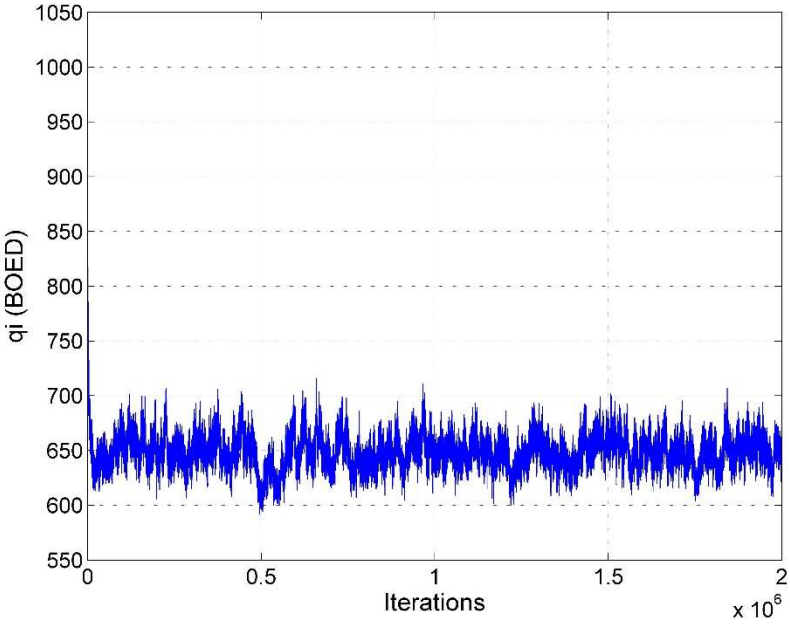

Fig. 150 — MCMC results of q_i for the MH model of Well 19 using the PLE model

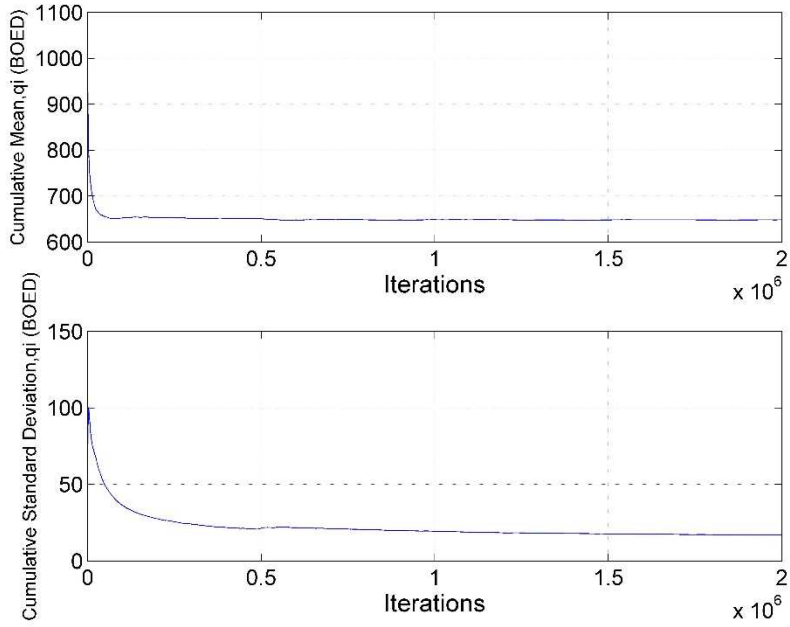

Fig. 151 — Cumulative mean and standard deviation of q_i of Well 19 using the PLE model

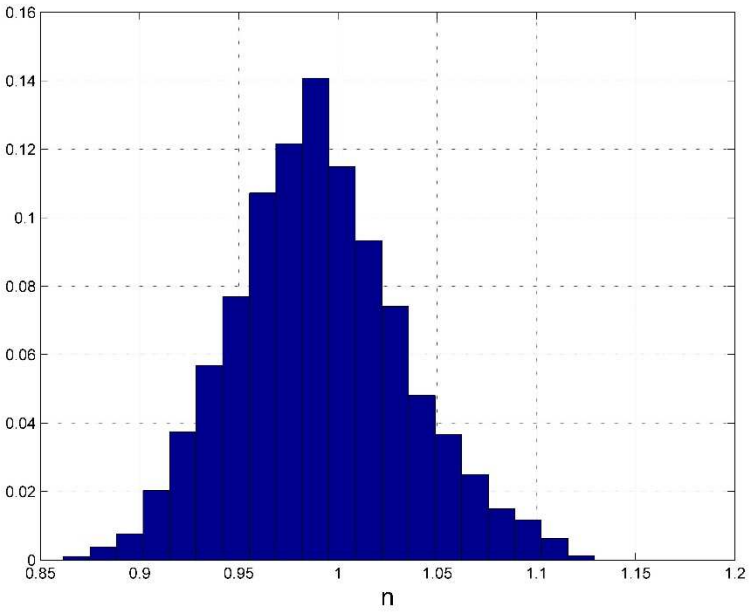

Fig. 152 — Posterior relative frequency histogram of *n* of Well 19 using the PLE model

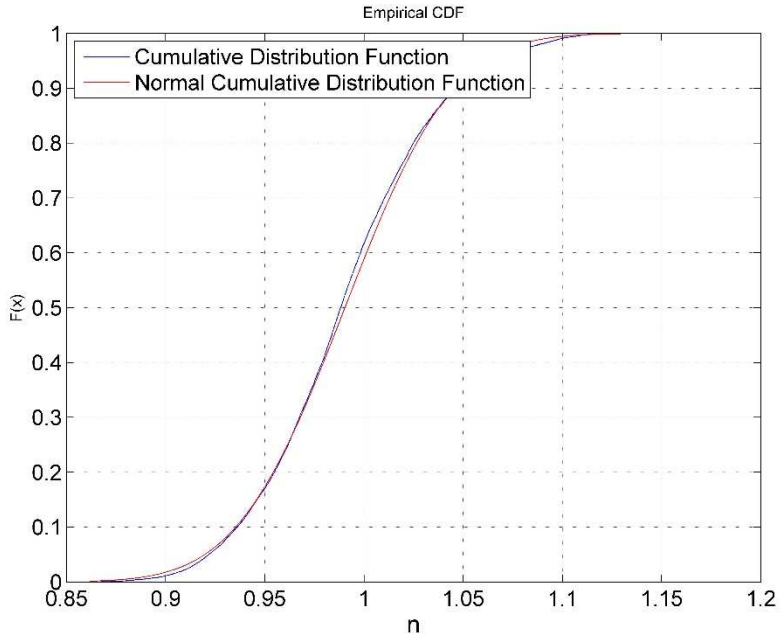

Fig. 153 — Cumulative posterior relative frequency histogram of *n* of Well 19 using the PLE model

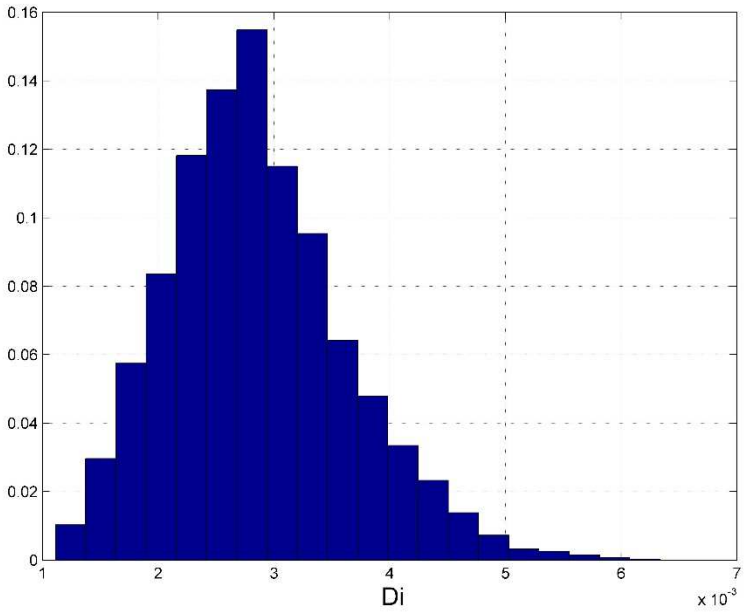

Fig. 154 — Posterior relative frequency histogram of D_i of Well 19 using the PLE model

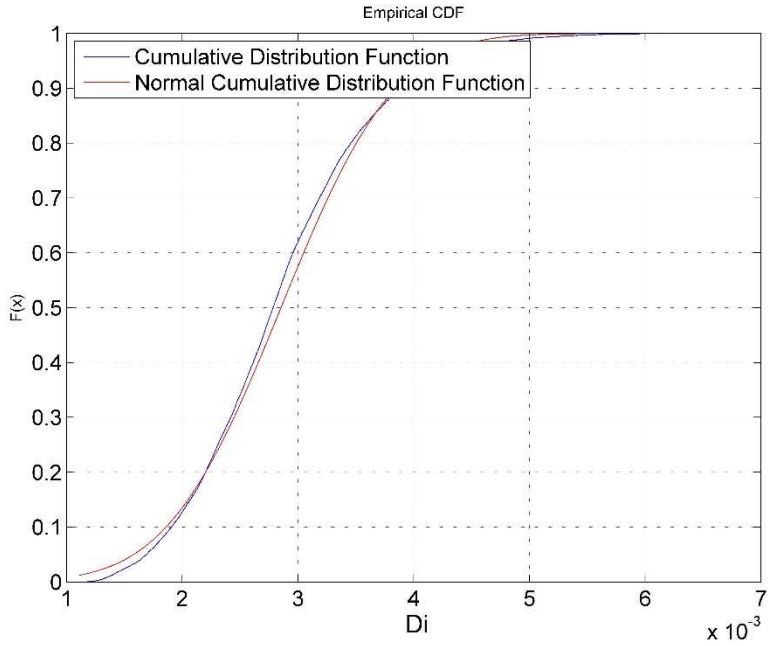

Fig. 155 — Cumulative posterior relative frequency histogram of D_i of Well 19 using the PLE model

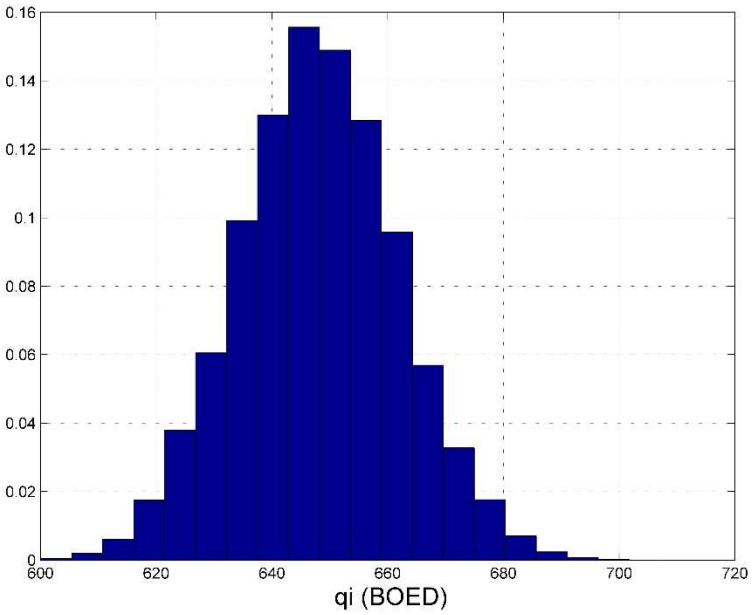

Fig. 156 — Posterior relative frequency histogram of q_i of Well 19 using the PLE model

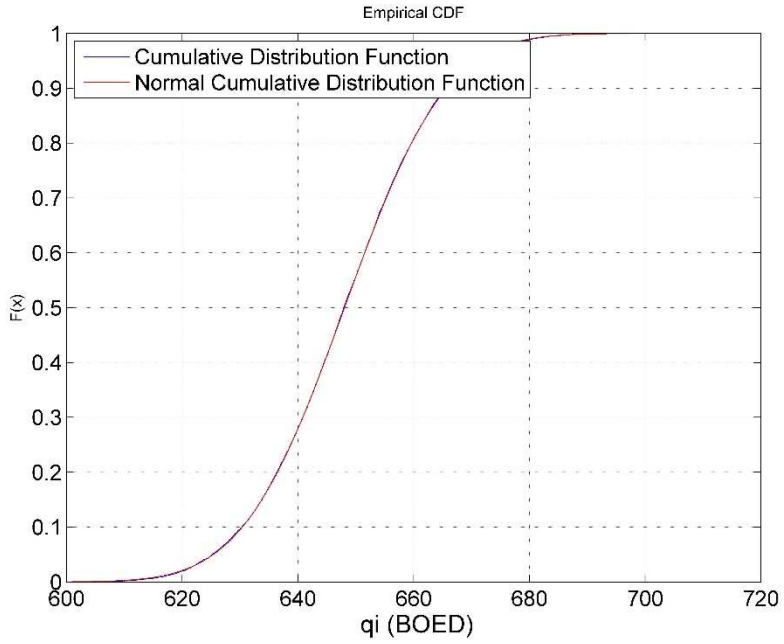

Fig. 157 — Cumulative posterior relative frequency histogram of q_i of Well 19 using the PLE model

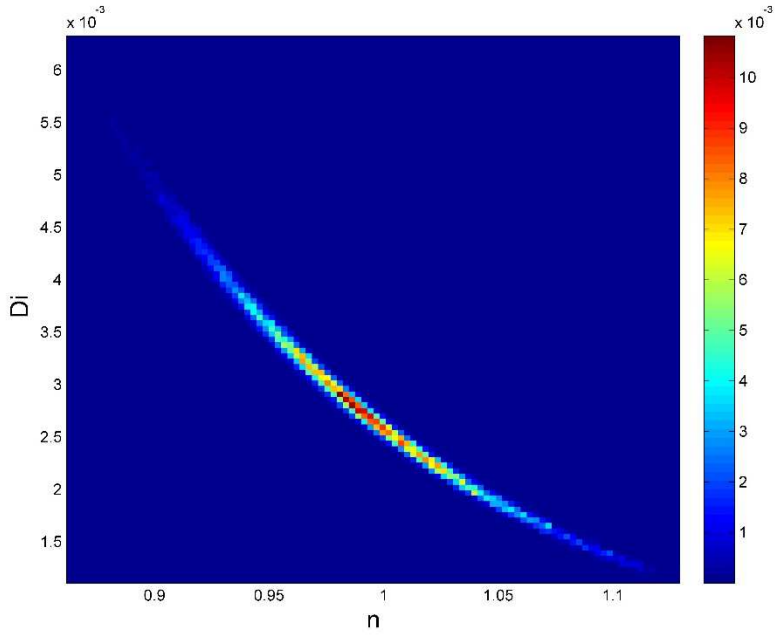

Fig. 158— Relative frequency diagram between D_i and n of Well 19 using the PLE model

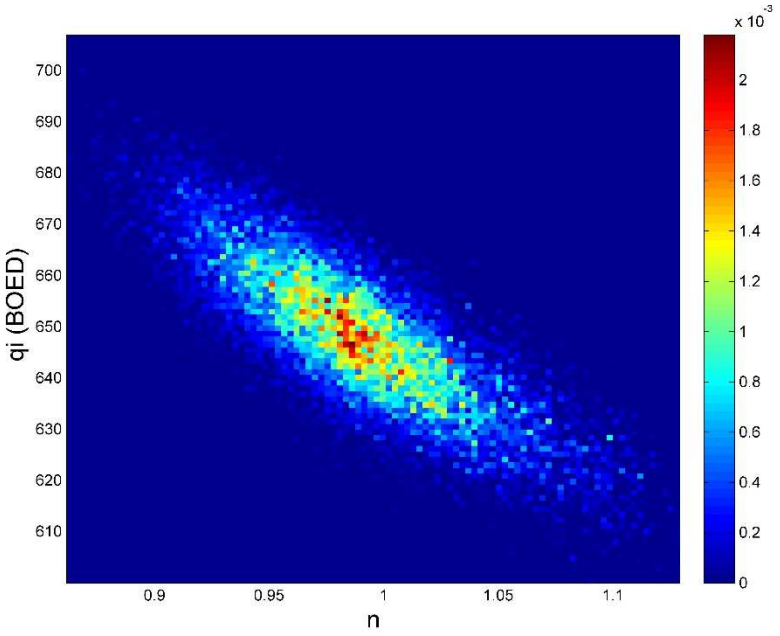

Fig. 159 — Relative frequency diagram between q_i and n of Well 19 using the PLE model

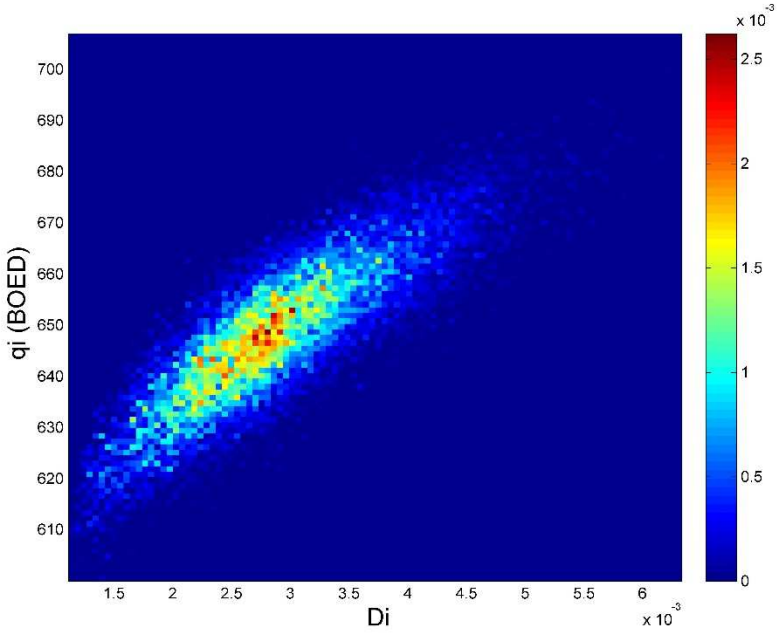

Fig. 160 — Relative frequency diagram between q_i and D_i of Well 19 using the PLE model

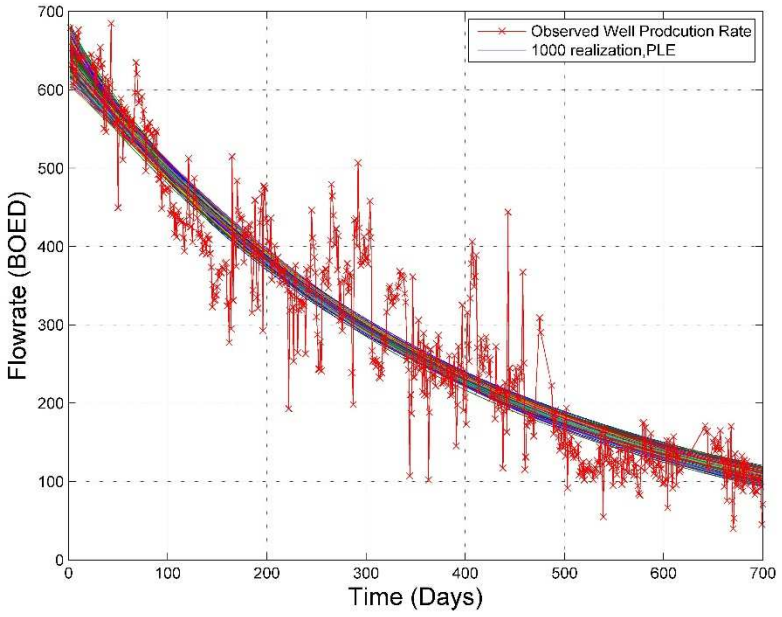

Fig. 161 — The 1,000 realizations of the model predictions using the Bayesian paradigm of Well 19 with the PLE model

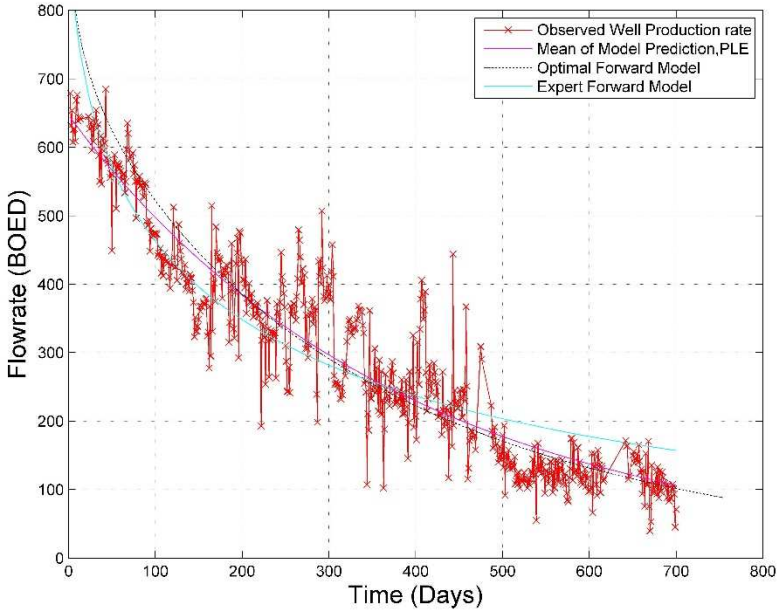

Fig. 162 — The production data with the mean of the realizations, the optimal forward model and the PLE model of Well 19

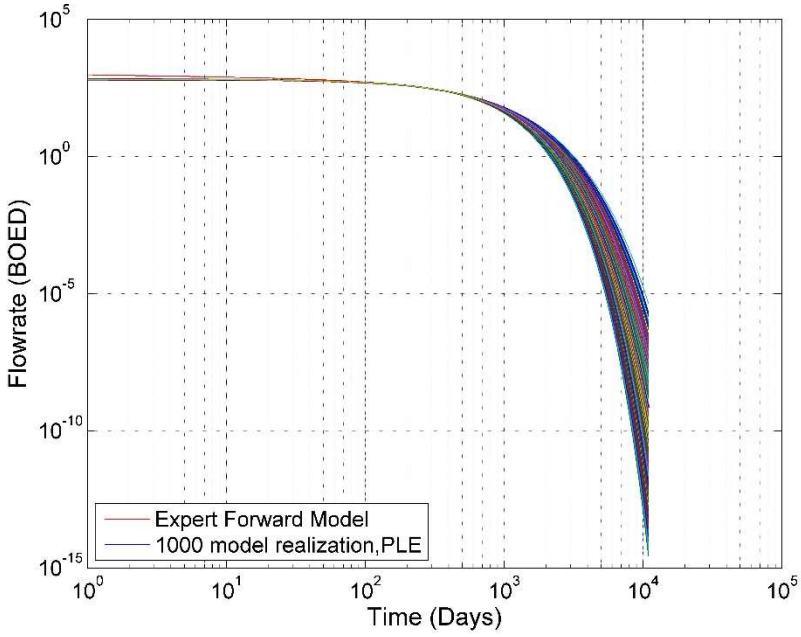

Fig. 163 — The 1,000 realizations of the model predictions using the Bayesian paradigm for 30 years of Well 19

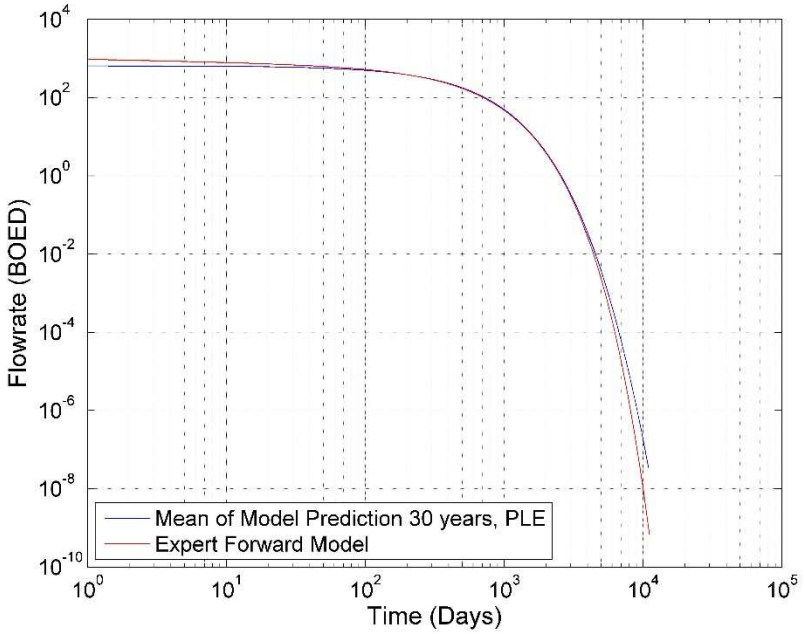

Fig. 164— The mean of the realizations and the PLE model, plotted for 30 years for Well 19

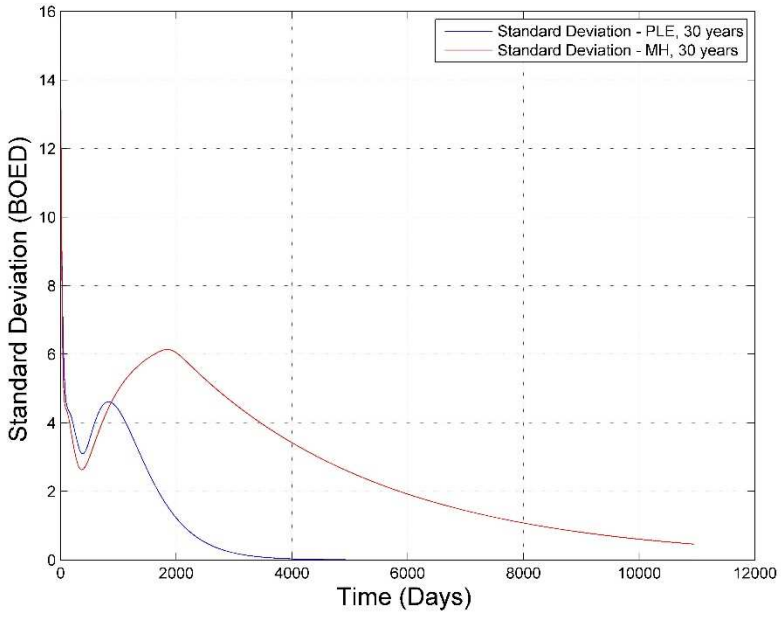

Fig. 165 — Comparison of the Standard Deviation of the two Bayesian forecasts using the MH and PLE models of Well 19

Analysis

Well 19 shows interesting results with the MCMC results, especially when determining the *b*-factor, shown in **Fig. 123**. From the theory, the *b*-factor should have converged and is not, even after 10 million iterations. This indicates to me that the restriction that we set of the *b*-factor being greater than 0 is incorrect because the values of *b* are close to 0, but the *b*-factor should set to 0 in this case, when using the MH model to apply the MCMC. However, we notice that the D_i converges immediately, as does the $q_{i,}$ which can be seen in **Fig. 125** and **127**. We applied the burn-in point and notice that the posterior distribution of the three parameters is quite different. We see a Gaussian distribution for both D_i and q_i in **Fig. 131** and **133**, however see a different distribution for the *b*-factor (**Fig. 129**), which is attributed to the non-convergence of the MCMC. We expect to obtain normally distributed posteriors because this was an assumption made initially. If we compare these MCMC results with the results produced when applying the PLE model, we notice that that model converges nicely for the *n*, the D_i and for the q_i, shown in **Fig. 146**, **148** and **150**, respectively, after only two million iterations. We obtain a clean mean of all three parameters, which lead to clear posterior distributions. The *n* and q_i posteriors are normally distributed (**Fig. 152** and **156**, respectively**)**, however we see a log-normal distribution for D_i (**Fig. 154).** It is a trend throughout the PLE results that the D_i shows a lognormal distribution, which, as previously stated, is an unexpected result because we expected the distribution to be normal.

Based on the posterior distributions of the three parameters, we created the relative frequency histograms that show the relationship between two different parameters -- D_i vs. *b*, q_i vs. *b* and q_i vs D_i for the MH model and D_i vs. *n*, q_i vs. *n* and q_i vs D_i for the PLE model. These results can be seen in **Fig. 135, 136** and **137**, respectively, for the MH model and **Fig. 158, 159** and **160**, respectively, for the PLE model. The quality of the relative frequency histograms is based upon the quality of the posterior of the parameters, because it is just a representation of the two parameters against each other. From Fig. 135 and 136, we see that because of the poor results due to the *b*-factor that the histograms become

skewed and we cannot determine the relationship of the two parameters. However, we see that in Fig. 137 that there is a linear relationship between q_i and D_i. The red part of the graph identifies the ideal set of the two parameters for this data set using the MH model. For the PLE results of the relative frequency histogram, we see interesting results. In Fig. 158, we see a very interesting relationship between D_i and n, which shows a curve. This may indicate that there is no set relationship between these two parameters, because there should not be. However, another interesting observation from Fig. 159 and 160 is that q_i has opposite relationships with D_i and the b-factor.

Finally we reach the realizations of the Bayesian paradigm using the MH and PLE models. We notice when we plot the mean of the realizations versus the optimal forward model (the results from the LSQ optimization), and the expert forward model (either MH or PLE), the mean of the model prediction and the expert forward model often times have close values for the 700 days plotted. However, when we extend the results to 30 years that there is a divergence between two sets of results. In general, the results show that the forward model underestimates the reserves, as seen in **Fig. 141** for the MH model and **Fig. 164** for the PLE model.

The most interesting graph to discuss, however, is the graph that compares the standard deviations of the two sets of Bayesian results, **Fig. 165**. This figure identifies the uncertainty of the two models. We can see that the uncertainty is approximately the same in early time, however as time progresses, the PLE model shows less uncertainty while the MH model's uncertainty increases and is prevalent through the 30 years. From this graph, I would determine that the most acceptable model to use would be the Bayesian forecast model, by applying the PLE model.

APPENDIX IV

RESULTS AND ANALYSIS OF WELL 20

Well 20 – Modified Hyperbolic Model

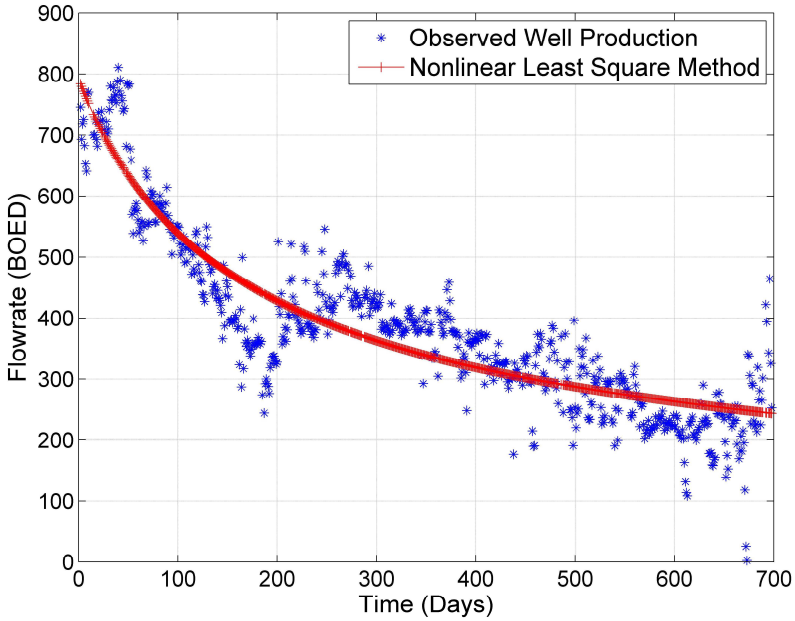

Fig. 166 — Results of the least squares optimization against the production data of Well 20 for the MH Model

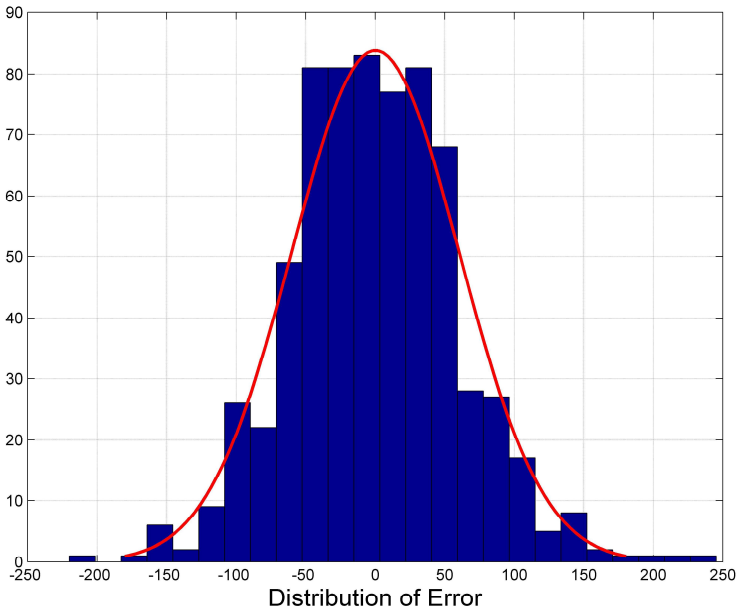

Fig. 167 — The distribution of error between the production data and the LSQ results for Well 20 for the MH Model

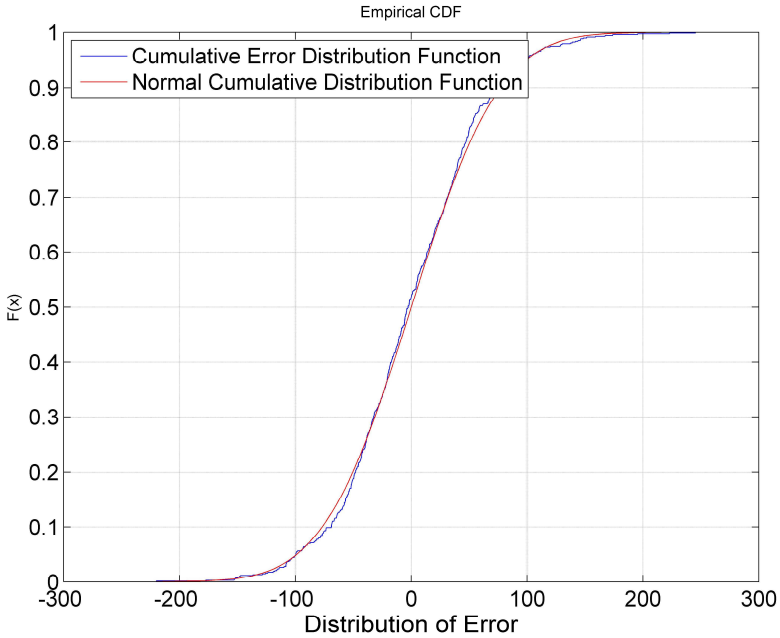

Fig. 168 — The cumulative distribution of error is plotted against the normal cumulative distribution function of Well 20 for the MH Model

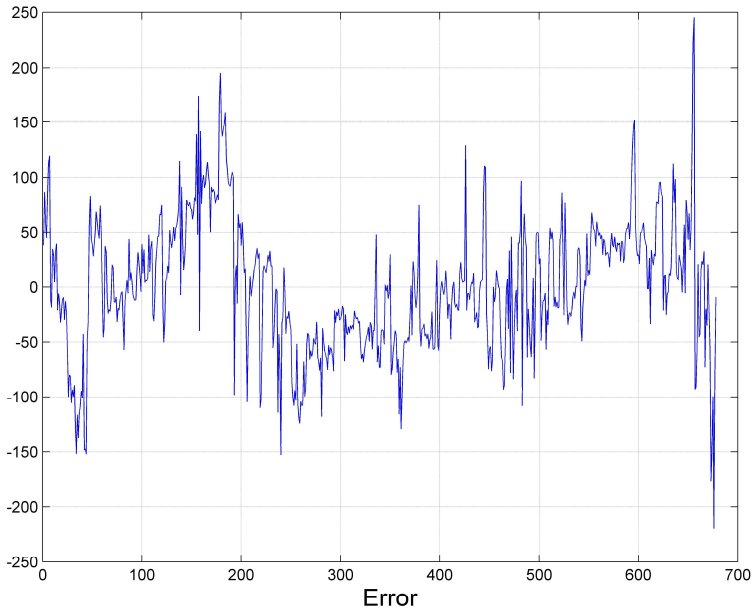

Fig. 169 — The error of the least squares optimization against the number of production days of Well 20 for the MH Model

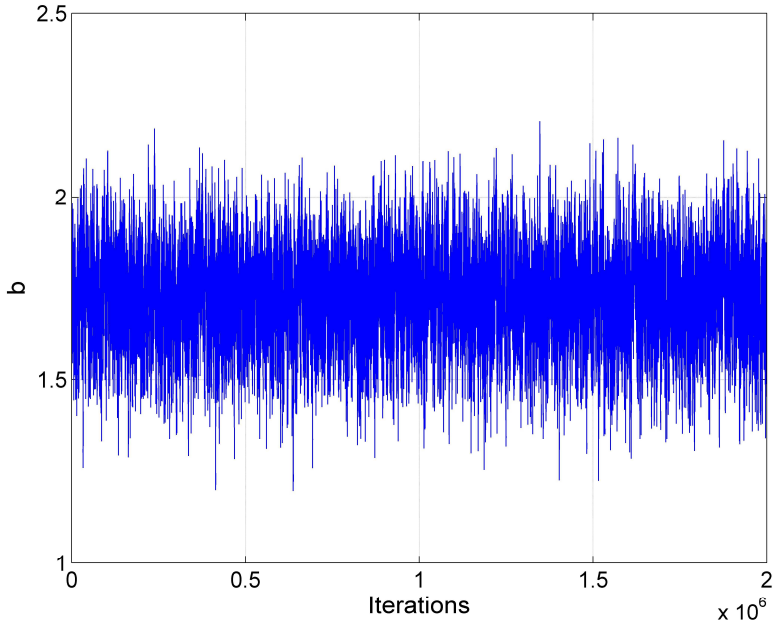

Fig. 170 — MCMC results of the *b*-factor for the MH model of Well 20 using the MH model

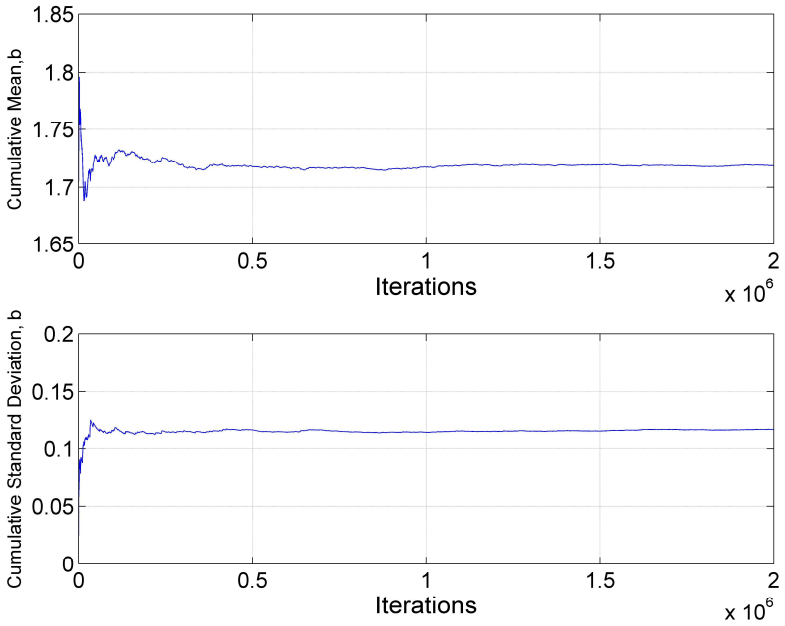

Fig. 171 — Cumulative mean and standard deviation of the *b*-factor of Well 20 using the MH model

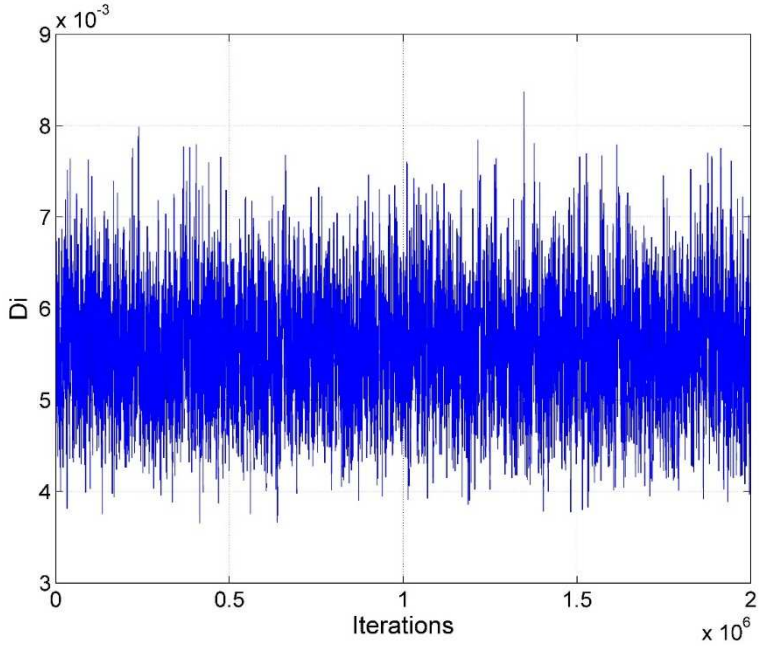

Fig. 172 — MCMC results of D_i for the MH model of Well 20 using the MH model

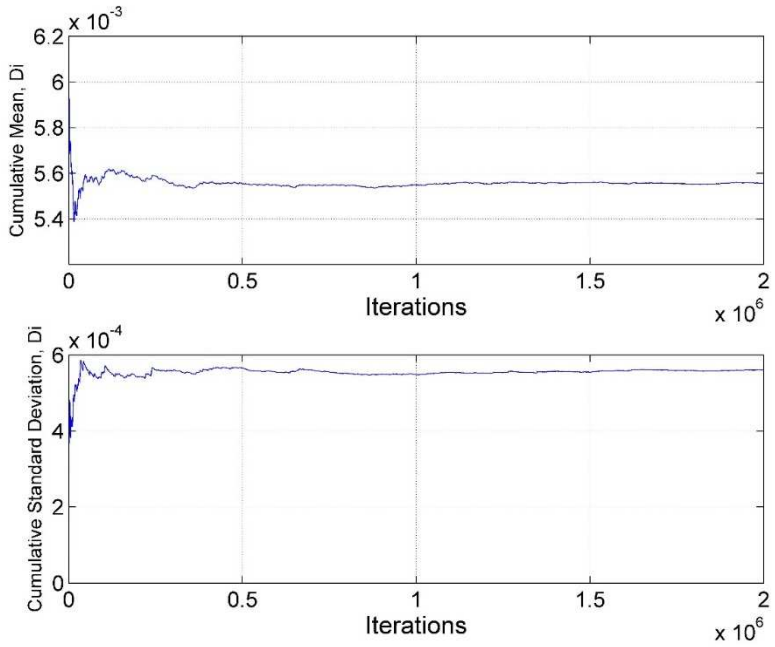

Fig. 173 — Cumulative mean and standard deviation of D_i of Well 20 using the MH model

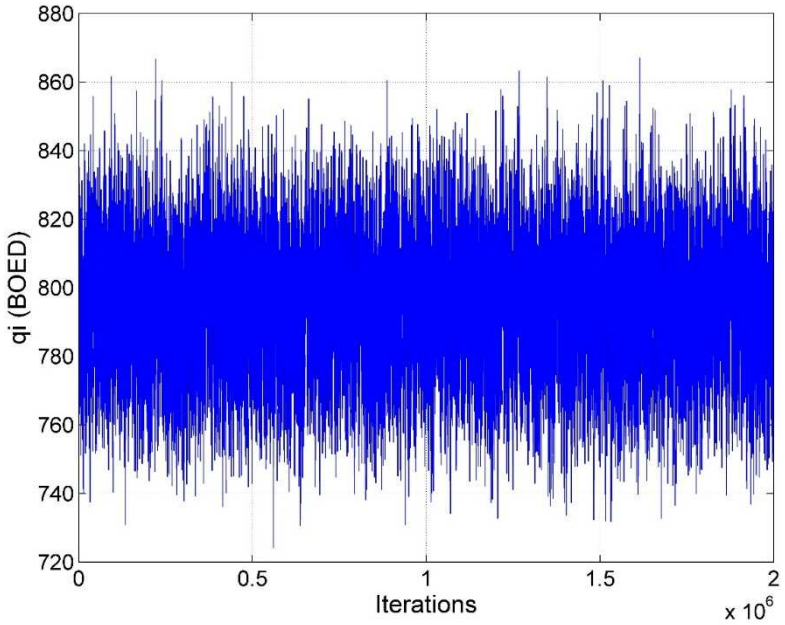

Fig. 174 — MCMC results of q_i for the MH model of Well 20 using the MH model

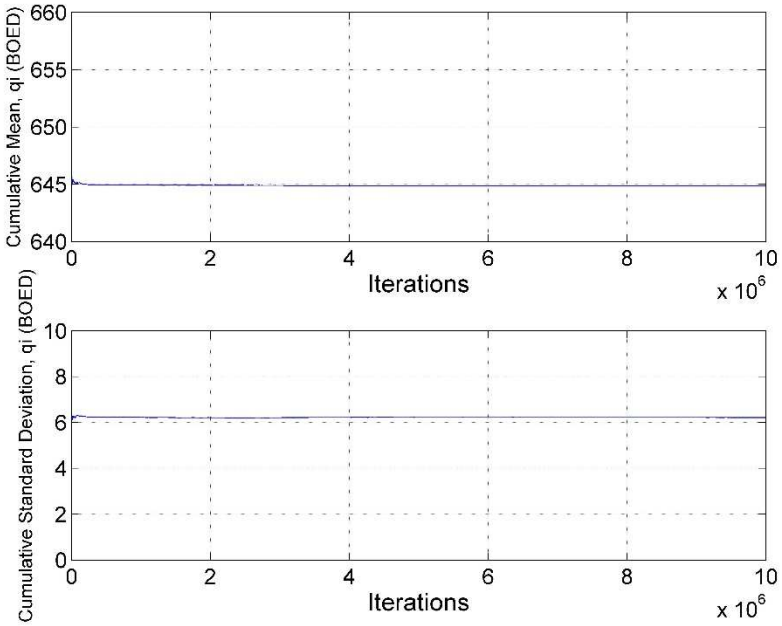

Fig. 175 — Cumulative mean and standard deviation of q_i of Well 20 using the MH model

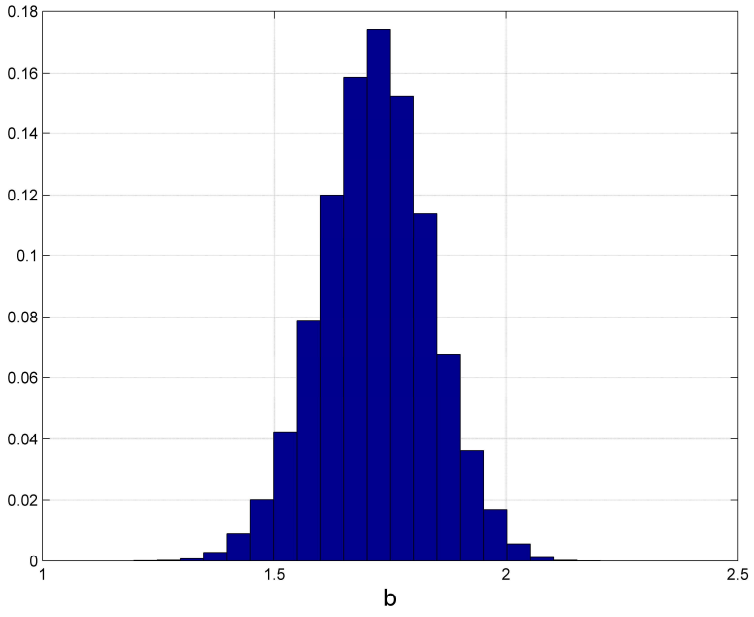

Fig. 176 — Posterior relative frequency histogram of *b* of Well 20 using the MH model

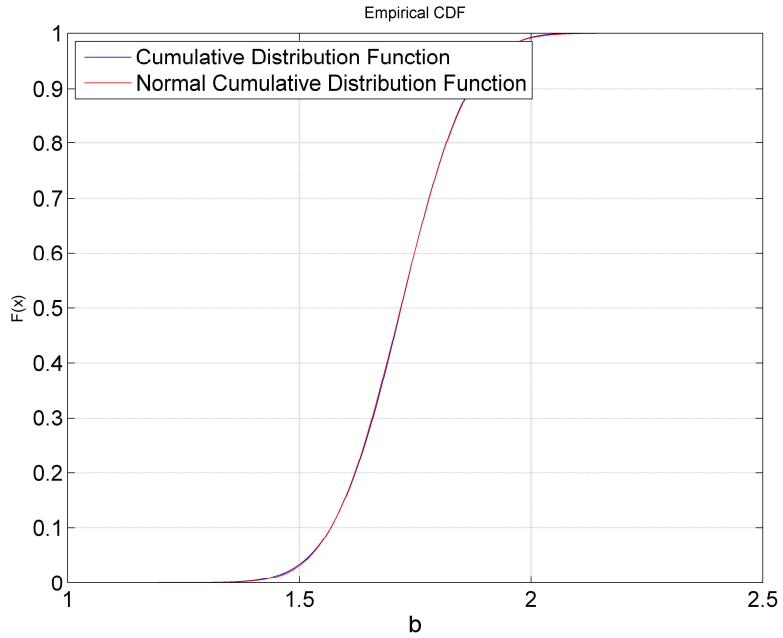

Fig. 177 — Cumulative posterior relative frequency histogram of the *b*-factor of Well 20 using the MH model

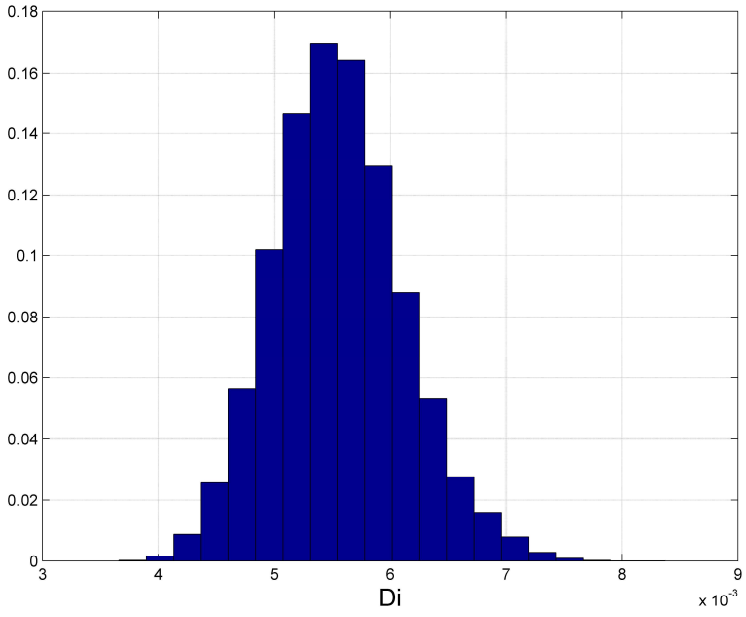

Fig. 178 — Posterior relative frequency histogram of D_i of Well 20 using the MH model

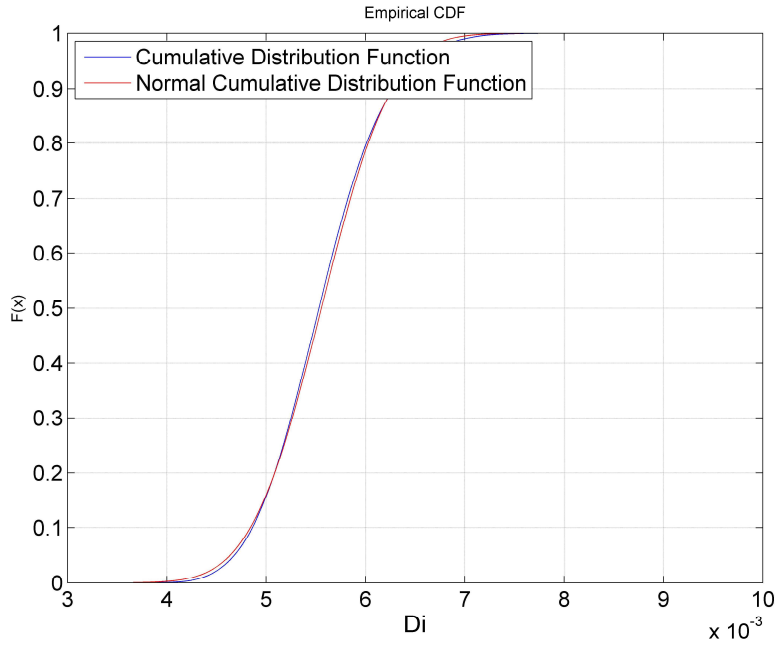

Fig. 179 — Cumulative posterior relative frequency histogram of D_i of Well 20 using the MH model

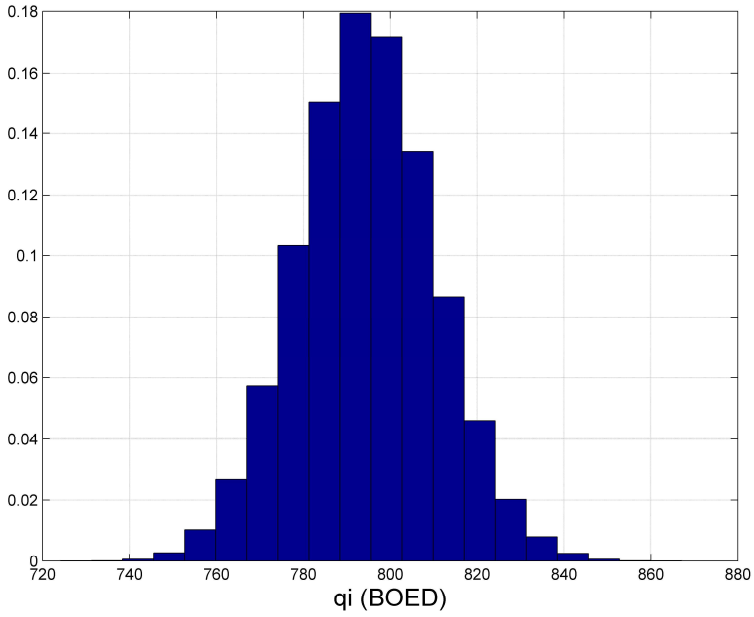

Fig. 180 — Posterior relative frequency histogram of q_i of Well 20 using the MH model

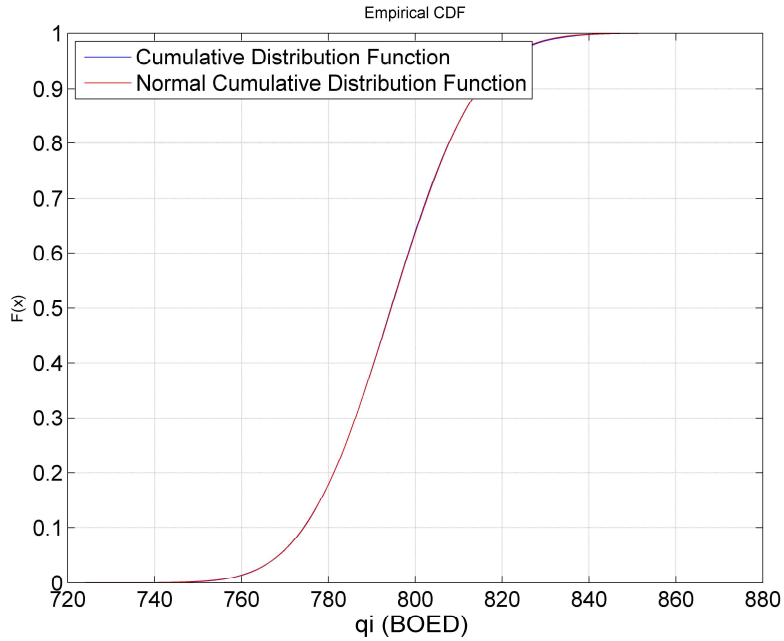

Fig. 181 — Cumulative posterior relative frequency histogram of q_i of Well 20 using the MH model

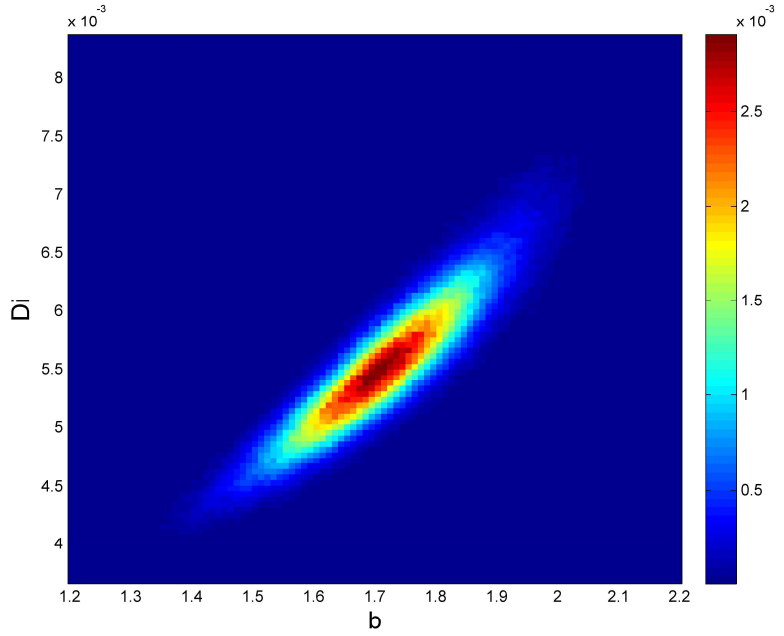

Fig. 182 — Relative frequency diagram between D_i and b of Well 20 using the MH model

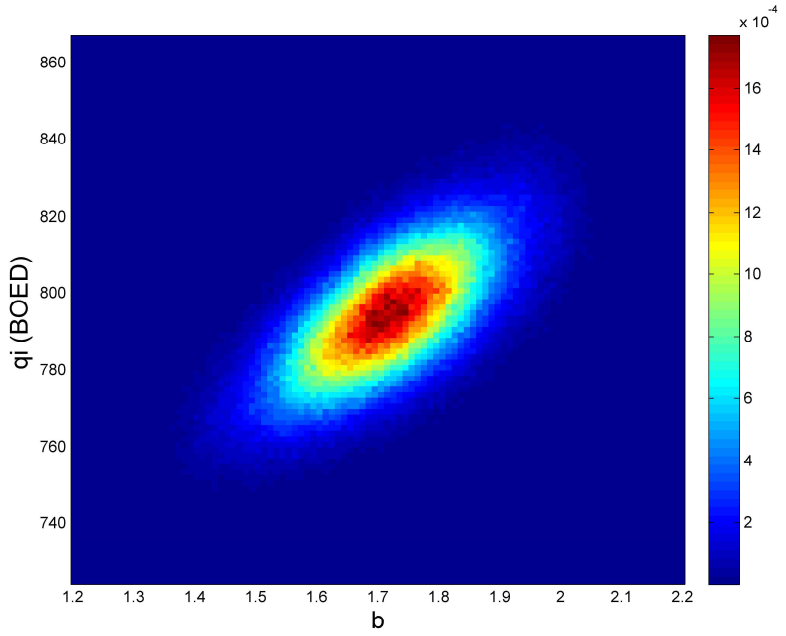

Fig. 183 — Relative frequency diagram between q_i and b of Well 20 using the MH model

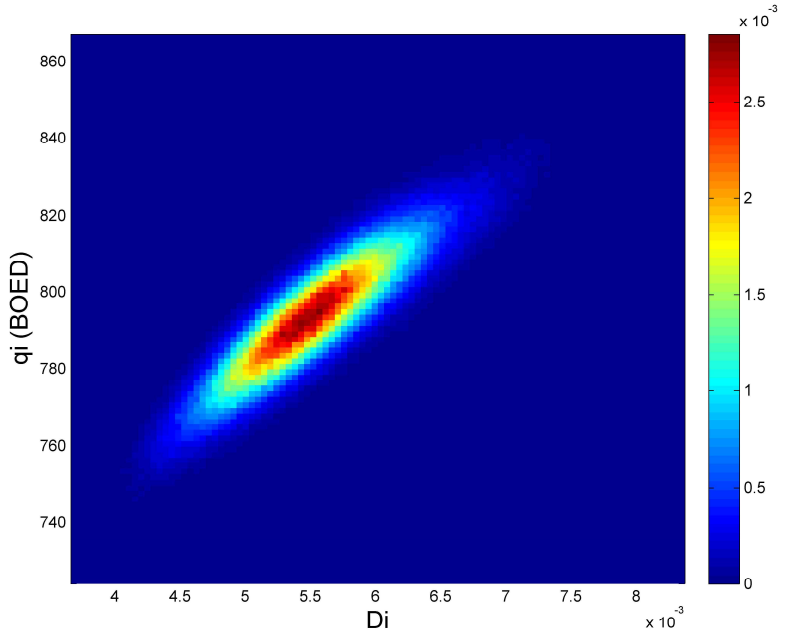

Fig. 184 — Relative frequency diagram between q_i and D_i of Well 20 using the MH model

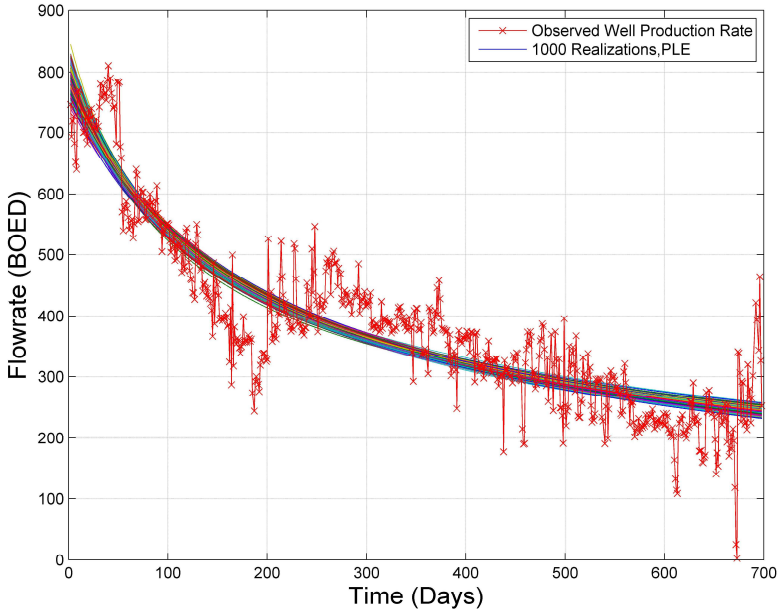

Fig. 185 — The 1,000 realizations of the model predictions using the Bayesian paradigm of Well 20 with the MH model

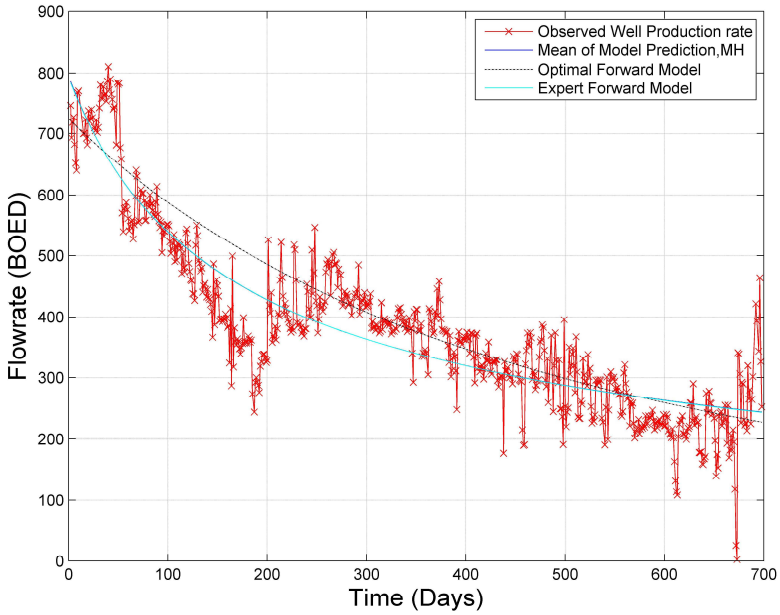

Fig. 186 — The production data with the mean of the realizations, the optimal forward model and the MH model of Well 20

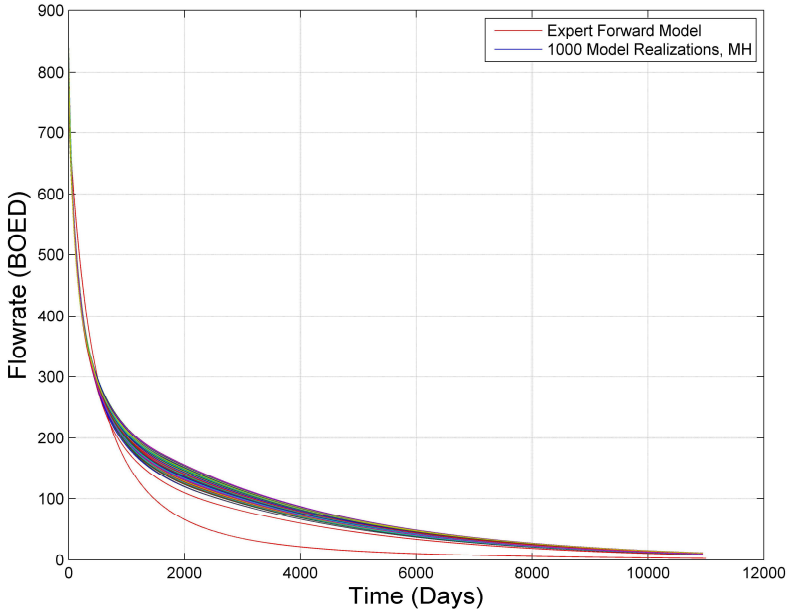

Fig. 187 — The 1,000 realizations of the model predictions using the Bayesian paradigm for 30 years of Well 20

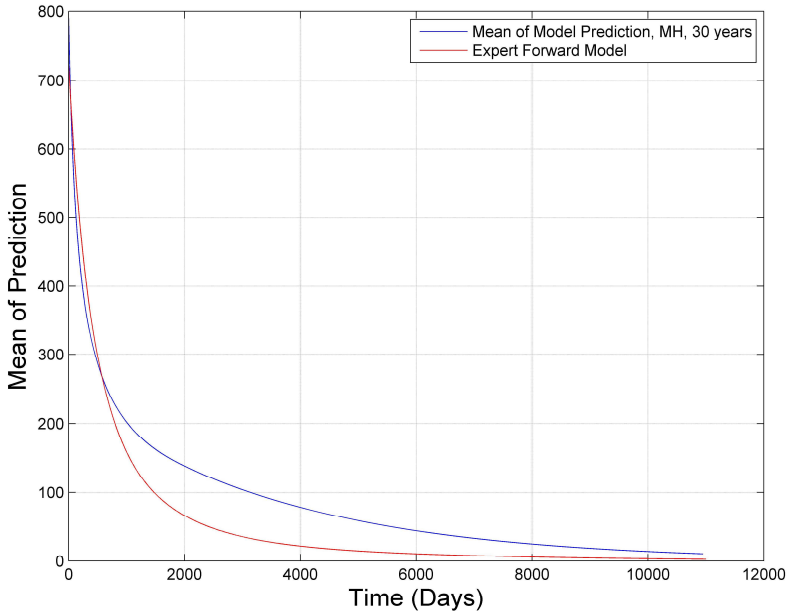

Fig. 188 — The mean of the realizations and the MH model, plotted for 30 years for Well 20

Well 20 – Power Law Exponential Model

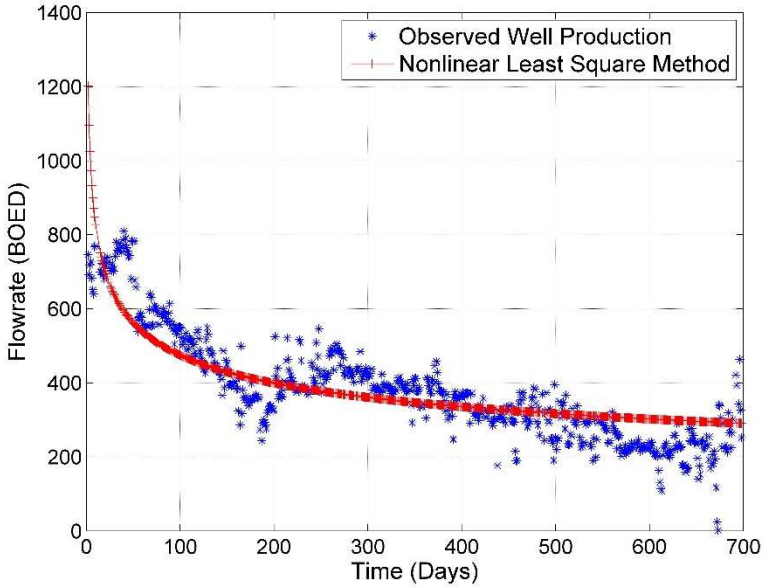

Fig. 189 — Results of the least squares optimization against the production data of Well 20 for the PLE Model

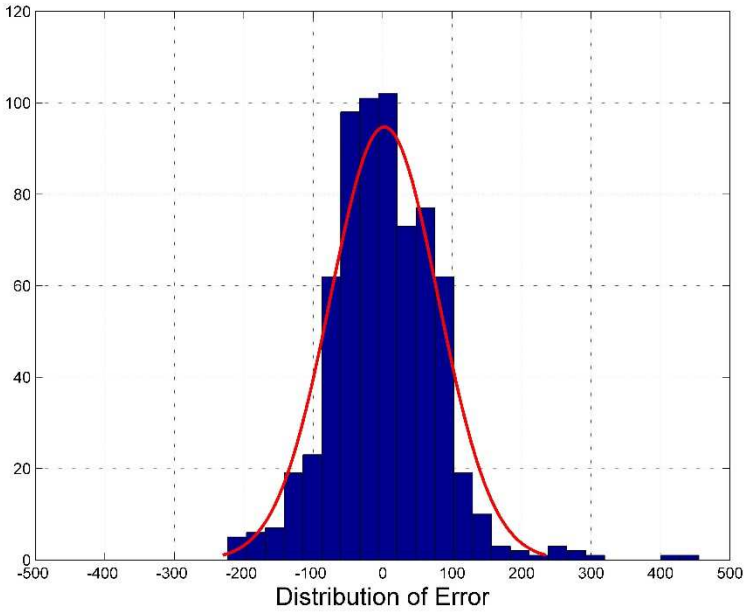

Fig. 190 — The distribution of error between the production data and the LSQ result for Well 20 for the PLE Model

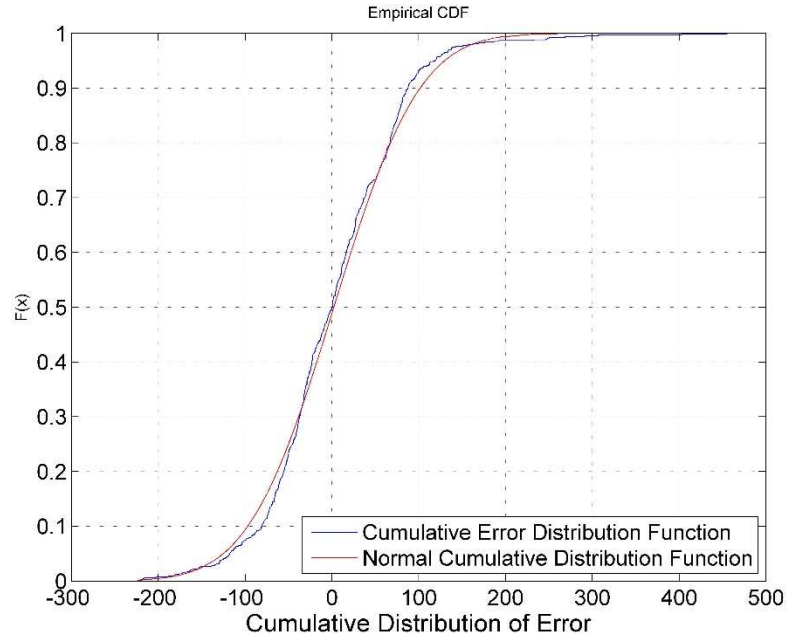

Fig. 191 — The cumulative distribution of error is plotted against the normal cumulative distribution function of Well 20 for the PLE Model

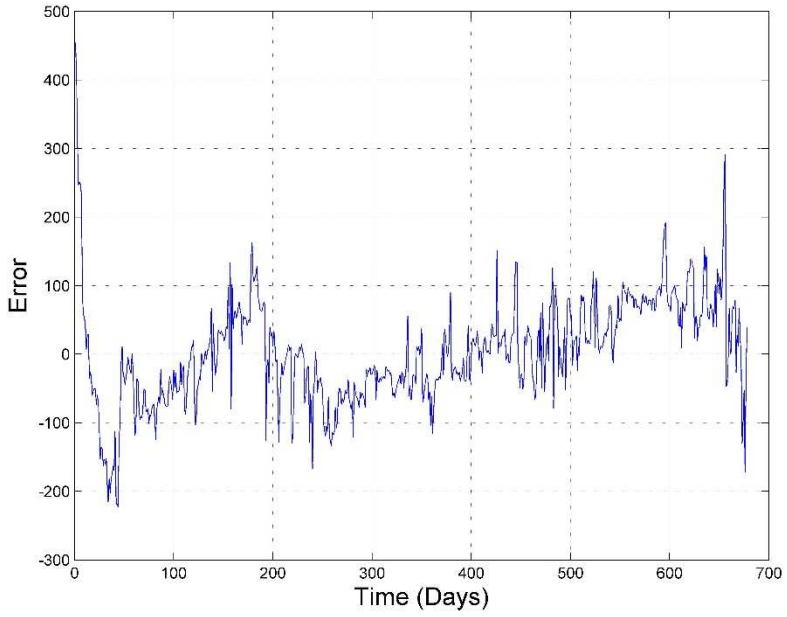

Fig. 192 — The error of the least squares optimization against the number of production days of Well 20 for the PLE Model

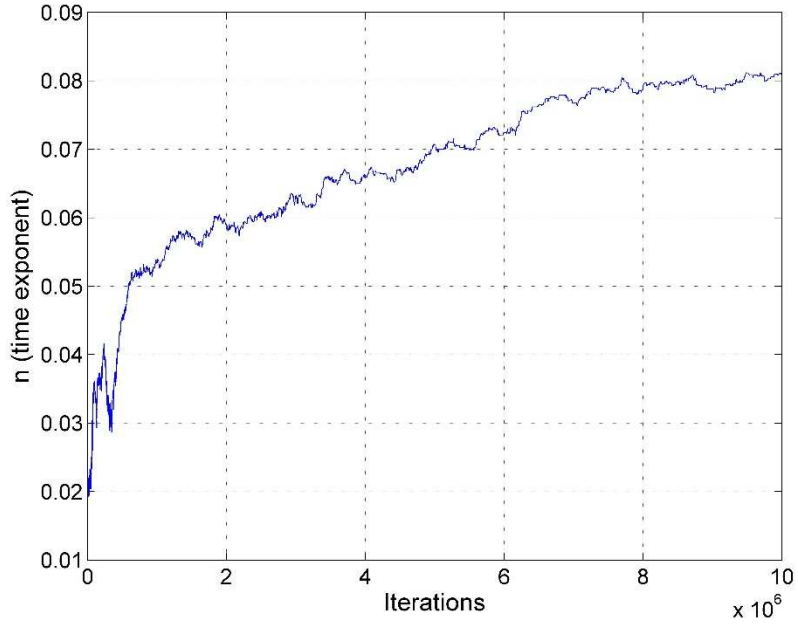

Fig. 193 — MCMC results of *n* for the PLE model of Well 20

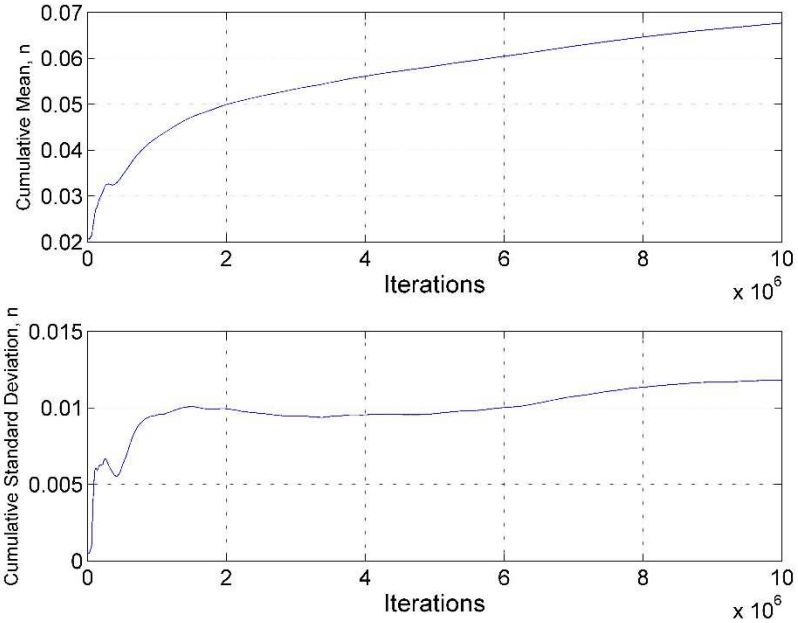

Fig. 194 — Cumulative mean and standard deviation of *n* of Well 20 using the PLE model

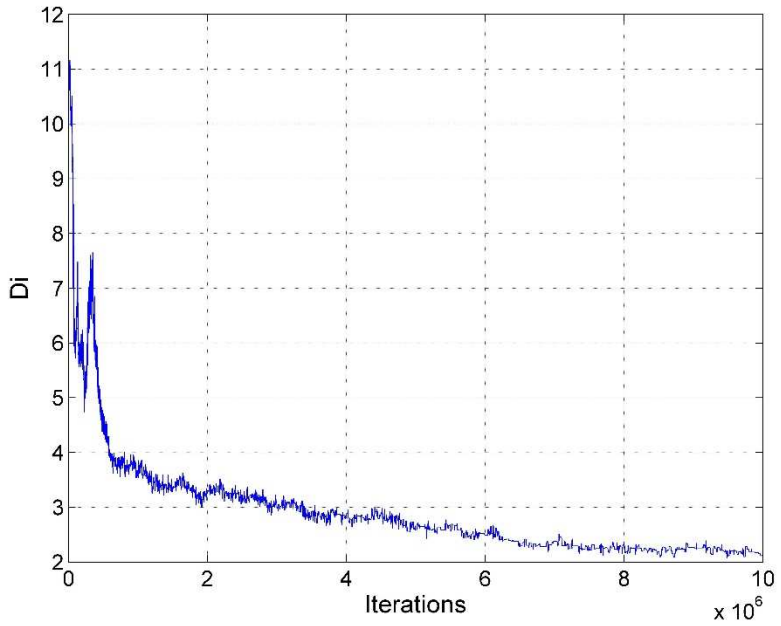

Fig. 195 — MCMC results of D_i for the MH model of Well 20 using the PLE model

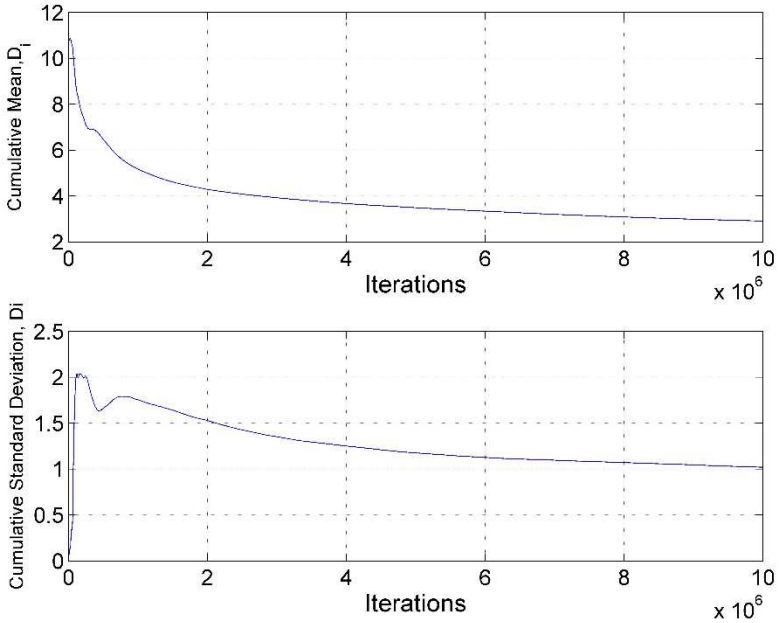

Fig. 196 — Cumulative mean and standard deviation of D_i of Well 20 using the PLE model

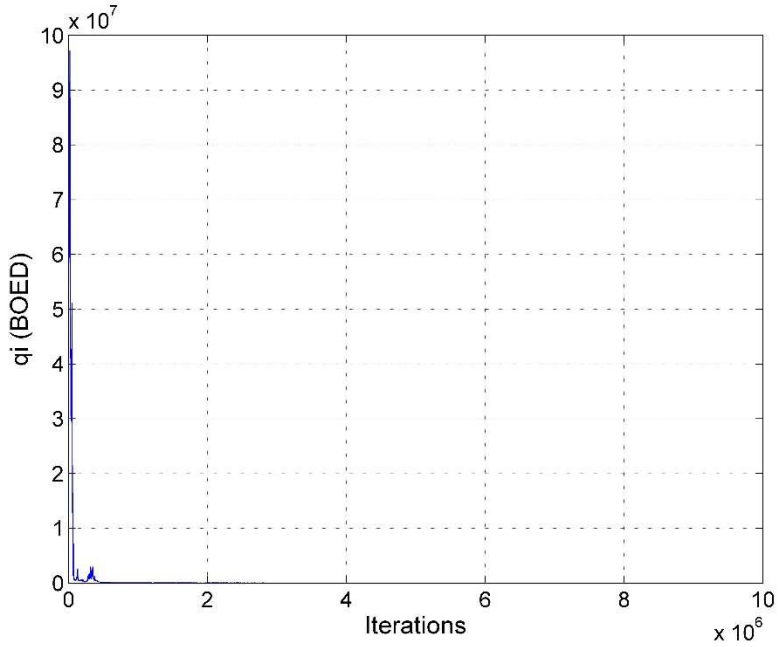

Fig. 197 — MCMC results of q_i for the MH model of Well 20 using the PLE model

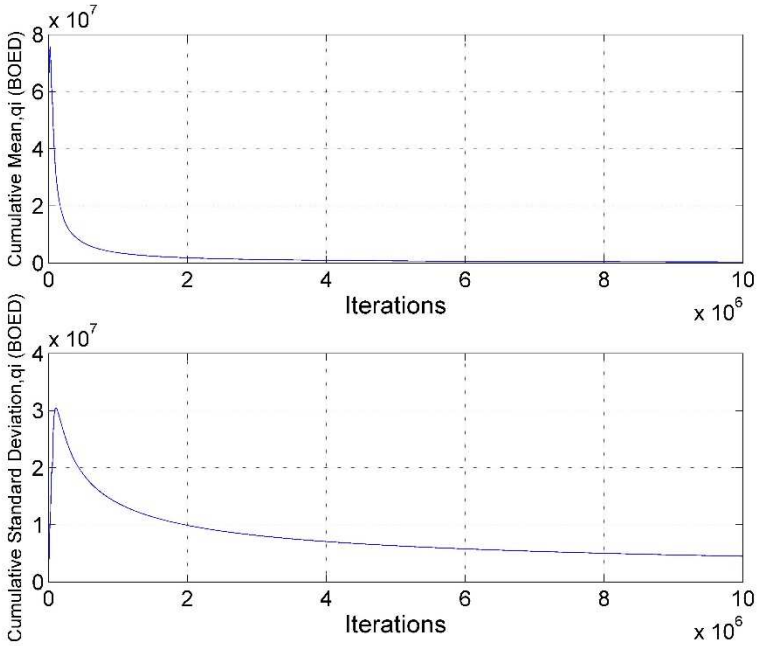

Fig. 198 — Cumulative mean and standard deviation of q_i of Well 20 using the PLE model

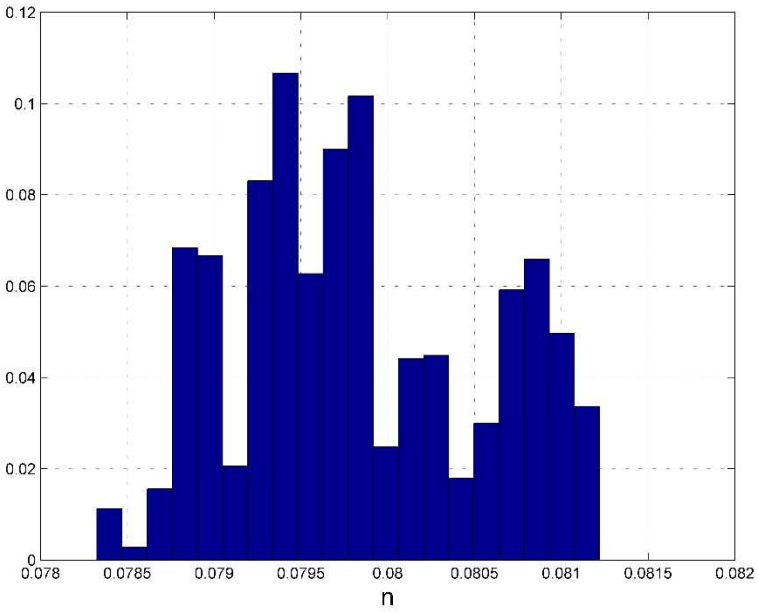

Fig. 199 — Posterior relative frequency histogram of *n* of Well 20 using the PLE model

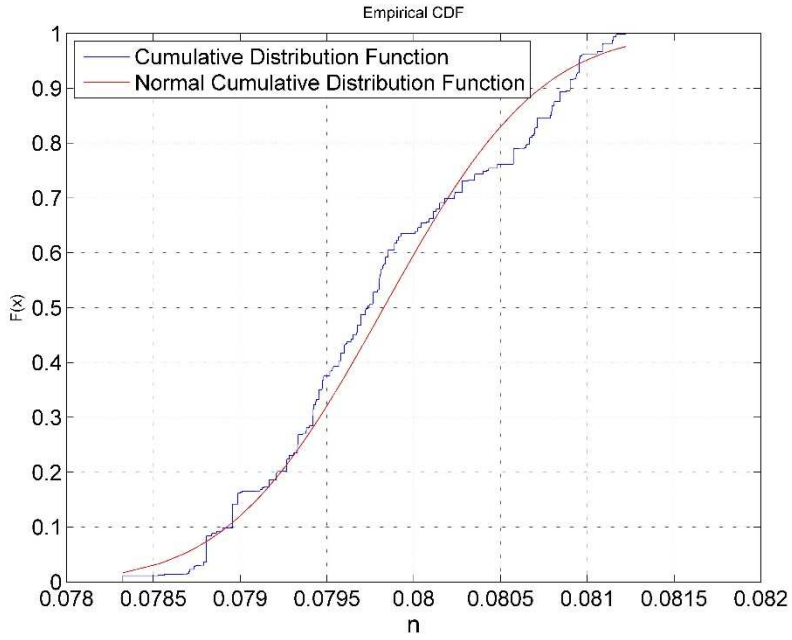

Fig. 200 — Cumulative posterior relative frequency histogram of *n* of Well 20 using the PLE model

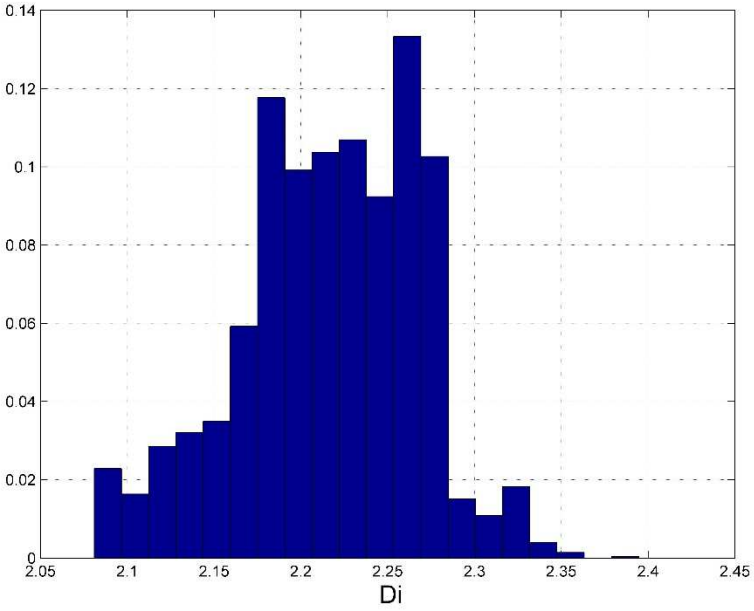

Fig. 201 — Posterior relative frequency histogram of D_i of Well 20 using the PLE model

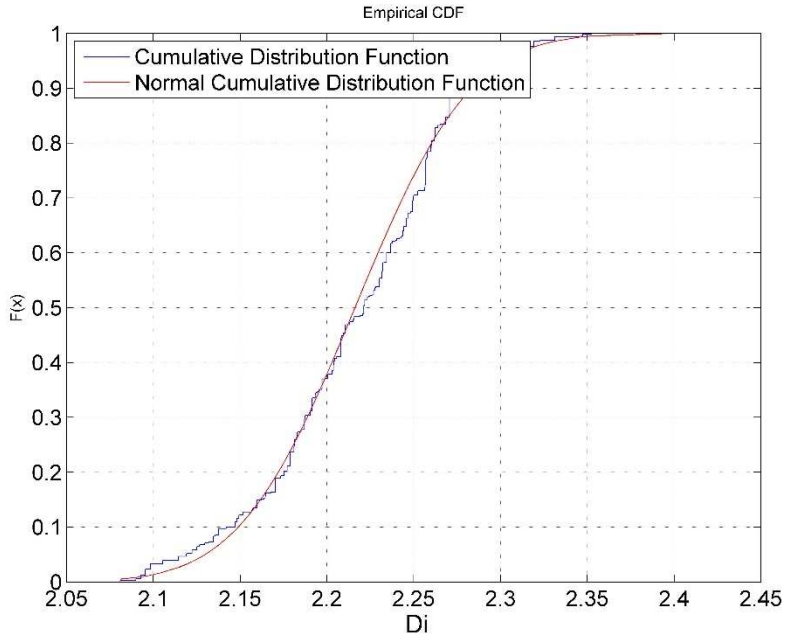

Fig. 202 — Cumulative posterior relative frequency histogram of D_i of Well 20 using the PLE model

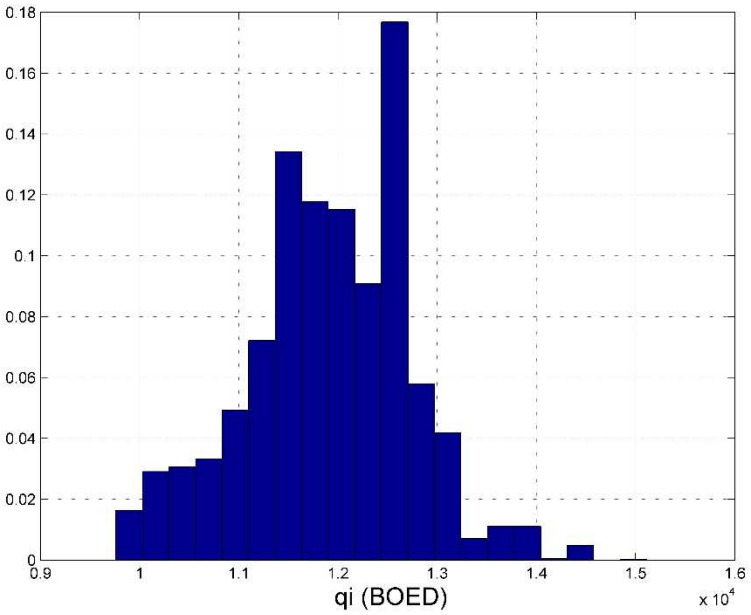

Fig. 203 — Posterior relative frequency histogram of q_i of Well 20 using the PLE model

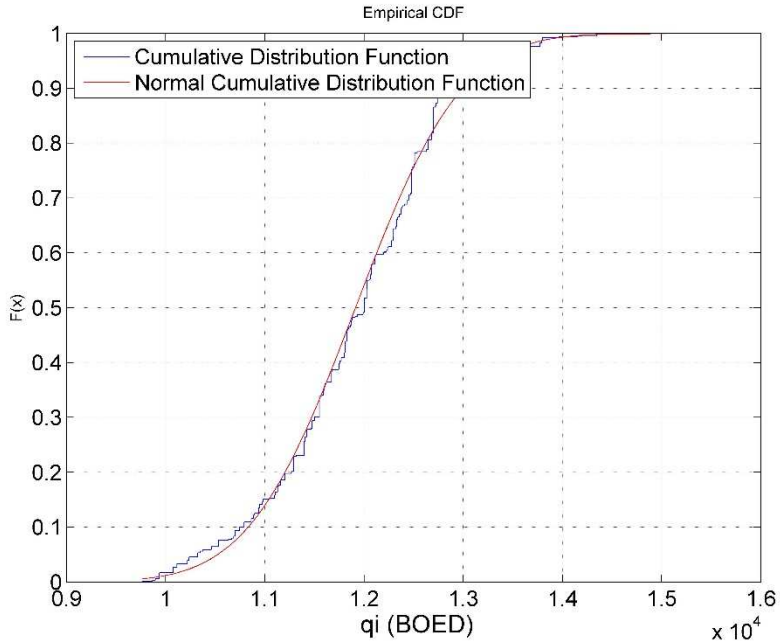

Fig. 204 — Cumulative posterior relative frequency histogram of q_i of Well 20 using the PLE model

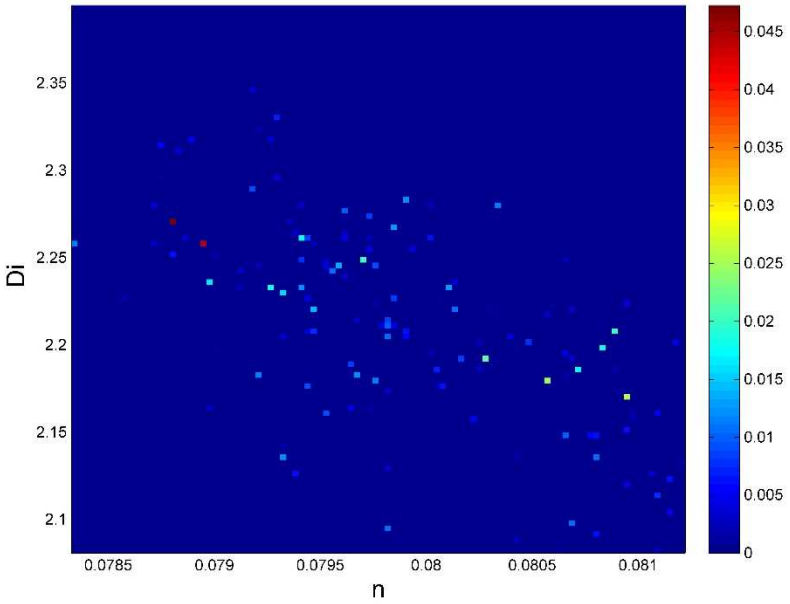

Fig. 205 — Relative frequency diagram between D_i and n of Well 20 using the PLE model

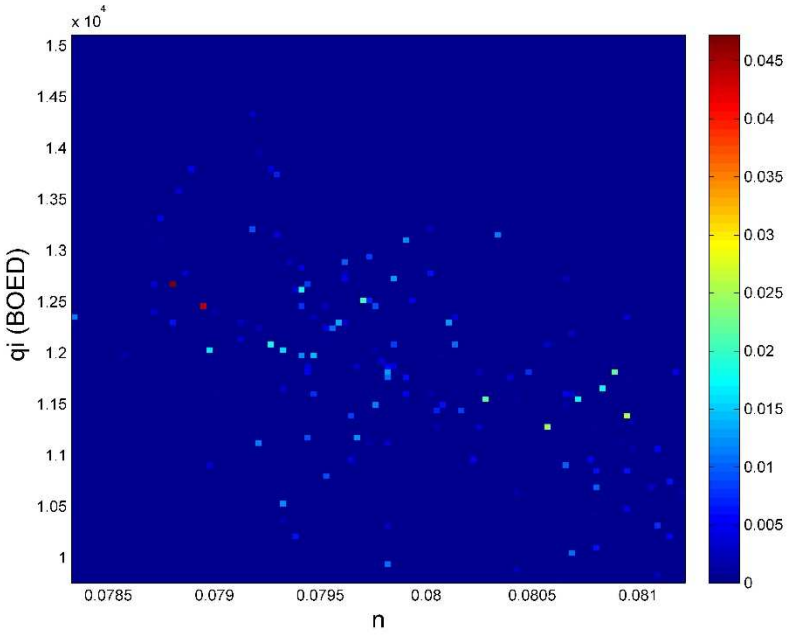

Fig. 206 — Relative frequency diagram between q_i and n of Well 20 using the PLE model

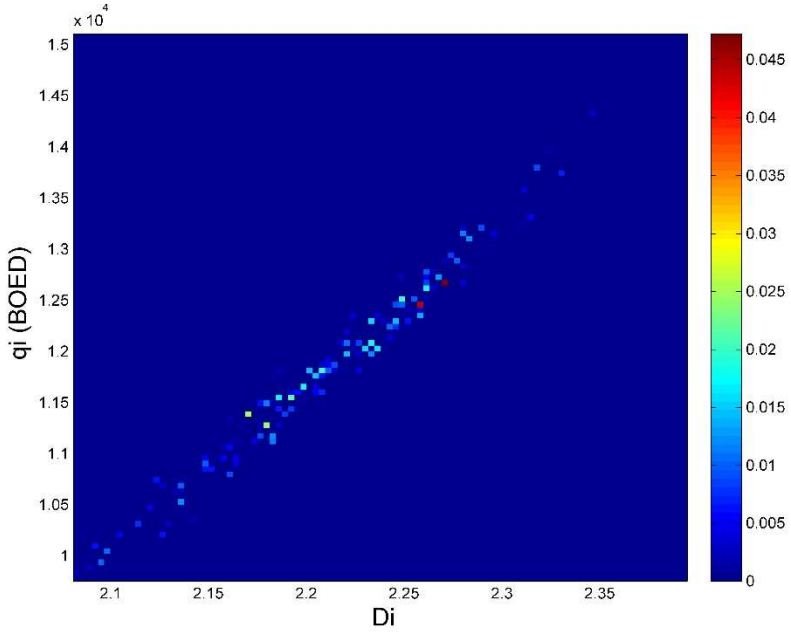

Fig. 207 — Relative frequency diagram between q_i and D_i of Well 20 using the PLE model

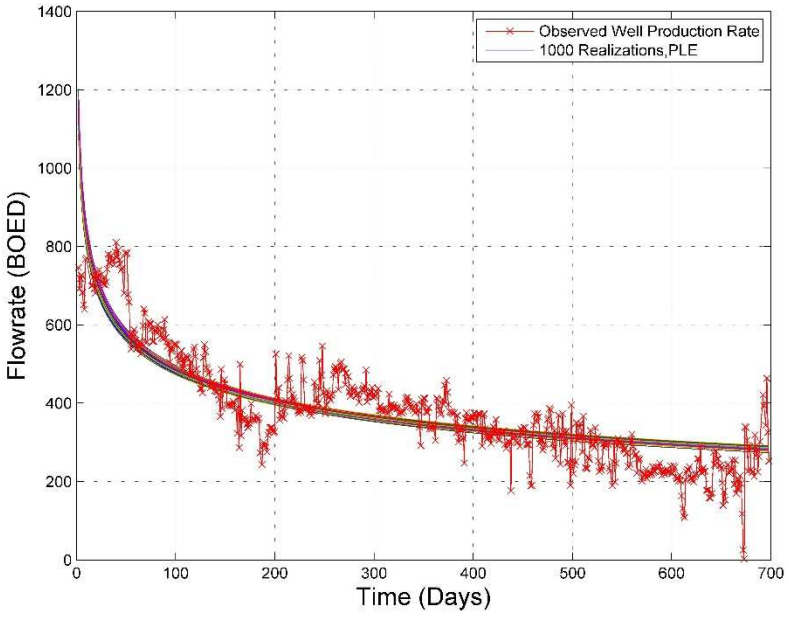

Fig. 208 — The 1,000 realizations of the model predictions using the Bayesian paradigm of Well 20 with the PLE model

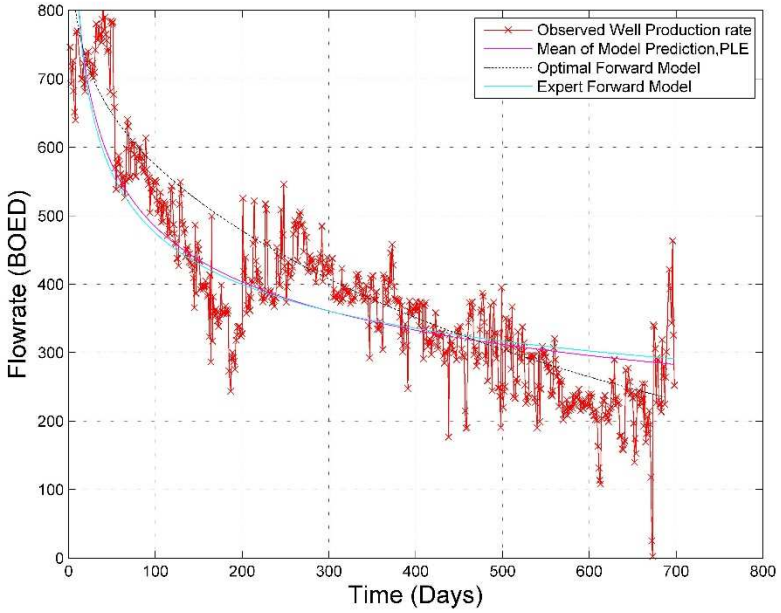

Fig. 209 — The production data with the mean of the realizations, the optimal forward model and the PLE model of Well 20

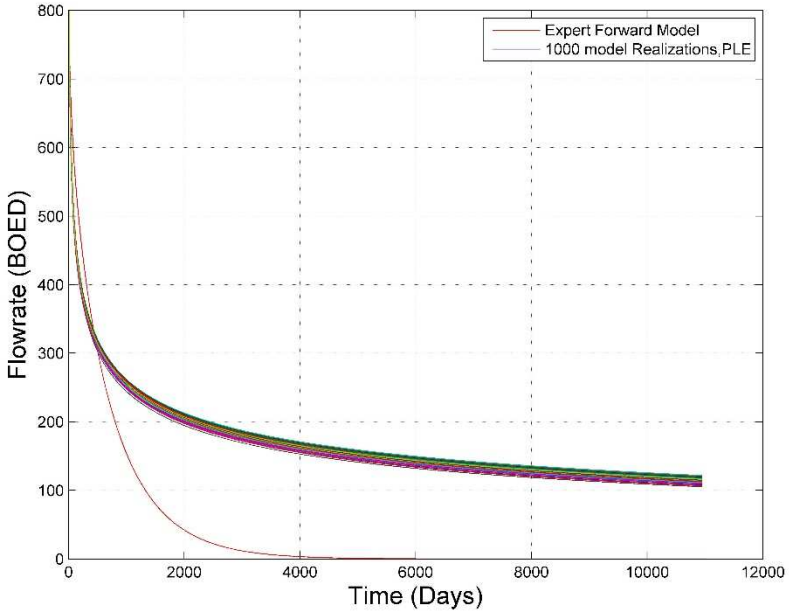

Fig. 210 — The 1,000 realizations of the model predictions using the Bayesian paradigm for 30 years of Well 20

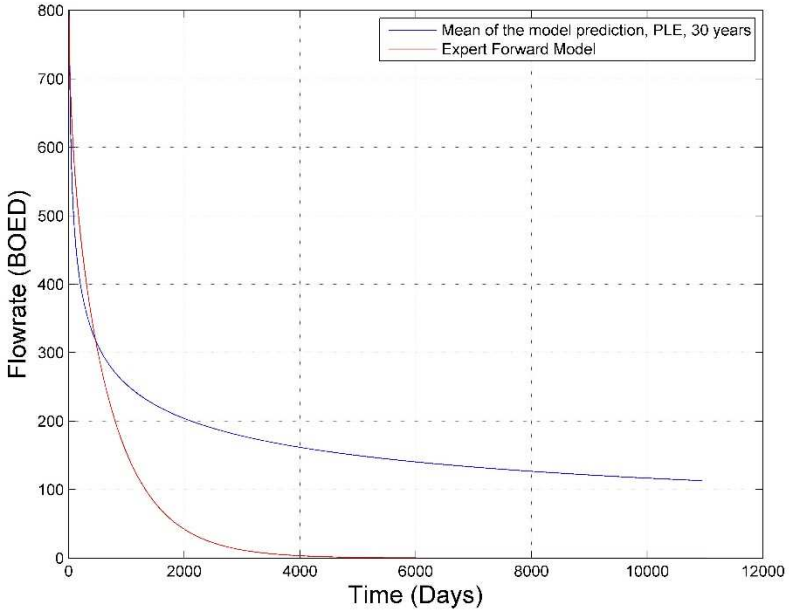

Fig. 211 — The mean of the realizations and the PLE model, plotted for 30 years for Well 20

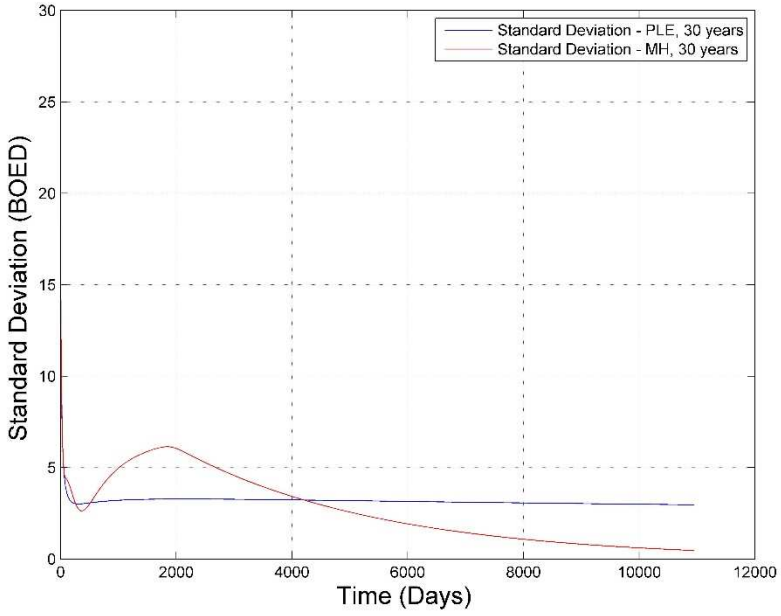

Fig. 212 — Comparison of the Standard Deviation of the two Bayesian forecasts using the MH and PLE models of Well 20

Analysis

The MCMC results of Well 20's three parameters converge after two million iterations when using the MH model, as seen in **Fig. 170**, **172** and **174**. This is an excellent example of the behavior expected when performing the MCMC on a given parameter. We applied the burn-in point and notice that the posterior distribution of the three parameters follow the similar distributions. We see a Gaussian distribution for both b and q_i in **Fig. 176** and **180**, however see more of a lognormal distribution for D_i (**Fig. 178**). This is consistent with the behavior of D_i for Well 19 PLE model, which is even more interesting because the two values of D_i have different meanings.

If we compare these MCMC results with the results produced when applying the PLE model, we notice that that model does not converges for any of the parameters (n, D_i, q_i) shown in **Fig. 193**, **195** and **197**, respectively, after 10 million iterations. Since none of the parameters converge, we do not obtain a clean mean, therefore the posterior distributions are incorrect. The n, D_i and q_i posteriors show a type of distribution (**Fig. 199, 201** and **203**, respectively**)**, however these distributions do not tell us much about the posterior.

In this instance, it is evident that Well 20 does not follow the PLE model. None of the three parameters converge, though the code ran for 10 million iterations and did not converge. The relative frequency histograms of the MH results show beautiful correlations between the parameters, however, unfortunately, the PLE results yield no information. The explanation can be that the well's production data is not following the PLE model, which is also visible in the unlikely results of EUR, n, D_i and q_i from the initial DCA work, presented in Table 2. The PLE relative frequency histograms are presented in **Fig. 205**, **206** and **207**.

Finally we reach the realizations of the Bayesian paradigm using the MH and PLE models. In this well's case, the results of the MH model are ideal, as presented in Fig. 196.

However, we cannot have faith in the results of the PLE model, and this is evident with the representation of the mean of the realizations. The curve created while implementing the Bayesian paradigm does not fit the data in the least, and neither does the curve of the forward model PLE results, seen in **Fig. 209**. However, the curve of the optimized results does capture a better trend of the data, which is an interesting result.

The graph that compares the standard deviations of the two sets of Bayesian results, **Fig. 212**, shows that the uncertainty of the PLE model remains constant as the uncertainty of the MH model decrease with time. From this result, and the inconclusive results of the PLE, I would say that this well follows the MH model. Furthermore, it is evident that the Bayesian implementation gives a more realistic decline than the forward model, and when comparing the mean of realizations against the forward model, in this case the MH model, it is evident that the forward model is underestimating the reserves (Fig. 198).

APPENDIX V

RESULTS AND ANALYSIS OF WELL 24

Well 24 – Modified Hyperbolic Model

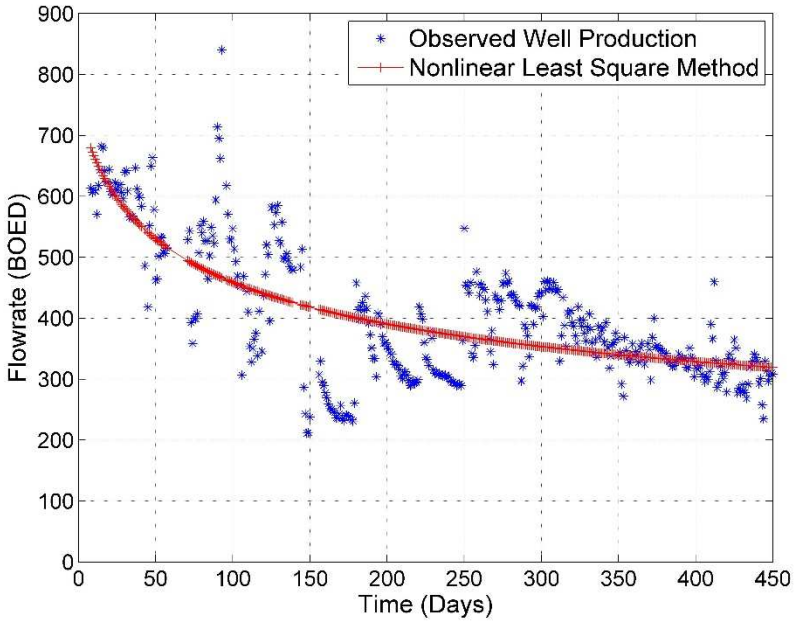

Fig. 213 — Results of the least squares optimization against the production data of Well 24 for the MH Model

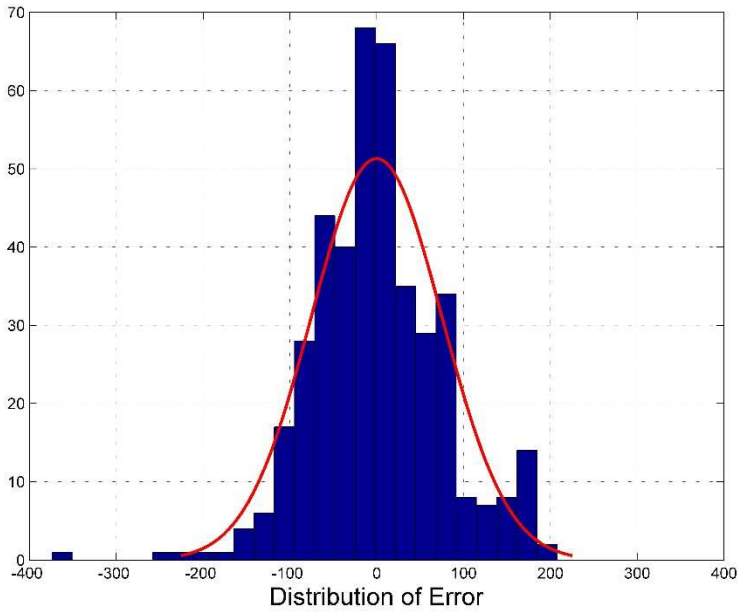

Fig. 214 — The distribution of error between the production data and the LSQ results for Well 24 for the MH Model

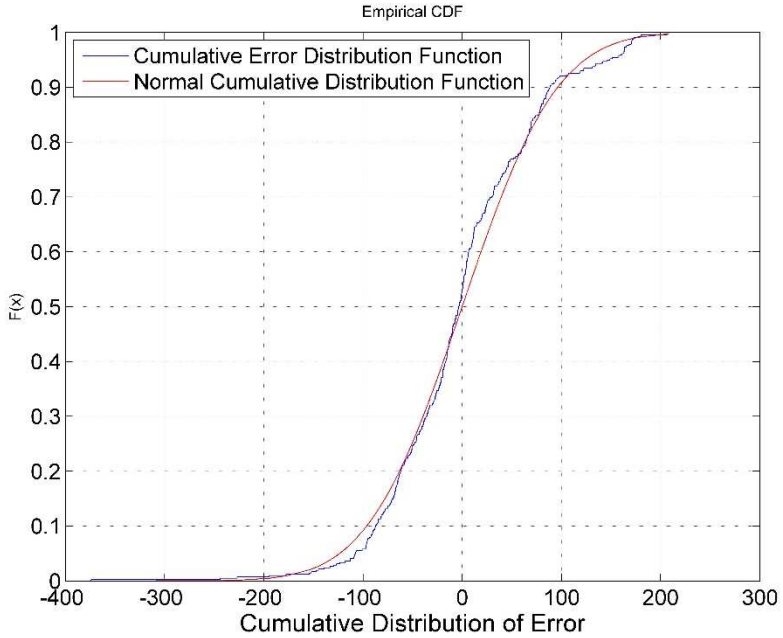

Fig. 215 — The cumulative distribution of error is plotted against the normal cumulative distribution function of Well 24 for the MH Model

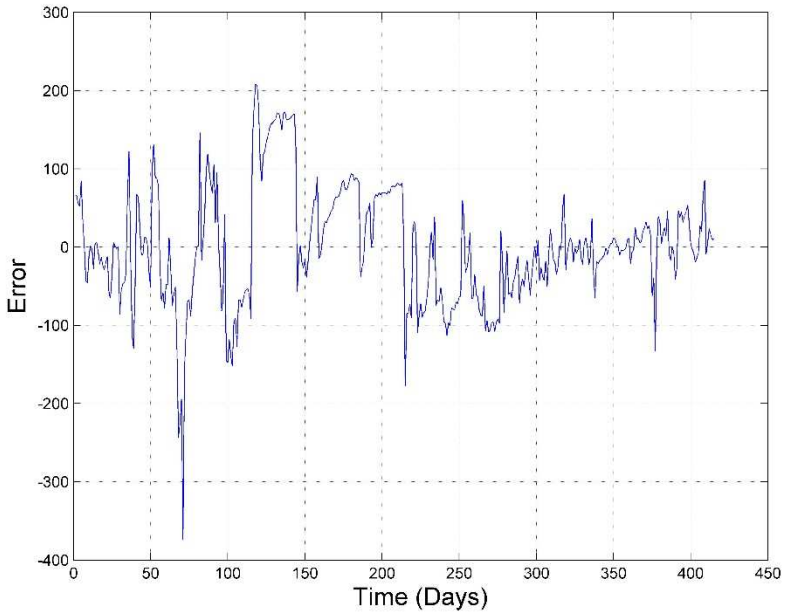

Fig. 216 — The error of the least squares optimization against the number of production days of Well 24 for the MH Model

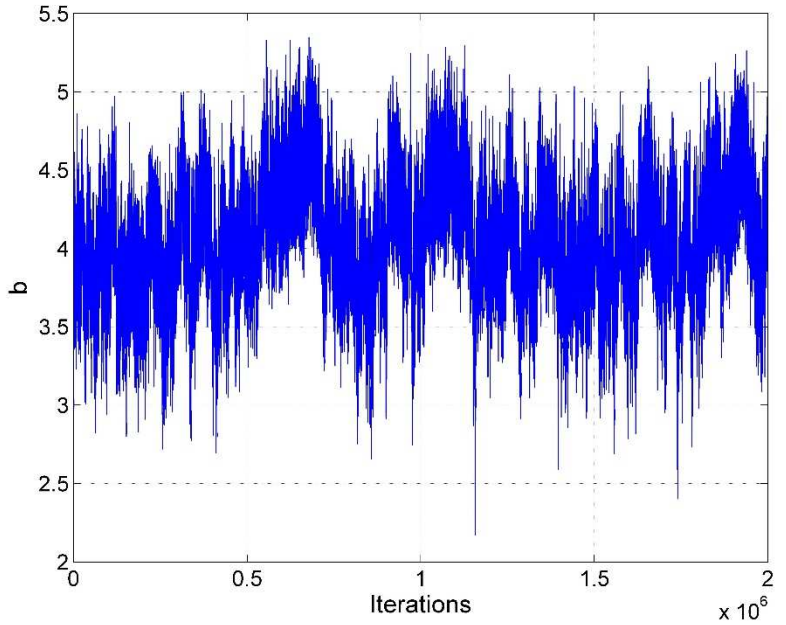

Fig. 217 — MCMC results of the *b*-factor for the MH model of Well 24 using the MH model

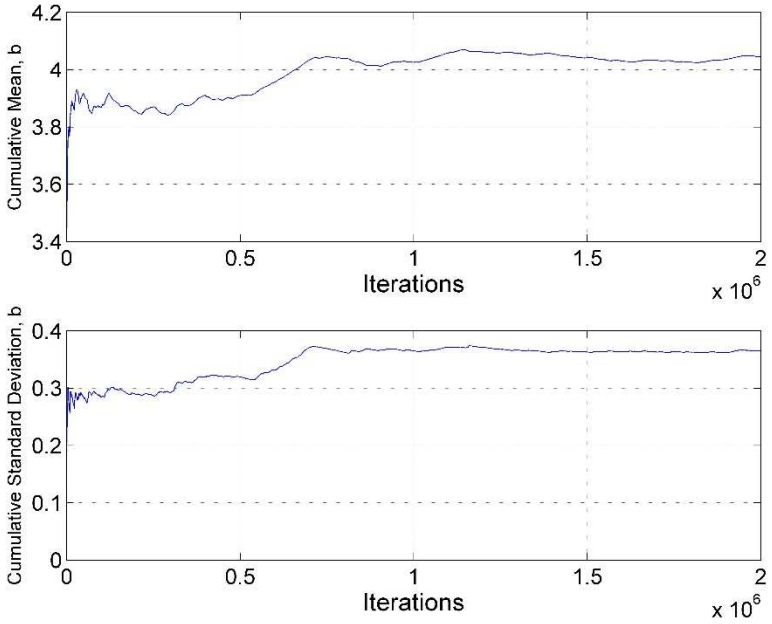

Fig. 218 — Cumulative mean and standard deviation of the *b*-factor of Well 24 using the MH model

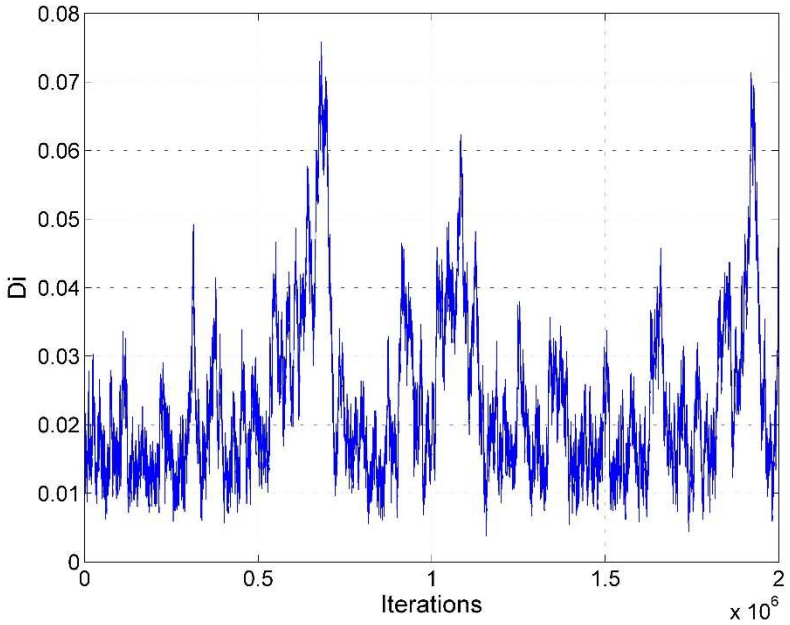

Fig. 219 — MCMC results of D_i for the MH model of Well 24 using the MH model

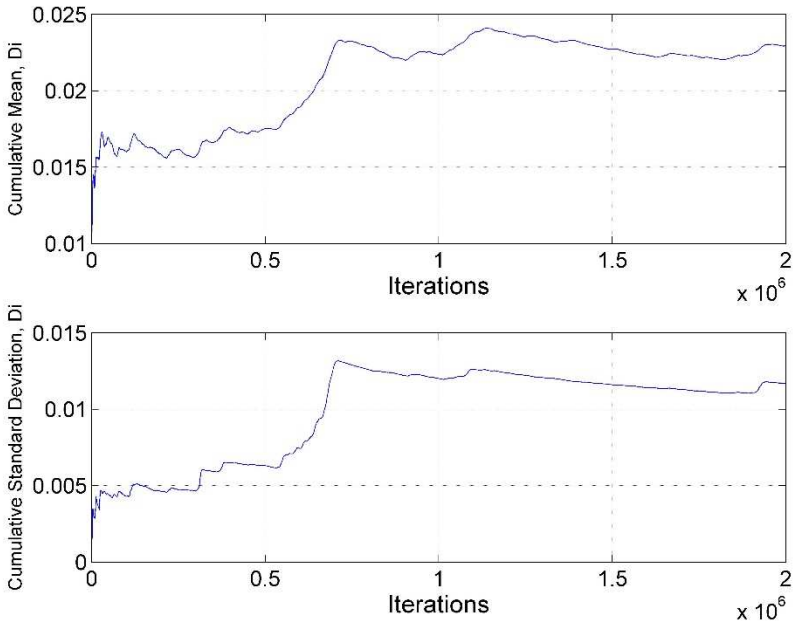

Fig. 220 — Cumulative mean and standard deviation of D_i of Well 24 using the MH model

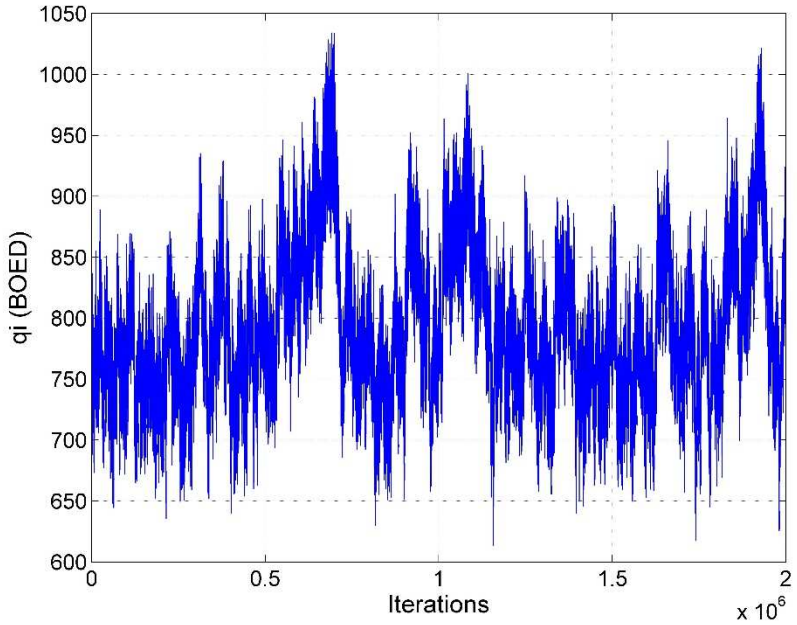

Fig. 221 — MCMC results of q_i for the MH model of Well 24 using the MH model

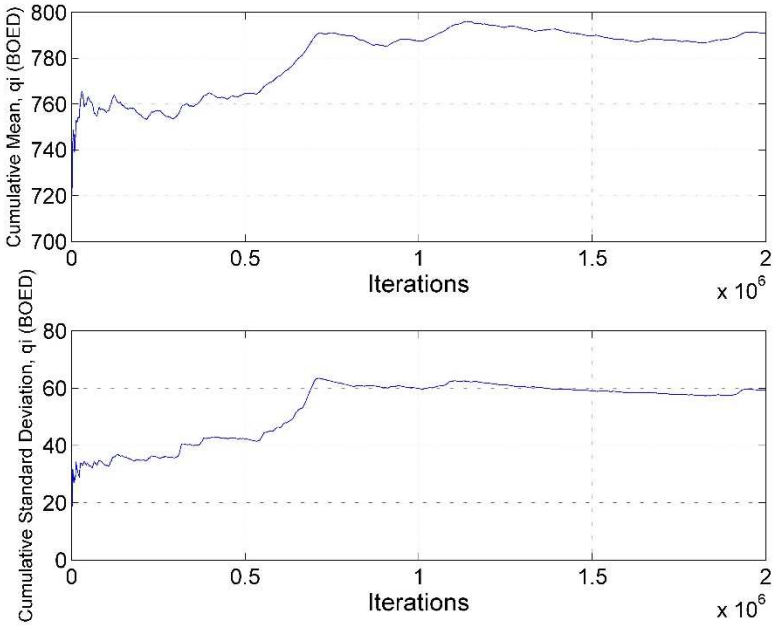

Fig. 222 — Cumulative mean and standard deviation of q_i of Well 24 using the MH model

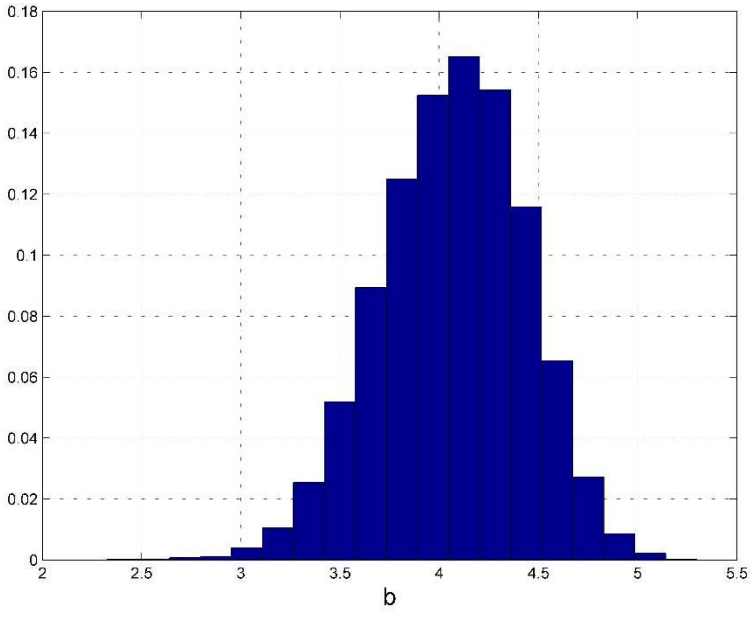

Fig. 223 — Posterior relative frequency histogram of *b* of Well 24 using the MH model

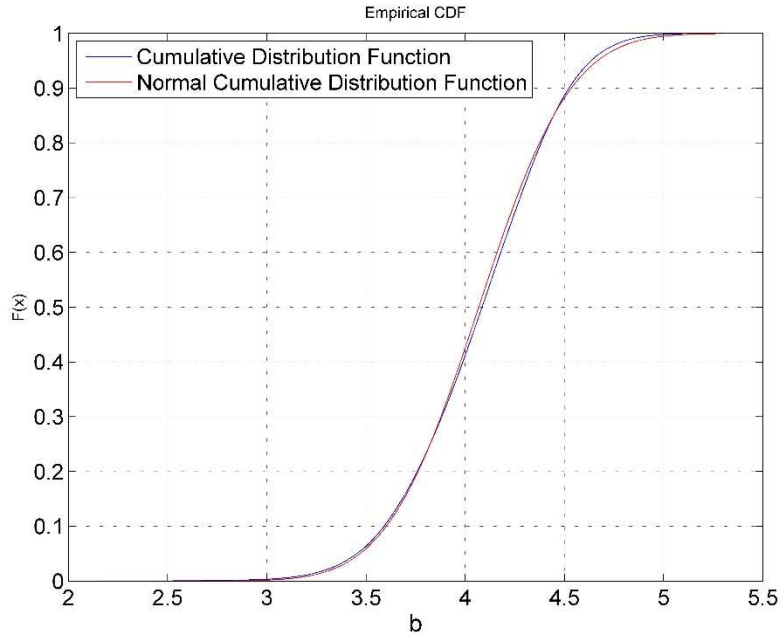

Fig. 224 — Cumulative posterior relative frequency histogram of the *b*-factor of Well 24 using the MH model

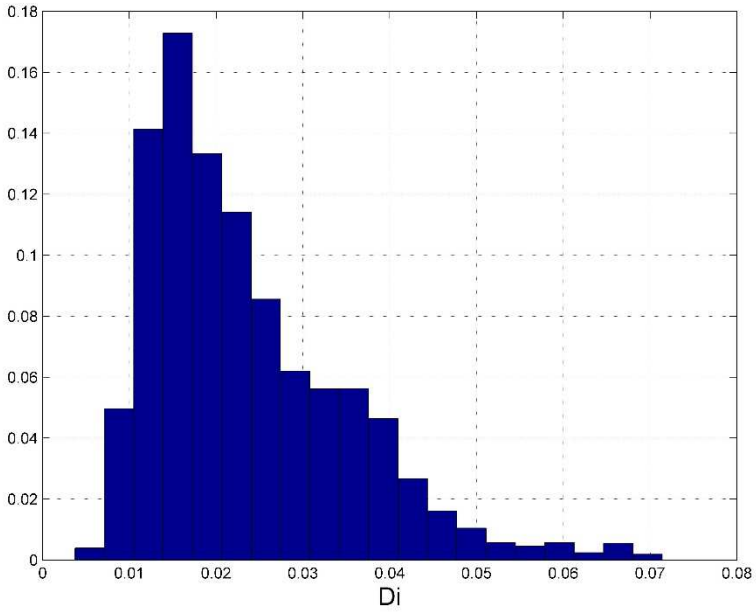

Fig. 225 — Posterior relative frequency histogram of D_i of Well 24 using the MH model

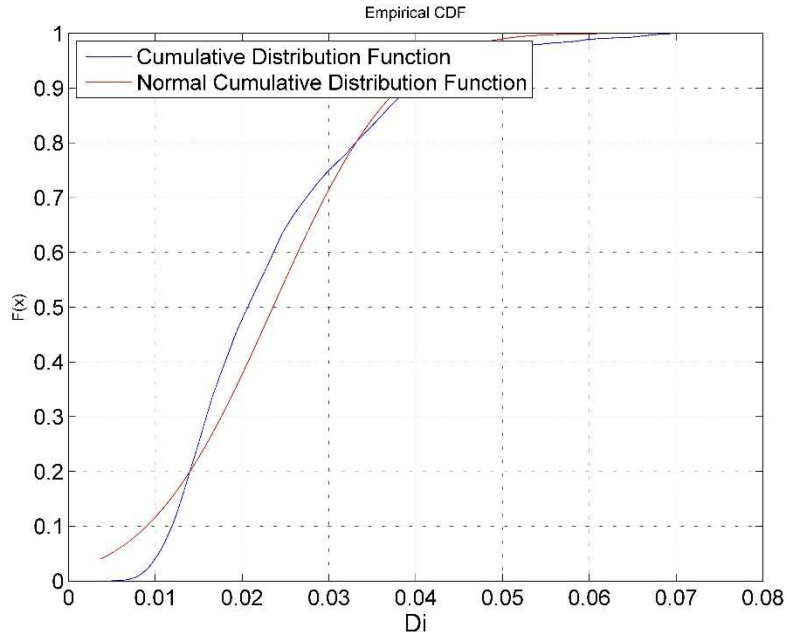

Fig. 226 — Cumulative posterior relative frequency histogram of D_i of Well 24 using the MH model

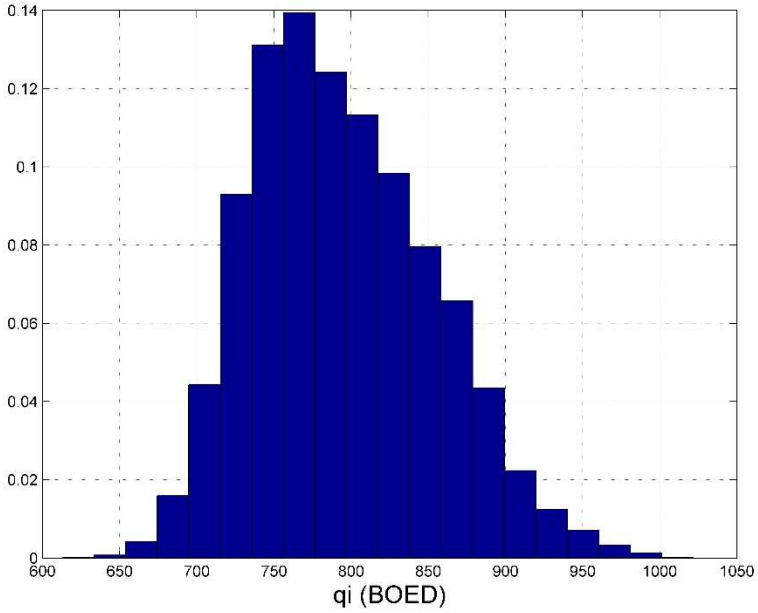

Fig. 227 — Posterior relative frequency histogram of q_i of Well 24 using the MH model

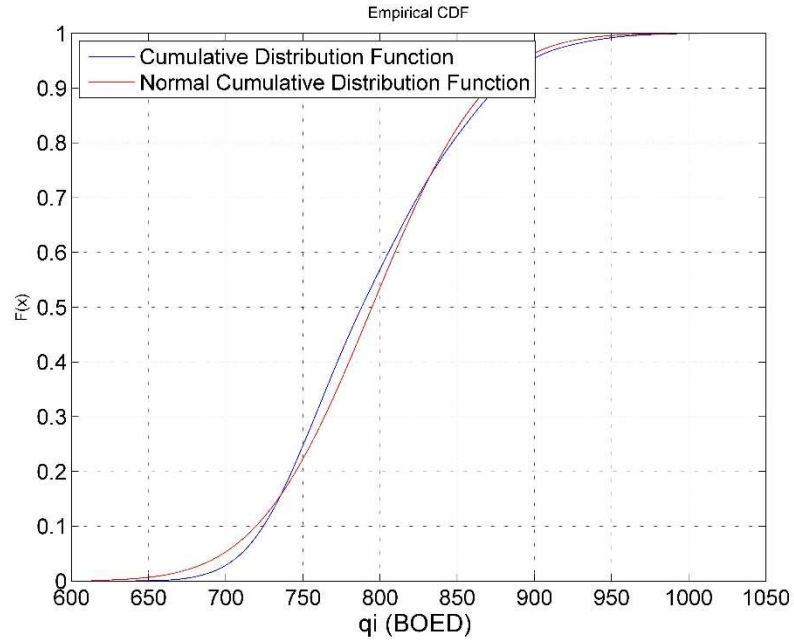

Fig. 228 — Cumulative posterior relative frequency histogram of q_i of Well 24 using the MH model

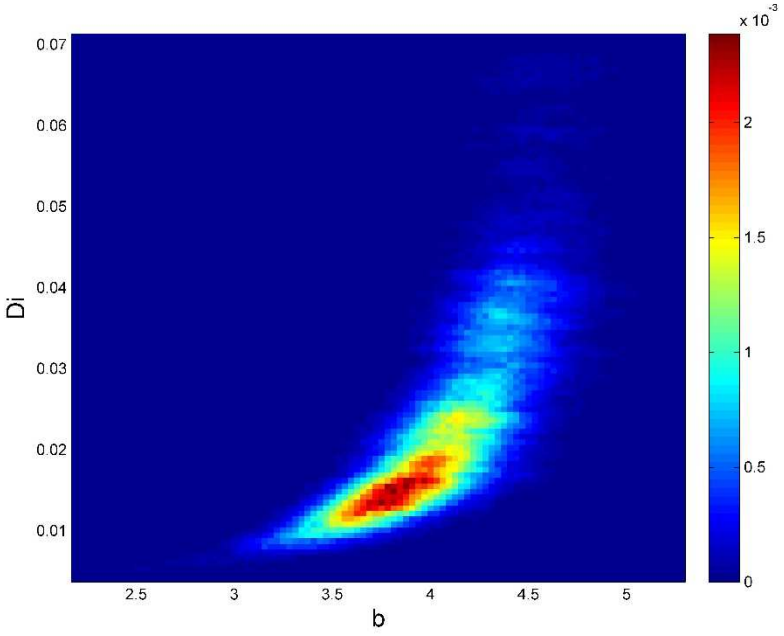

Fig. 229 — Relative frequency diagram between D_i and b of Well 24 using the MH model

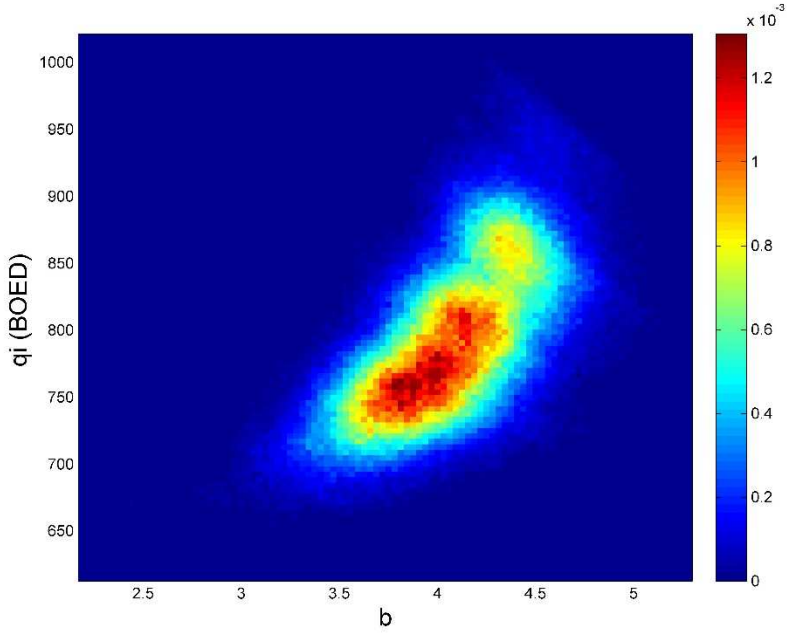

Fig. 230 — Relative frequency diagram between q_i and b of Well 24 using the MH model

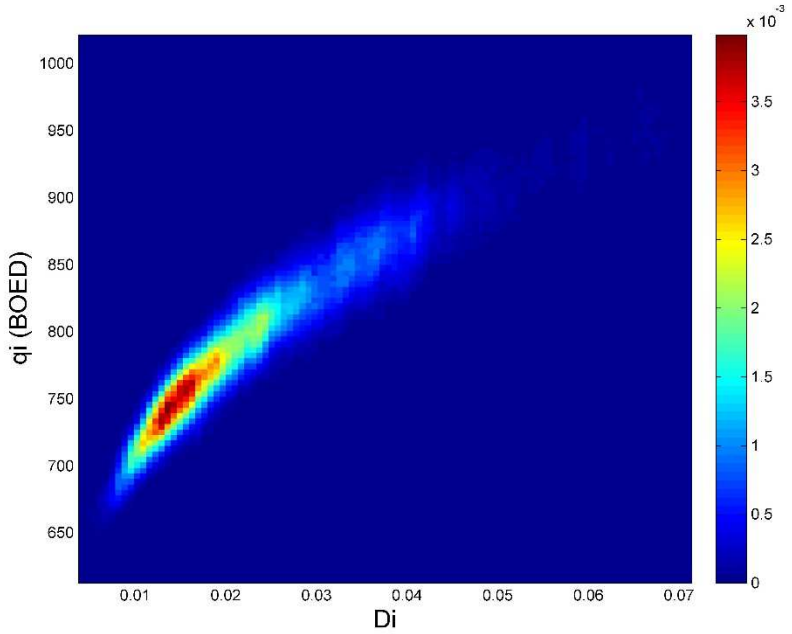

Fig. 231 — Relative frequency diagram between q_i and D_i of Well 24 using the MH model

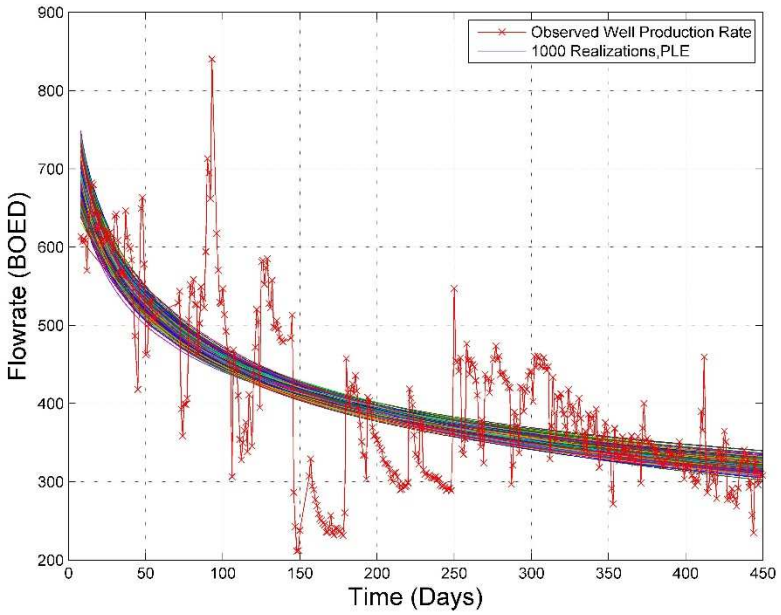

Fig. 232 — The 1,000 realizations of the model predictions using the Bayesian paradigm of Well 24 with the MH model

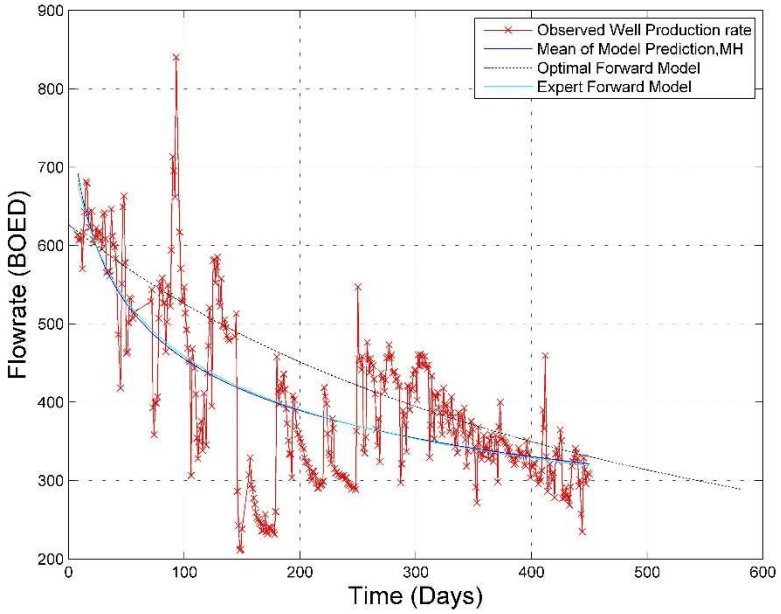

Fig. 233 — The production data with the mean of the realizations, the optimal forward model and the MH model of Well 24

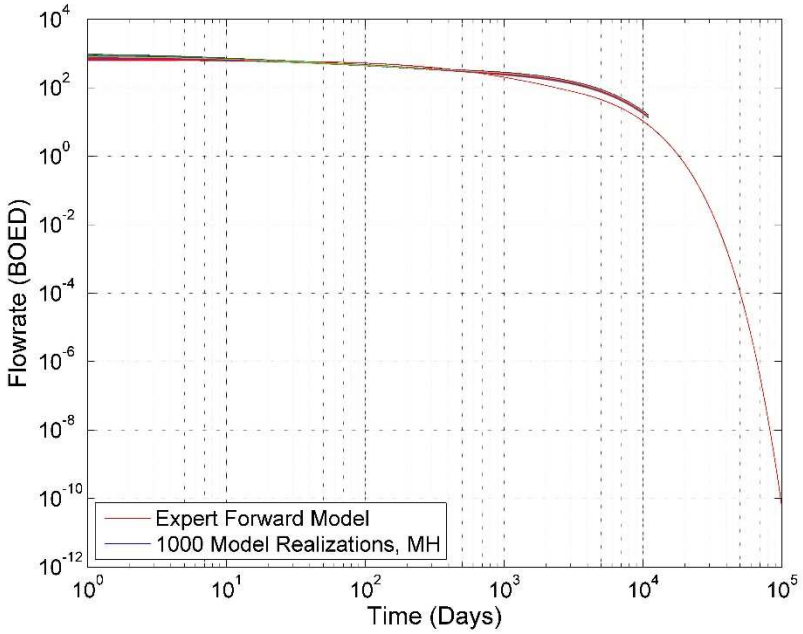

Fig. 234 — The 1,000 realizations of the model predictions using the Bayesian paradigm for 30 years of Well 24

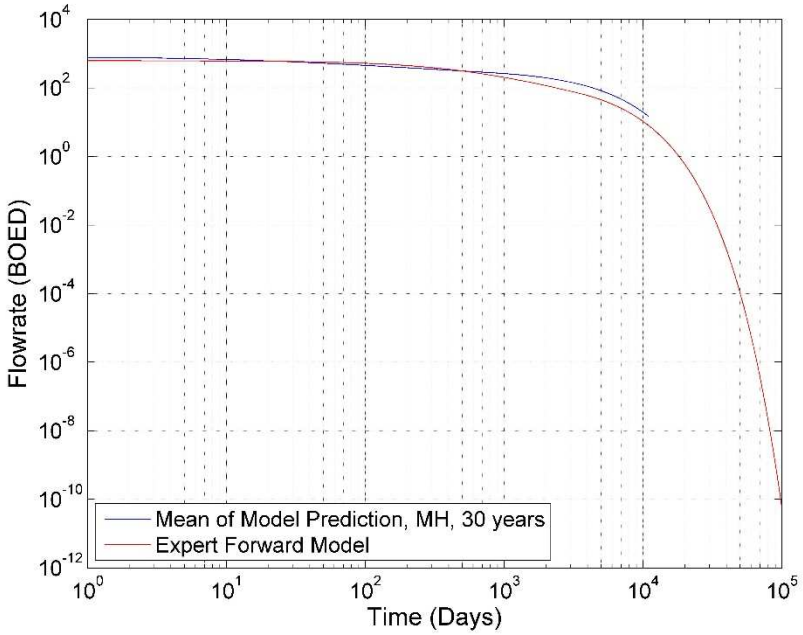

Fig. 235 — The mean of the realizations and the MH model, plotted for 30 years for Well 24

Well 24 – Power Law Exponential Model

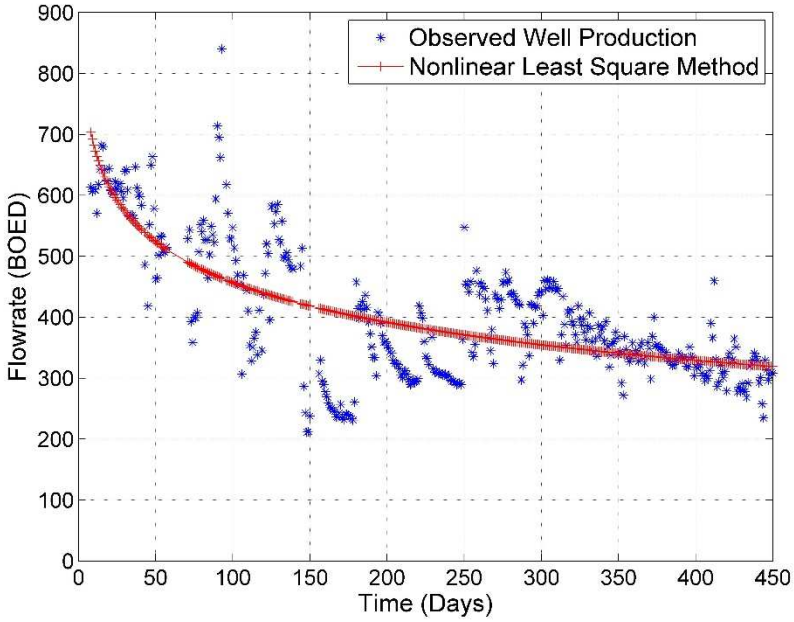

Fig. 236 — Results of the least squares optimization against the production data of Well 19 for the PLE Model

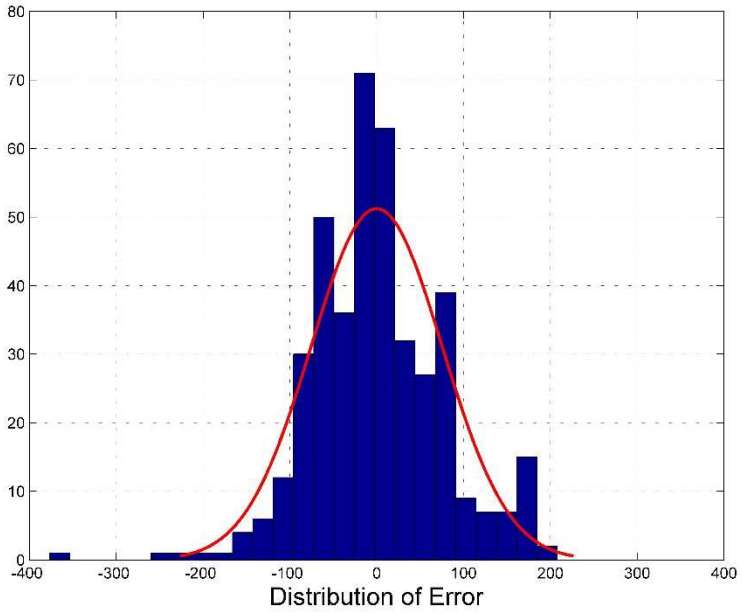

Fig. 237 — The distribution of error between the production data and the LSQ results for Well 24 for the PLE Model

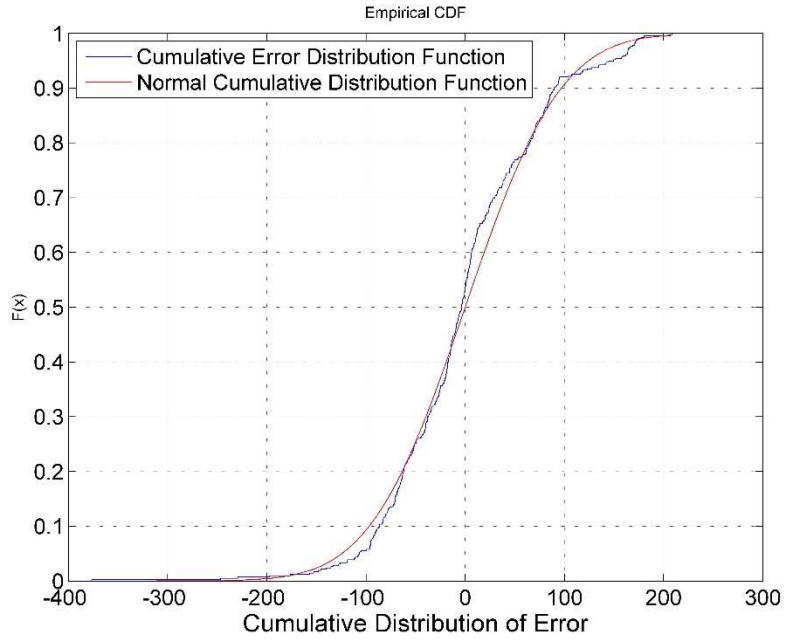

Fig. 238 — The cumulative distribution of error is plotted against the normal cumulative distribution function of Well 24 for the PLE Model

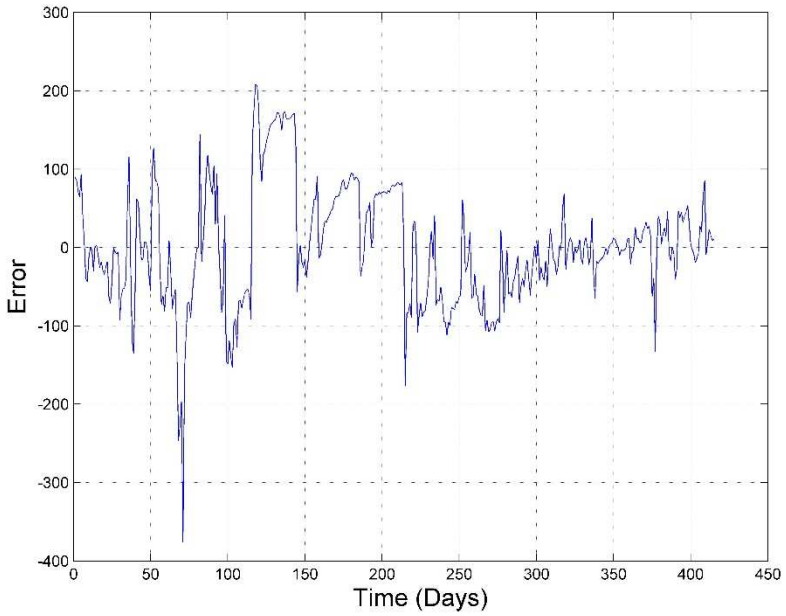

Fig. 239 — The error of the least squares optimization against the number of production days of Well 24 for the PLE Model

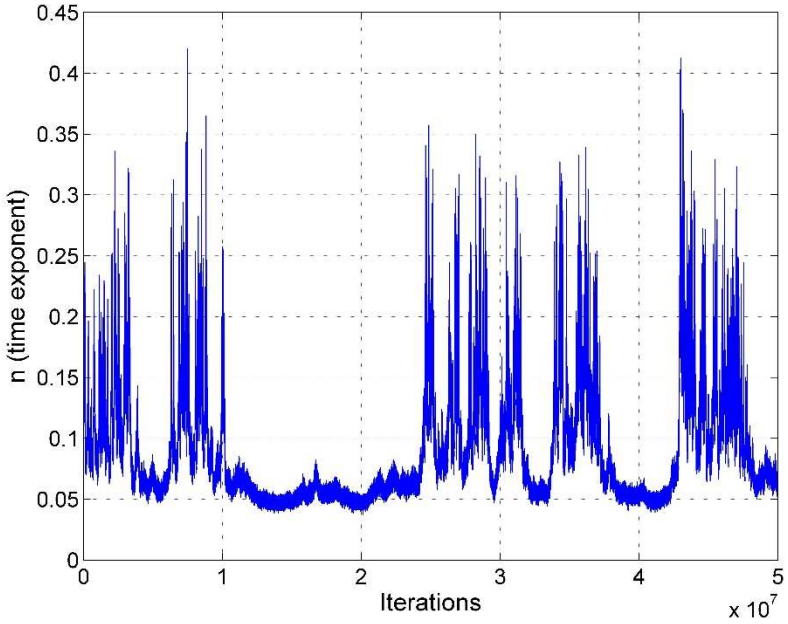

Fig. 240 — MCMC results of *n* for the PLE model of Well 24

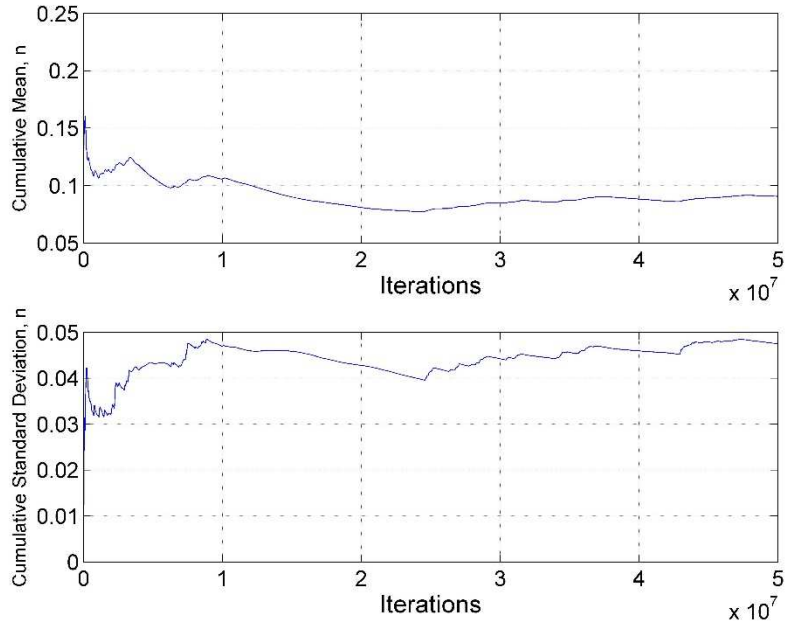

Fig. 241 — Cumulative mean and standard deviation of *n* of Well 24 using the PLE model

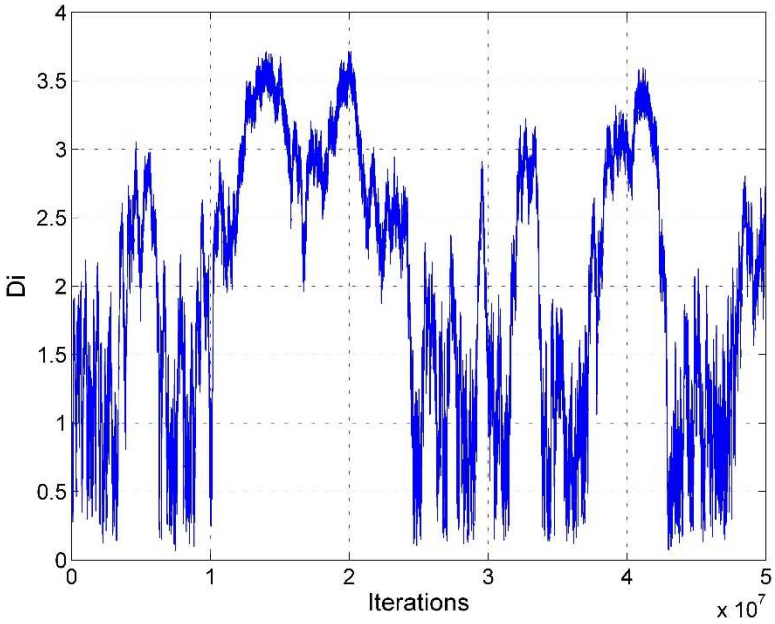

Fig. 242 — MCMC results of D_i for the MH model of Well 24 using the PLE model

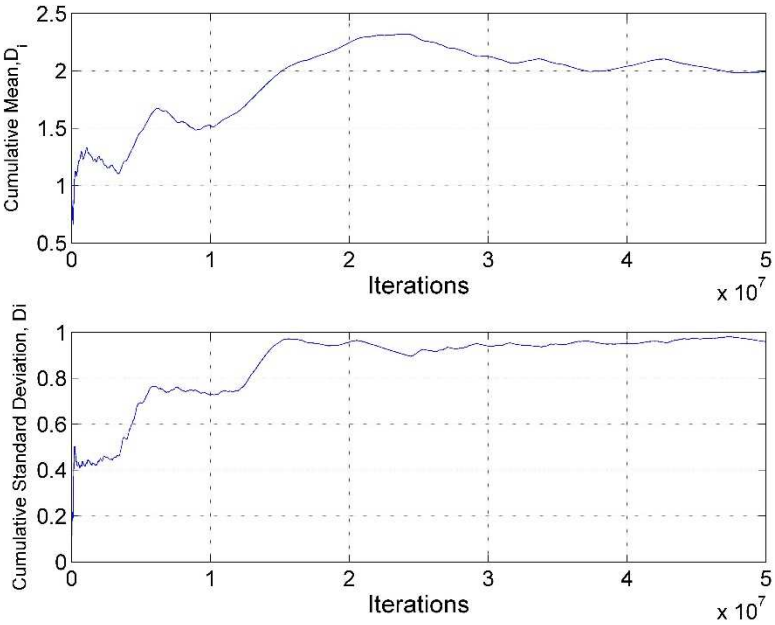

Fig. 243 — Cumulative mean and standard deviation of D_i of Well 24 using the PLE model

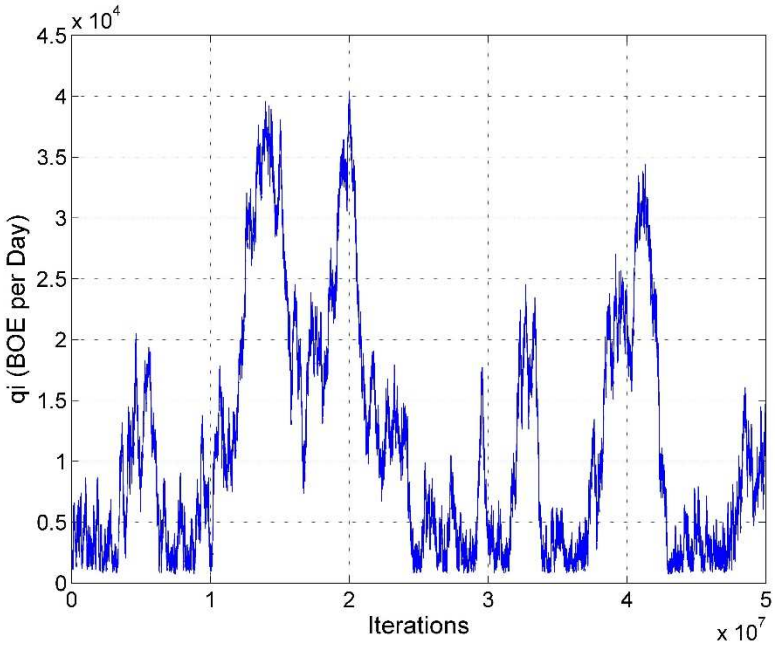

Fig. 244 — MCMC results of q_i for the MH model of Well 24 using the PLE model

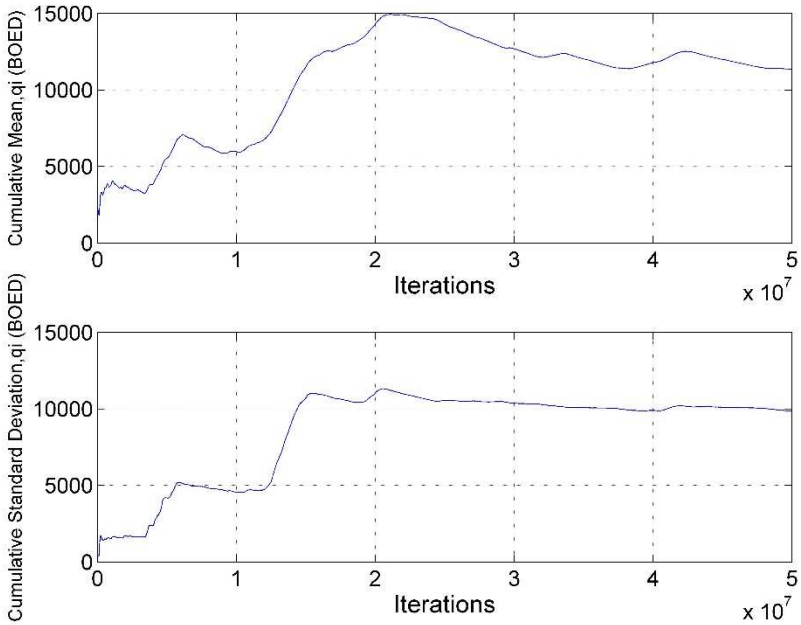

Fig. 245 — Cumulative mean and standard deviation of q_i of Well 24 using the PLE model

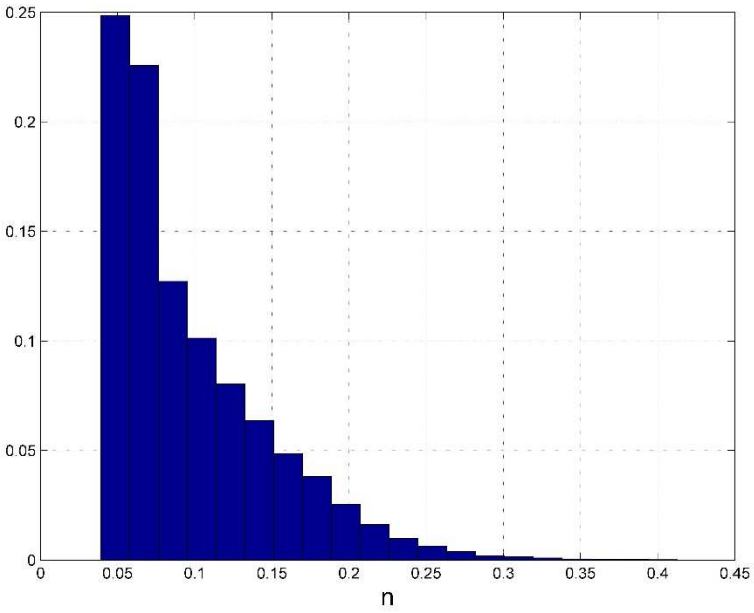

Fig. 246 — Posterior relative frequency histogram of *n* of Well 24 using the PLE model

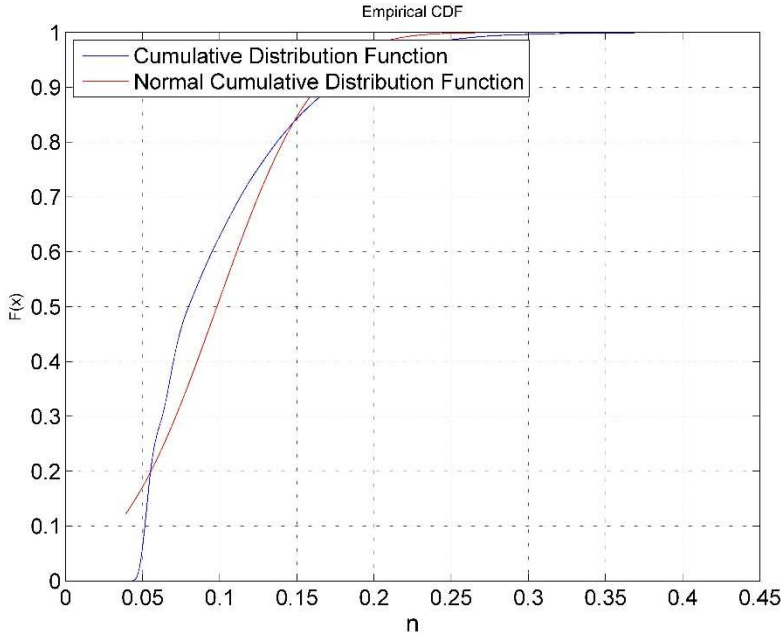

Fig. 247 — Cumulative posterior relative frequency histogram of *n* of Well 24 using the PLE model

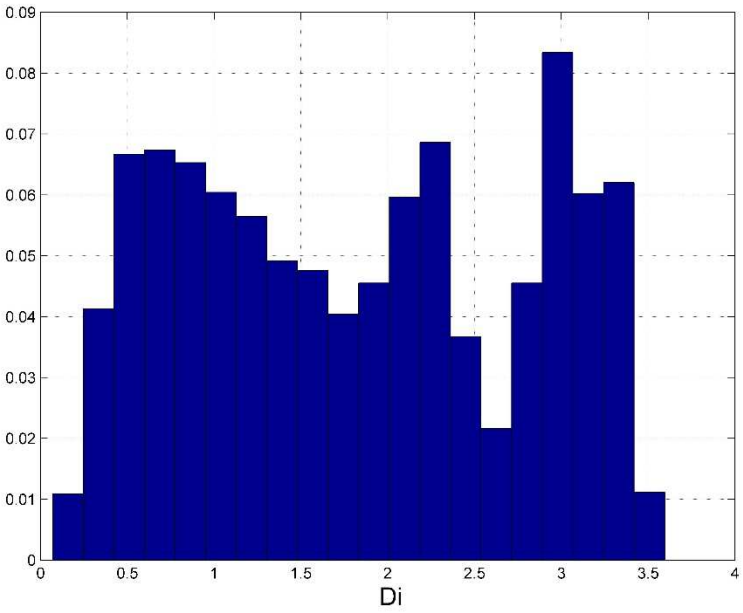

Fig. 248 — Posterior relative frequency histogram of D_i of Well 24 using the PLE model

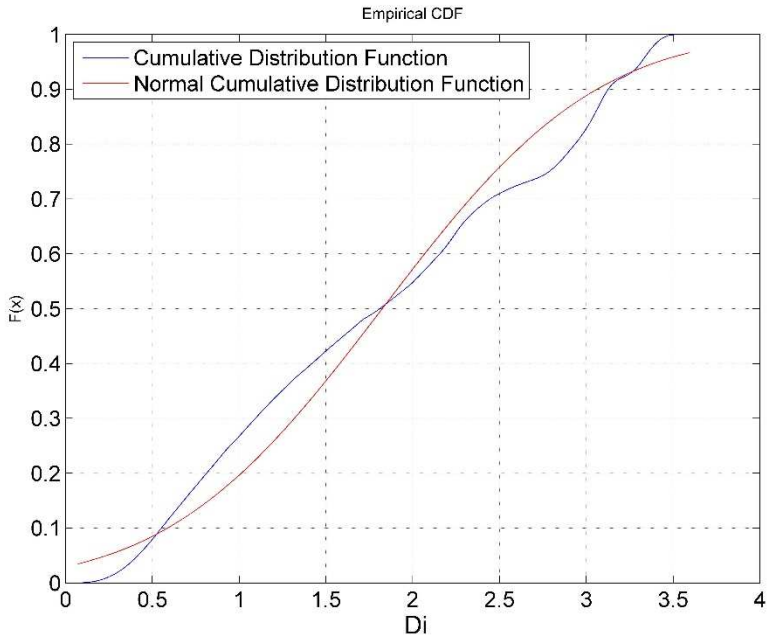

Fig. 249 — Cumulative posterior relative frequency histogram of D_i of Well 24 using the PLE model

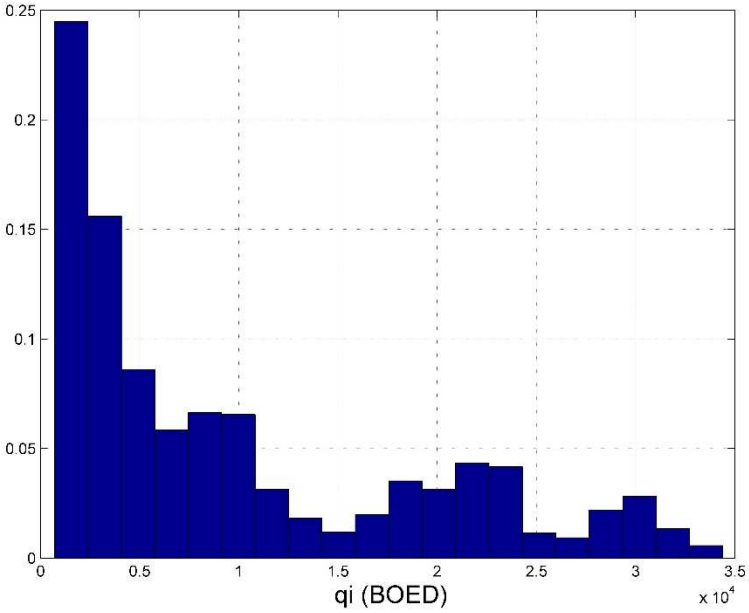

Fig. 250 — Posterior relative frequency histogram of q_i of Well 24 using the PLE model

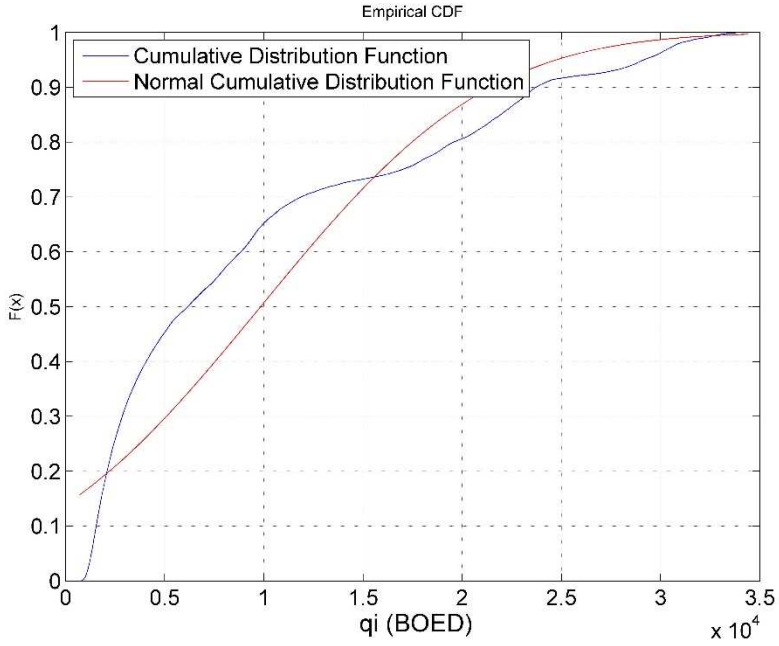

Fig. 251 — Cumulative posterior relative frequency histogram of q_i of Well 24 using the PLE model

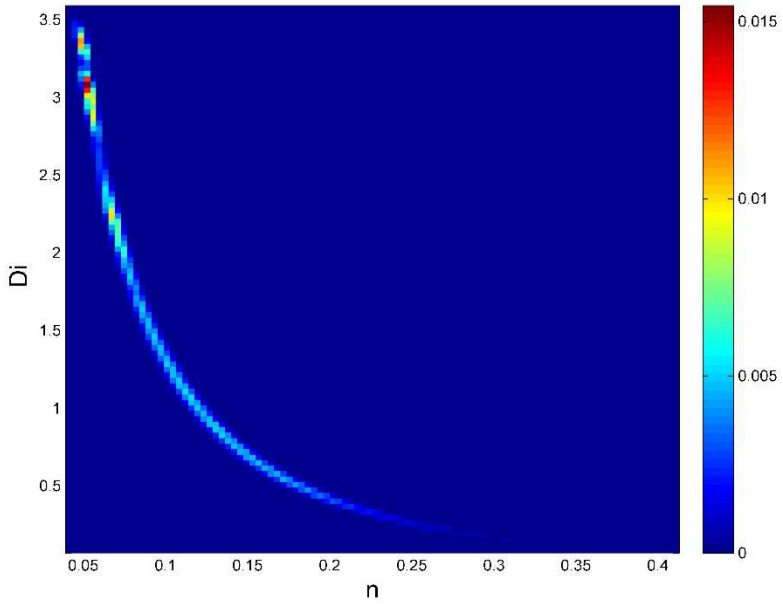

Fig. 252 — Relative frequency diagram between D_i and n of Well 24 using the PLE model

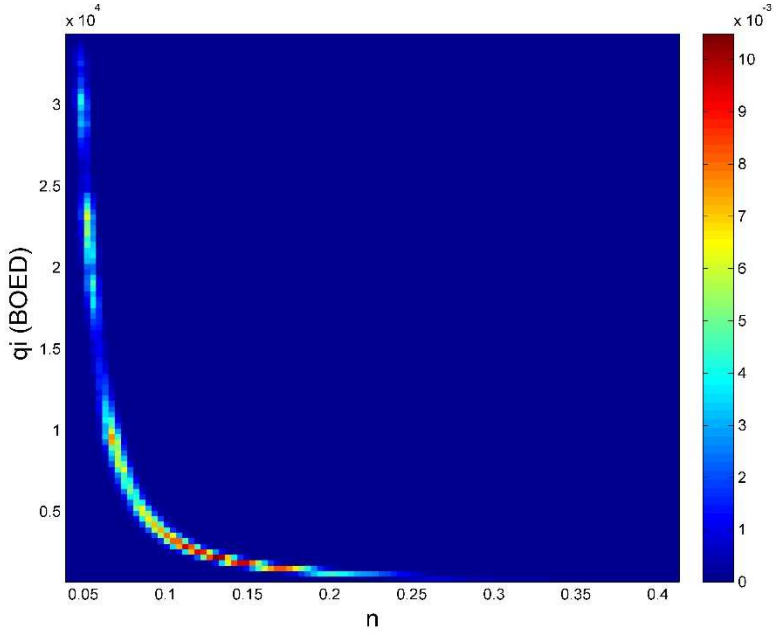

Fig. 253 — Relative frequency diagram between q_i and n of Well 24 using the PLE model

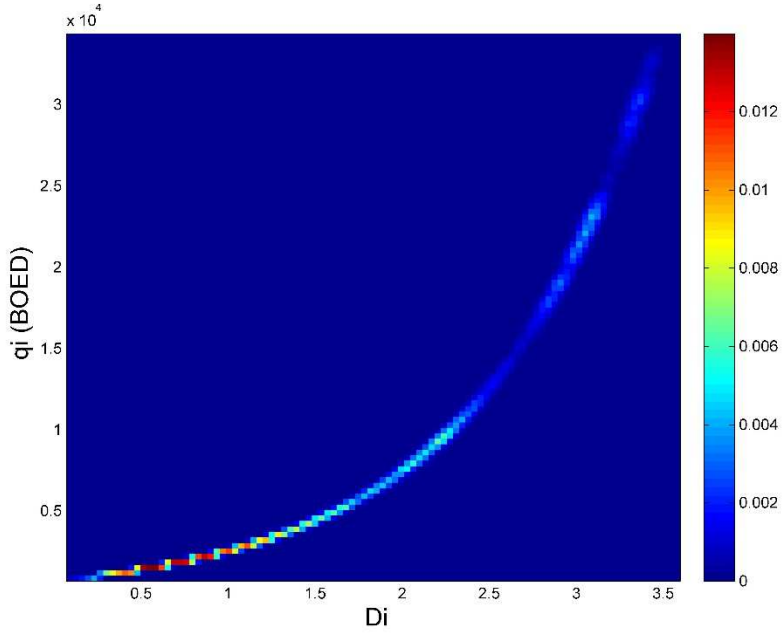

Fig. 254 — Relative frequency diagram between q_i and D_i of Well 24 using the PLE model

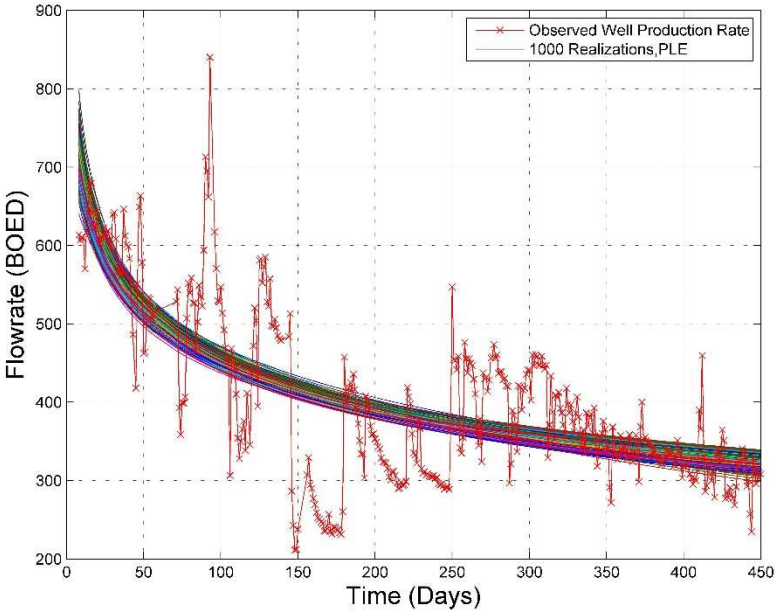

Fig. 255 — The 1,000 realizations of the model predictions using the Bayesian paradigm of Well 24 with the PLE model

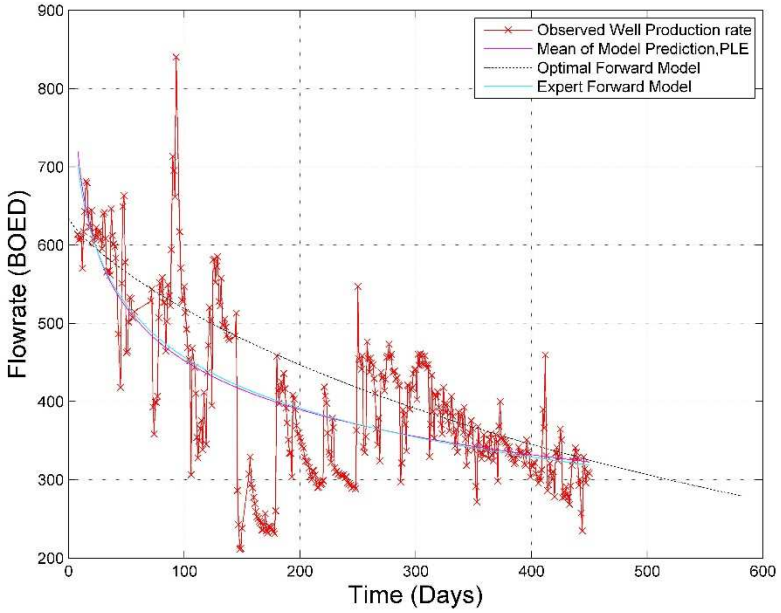

Fig. 256 — The production data with the mean of the realizations, the optimal forward model and the PLE model of Well 24

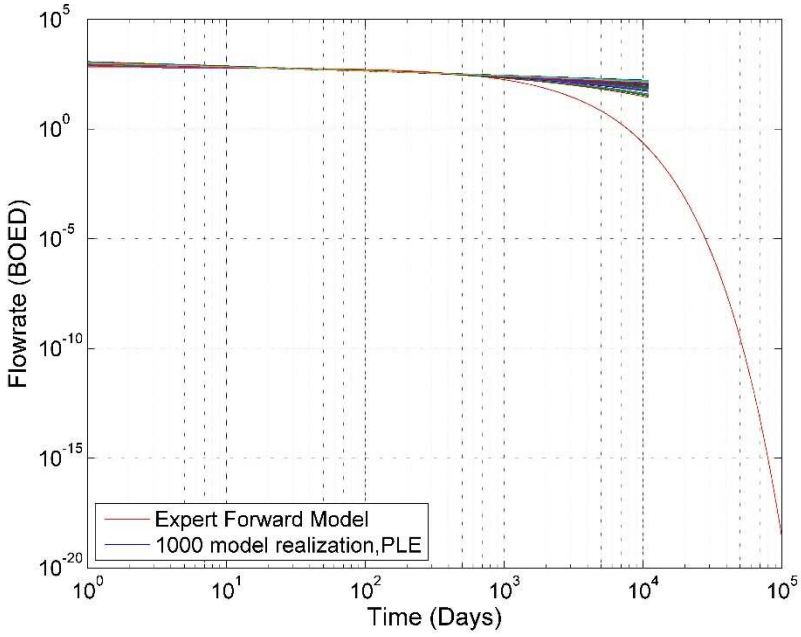

Fig. 257 — The 1,000 realizations of the model predictions using the Bayesian paradigm for 30 years of Well 24

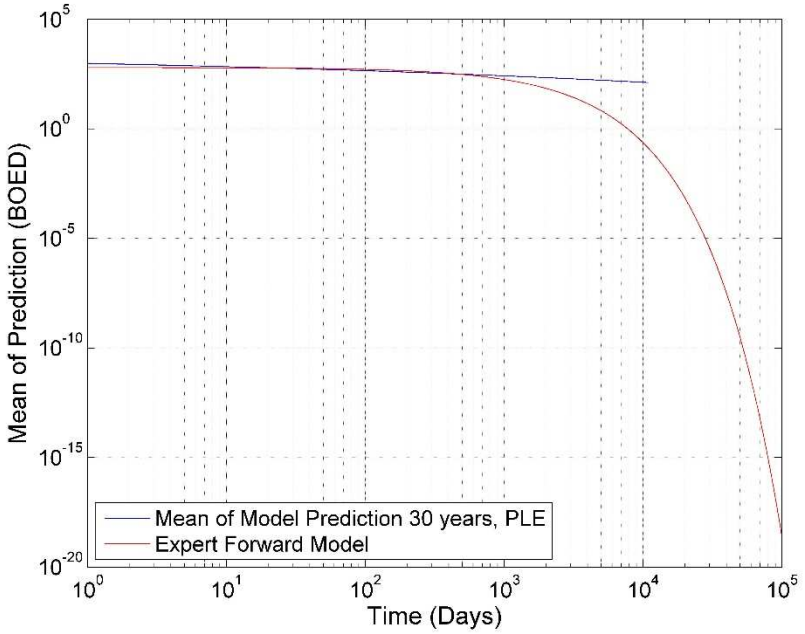

Fig. 258 — The mean of the realizations and the PLE model, plotted for 30 years for Well 24

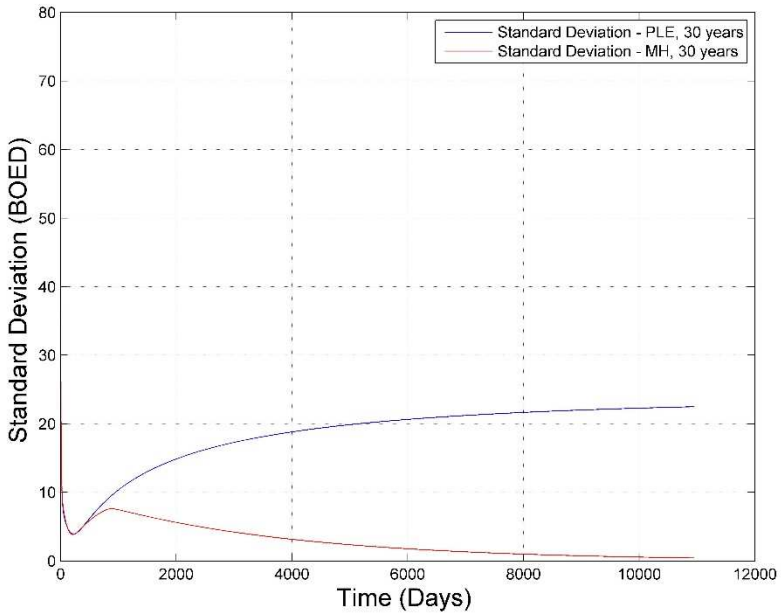

Fig. 259 — Comparison of the Standard Deviation of the two Bayesian forecasts using the MH and PLE models of Well 24

Analysis

Well 24 is an interesting case because there is a lot of disruption in the production data. Though we cleaned the data before beginning the analysis, the truncation of the data, along with the different completions changes are challenges to apply any DCA, but also to obtain accurate results using the LSQ optimization and the Bayesian paradigm.

The MCMC results do not converge for any of the three parameters of the MH model, as seen in **Fig. 217**, **219** and **221**. The best conversion of the three parameters is the *b*-factor, shown in Fig. 236. Because of the lack of convergence of the three parameters, the posterior distribution of the three parameters is interesting. It seems that the posteriors of *b* and q_i, shown in **Fig. 223** and **227**, respectively, are trying to be normally distributed, but because of the lack of convergence, they are not. We do see a lognormal distribution of D_i in **Fig. 225**. This is consistent with the trend we have seen throughout this study.

When we compare these MCMC results with the results produced when applying the PLE model, we notice that that model does not converges for any of the three PLE parameters, shown in **Fig. 240**, **242** and **244**, after 50 million iterations. This is a very strange result because it is expected that after 50 million iterations, the parameters would converge. This may be due to the production data, but also to the data not following the PLE model. Due to the results of the MCMC, the posterior distributions for all three parameters are meaningless, seen in **Fig. 246**, **248** and **250**.

Based on the posterior distributions of the three parameters, we created the relative frequency histograms that show the relationship between two different parameters -- D_i vs. *b*, q_i vs. *b* and q_i vs D_i for the MH model and D_i vs. *n*, q_i vs. *n* and q_i vs D_i for the PLE model. These results can be seen in **Fig. 229, 230** and **231**, respectively, for the MH model and **Fig. 252, 253** and **254**, respectively, for the PLE model. The quality of the relative frequency histograms is based upon the quality of the posterior of the parameters, because it is just a representation of the two parameters against each other. From Fig. 252, 253 and

254, we see that because of the poor results due to the lack of convergence of all three parameters. However the trend of the relationship between the parameters is still visible. These are same results we have seen in other wells, and have encountered the same problem due to poor convergence of parameters. The PLE results of the relative frequency histograms do not show results.

Finally we reach the realizations of the Bayesian paradigm using the MH and PLE models. We notice when we plot the mean of the realizations versus the optimal forward model (the results from the LSQ optimization), and the expert forward model (either MH or PLE), the mean of the model prediction and the expert forward model often times have close values for the 700 days plotted. However, when we extend the results to 30 years that there is a divergence between two sets of results. In this case, the MH forward model underestimates the reserves, as seen in **Fig. 235** for the MH model and **Fig. 258** for the PLE model. Both models show that they underestimate the reserves.

Finally, the standard deviation comparison of the two sets of Bayesian results, **Fig. 259**, identifies the uncertainty of the two models. In the case of this well, the standard deviation is very interesting because it shows that the two models have the same uncertainty in early time, and then the uncertainty of the MH model decreases, while the uncertainty of the PLE model increases. This gives little faith in the results of the PLE model for this well.

APPENDIX VI

RESULTS AND ANALYSIS OF WELL 38

Well 38 – Modified Hyperbolic Model

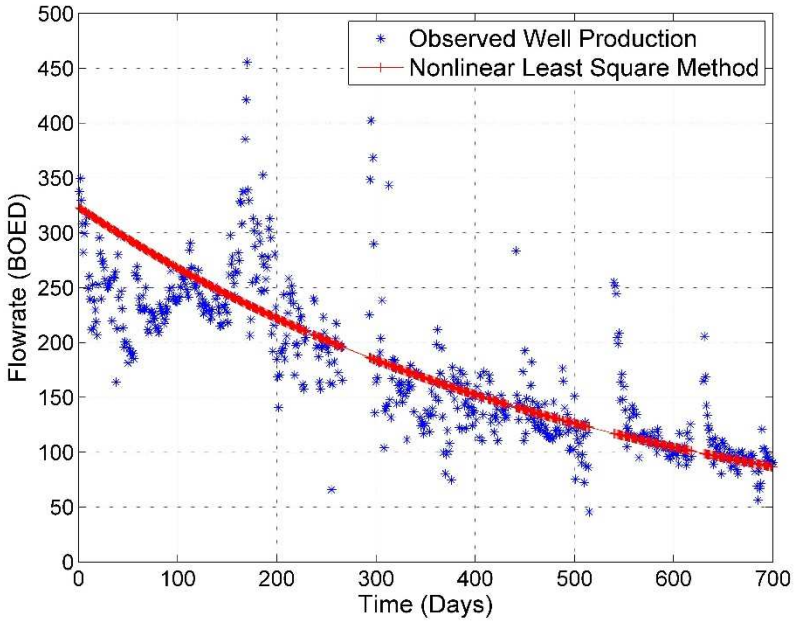

Fig. 260 — Results of the least squares optimization against the production data of Well 38 for the MH Model

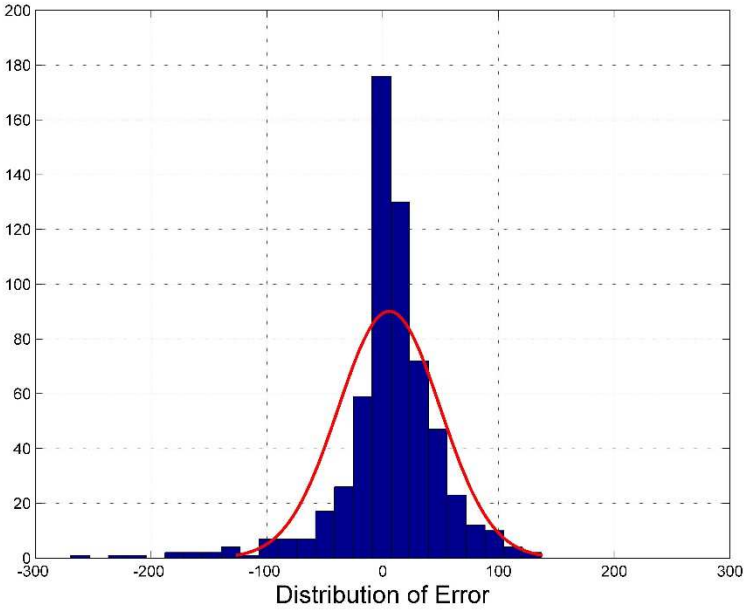

Fig. 261 — The distribution of error between the production data and the LSQ results for Well 38 for the MH Model

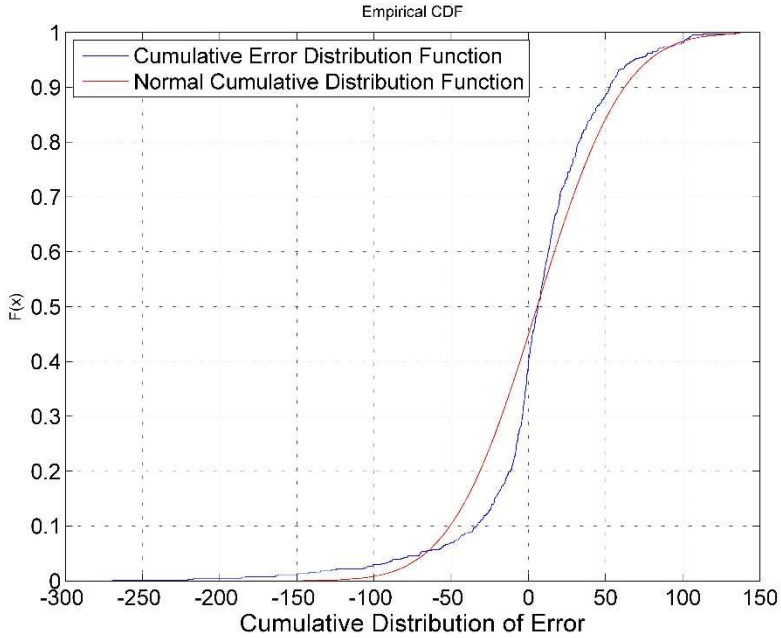

Fig. 262 — The cumulative distribution of error is plotted against the normal cumulative distribution function of Well 38 for the MH Model

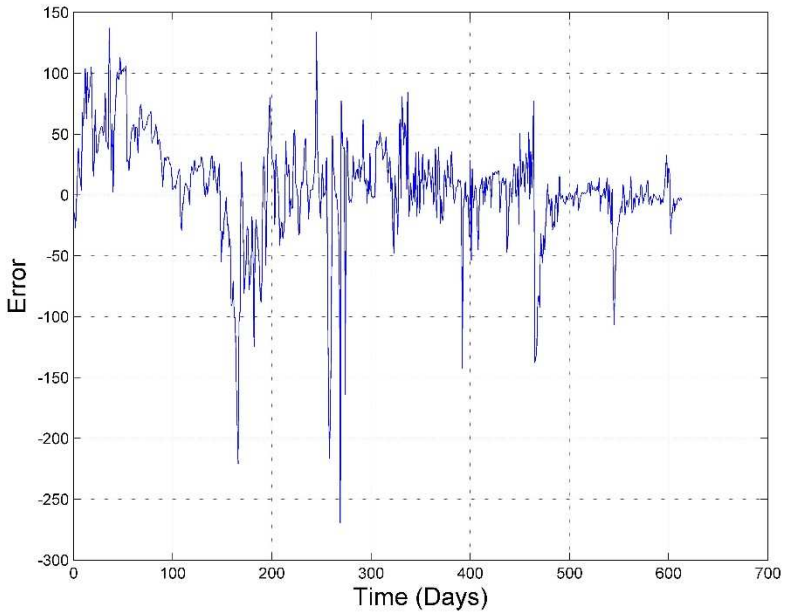

Fig. 263 — The error of the least squares optimization against the number of production days of Well 38 for the MH Model

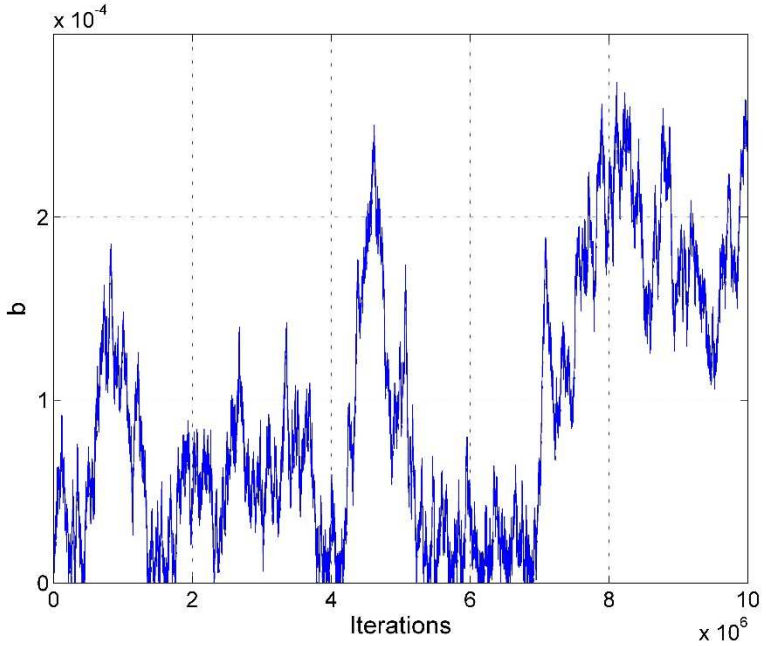

Fig. 264 — MCMC results of the *b*-factor for the MH model of Well 38 using the MH model

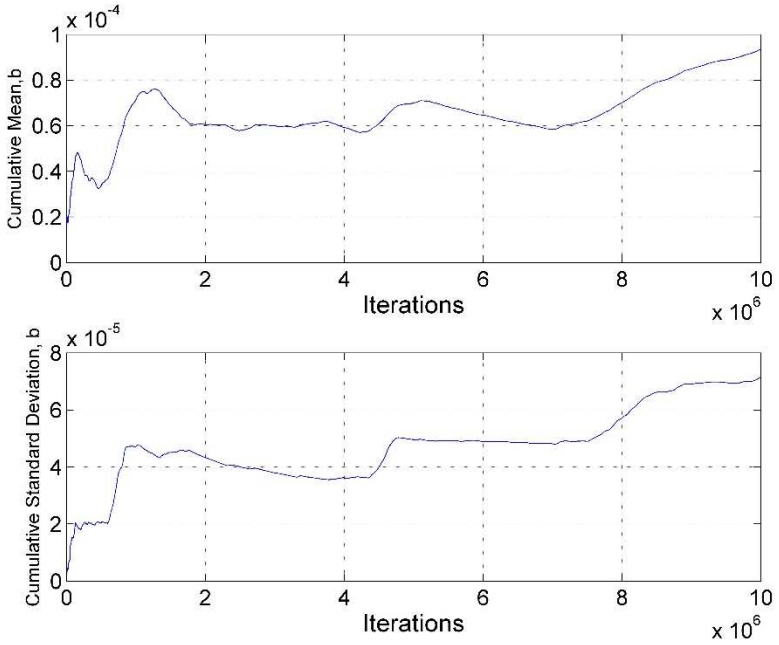

Fig. 265 — Cumulative mean and standard deviation of the *b*-factor of Well 38 using the MH model

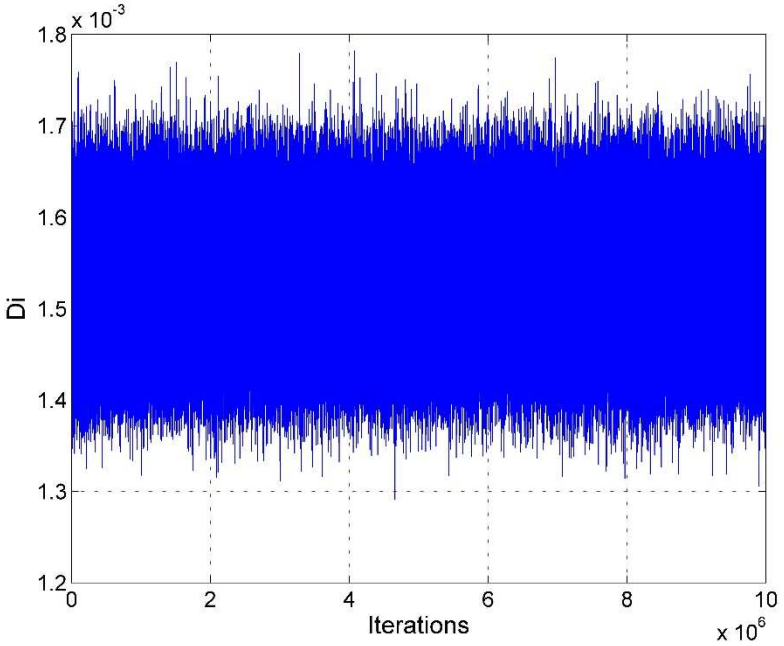

Fig. 266 — MCMC results of D_i for the MH model of Well 38 using the MH model

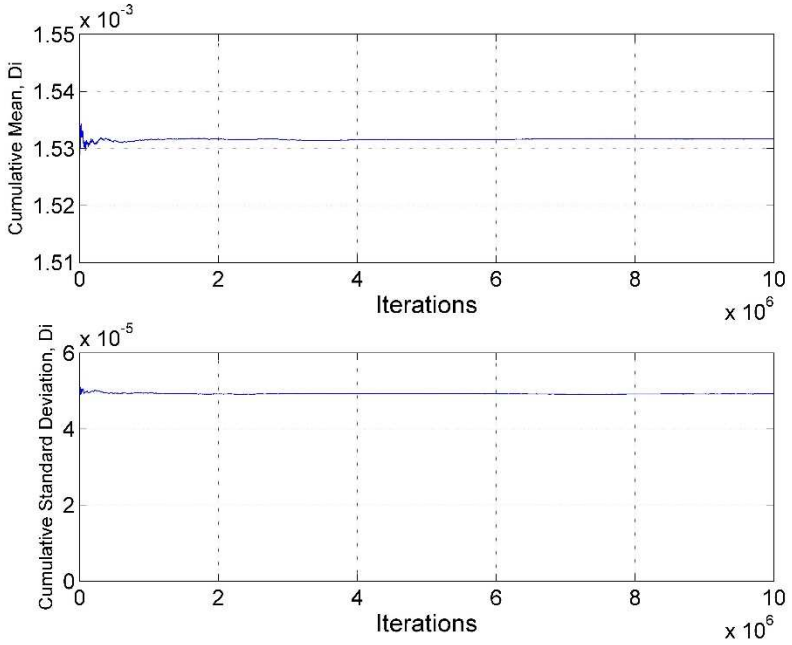

Fig. 267 — Cumulative mean and standard deviation of D_i of Well 38 using the MH model

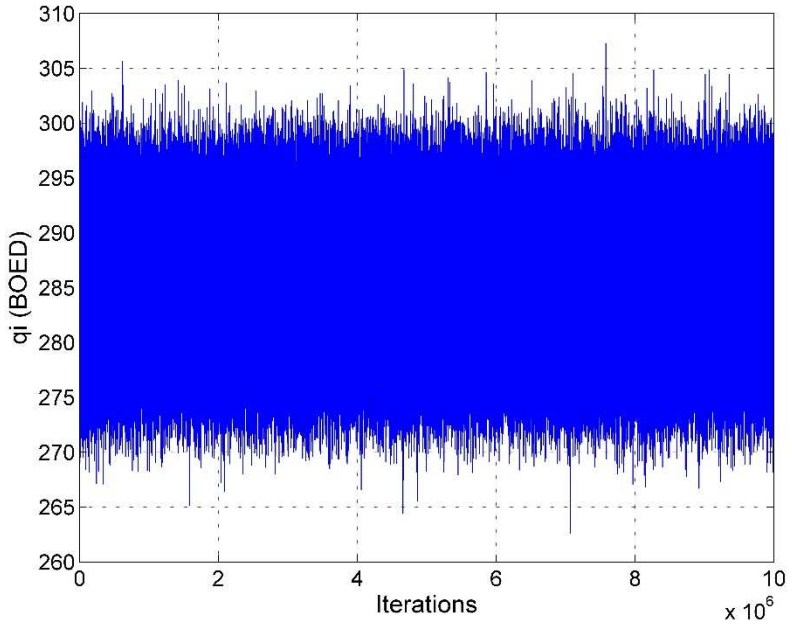

Fig. 268 — MCMC results of q_i for the MH model of Well 38 using the MH model

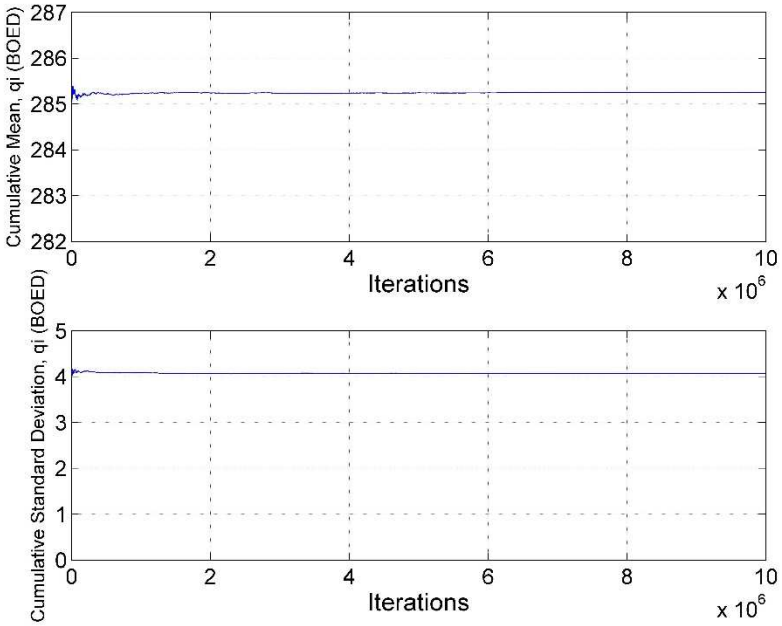

Fig. 269 — Cumulative mean and standard deviation of q_i of Well 38 using the MH model

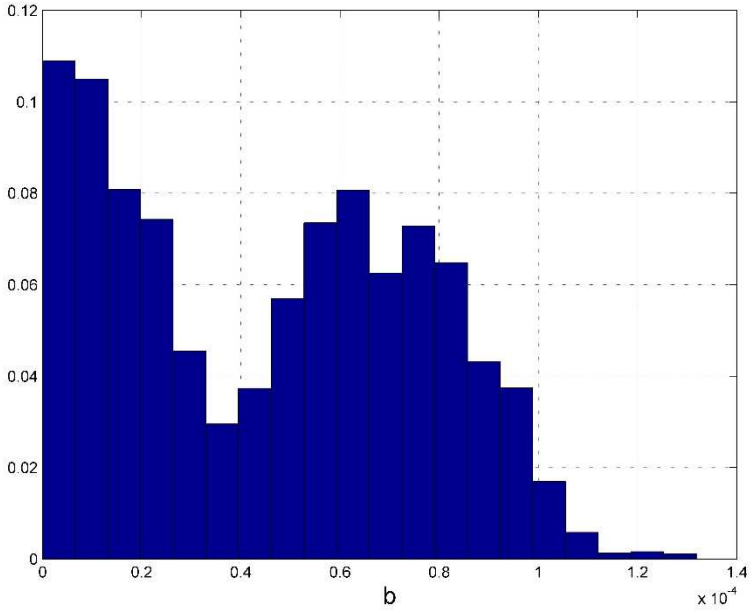

Fig. 270 — Posterior relative frequency histogram of *b* of Well 38 using the MH model

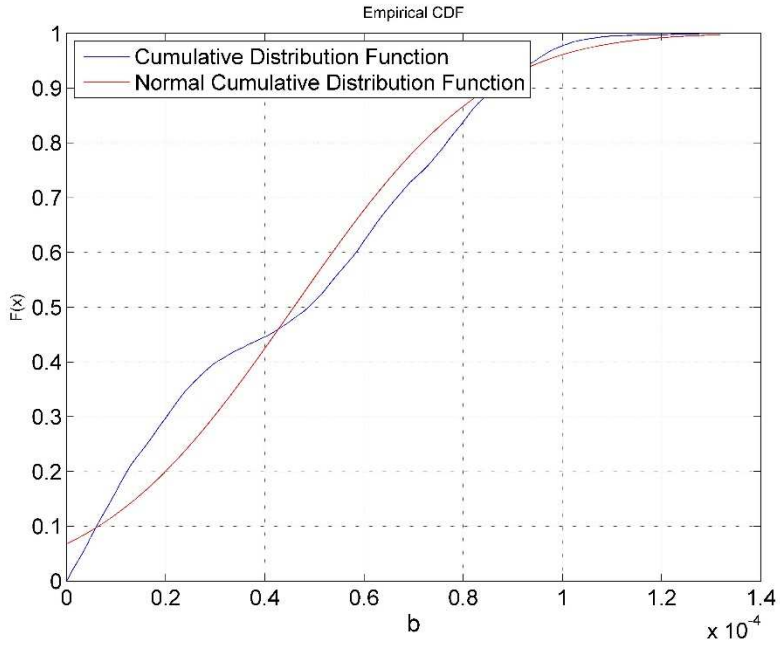

Fig. 271 — Cumulative posterior relative frequency histogram of the *b*-factor of Well 38 using the MH model

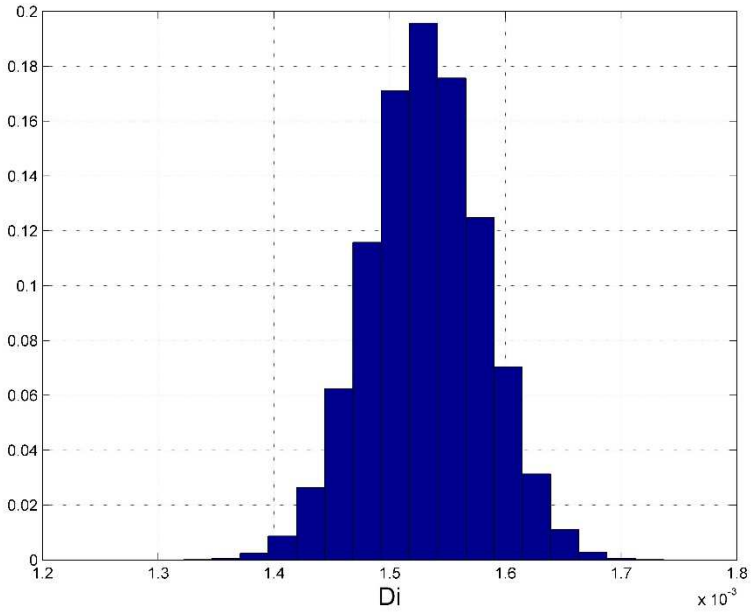

Fig. 272 — Posterior relative frequency histogram of D_i of Well 38 using the MH model

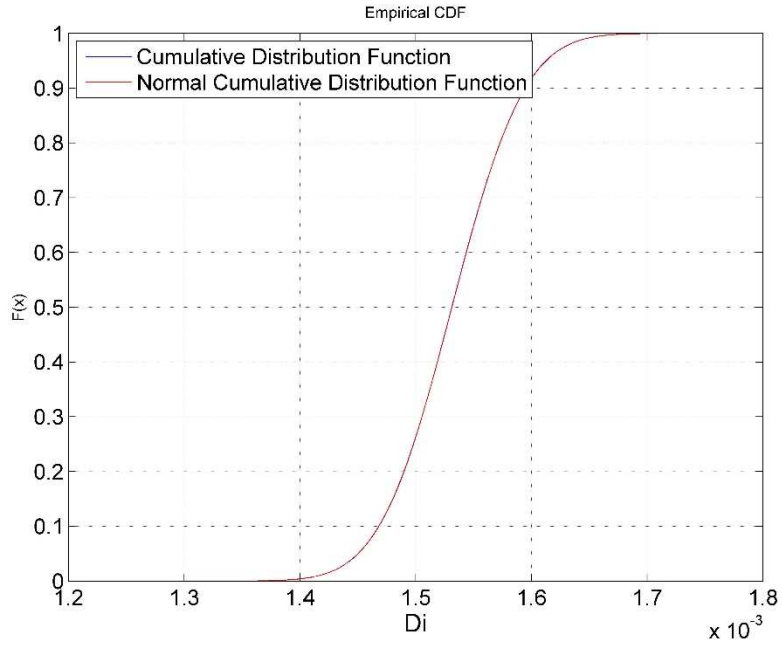

Fig. 273 — Cumulative posterior relative frequency histogram of D_i of Well 38 using the MH model

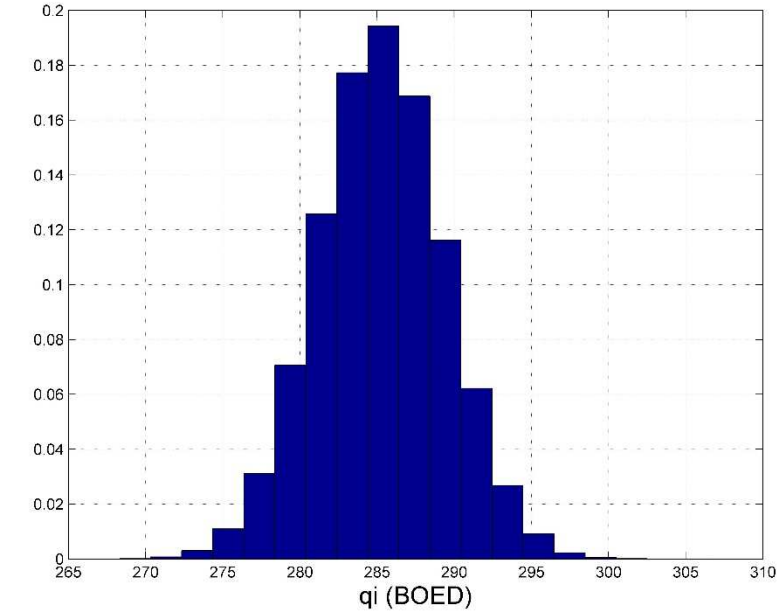

Fig. 274 — Posterior relative frequency histogram of q_i of Well 38 using the MH model

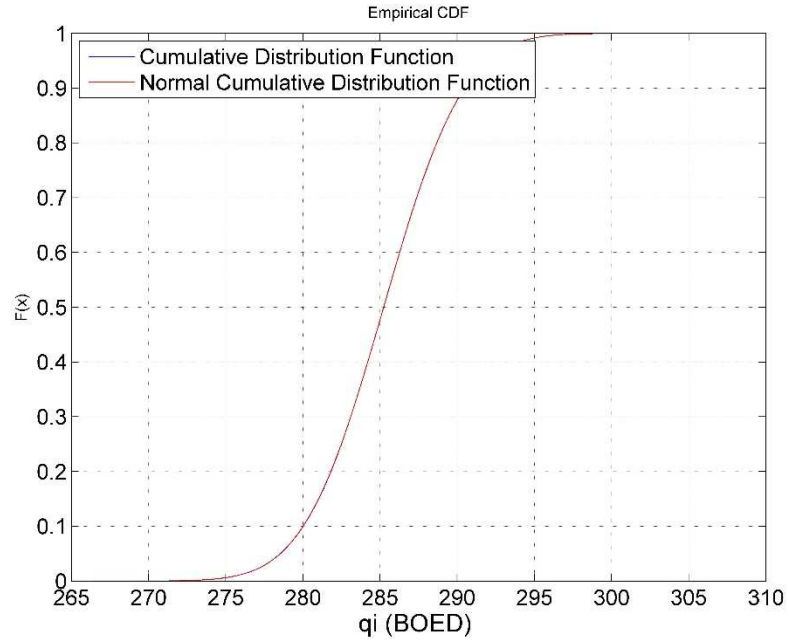

Fig. 275 — Cumulative posterior relative frequency histogram of q_i of Well 38 using the MH model

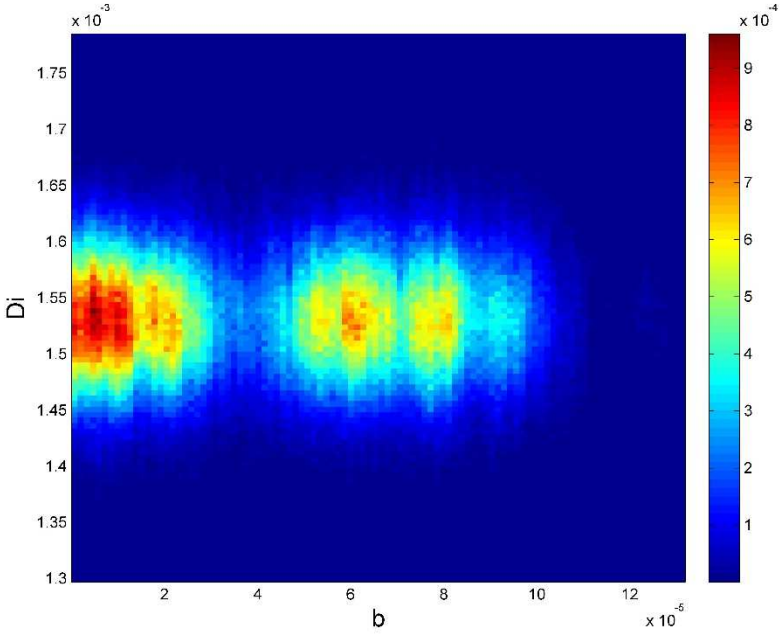

Fig. 276 — Relative frequency diagram between D_i and b of Well 38 using the MH model

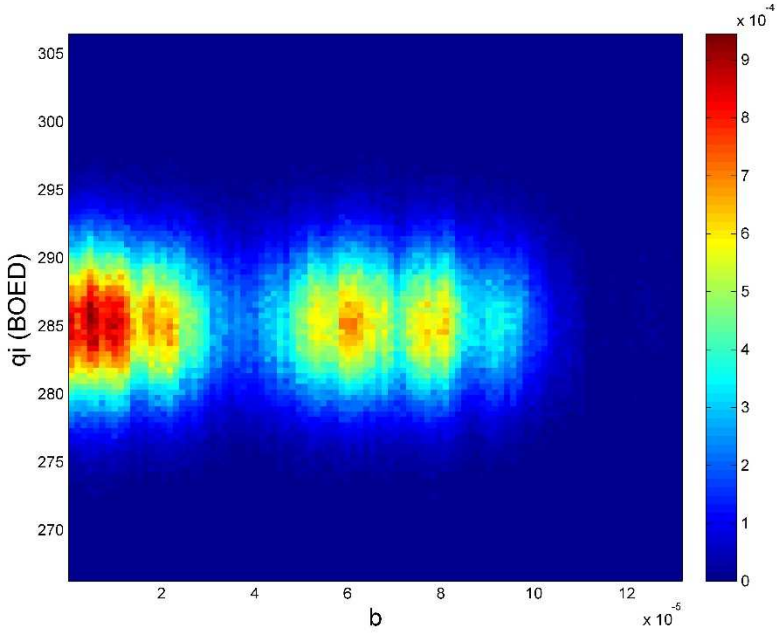

Fig. 277 — Relative frequency diagram between q_i and b of Well 38 using the MH model

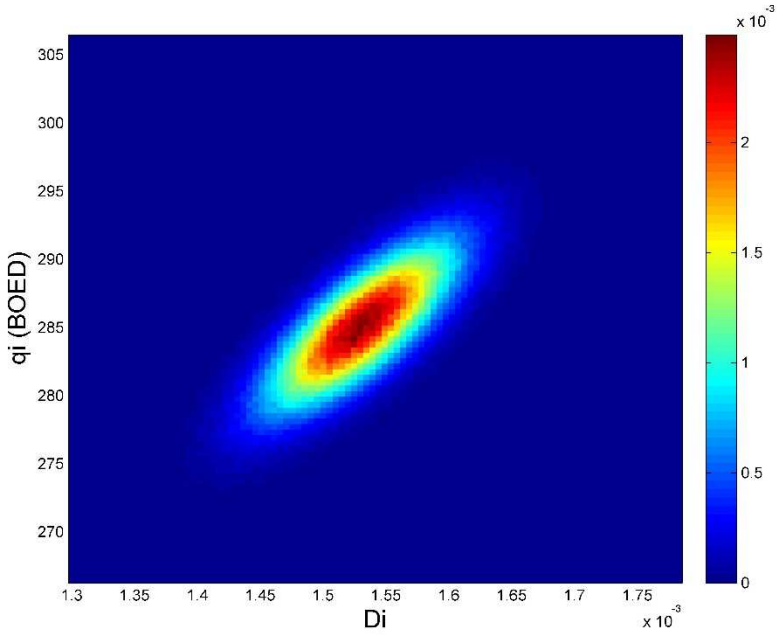

Fig. 278 — Relative frequency diagram between q_i and D_i of Well 38 using the MH model

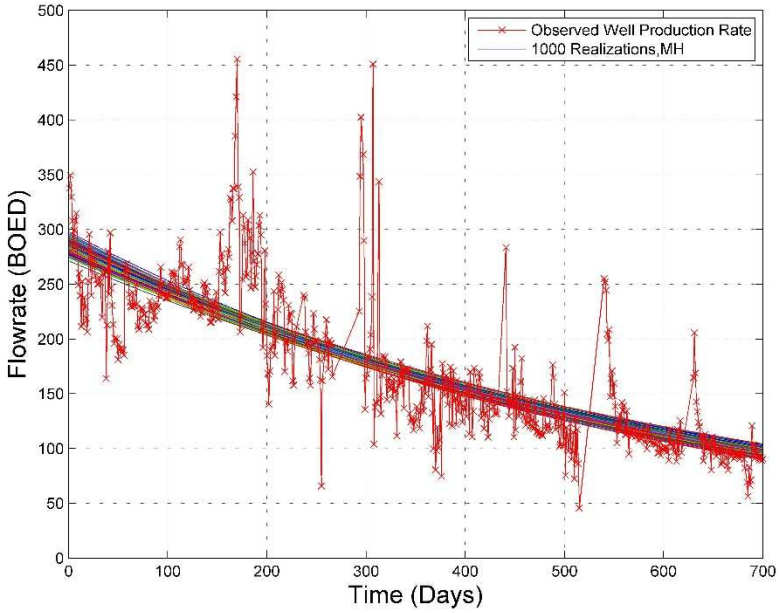

Fig. 279 — The 1,000 realizations of the model predictions using the Bayesian paradigm of Well 38 with the MH model

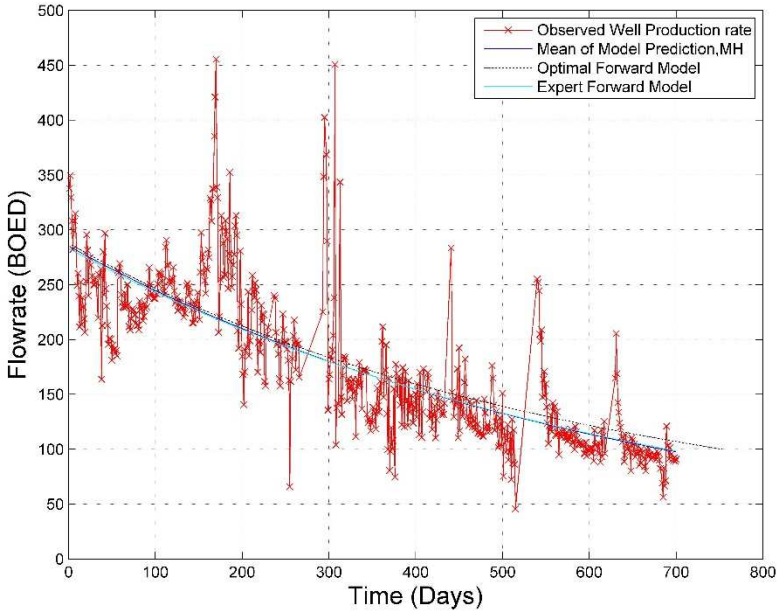

Fig. 280 — The production data with the mean of the realizations, the optimal forward model and the MH model of Well 38

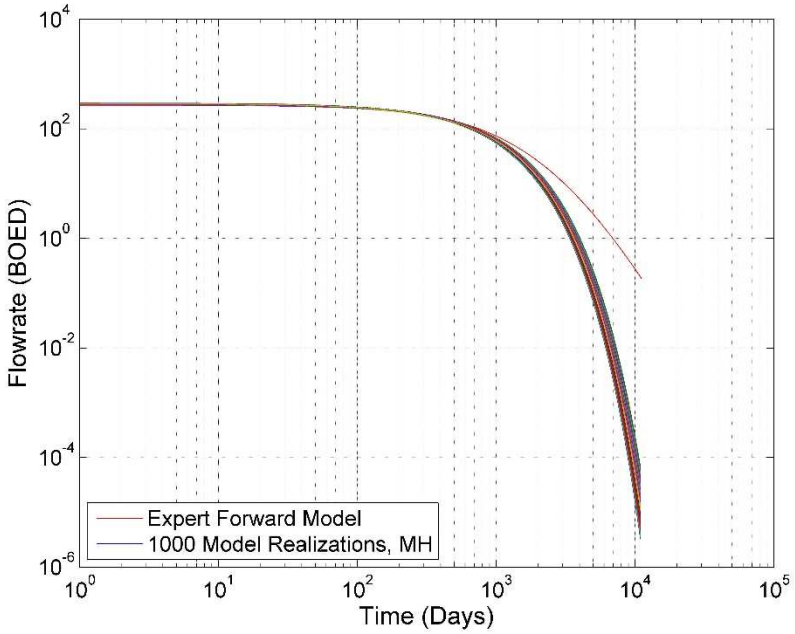

Fig. 281 — The 1,000 realizations of the model predictions using the Bayesian paradigm for 30 years of Well 38

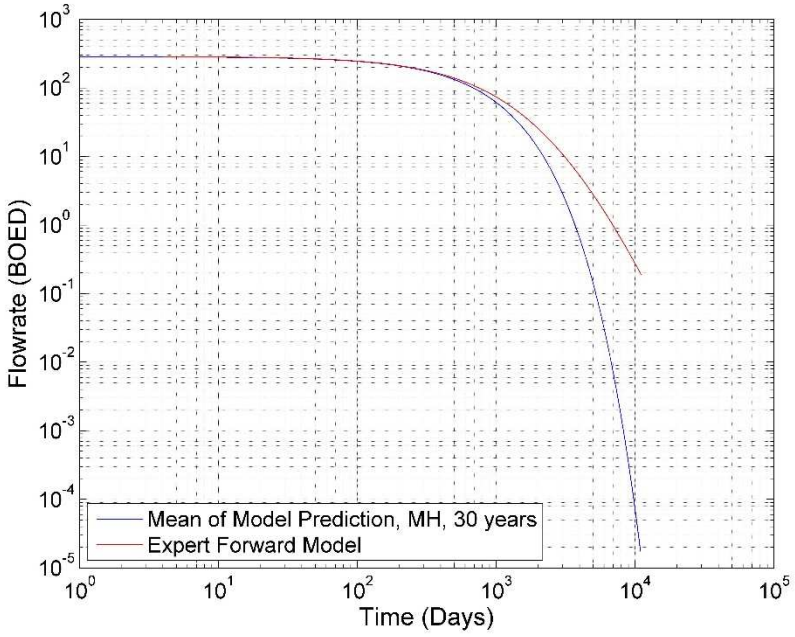

Fig. 282 — The mean of the realizations and the MH model, plotted for 30 years for Well 38

Well 38 – Power Law Exponential Model

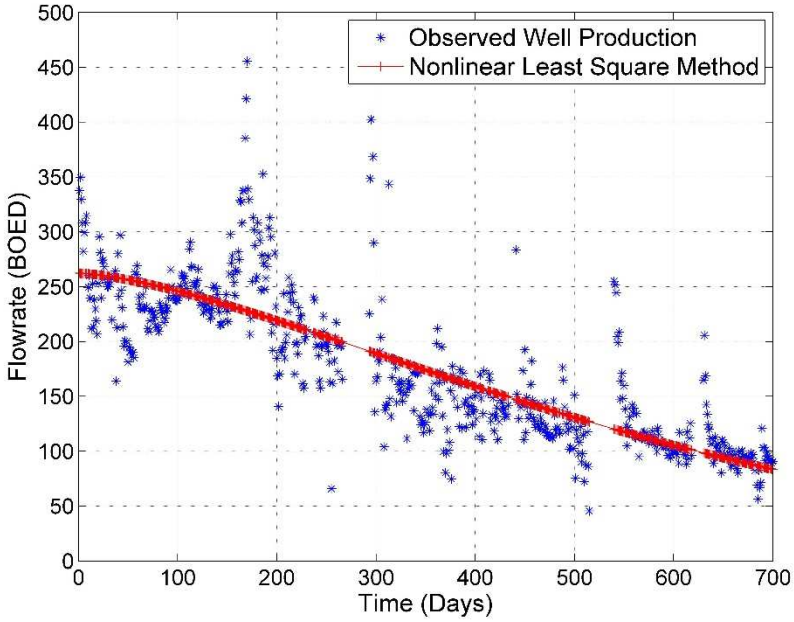

Fig. 283 — Results of the least squares optimization against the production data of Well 38 for the PLE Model

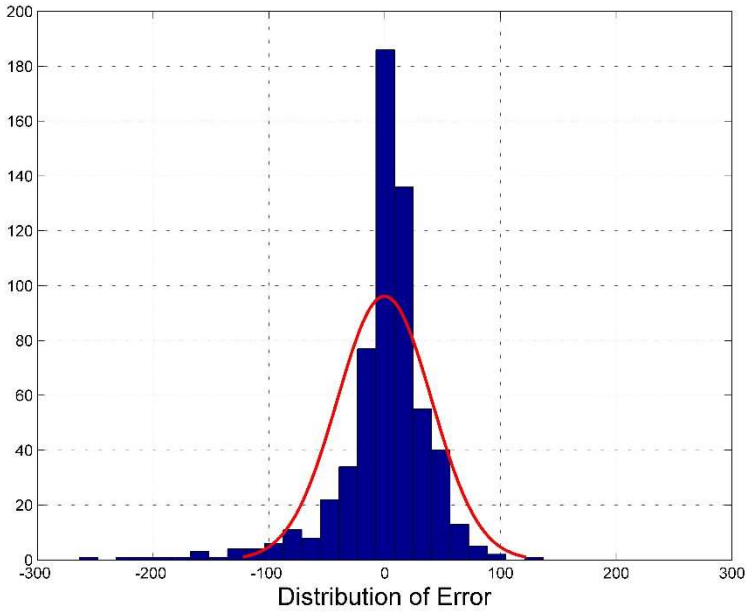

Fig. 284 — The distribution of error between the production data and the LSQ results for Well 38 for the PLE Model

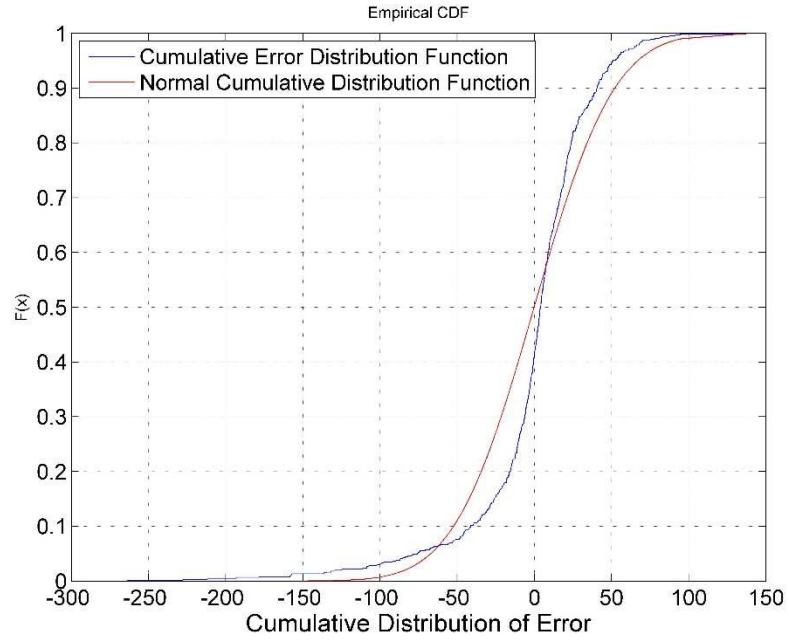

Fig. 285 — The cumulative distribution of error is plotted against the normal cumulative distribution function of Well 38 for the PLE Model

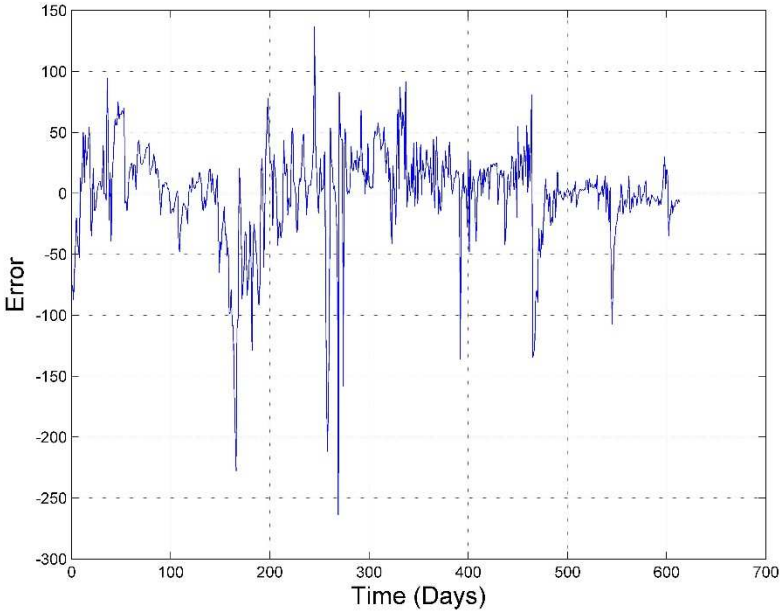

Fig. 286 — The error of the least squares optimization against the number of production days of Well 38 for the PLE Model

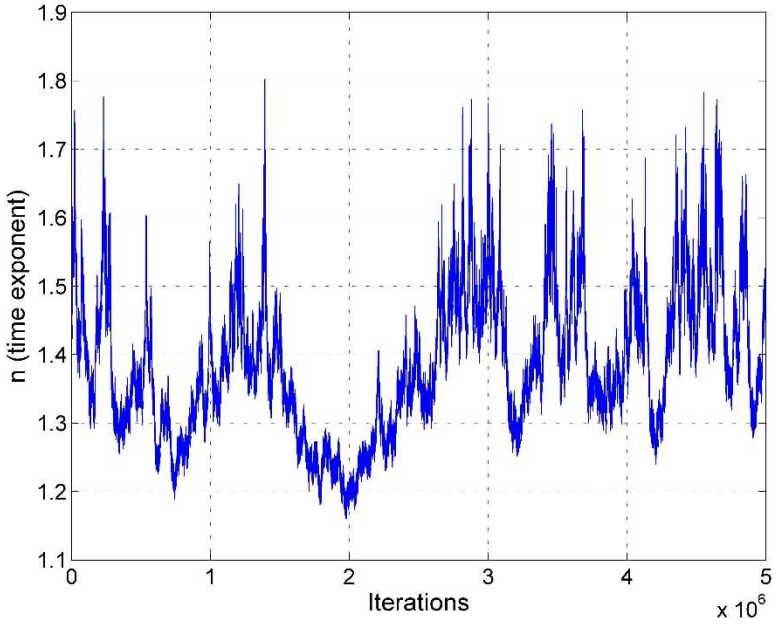

Fig. 287 — MCMC results of *n* for the PLE model of Well 38

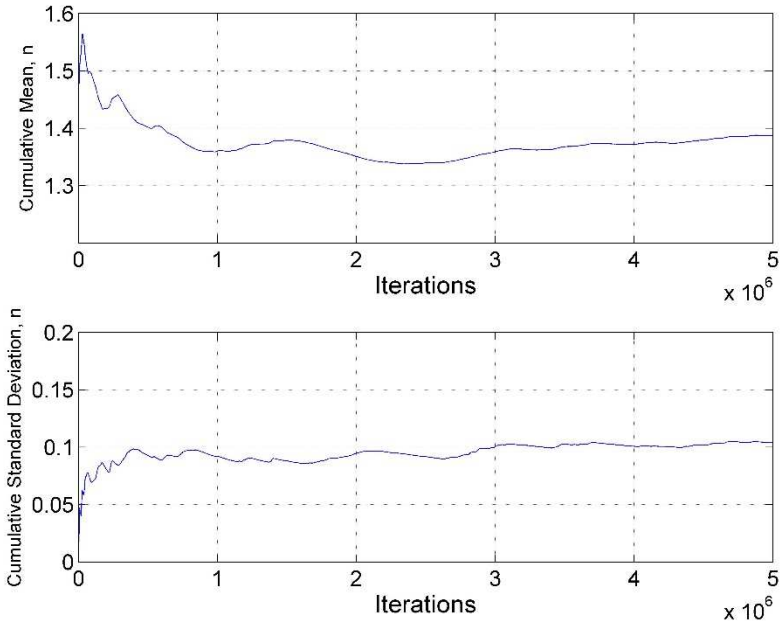

Fig. 288 — Cumulative mean and standard deviation of *n* of Well 38 using the PLE model

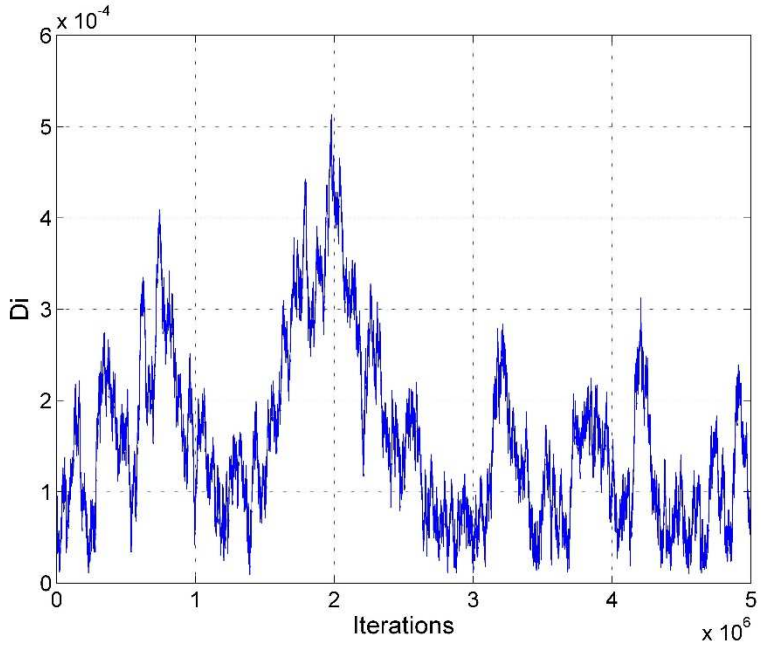

Fig. 289 — MCMC results of D_i for the MH model of Well 38 using the PLE model

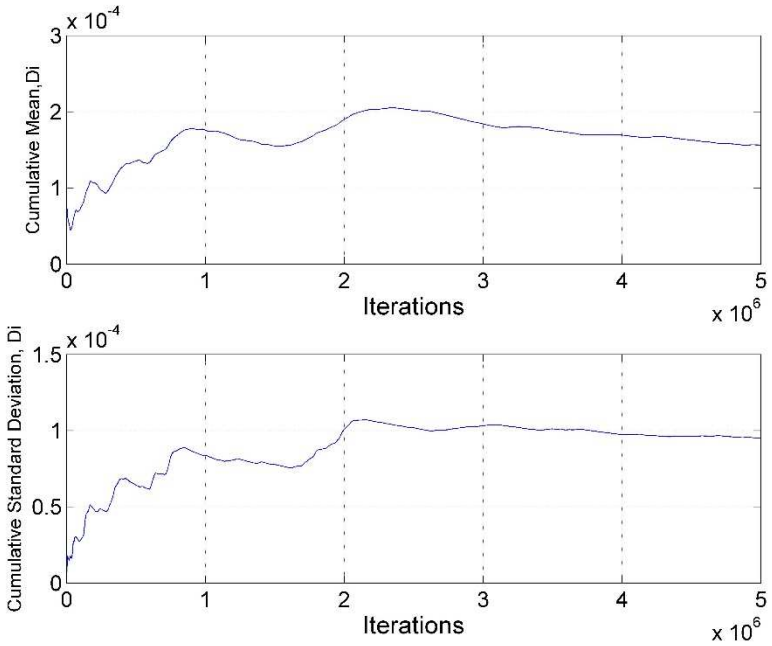

Fig. 290 — Cumulative mean and standard deviation of D_i of Well 38 using the PLE model

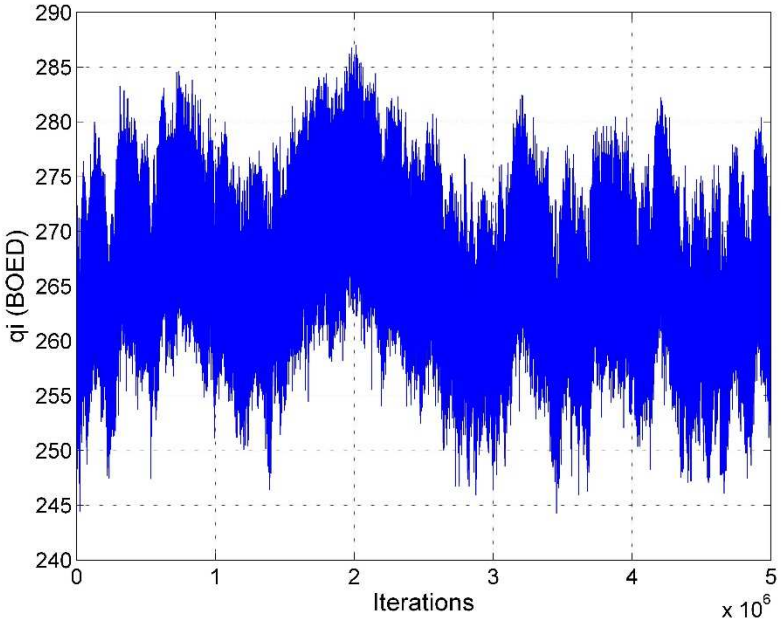

Fig. 291 — MCMC results of q_i for the MH model of Well 38 using the PLE model

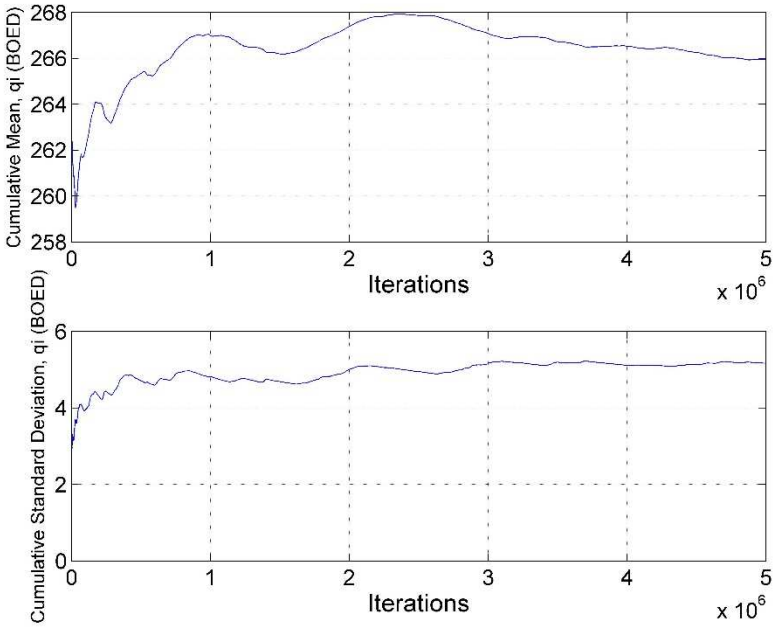

Fig. 292 — Cumulative mean and standard deviation of q_i of Well 38 using the PLE model

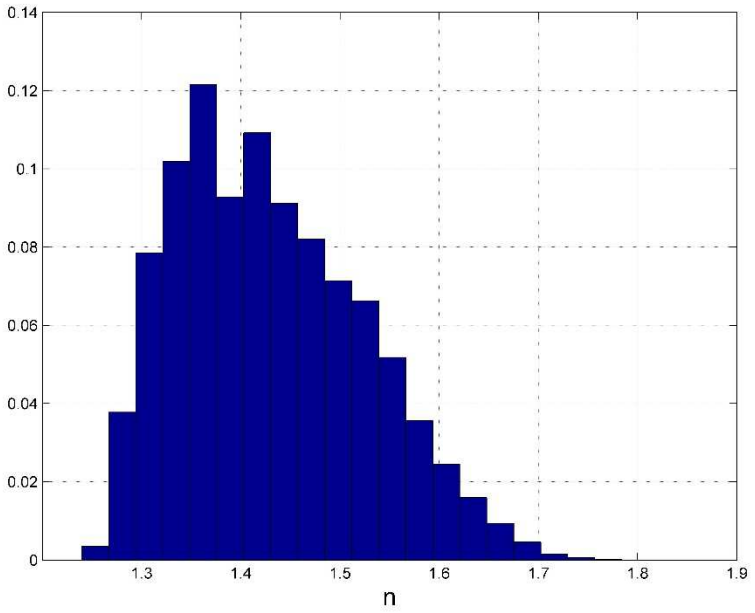

Fig. 293 — Posterior relative frequency histogram of *n* of Well 38 using the PLE model

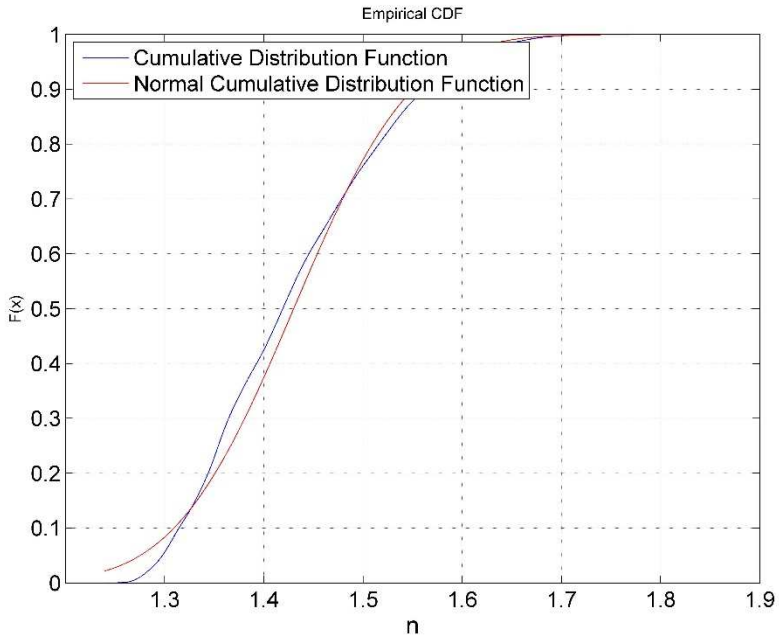

Fig. 294 — Cumulative posterior relative frequency histogram of *n* of Well 38 using the PLE model

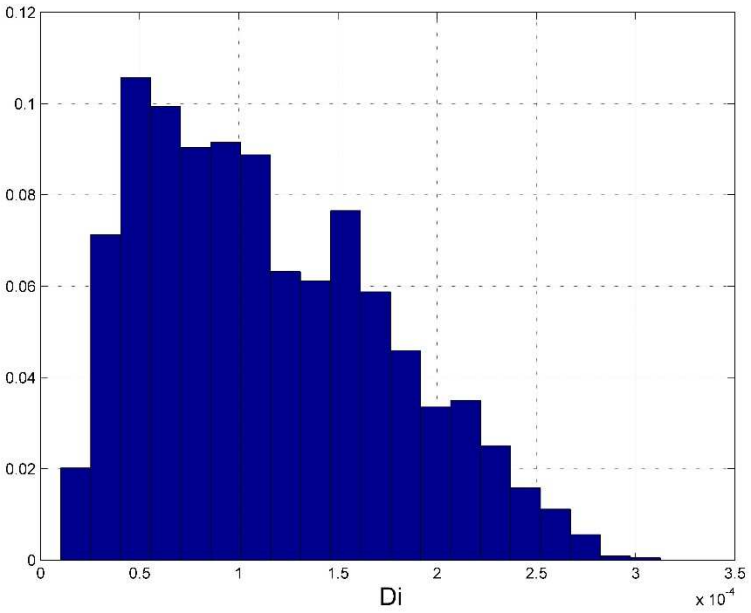

Fig. 295 — Posterior relative frequency histogram of D_i of Well 38 using the PLE model

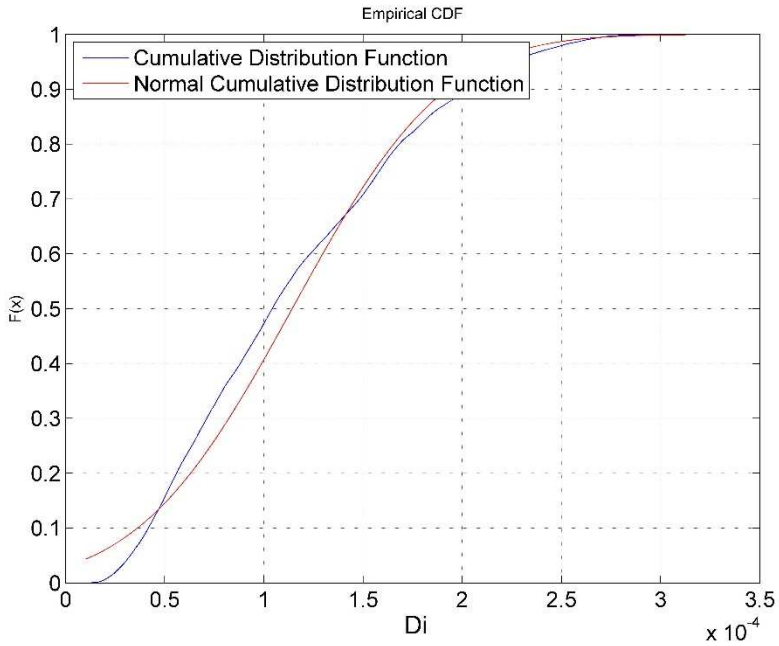

Fig. 296 — Cumulative posterior relative frequency histogram of D_i of Well 38 using the PLE model

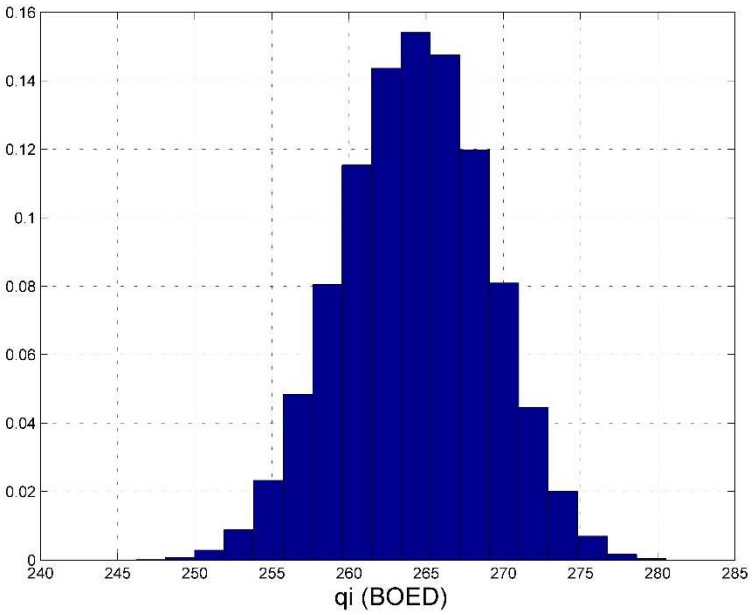

Fig. 297 — Posterior relative frequency histogram of q_i of Well 38 using the PLE model

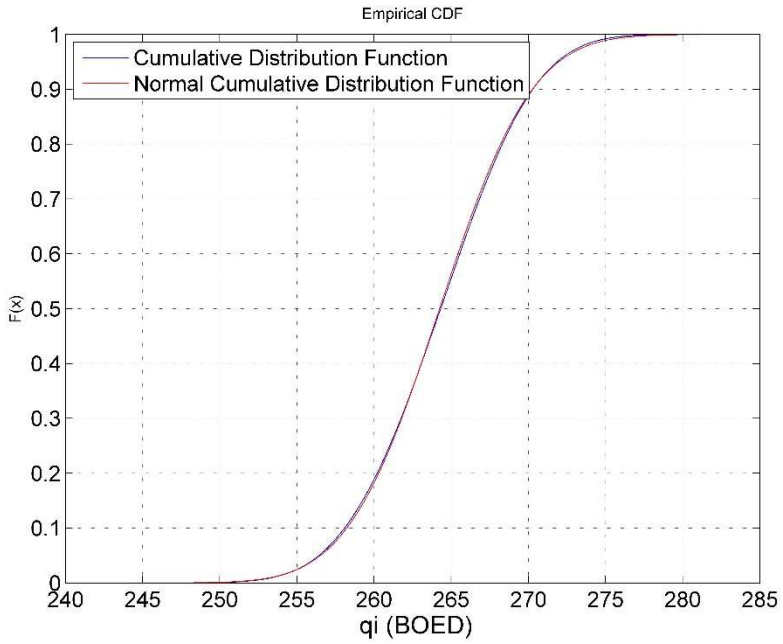

Fig. 298 — Cumulative posterior relative frequency histogram of q_i of Well 38 using the PLE model

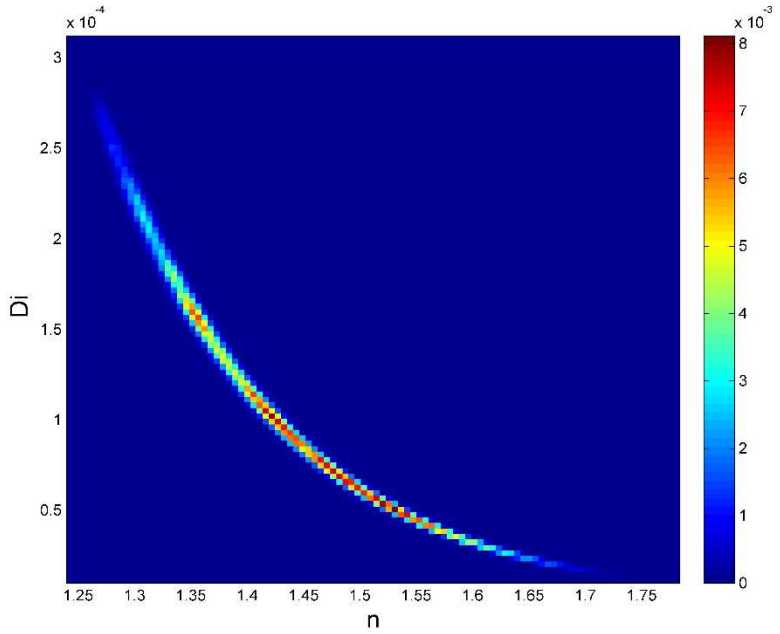

Fig. 299 — Relative frequency diagram between D_i and n of Well 38 using the PLE model

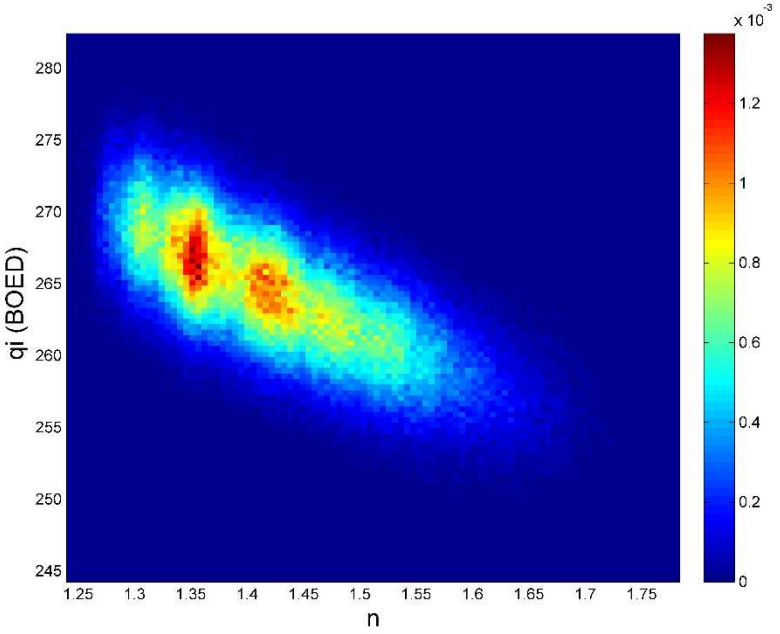

Fig. 300 — Relative frequency diagram between q_i and n of Well 38 using the PLE model

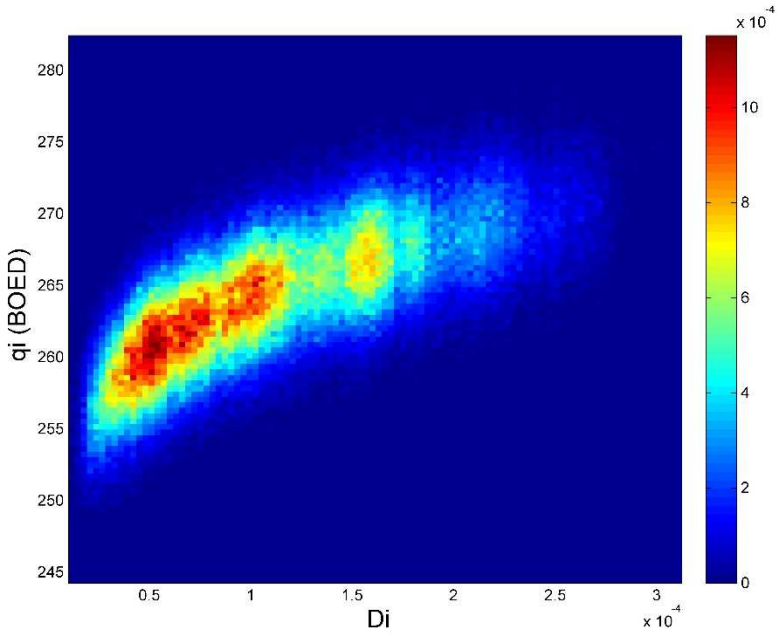

Fig. 301 — Relative frequency diagram between q_i and D_i of Well 38 using the PLE model

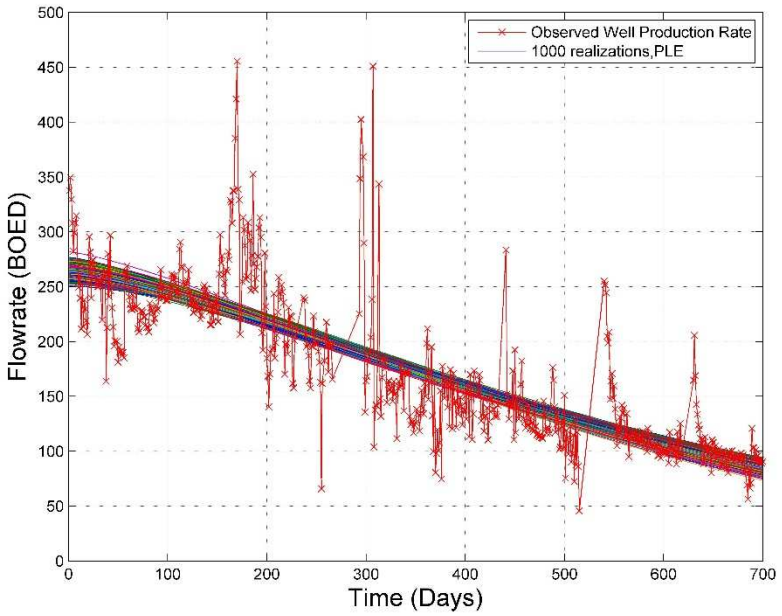

Fig. 302 — The 1,000 realizations of the model predictions using the Bayesian paradigm of Well 38 with the PLE model

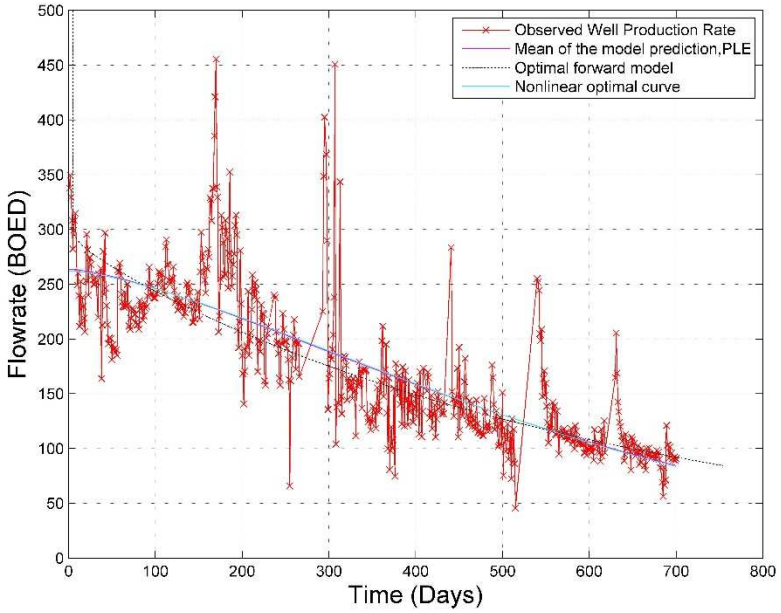

Fig. 303 — The production data with the mean of the realizations, the optimal forward model and the PLE model of Well 38

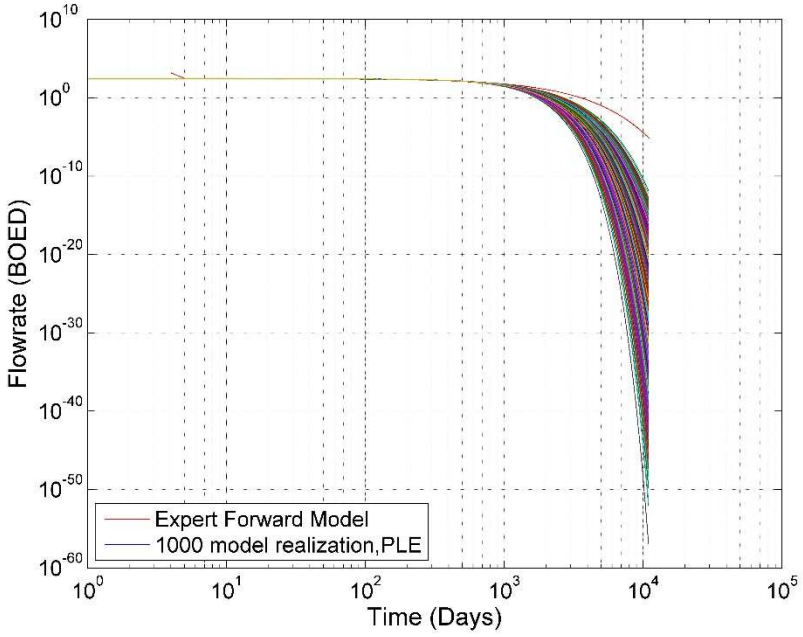

Fig. 304 — The 1,000 realizations of the model predictions using the Bayesian paradigm for 30 years of Well 38

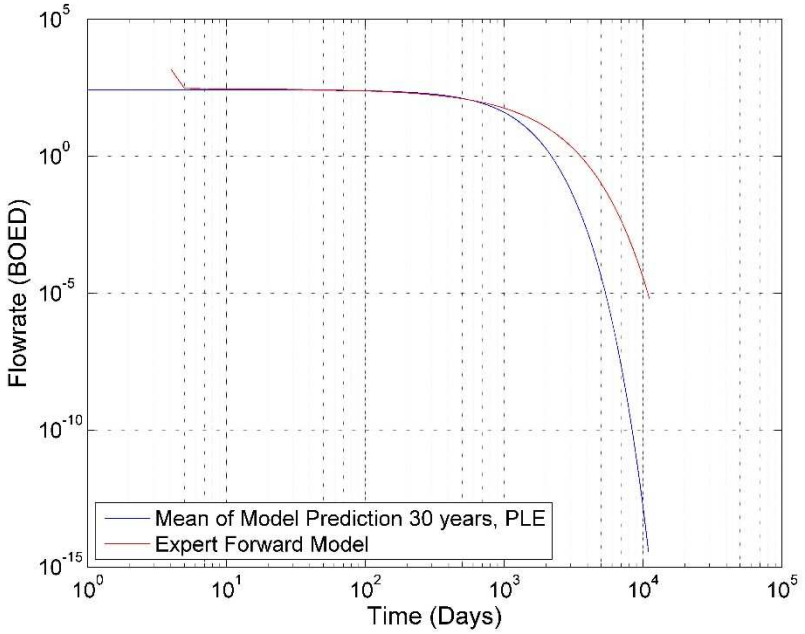

Fig. 305 — The mean of the realizations and the PLE model, plotted for 30 years for Well 38

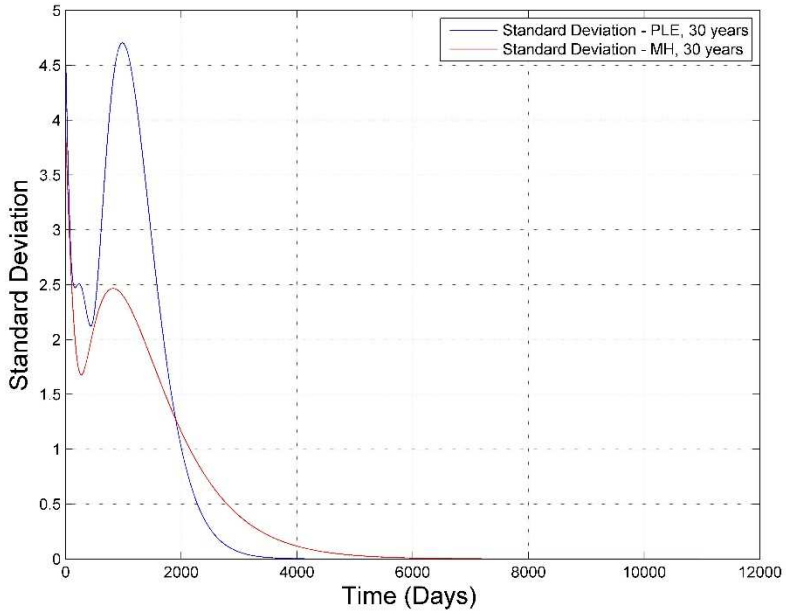

Fig. 306 — Comparison of the Standard Deviation of the two Bayesian forecasts using the MH and PLE models of Well 38

Analysis

Well 38 also shows interesting results with the MCMC results, especially when determining the *b*-factor, shown in **Fig. 264**. From the theory, the *b*-factor should have converged and is not, even after 10 million iterations. I draw the same conclusion as with Well 19, that the restriction that was set on the *b*-factor being greater than 0 is incorrect because the values of *b* are close to 0, but the *b*-factor should be set to 0 in this case, when using the MH model to apply the MCMC. However, we notice that the D_i converges immediately, as does the $q_{i,}$ which can be seen in **Fig. 266** and **270**. We applied the burn-in point and notice that the posterior distribution of the three parameters is quite different. We see a Gaussian distribution for both D_i and q_i in **Fig. 272** and **274**, however see a different distribution for the *b*-factor (**Fig. 270**), which is attributed to the non-convergence of the MCMC.

If we compare these MCMC results with the results produced when applying the PLE model, we notice that this model does not converge well for *n* and $D_{i,}$ shown in **Fig. 287** and **289**, respectively, however does converge for q_i, shown in **Fig. 291**. This model was let to run for five million iterations, as we were hoping for a better convergence in the two first parameters mentioned above.

Since the *n* and D_i MCMC results do not converge, the posteriors of these two parameters are also inaccurate, seen in **Fig. 293** and **295**, respectively. From these results, we also notice that *n* is greater than 1, even though we expect it to remain between 0 and 1. This is most likely due to the fact that the Eagle Ford Shale is an unconventional reservoir, and the PLE model is meant for conventional reservoirs, even though it is applied to the unconventional ones as well. D_i somewhat converges after four million iterations, however it is evident that it is not a stable result. The only accurate representation of the posterior is the q_i (**Fig. 298**) because it converged.

Based on the posterior distributions of the three parameters, we created the relative frequency histograms that show the relationship between two different parameters -- D_i vs. b, q_i vs. b and q_i vs D_i for the MH model and D_i vs. n, q_i vs. n and q_i vs D_i for the PLE model. These results can be seen in **Fig. 276, 277** and **278**, respectively, for the MH model and **Fig. 299, 300** and **301**, respectively, for the PLE model.

From Fig. 276 and 277, we see that the poor results due to the b-factor that the histograms become skewed and we cannot determine a good relationship of the two parameters. However, we see that in Fig. 278 that there is a linear relationship between q_i and D_i. The red part of the graph identifies the ideal set of the two parameters for this data set using the MH model.

For the PLE results of the relative frequency histogram, we see interesting results. In Fig. 299, we see a very interesting relationship between D_i and n, which shows a curve. This may indicate that there is no set relationship between these two parameters, because there should not be. However, another interesting observation from Fig. 300 and 301 is that q_i has opposite relationships with D_i and the b-factor. This is similar to the trend seen for Well 19, however the relationship is not as clear in this well. However, we see a consistent trend between parameters which is an interesting result.

Finally we reach the realizations of the Bayesian paradigm using the MH and PLE models. We notice when we plot the mean of the realizations versus the optimal forward model (the results from the LSQ optimization), and the expert forward model (either MH or PLE), the mean of the model prediction and the expert forward model often times have close values for the 700 days plotted. However, when we extend the results to 30 years that there is a divergence between two sets of results. In this case, the MH model, when applied to the Bayesian paradigm overestimates reserves, as seen in **Fig. 282.** This is the same result that is presented for the PLE model when applied to the Bayesian paradigm,

shown in **Fig. 305**. These results show that the forward models can overestimate or underestimate the reserves.

The graph that compares the standard deviations of the two sets of Bayesian results, **Fig. 306**, identifies the uncertainty of the two models. From the results of the two standard deviations plotted against each other, it is evident that in early time (to approximately 2,000 days), the PLE model shows a higher uncertainty. However in later time, the uncertainty of the PLE model decreases. This result is unexpected due to the results of the MCMC.

APPENDIX VII

RESULTS AND ANALYSIS OF WELL 40

Well 40 – Modified Hyperbolic Model

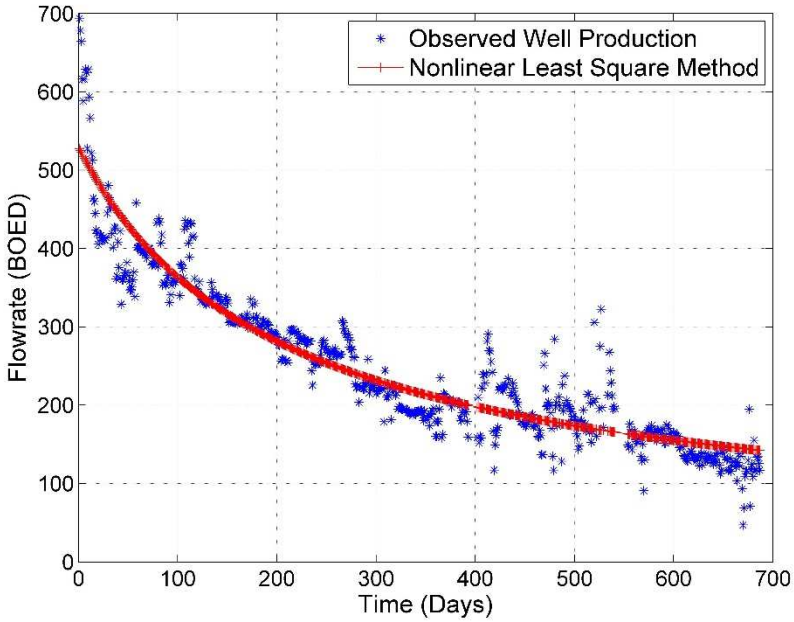

Fig. 307 — Results of the least squares optimization against the production data of Well 40 for the MH Model

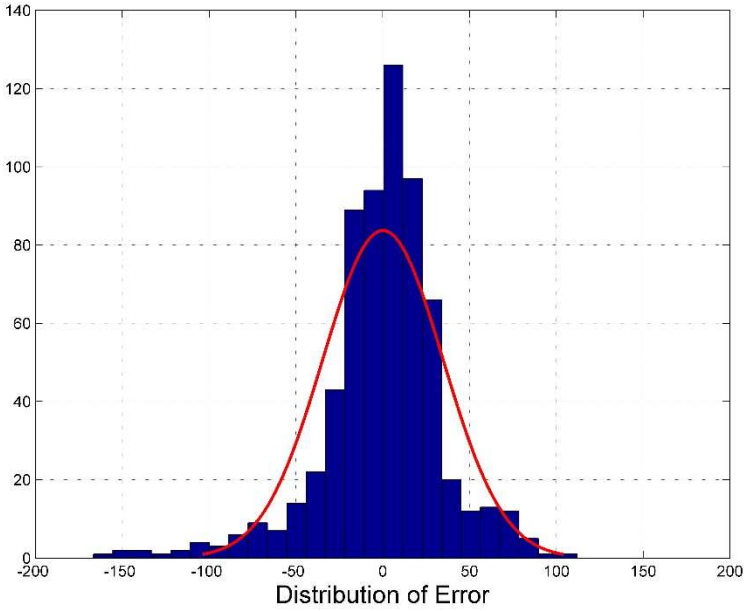

Fig. 308 — The distribution of error between the production data and the LSQ results for Well 40 for the MH Model

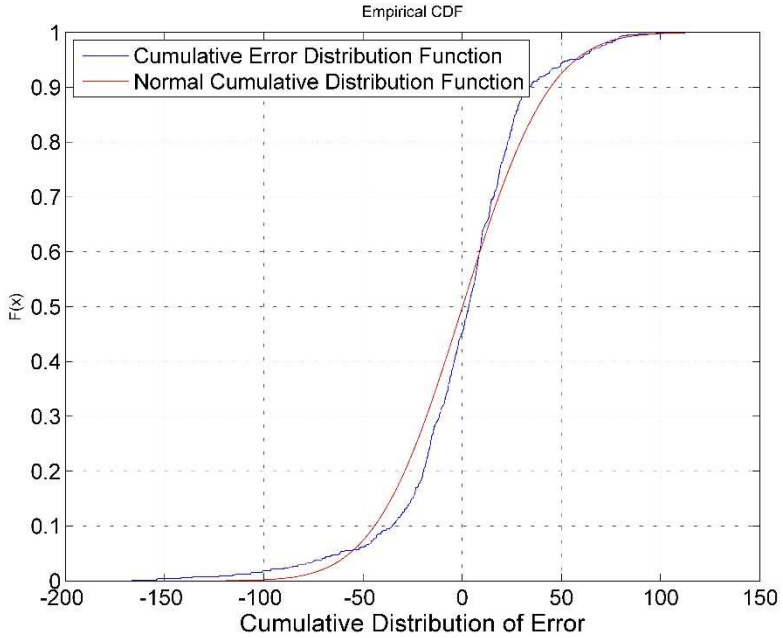

Fig. 309 — The cumulative distribution of error is plotted against the normal cumulative distribution function of Well 40 for the MH Model

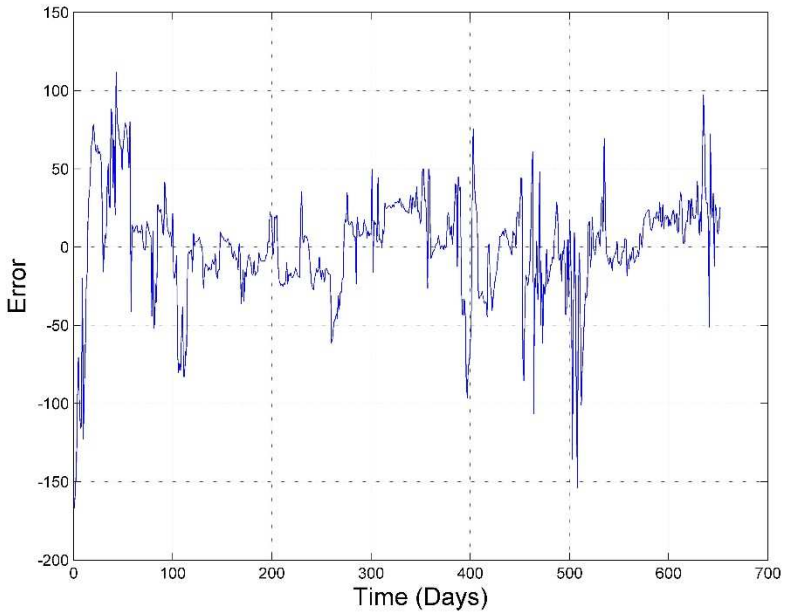

Fig. 310 — The error of the least squares optimization against the number of production days of Well 40 for the MH Model

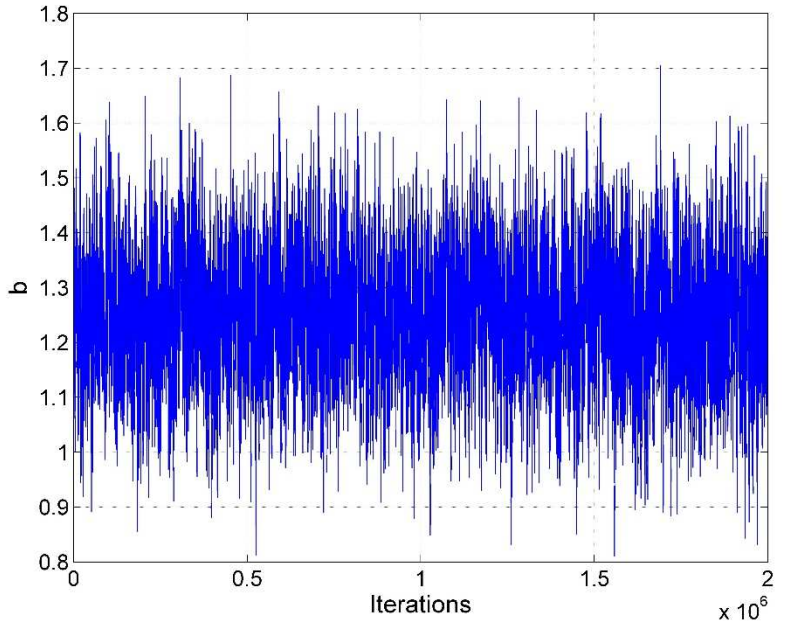

Fig. 311 — MCMC results of the *b*-factor for the MH model of Well 40 using the MH model

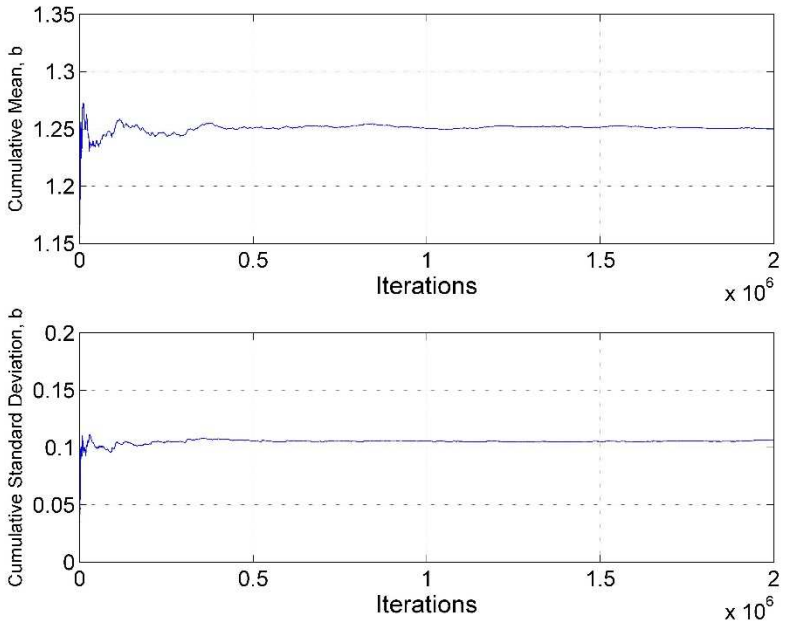

Fig. 312 — Cumulative mean and standard deviation of the *b*-factor of Well 40 using the MH model

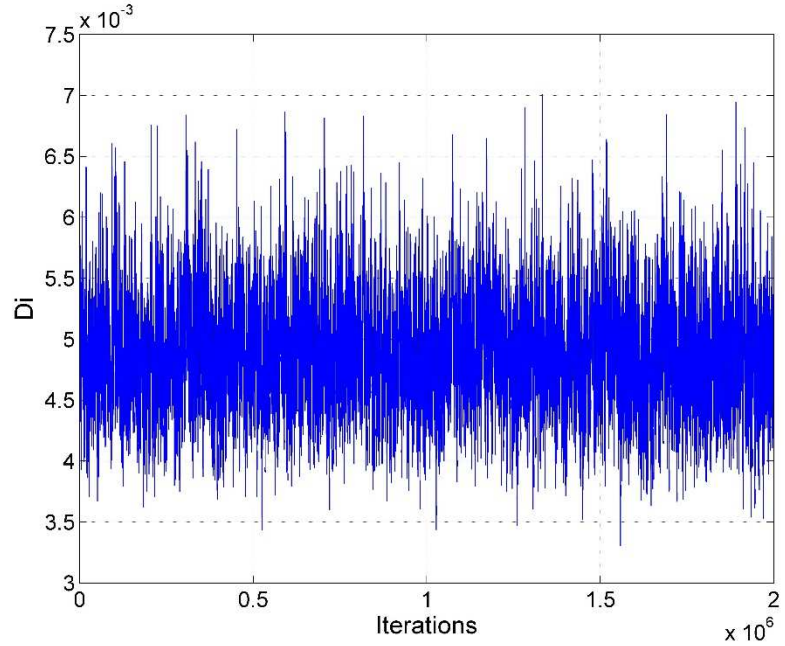

Fig. 313 — MCMC results of D_i for the MH model of Well 40 using the MH model

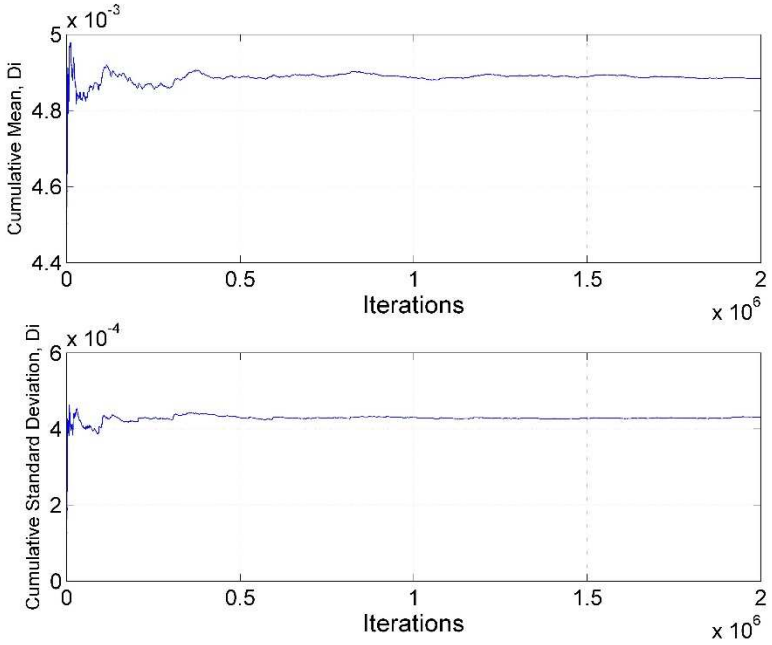

Fig. 314 — Cumulative mean and standard deviation of D_i of Well 40 using the MH model

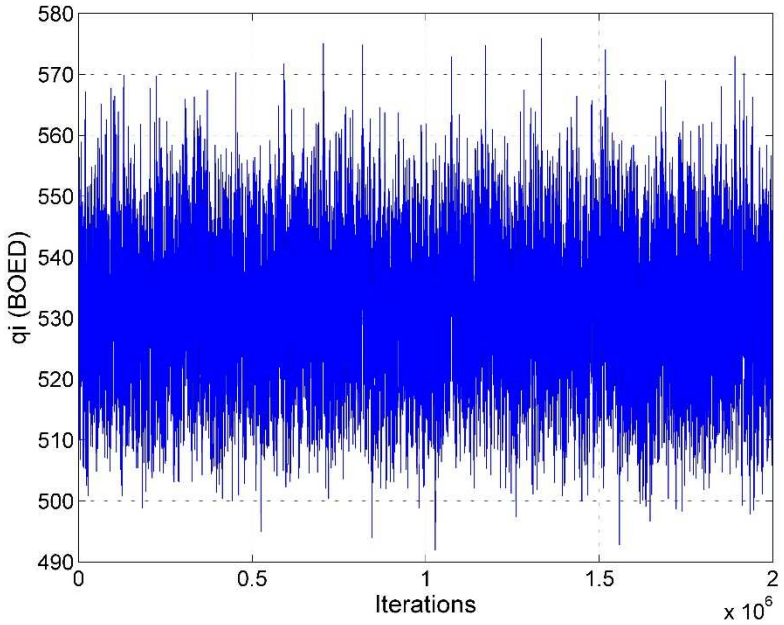

Fig. 315 — MCMC results of q_i for the MH model of Well 40 using the MH model

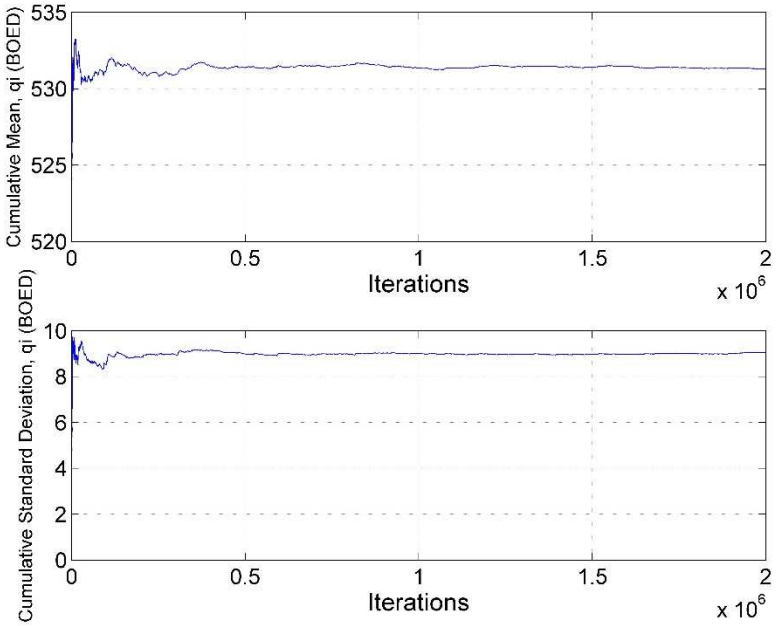

Fig. 316 — Cumulative mean and standard deviation of q_i of Well 40 using the MH model

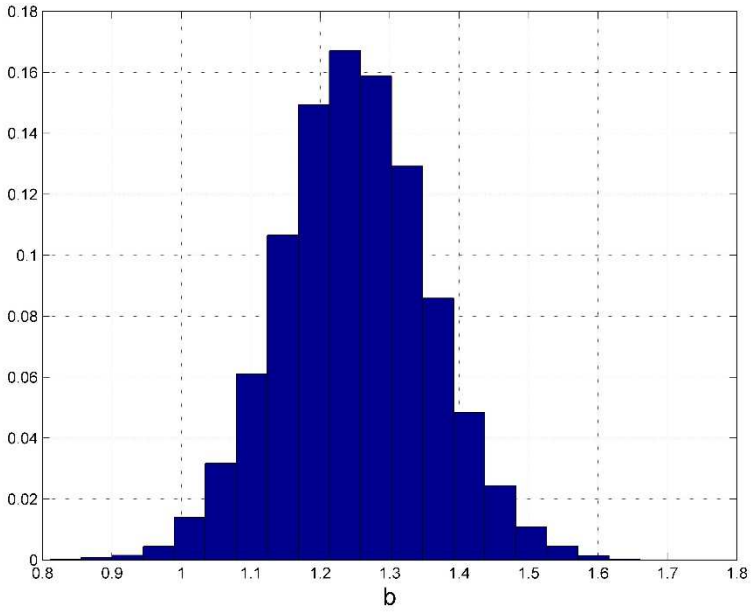

Fig. 317 — Posterior relative frequency histogram of *b* of Well 40 using the MH model

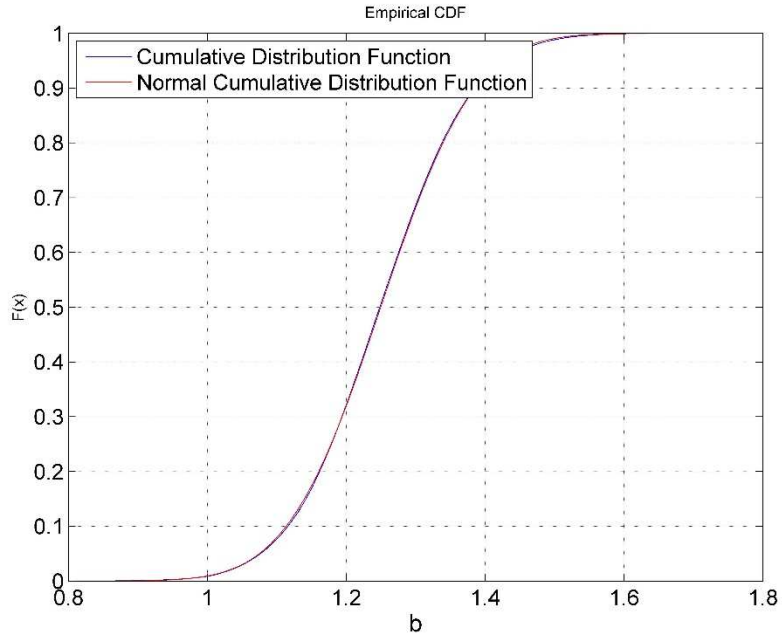

Fig. 318 — Cumulative posterior relative frequency histogram of the *b*-factor of Well 40 using the MH model

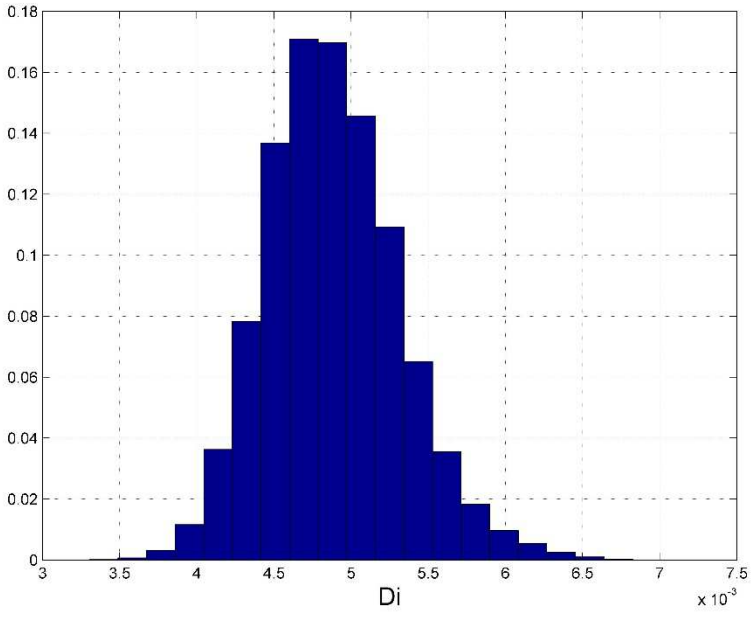

Fig. 319 — Posterior relative frequency histogram of D_i of Well 40 using the MH model

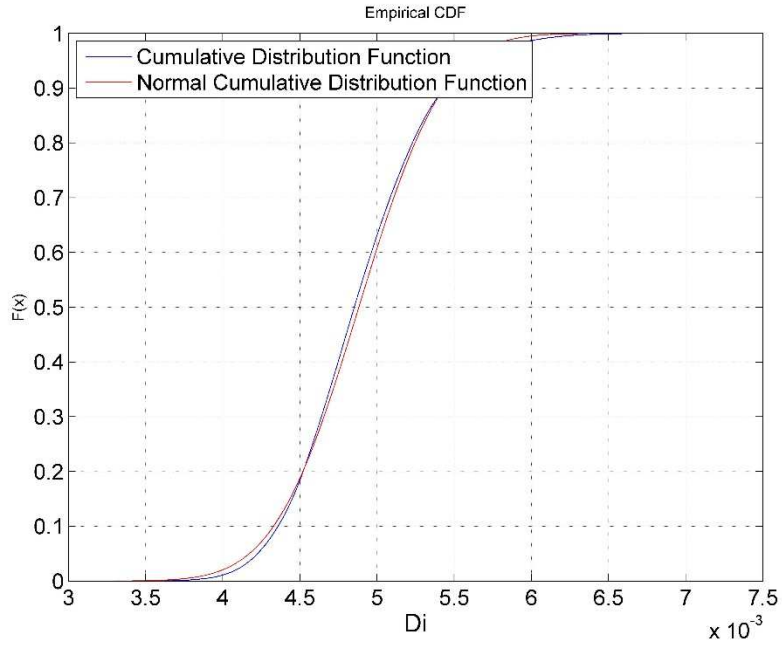

Fig. 320 — Cumulative posterior relative frequency histogram of D_i of Well 40 using the MH model

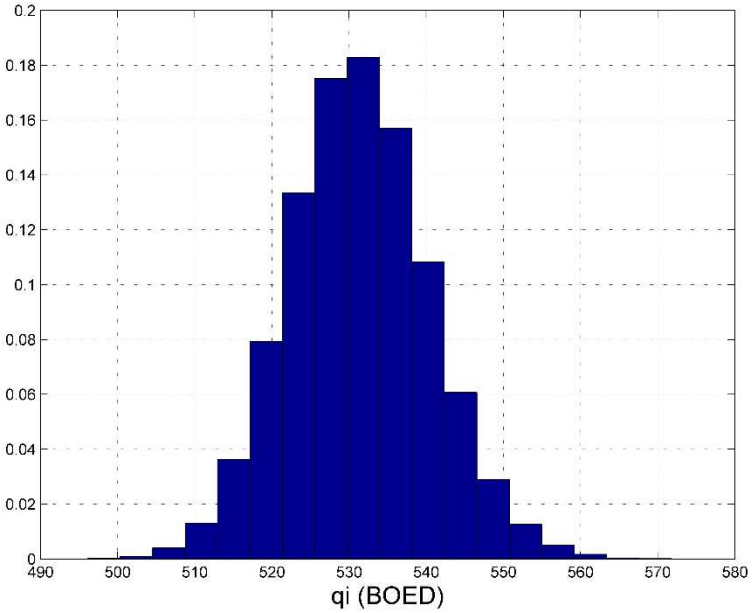

Fig. 321 — Posterior relative frequency histogram of q_i of Well 40 using the MH model

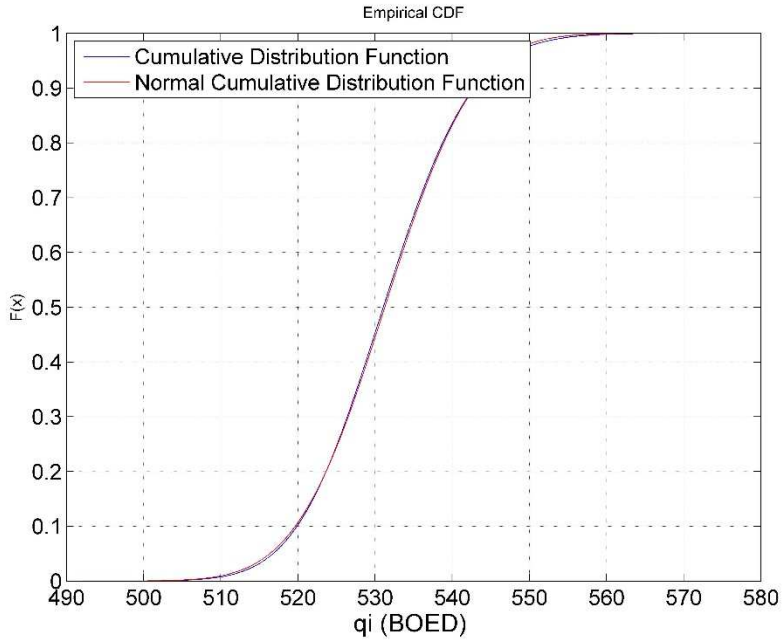

Fig. 322 — Cumulative posterior relative frequency histogram of q_i of Well 40 using the MH model

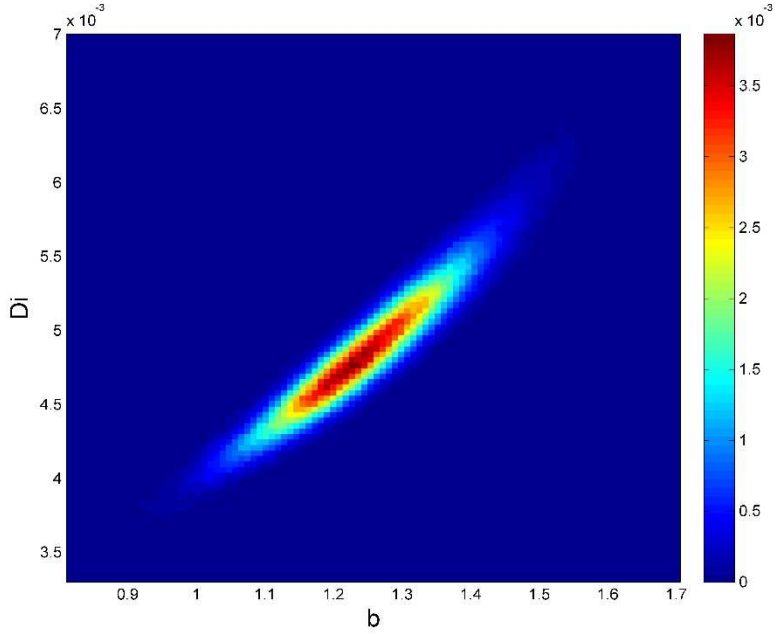

Fig. 323 — Relative frequency diagram between D_i and b of Well 40 using the MH model

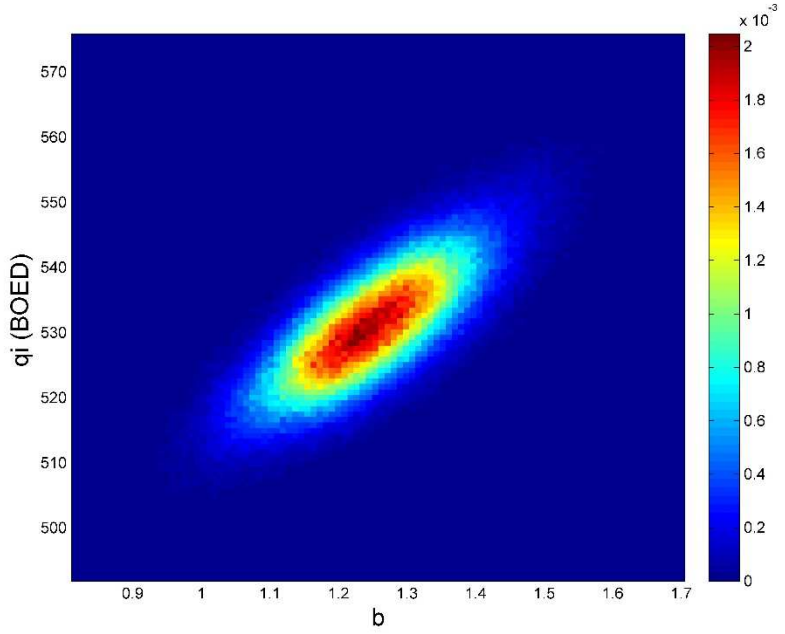

Fig. 324 — Relative frequency diagram between q_i and b of Well 40 using the MH model

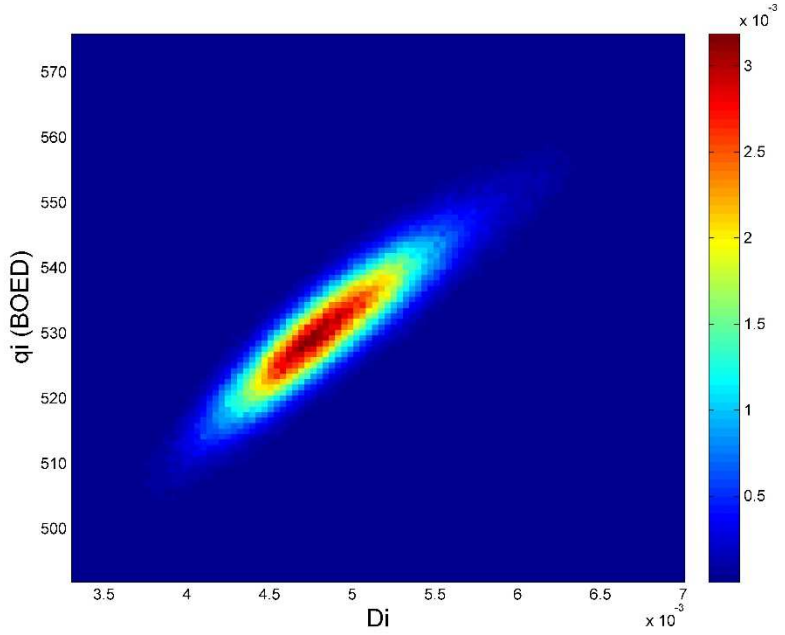

Fig. 325 — Relative frequency diagram between q_i and D_i of Well 40 using the MH model

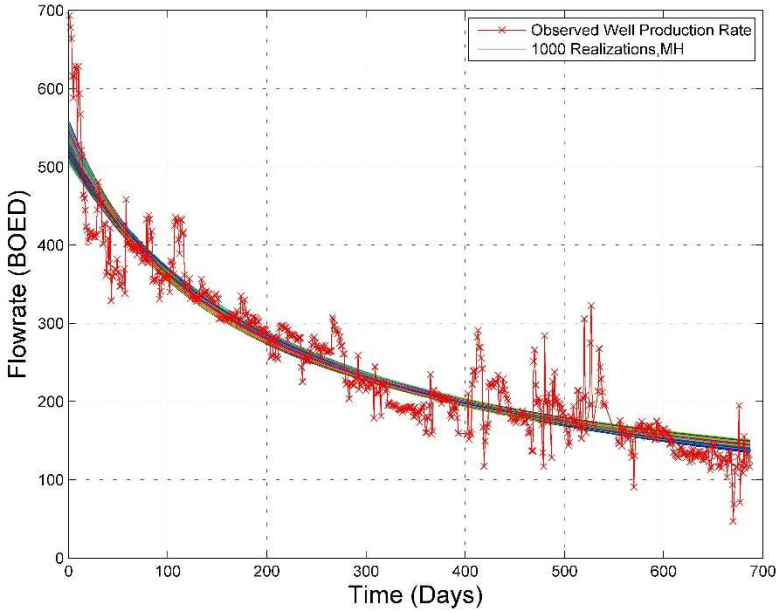

Fig. 326 — The 1,000 realizations of the model predictions using the Bayesian paradigm of Well 40 with the MH model

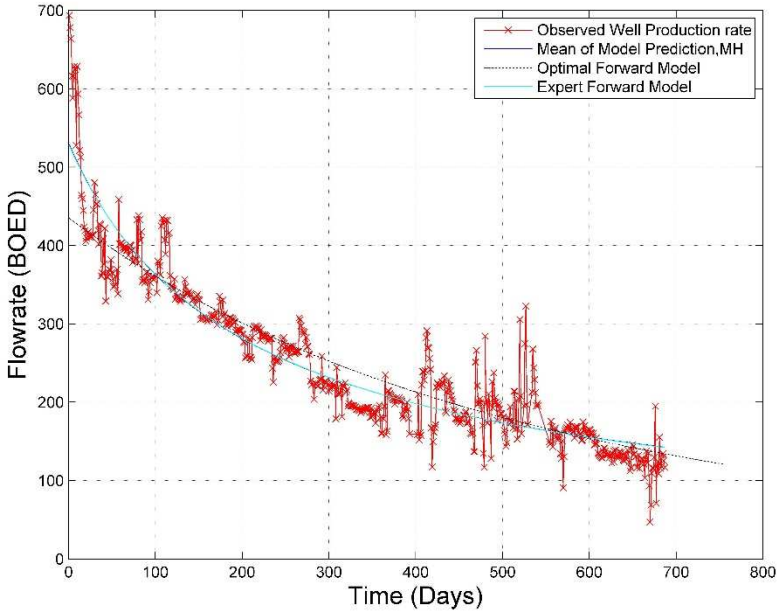

Fig. 327 — The production data with the mean of the realizations, the optimal forward model and the MH model of Well 40

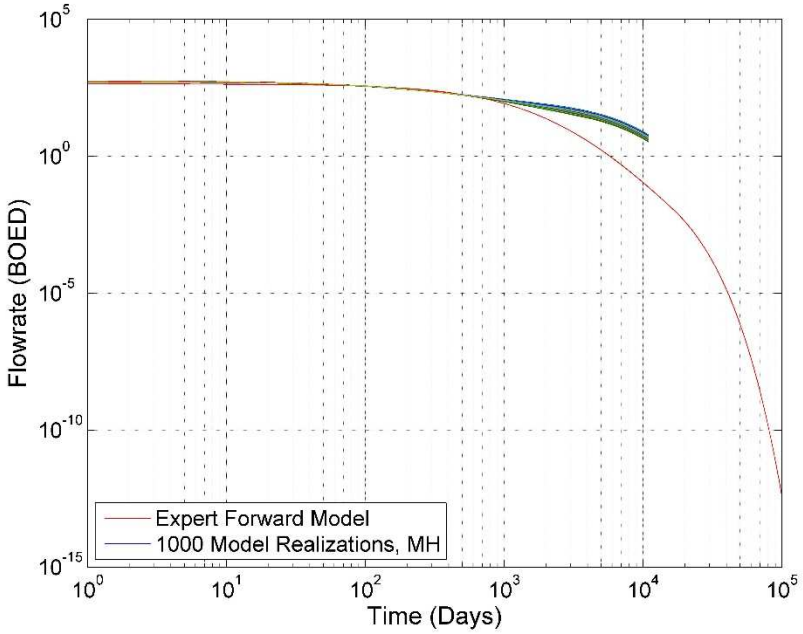

Fig. 328 — The 1,000 realizations of the model predictions using the Bayesian paradigm for 30 years of Well 40

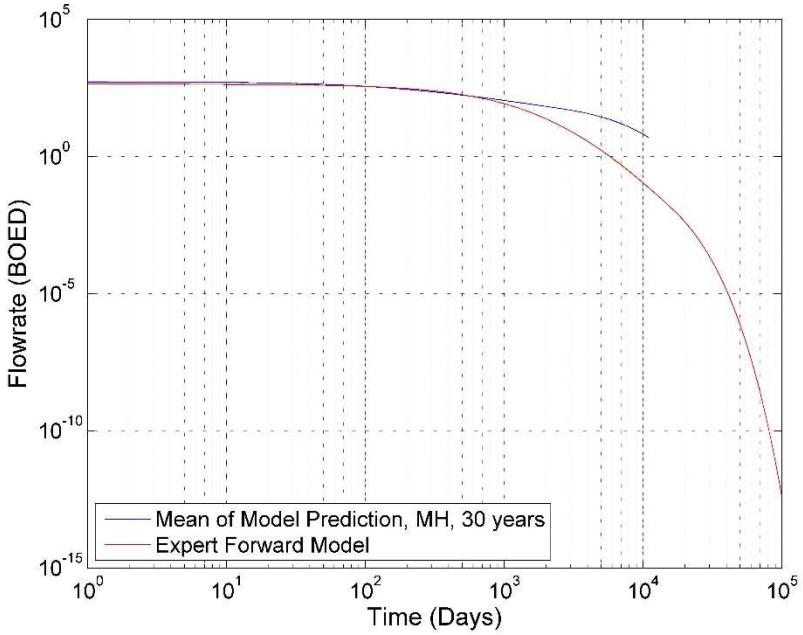

Fig. 329 — The mean of the realizations and the MH model, plotted for 30 years for Well 40

Well 40 – Power Law Exponential Model

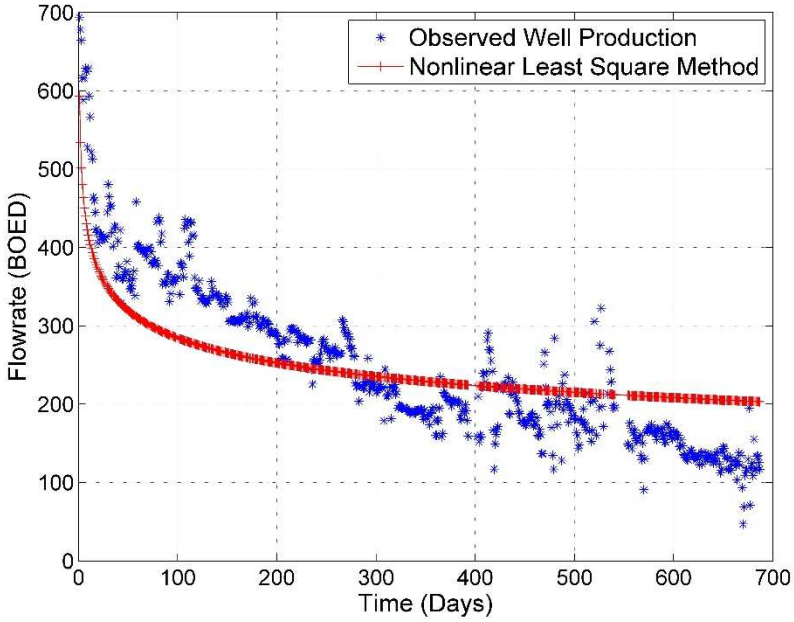

Fig. 330 — Results of the least squares optimization against the production data of Well 40 for the PLE Model

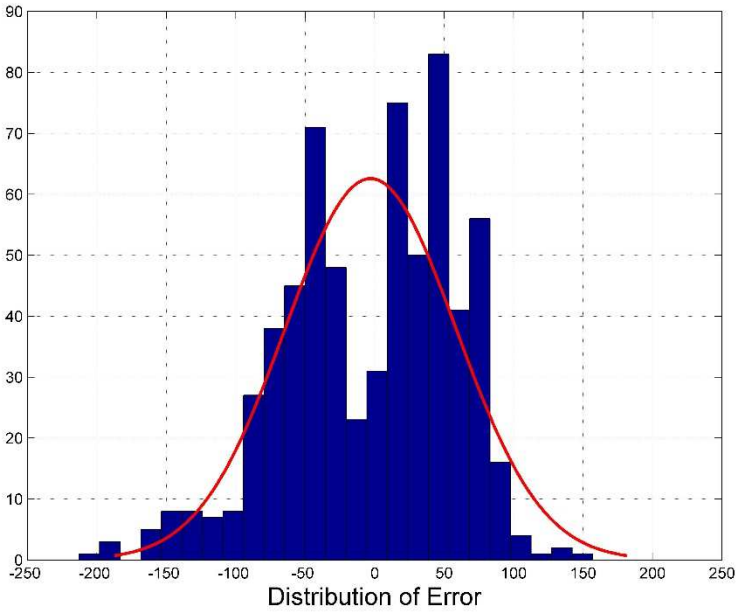

Fig. 331 — The distribution of error between the production data and the LSQ results for Well 40 for the PLE Model

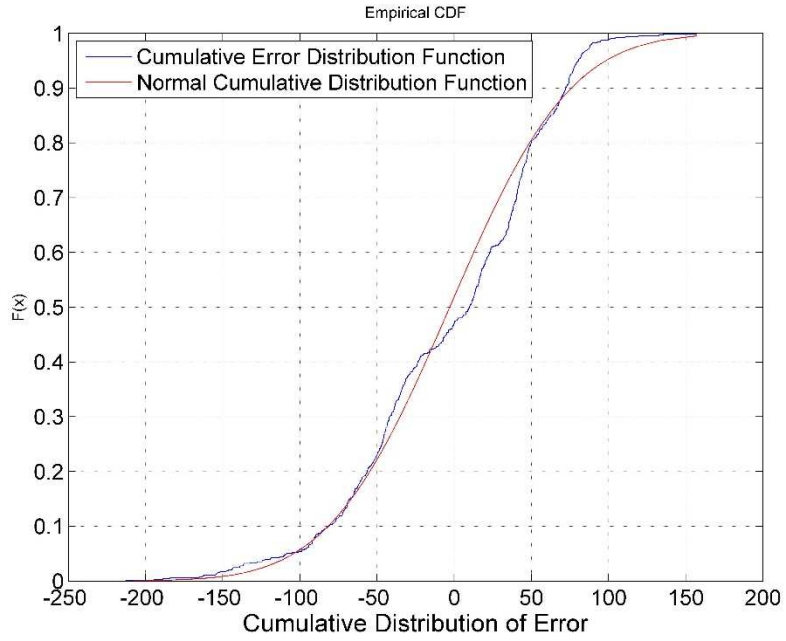

Fig. 332 — The cumulative distribution of error is plotted against the normal cumulative distribution function of Well 40 for the PLE Model

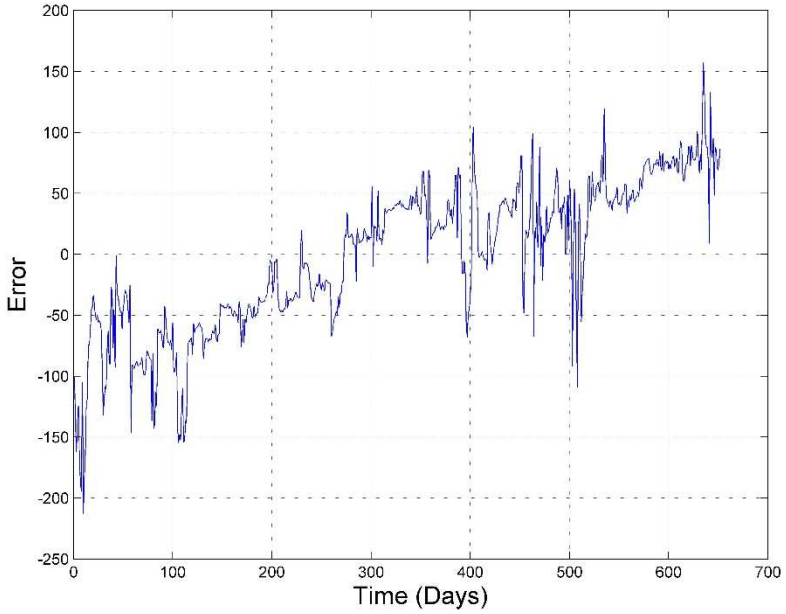

Fig. 333 — The error of the least squares optimization against the number of production days of Well 40 for the PLE Model

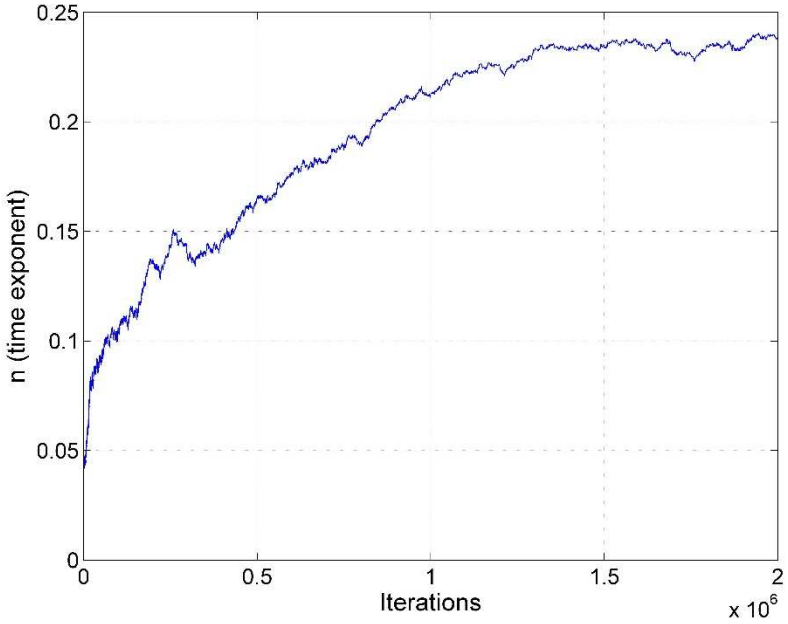

Fig. 334 — MCMC results of *n* for the PLE model of Well 40

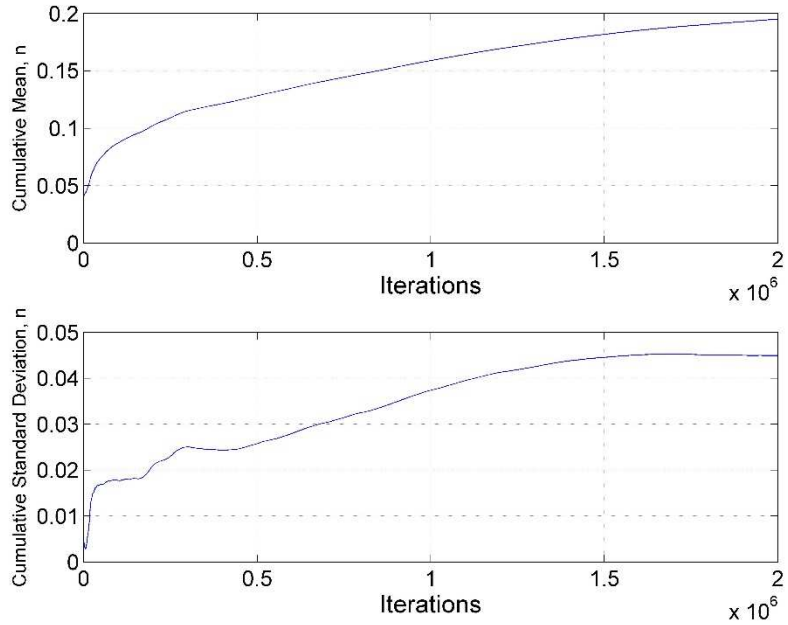

Fig. 335 — Cumulative mean and standard deviation of *n* of Well 40 using the PLE model

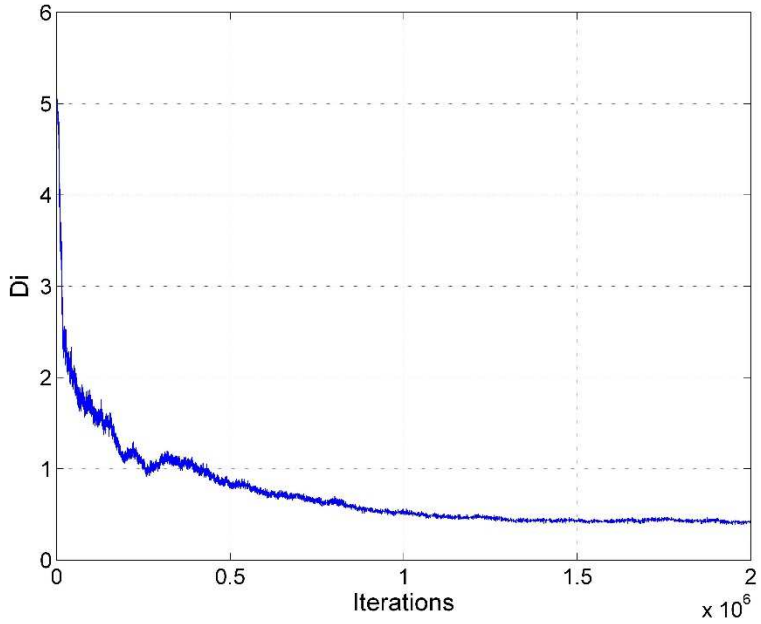

Fig. 336 — MCMC results of D_i for the MH model of Well 40 using the PLE model

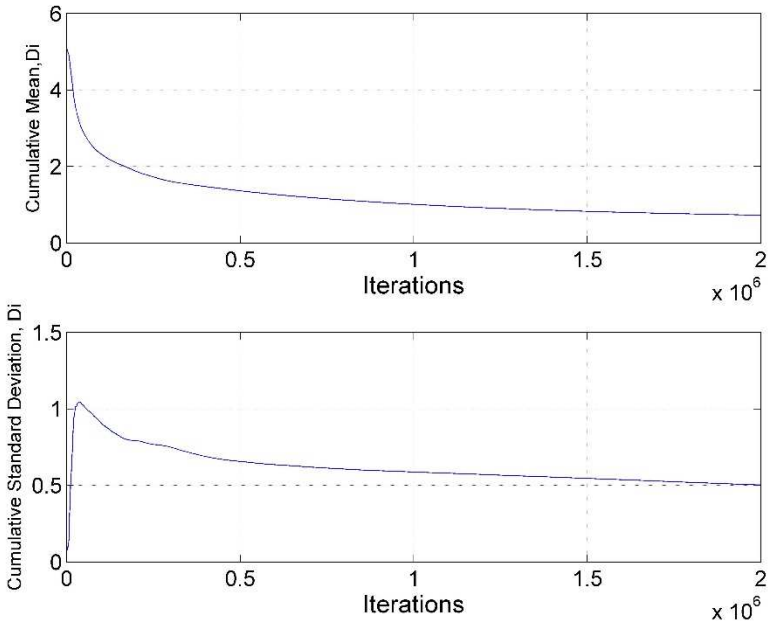

Fig. 337 — Cumulative mean and standard deviation of D_i of Well 40 using the PLE model

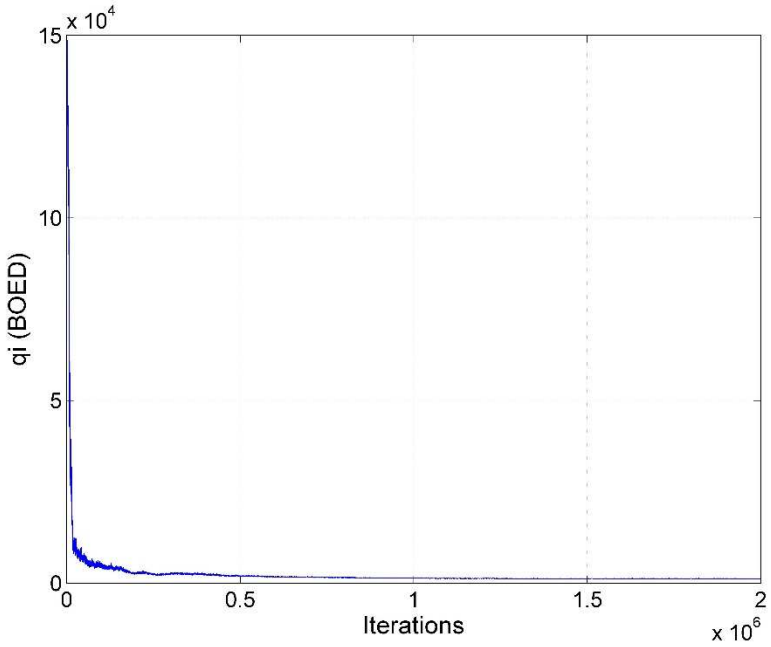

Fig. 338 — MCMC results of q_i for the MH model of Well 40 using the PLE model

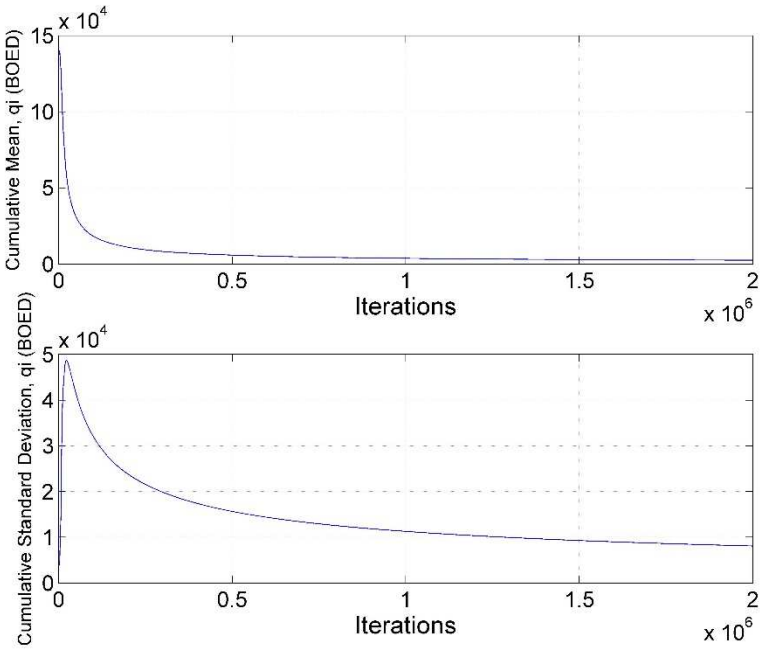

Fig. 339 — Cumulative mean and standard deviation of q_i of Well 40 using the PLE model

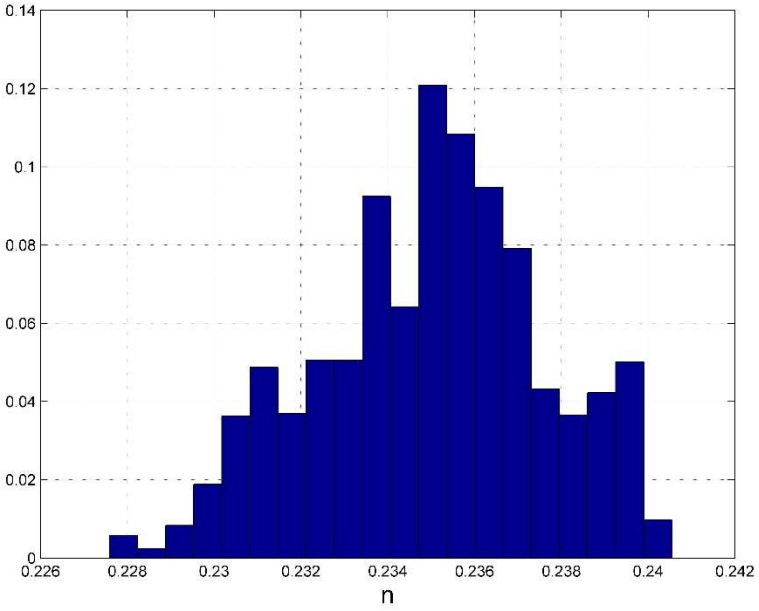

Fig. 340 — Posterior relative frequency histogram of *n* of Well 40 using the PLE model

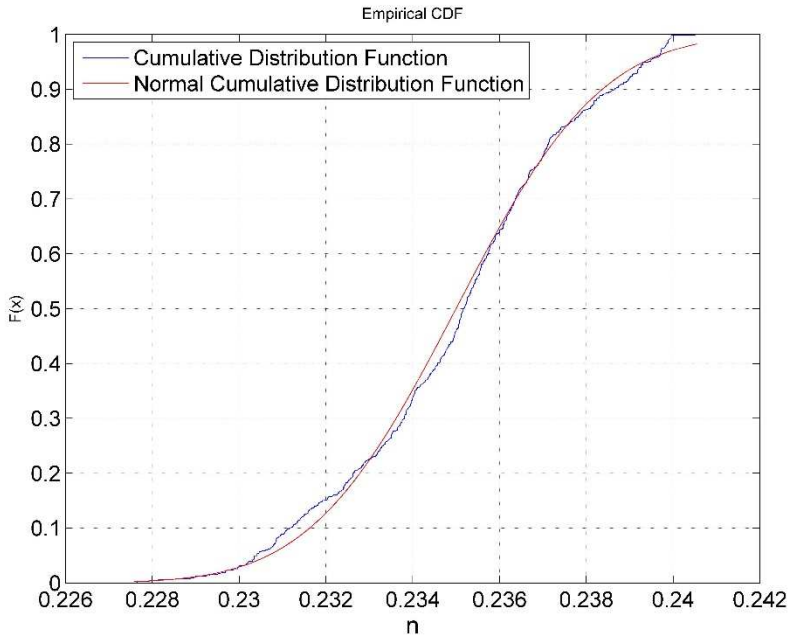

Fig. 341 — Cumulative posterior relative frequency histogram of *n* of Well 40 using the PLE model

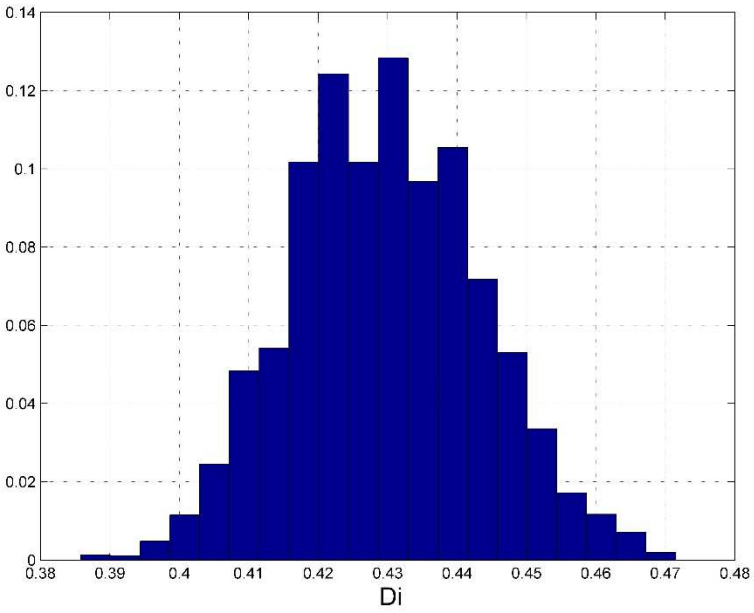

Fig. 342 — Posterior relative frequency histogram of D_i of Well 40 using the PLE model

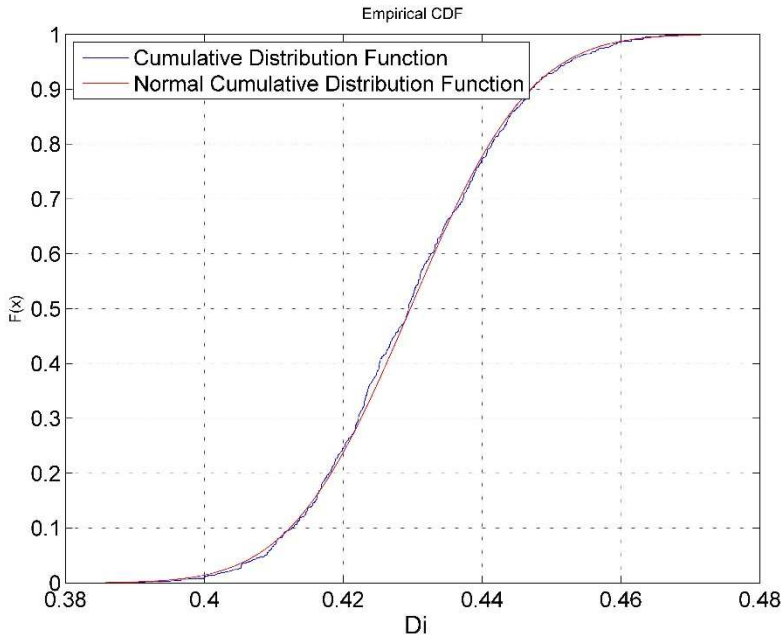

Fig. 343 — Cumulative posterior relative frequency histogram of D_i of Well 40 using the PLE model

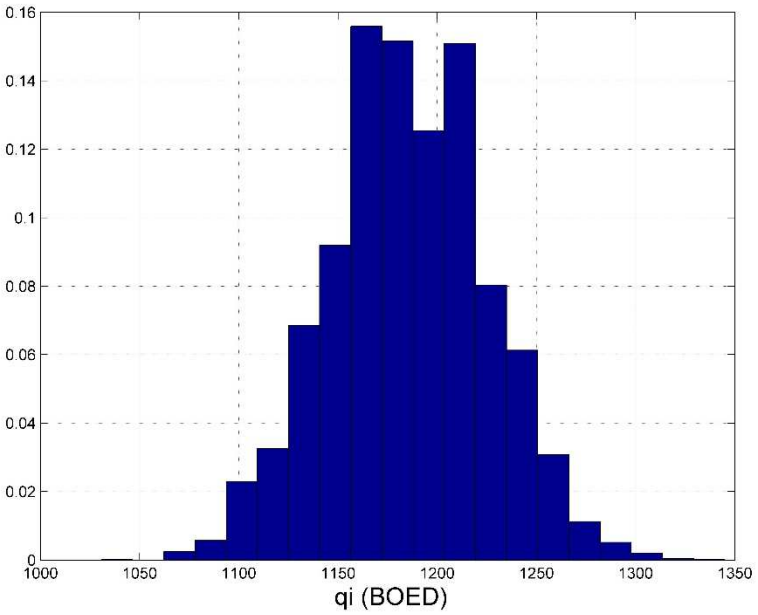

Fig. 344 — Posterior relative frequency histogram of q_i of Well 40 using the PLE model

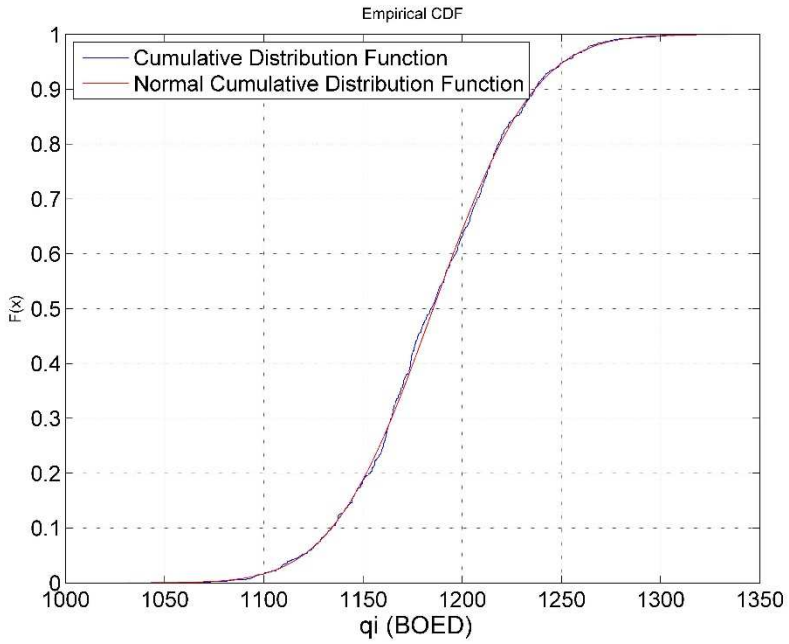

Fig. 345 — Cumulative posterior relative frequency histogram of q_i of Well 40 using the PLE model

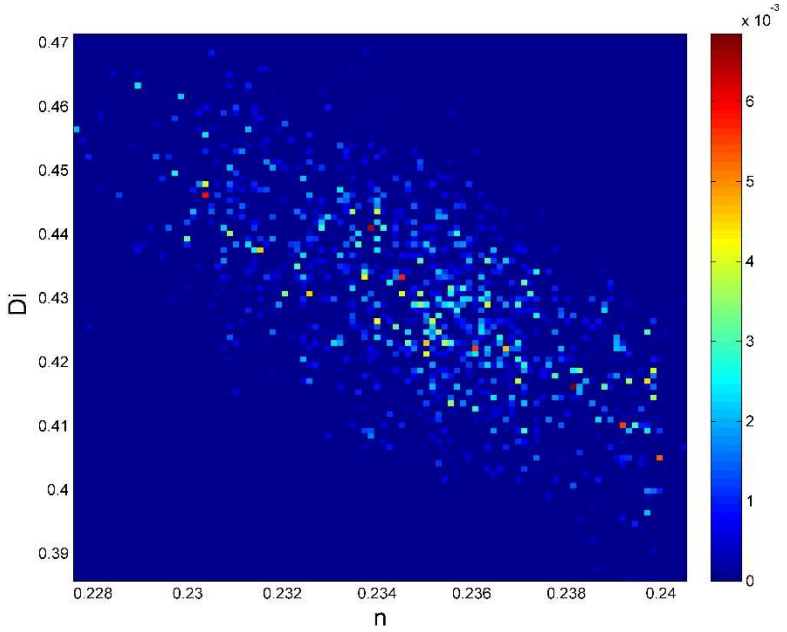

Fig. 346 — Relative frequency diagram between D_i and n of Well 40 using the PLE model

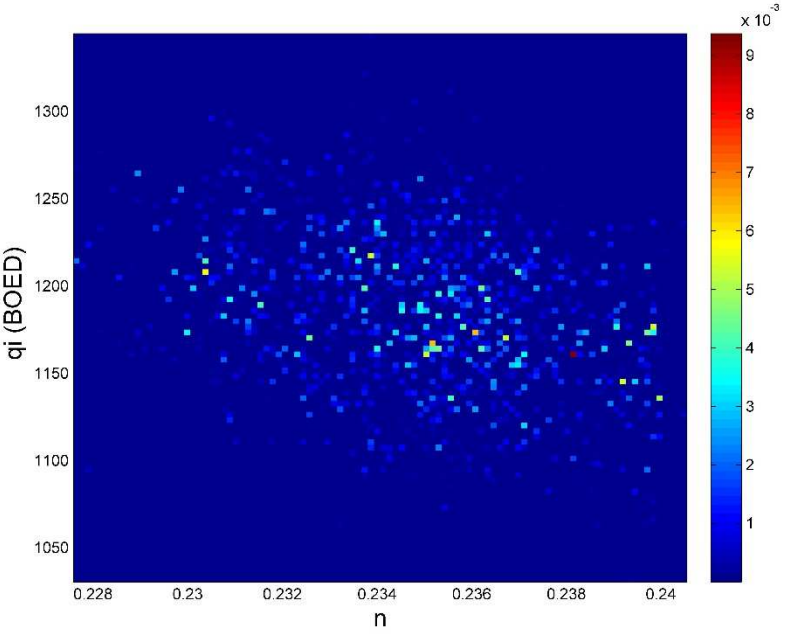

Fig. 347 — Relative frequency diagram between q_i and n of Well 40 using the PLE model

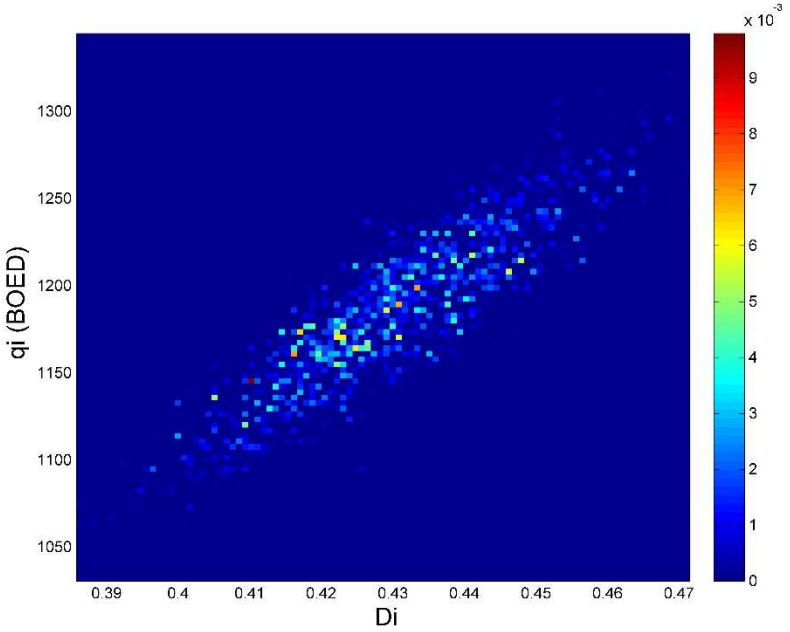

Fig. 348 — Relative frequency diagram between q_i and D_i of Well 40 using the PLE model

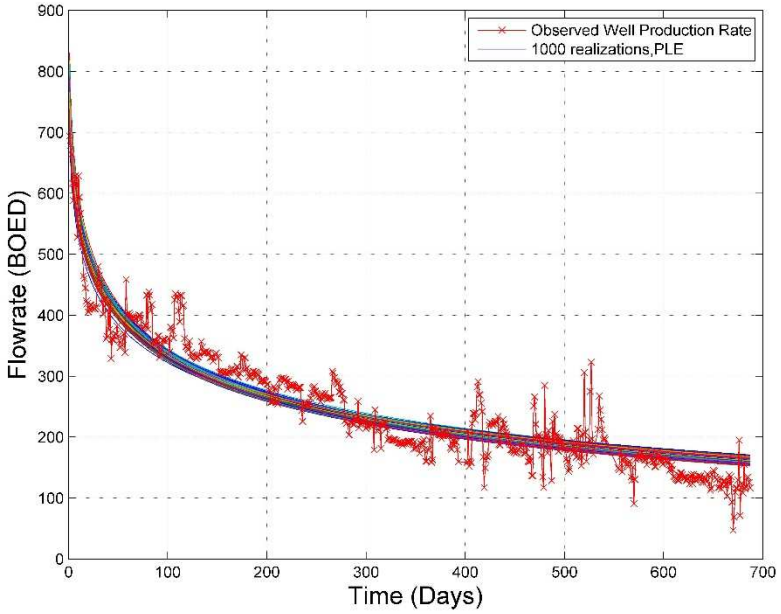

Fig. 349 — The 1,000 realizations of the model predictions using the Bayesian paradigm of Well 40 with the PLE model

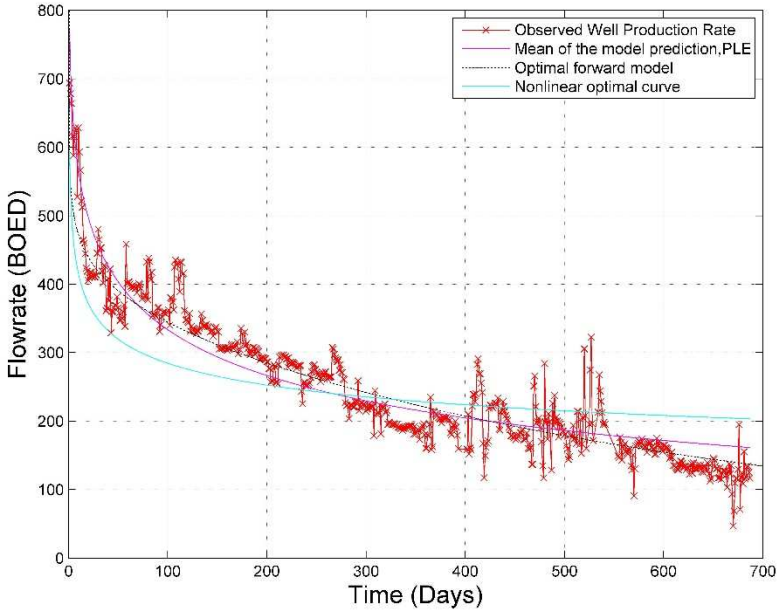

Fig. 350 — The production data with the mean of the realizations, the optimal forward model and the PLE model of Well 40

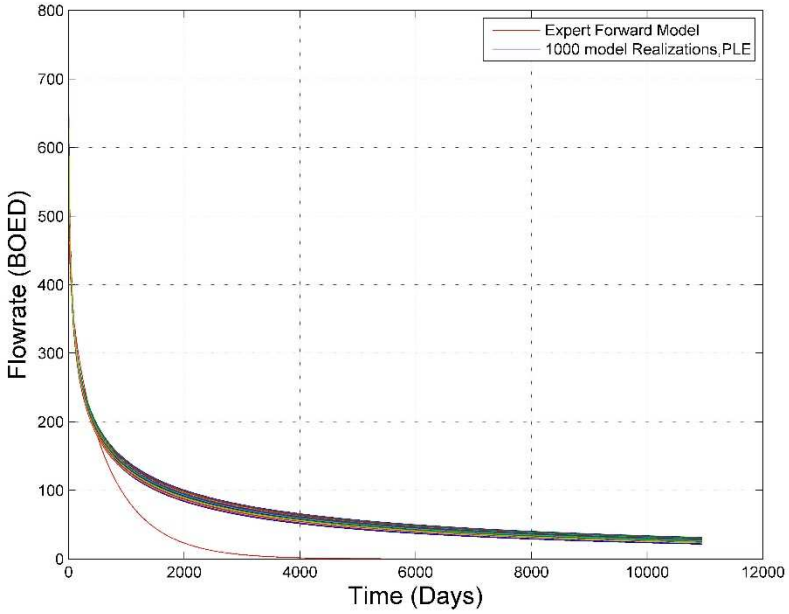

Fig. 351 — The 1,000 realizations of the model predictions using the Bayesian paradigm for 30 years of Well 40

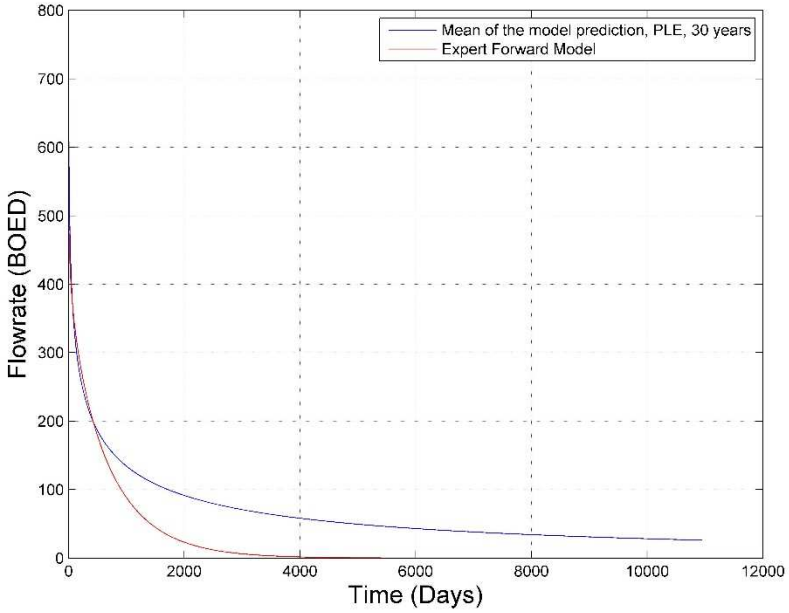

Fig. 352 — The mean of the realizations and the PLE model, plotted for 30 years for Well 40

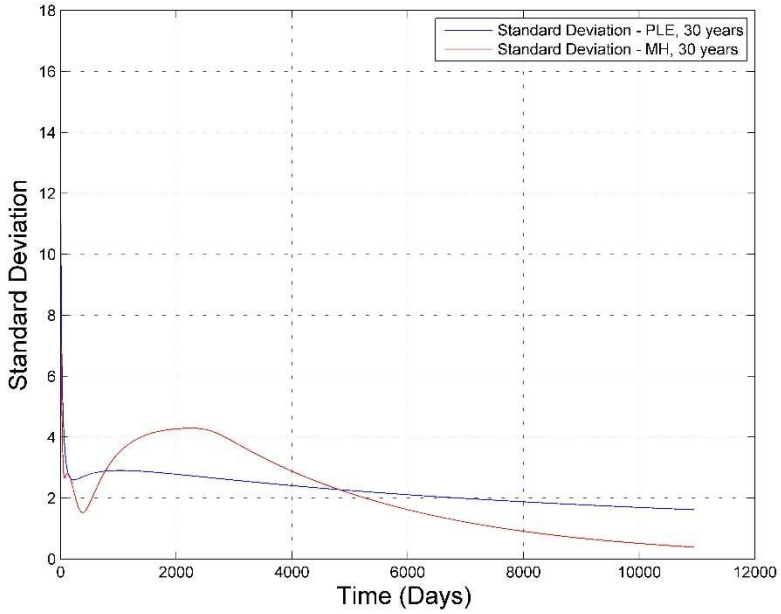

Fig. 353 — Comparison of the Standard Deviation of the two Bayesian forecasts using the MH and PLE models of Well 40

Analysis

Well 40 shows a beautiful convergence of the MCMC results for all three parameter of the MH model, seen in **Fig. 311**, **313** and **315**. The posterior distributions are also as expected – Gaussian for the *b*-factor and for q_i, seen in **Fig. 317** and **321**, respectively, and lognormal for $D_{i,}$ which has been a trend in this study, shown in **Fig. 319**.

If we compare the MCMC results while applying the MH model with the results produced when applying the PLE model, we notice that this model does not converge well for any of the parameters, shown in **Fig. 334, 336** and **338**. This model was let to run for 20 million iterations, as we were hoping for a better convergence for all the parameters.

Since the parameters did not converge when the MCMC was applied, the posteriors of all three parameters are also inaccurate, seen in **Fig. 340**, **342** and **344**. If the model ran for more iterations, it is probable that the parameters would converge, because it is evident that they beginning to towards the end of the 20 million iterations.

Based on the posterior distributions of the three parameters, we created the relative frequency histograms that show the relationship between two different parameters -- D_i vs. *b*, q_i vs. *b* and q_i vs D_i for the MH model and D_i vs. *n*, q_i vs. *n* and q_i vs D_i for the PLE model. These results can be seen in **Fig. 323, 324** and **325**, respectively, for the MH model and **Fig. 346, 347** and **348**, respectively, for the PLE model.

From Fig. 323, 324 and 325, we see beautiful representations of the relationship between these parameters. It seems that Fig. 323 shows an exponential relationship between *Di* and *b*, whereas Fig. 324 shows a linear relationship between *qi* and *b*, as does Fig. 325.

For the PLE results of the relative frequency histograms, the trend is visible, and it is the same trend that has been visible in other PLE results, however there is no definition of the

relationship between the parameters. This is due to the lack of convergence in the MCMC results.

Finally we reach the realizations of the Bayesian paradigm using the MH and PLE models. We notice when we plot the mean of the realizations versus the optimal forward model (the results from the LSQ optimization), and the expert forward model (either MH or PLE), the mean of the model prediction and the expert forward model often times have close values for the 700 production days plotted. However, when we extend the results to 30 years that there is a divergence between two sets of results. In this case, the MH model, when applied to the Bayesian paradigm underestimates reserves, as seen in **Fig. 329.** This is the same result that is presented for the PLE model when applied to the Bayesian paradigm, shown in **Fig. 352**. These results show that the forward models can overestimate or underestimate the reserves.

The graph that compares the standard deviations of the two sets of Bayesian results, **Fig. 353**, identifies the uncertainty of the two models. From the results, it can be seen that the uncertainty of the MH model reaches a maximum around 2,000 days, however it decreases rapidly, and we can see that the uncertainty is very close to 0 after the 30 years forecasted. However, we see that the PLE model's uncertainty remains almost constant throughout the forecast, which is not ideal. When applying the Bayesian paradigm, we expect the uncertainty of the model to decrease because the model is gaining more knowledge and better estimating the following point of the forecast. From these results, we can see that the MH model is doing just that but the PLE model is not.

APPENDIX VIII

RESULTS AND ANALYSIS OF WELL 67

Well 67 – Modified Hyperbolic Model

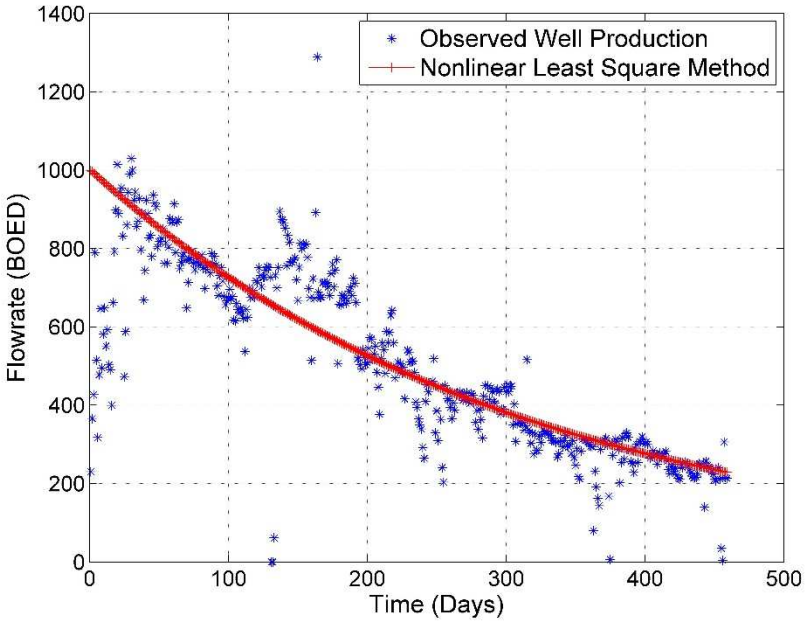

Fig. 354 — Results of the least squares optimization against the production data of Well 67 for the MH Model

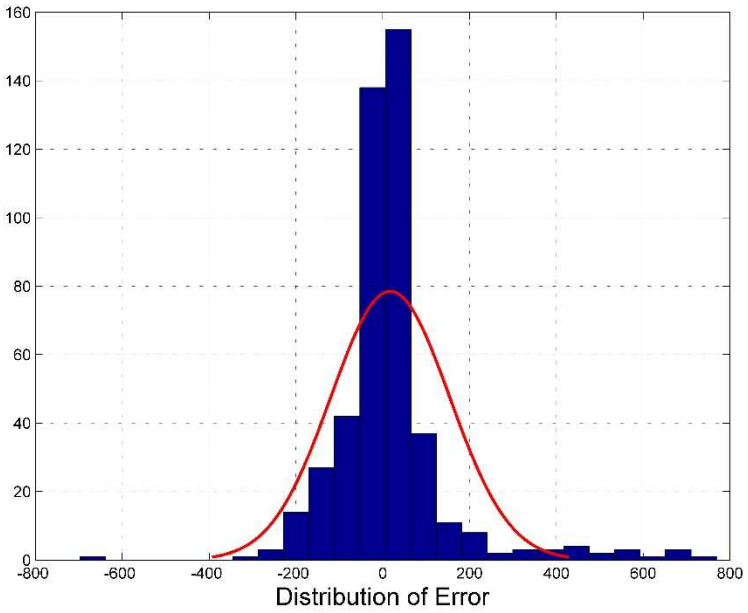

Fig. 355 — The distribution of error between the production data and the LSQ results for Well 67 for the MH Model

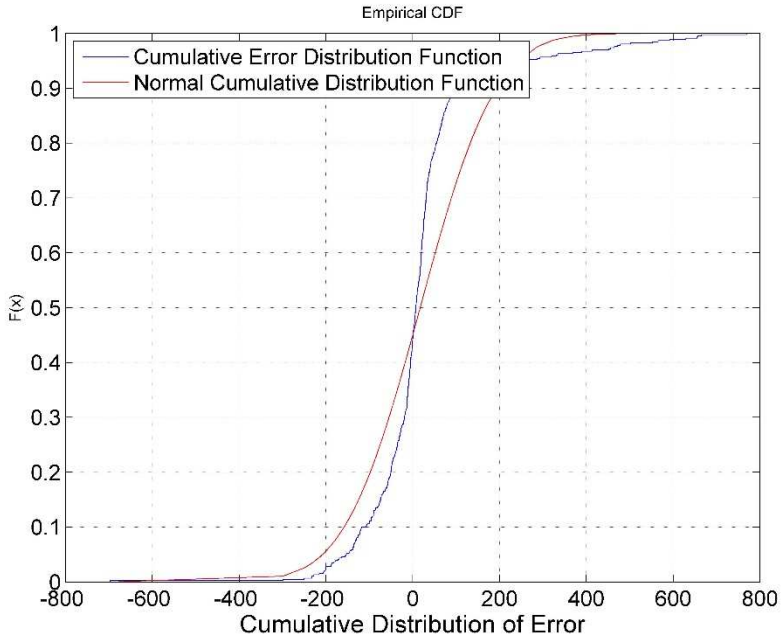

Fig. 356 — The cumulative distribution of error is plotted against the normal cumulative distribution function of Well 67 for the MH Model

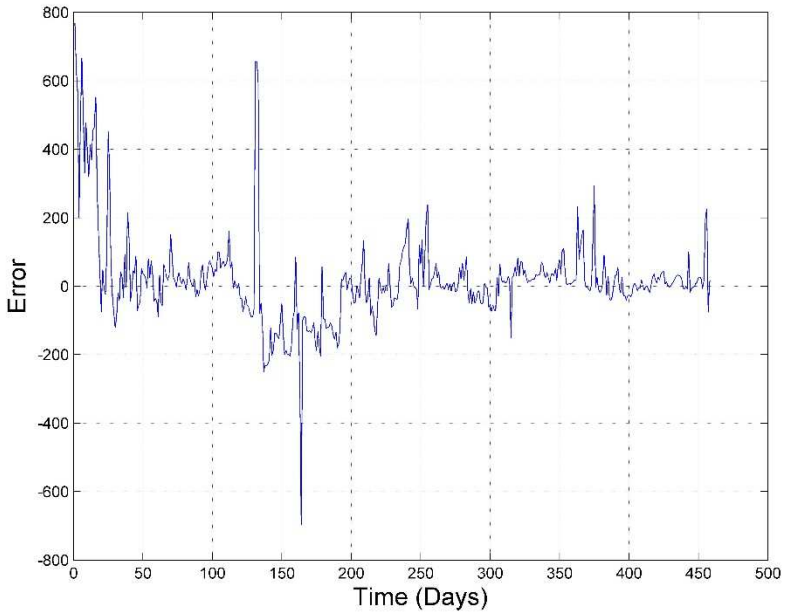

Fig. 357 — The error of the least squares optimization against the number of production days of Well 67 for the MH Model

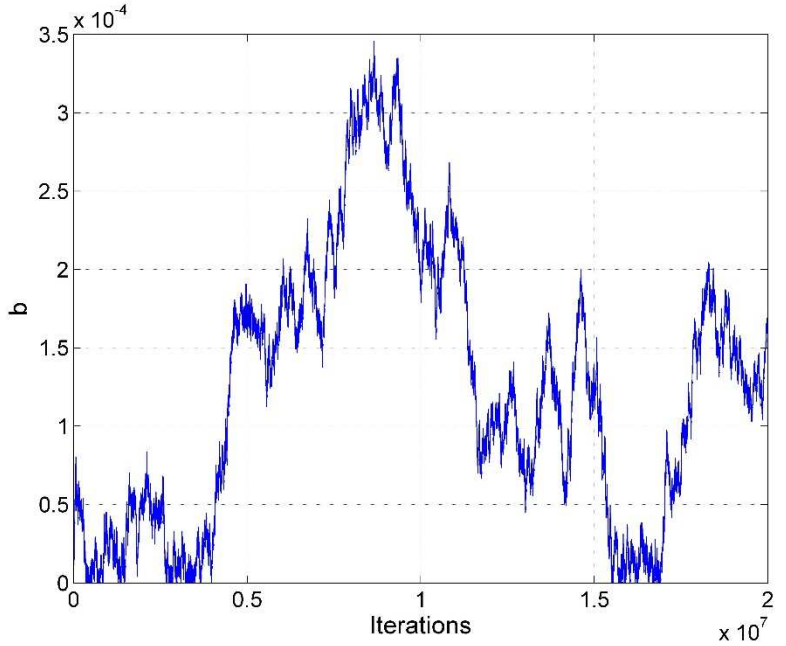

Fig. 358 — MCMC results of the *b*-factor for the MH model of Well 67 using the MH model

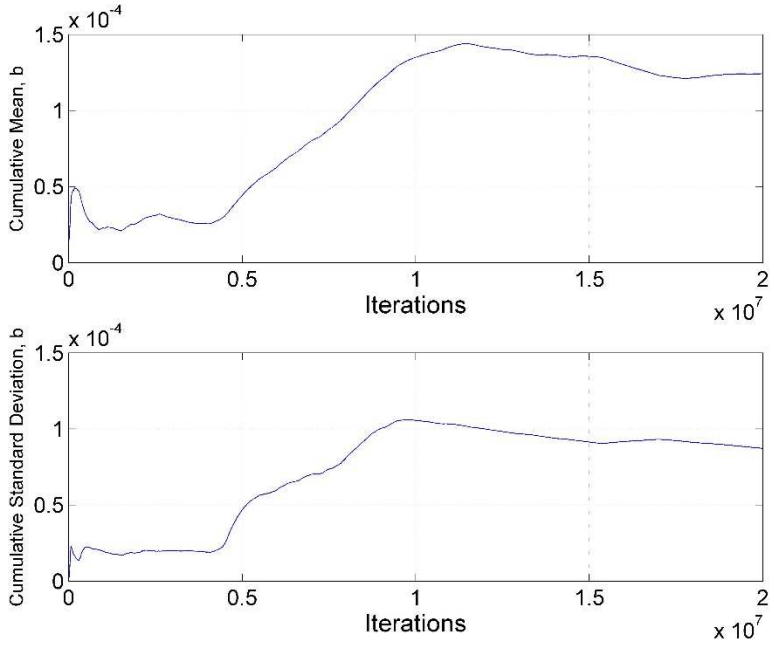

Fig. 359 — Cumulative mean and standard deviation of the *b*-factor of Well 67 using the MH model

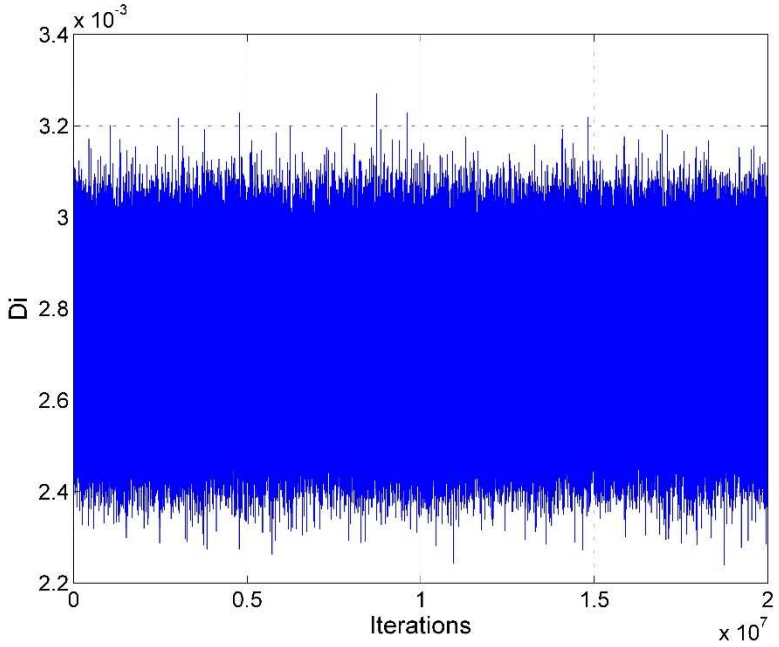

Fig. 360 — MCMC results of D_i for the MH model of Well 67 using the MH model

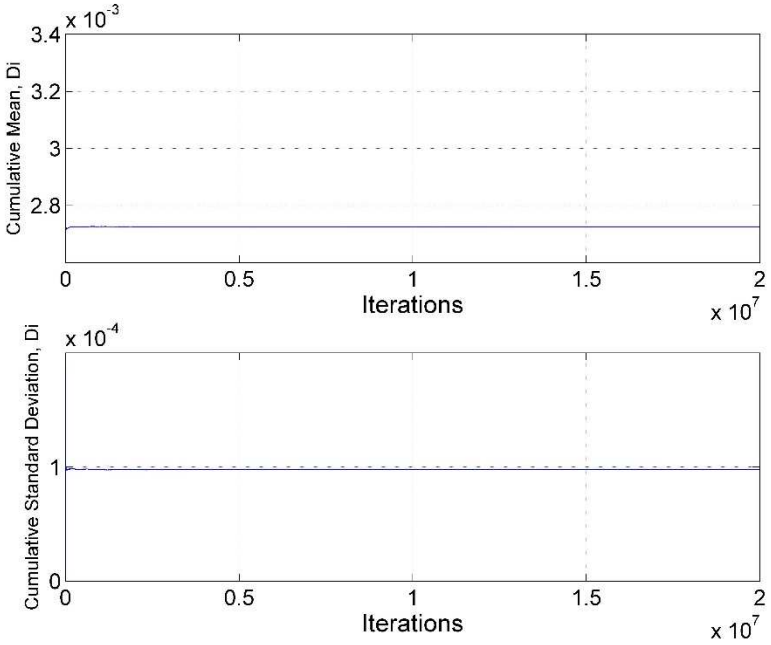

Fig. 361 — Cumulative mean and standard deviation of D_i of Well 67 using the MH model

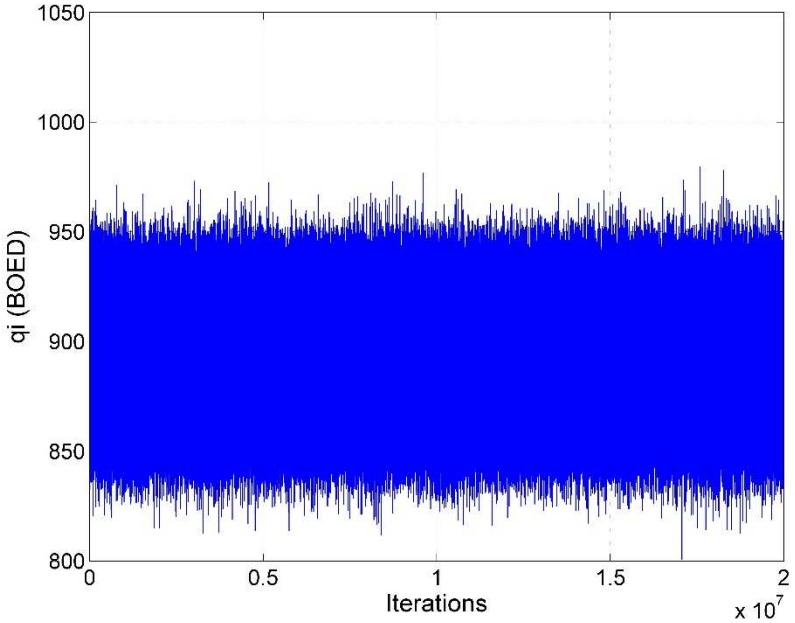

Fig. 362 — MCMC results of q_i for the MH model of Well 67 using the MH model

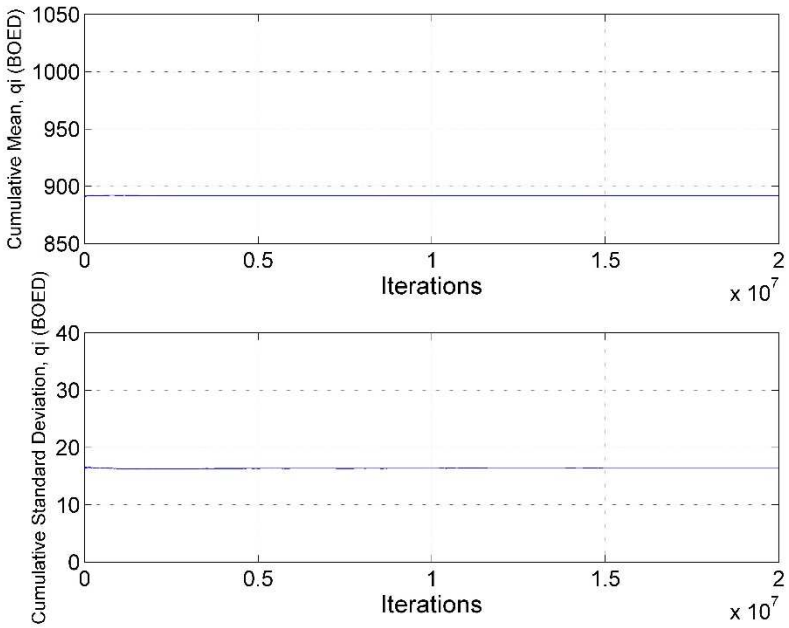

Fig. 363 — Cumulative mean and standard deviation of q_i of Well 67 using the MH model

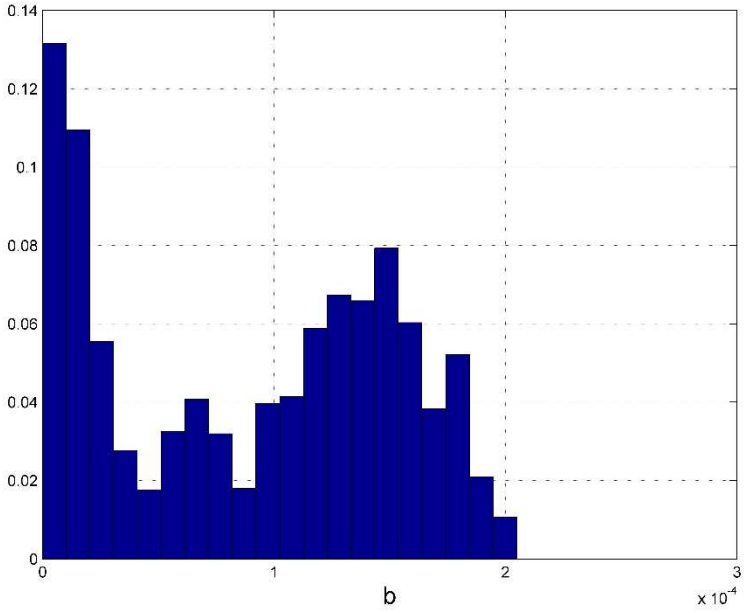

Fig. 364 — Posterior relative frequency histogram of *b* of Well 67 using the MH model

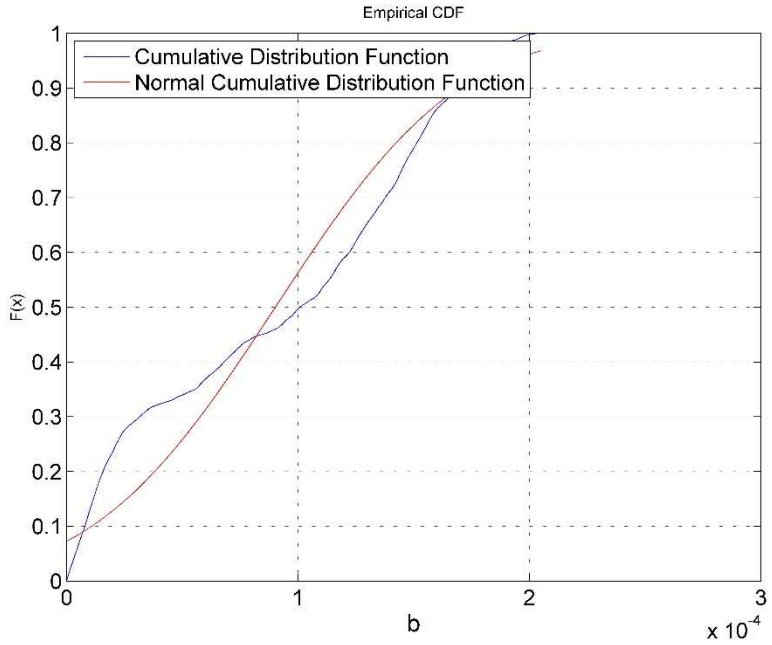

Fig. 365 — Cumulative posterior relative frequency histogram of the *b*-factor of Well 67 using the MH model

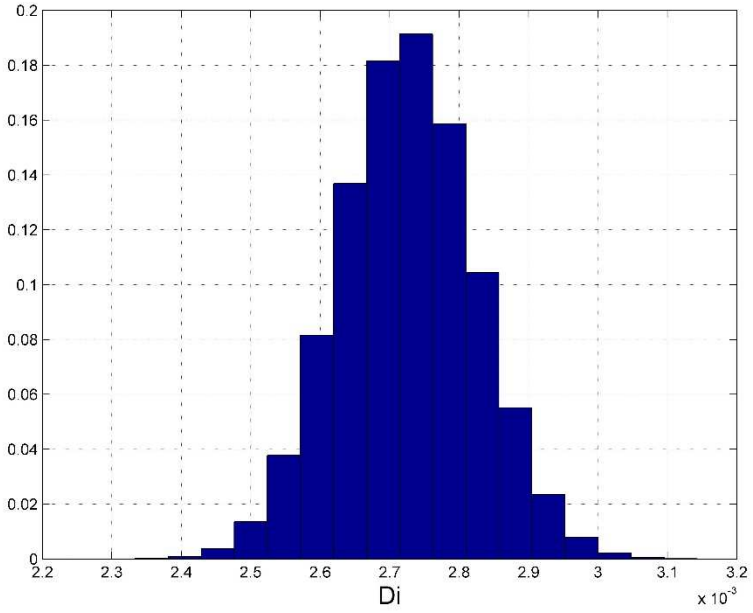

Fig. 366 — Posterior relative frequency histogram of D_i of Well 67 using the MH model

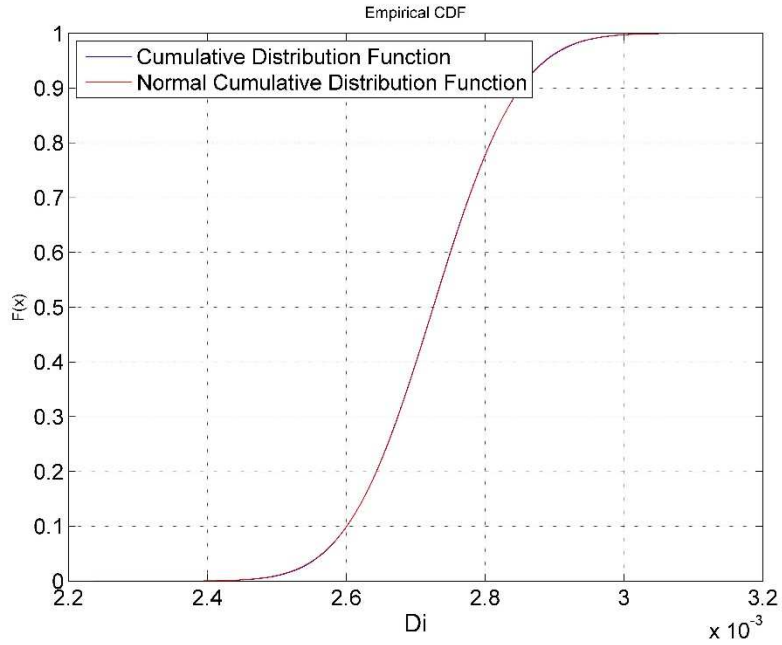

Fig. 367 — Cumulative posterior relative frequency histogram of D_i of Well 67 using the MH model

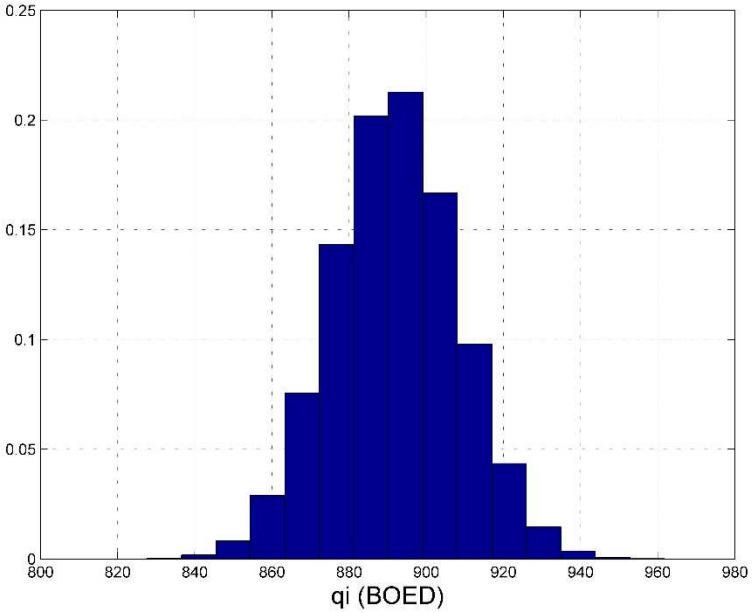

Fig. 368 — Posterior relative frequency histogram of q_i of Well 67 using the MH model

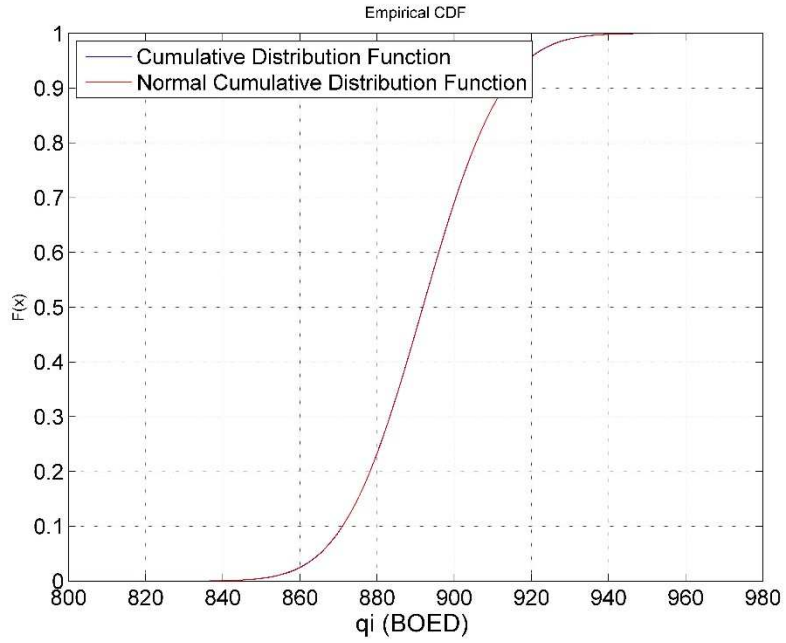

Fig. 369 — Cumulative posterior relative frequency histogram of q_i of Well 67 using the MH model

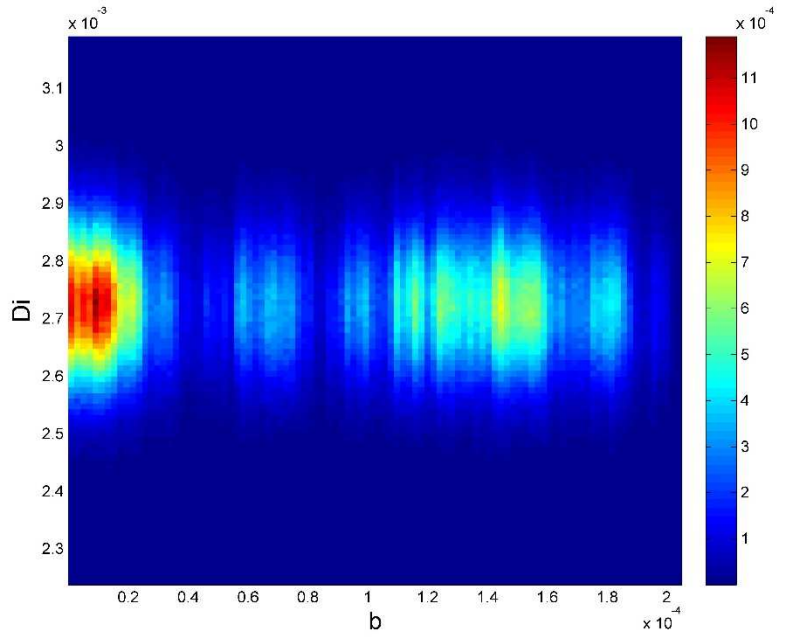

Fig. 370 — Relative frequency diagram between D_i and b of Well 67 using the MH model

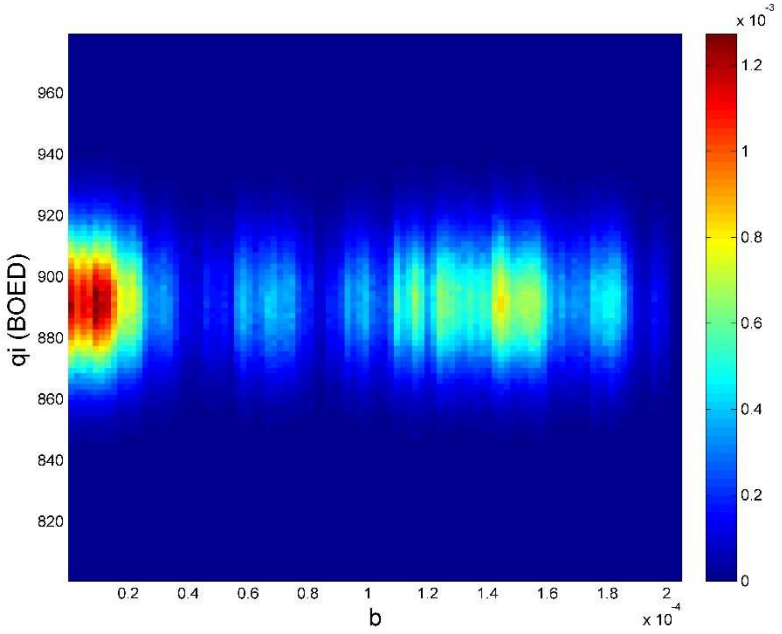

Fig. 371 — Relative frequency diagram between q_i and b of Well 67 using the MH model

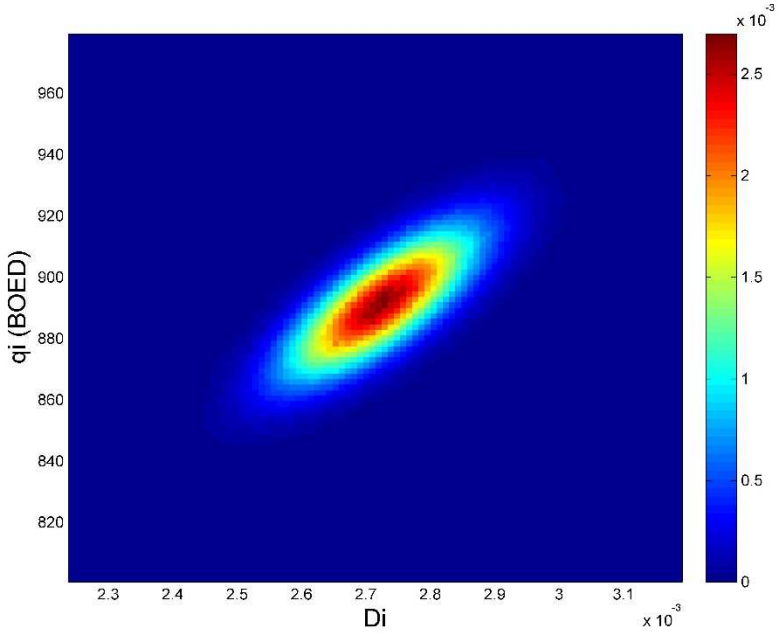

Fig. 372 — Relative frequency diagram between q_i and D_i of Well 67 using the MH model

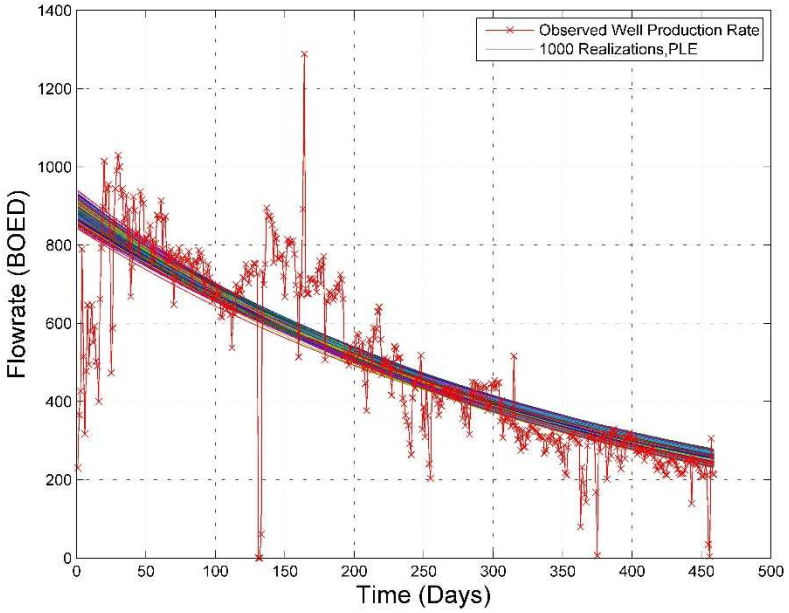

Fig. 373 — The 1,000 realizations of the model predictions using the Bayesian paradigm of Well 67 with the MH model

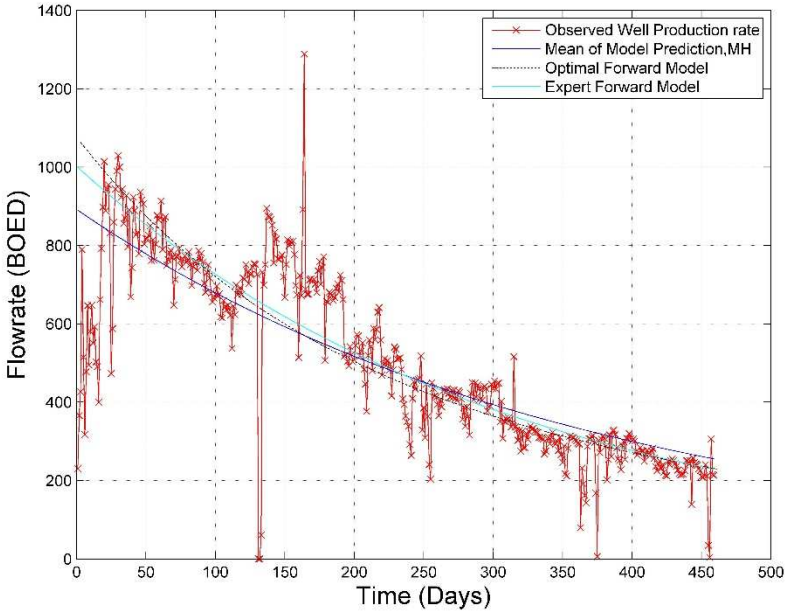

Fig. 374 — The production data with the mean of the realizations, the optimal forward model and the MH model of Well 67

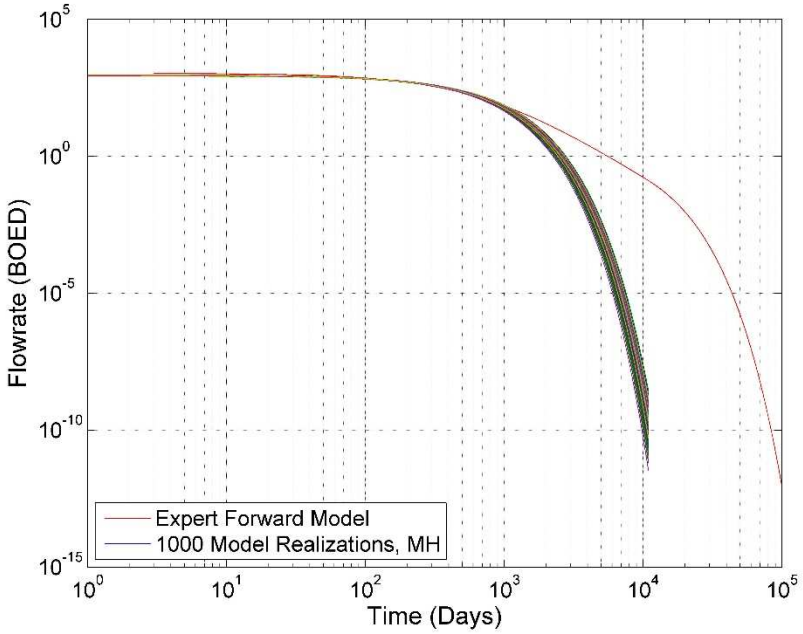

Fig. 375 — The 1,000 realizations of the model predictions using the Bayesian paradigm for 30 years of Well 67

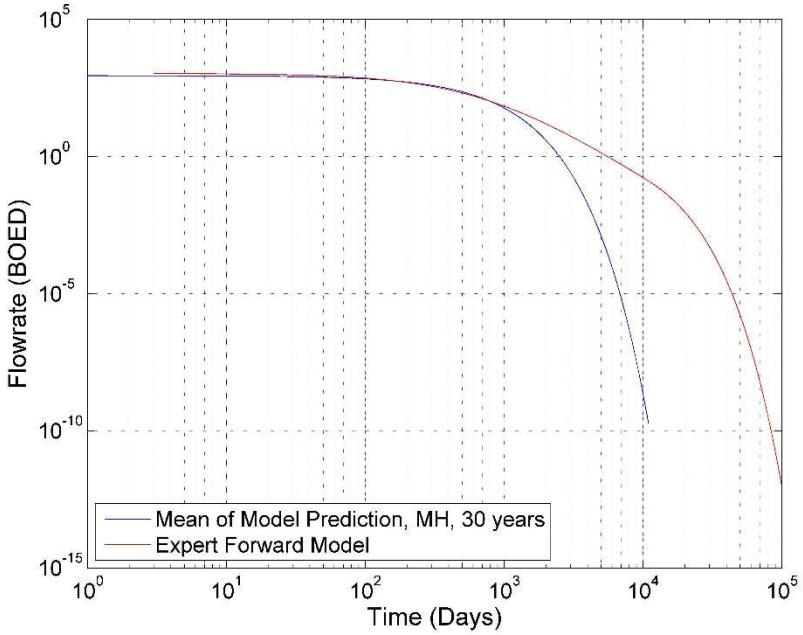

Fig. 376 — The mean of the realizations and the MH model, plotted for 30 years for Well 67

Well 67 – Power Law Exponential Model

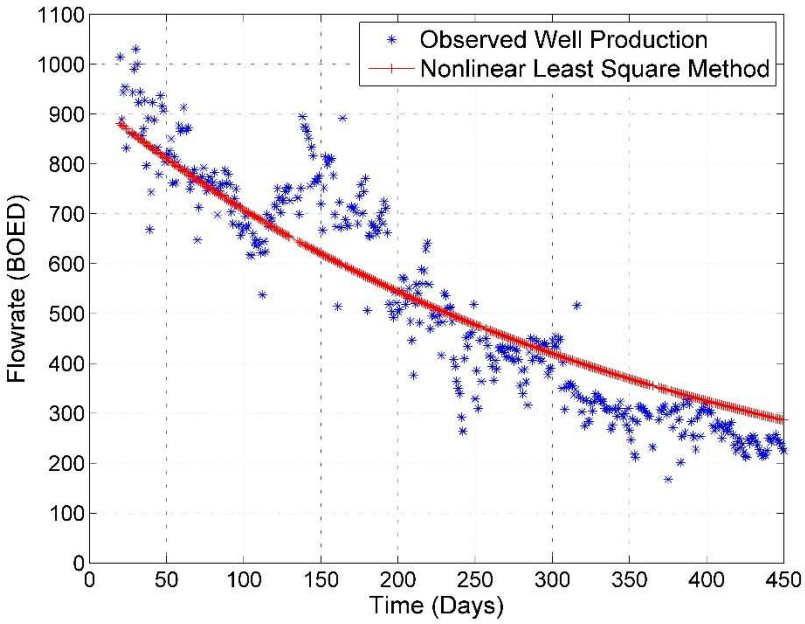

Fig. 377 — Results of the least squares optimization against the production data of Well 67 for the PLE Model

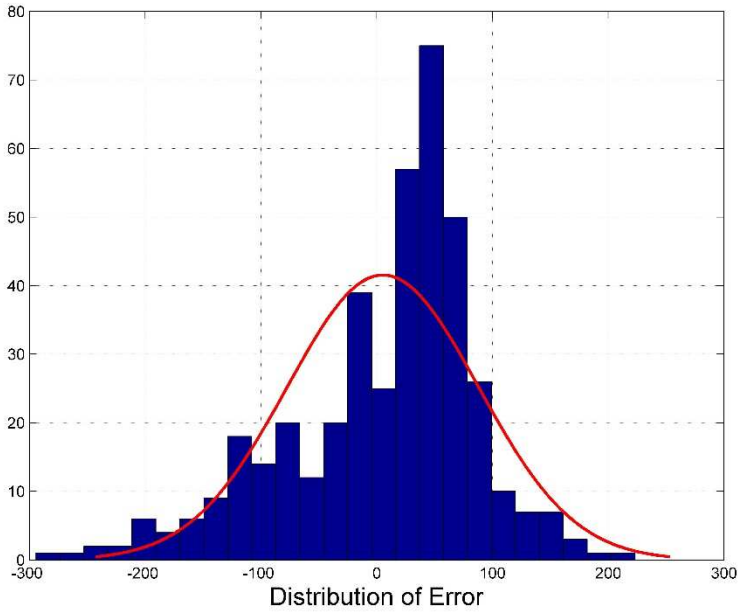

Fig. 378 — The distribution of error between the production data and the LSQ results for Well 67 for the PLE Model

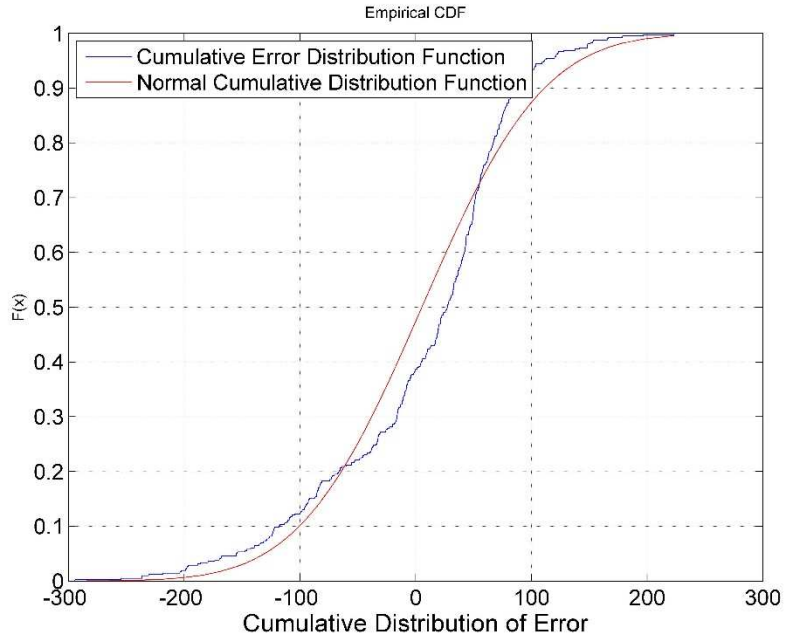

Fig. 379 — The cumulative distribution of error is plotted against the normal cumulative distribution function of Well 67 for the PLE Model

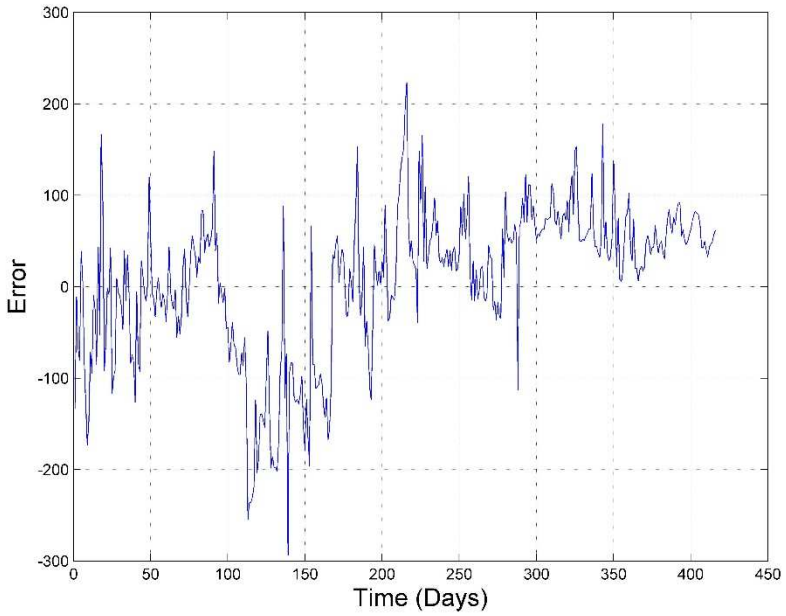

Fig. 380 — The error of the least squares optimization against the number of production days of Well 67 for the PLE Model

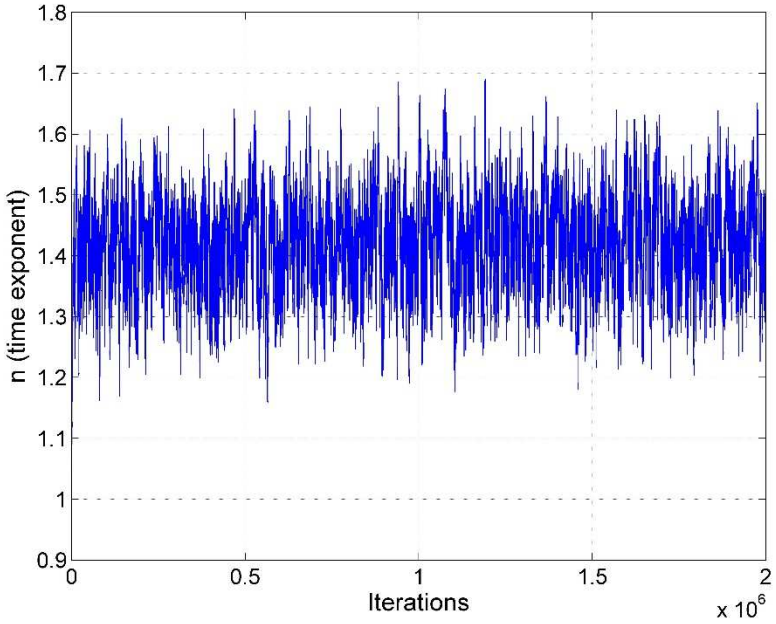

Fig. 381 — MCMC results of *n* for the PLE model of Well 67

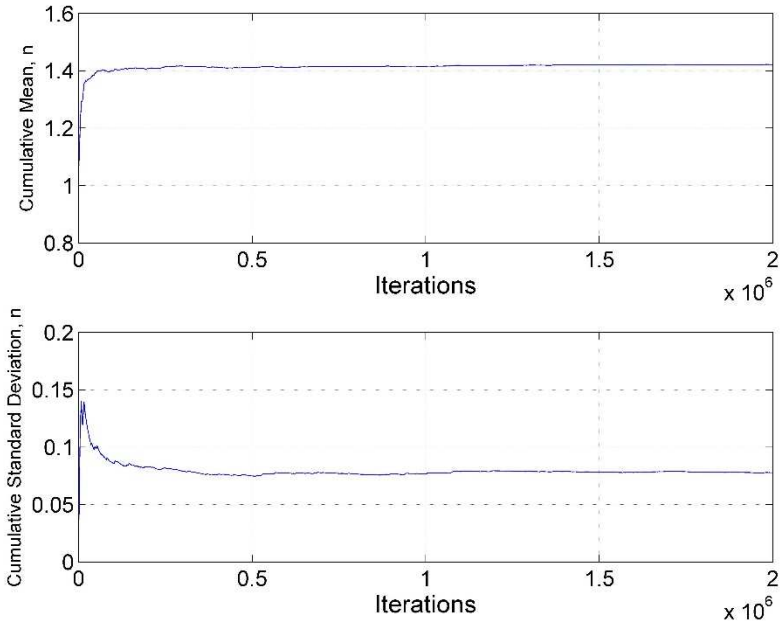

Fig. 382 — Cumulative mean and standard deviation of *n* of Well 67 using the PLE model

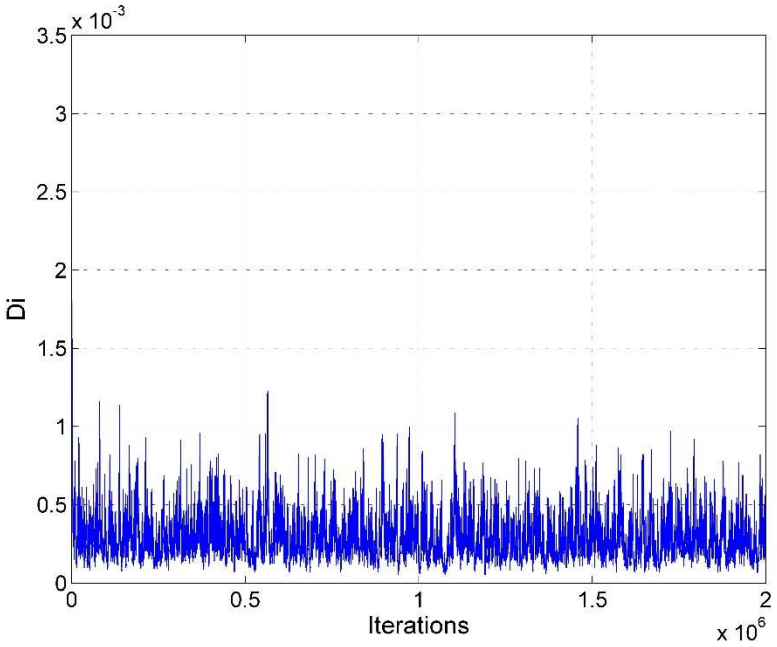

Fig. 383 — MCMC results of D_i for the MH model of Well 67 using the PLE model

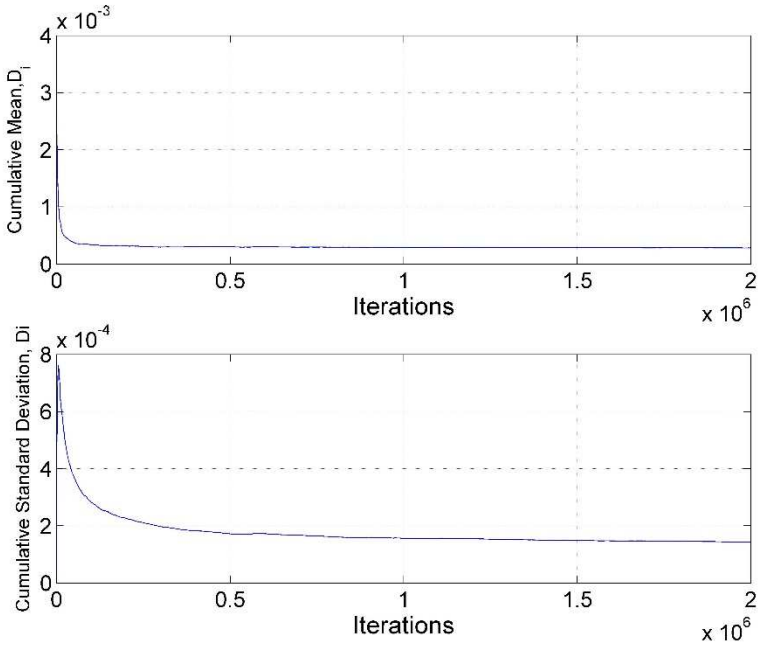

Fig. 384 — Cumulative mean and standard deviation of D_i of Well 67 using the PLE model

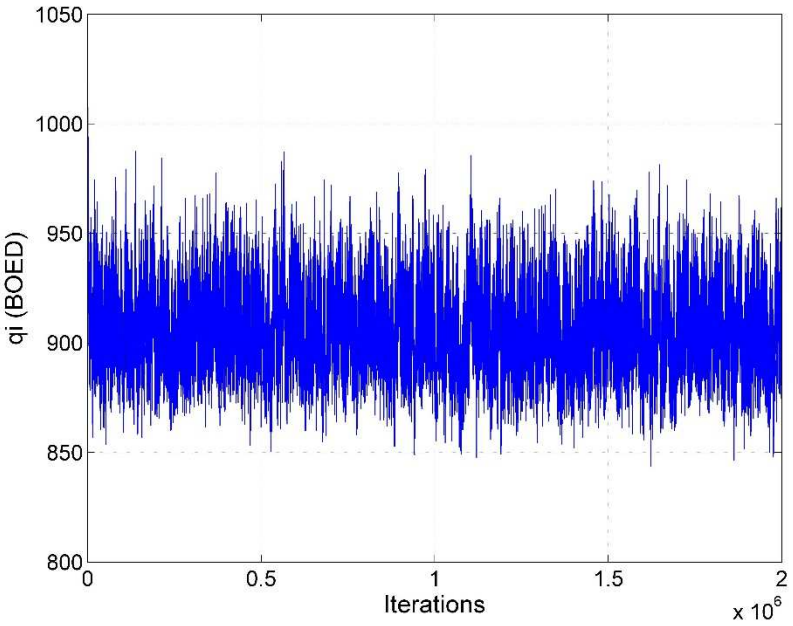

Fig. 385 — MCMC results of q_i for the MH model of Well 67 using the PLE model

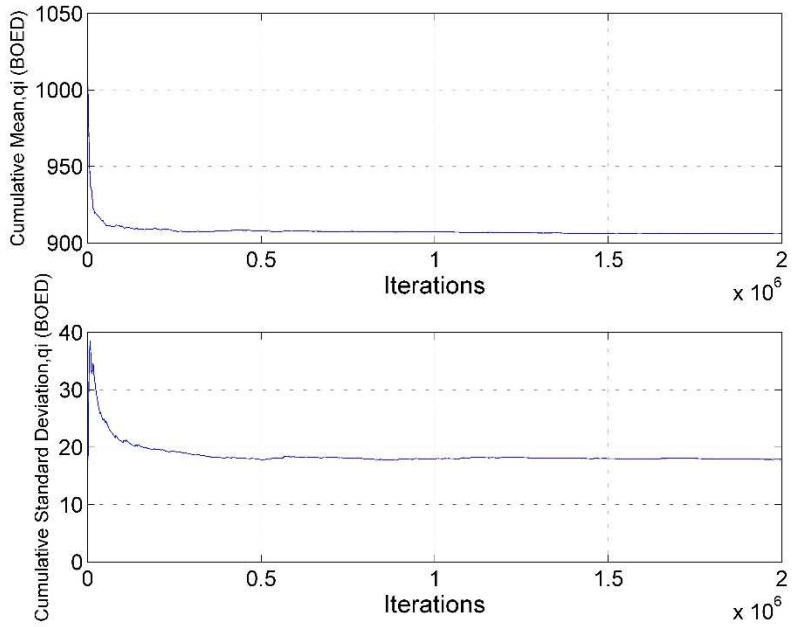

Fig. 386 — Cumulative mean and standard deviation of q_i of Well 67 using the PLE model

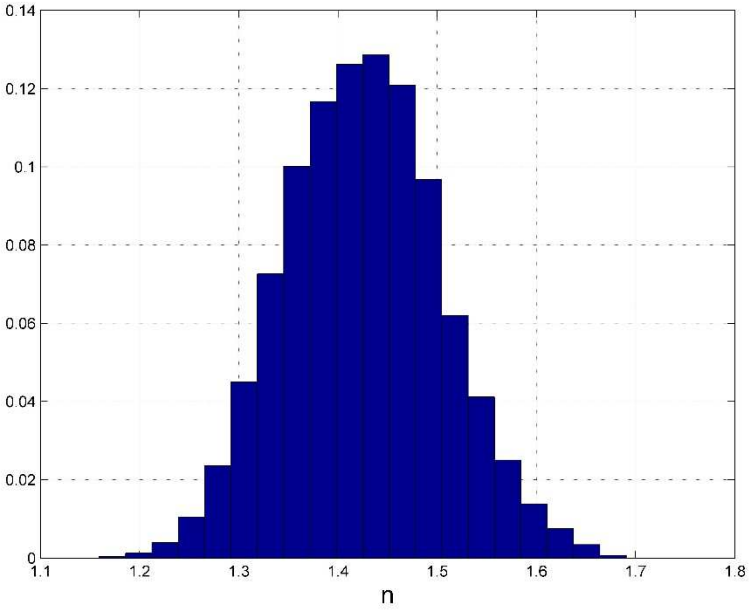

Fig. 387 — Posterior relative frequency histogram of *n* of Well 67 using the PLE model

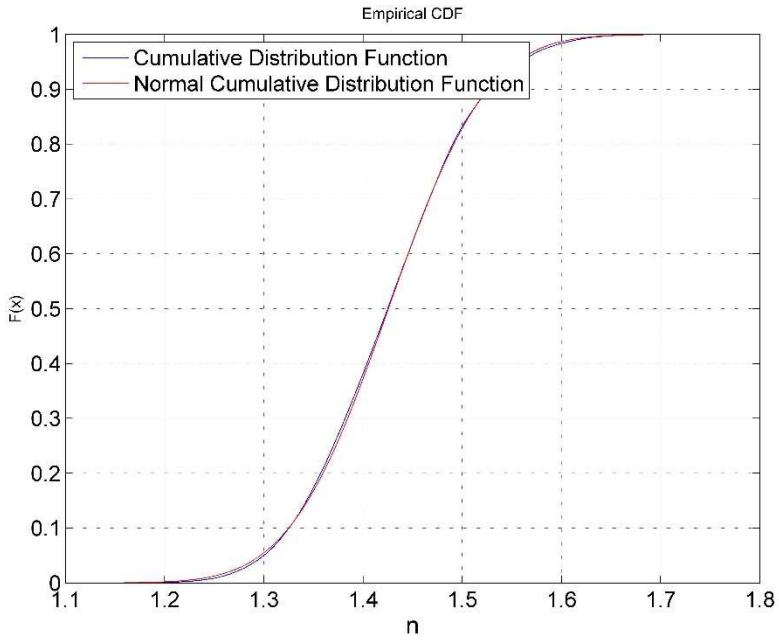

Fig. 388 — Cumulative posterior relative frequency histogram of *n* of Well 67 using the PLE model

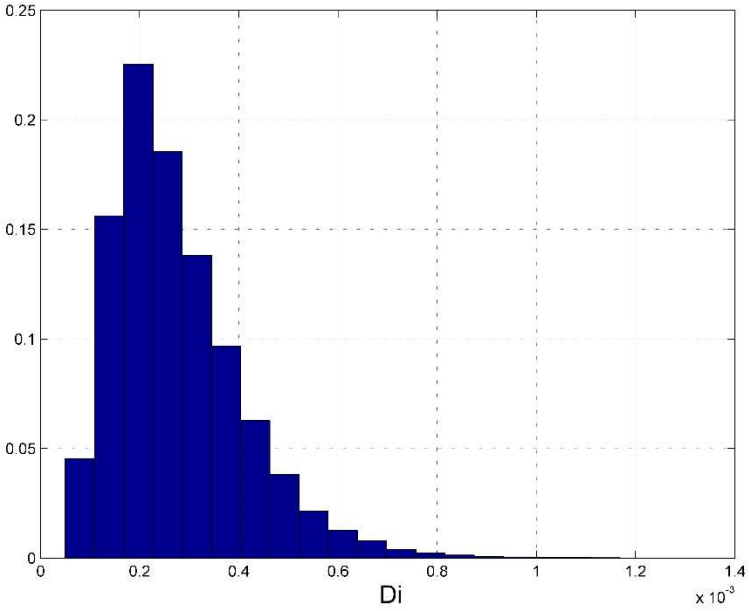

Fig. 389 — Posterior relative frequency histogram of D_i of Well 67 using the PLE model

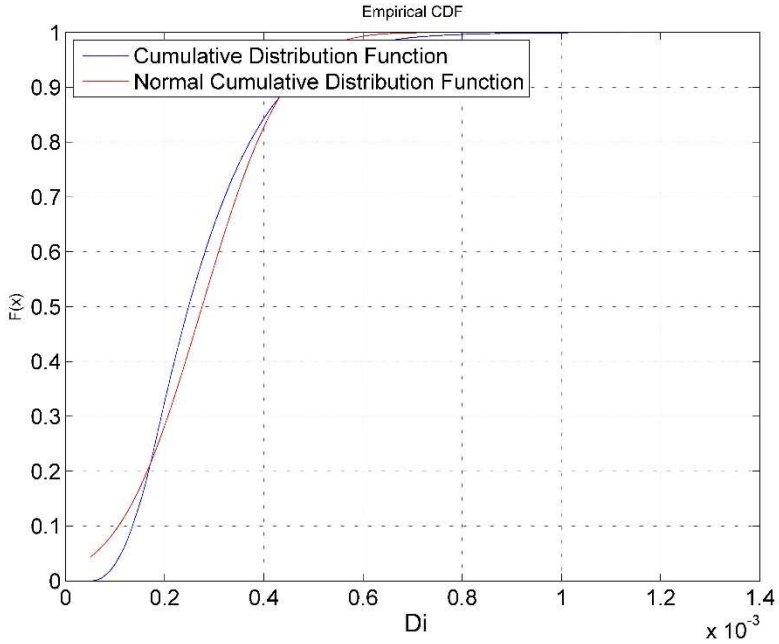

Fig. 390 — Cumulative posterior relative frequency histogram of D_i of Well 67 using the PLE model

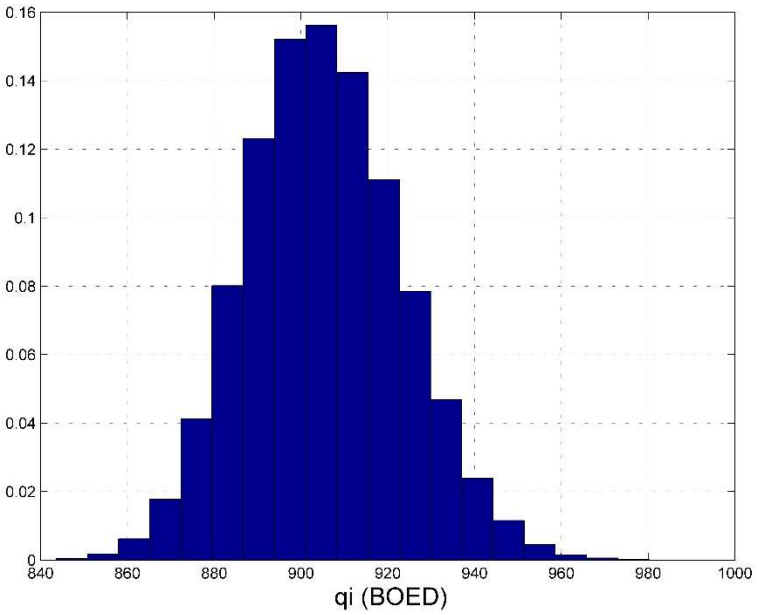

Fig. 391 — Posterior relative frequency histogram of q_i of Well 67 using the PLE model

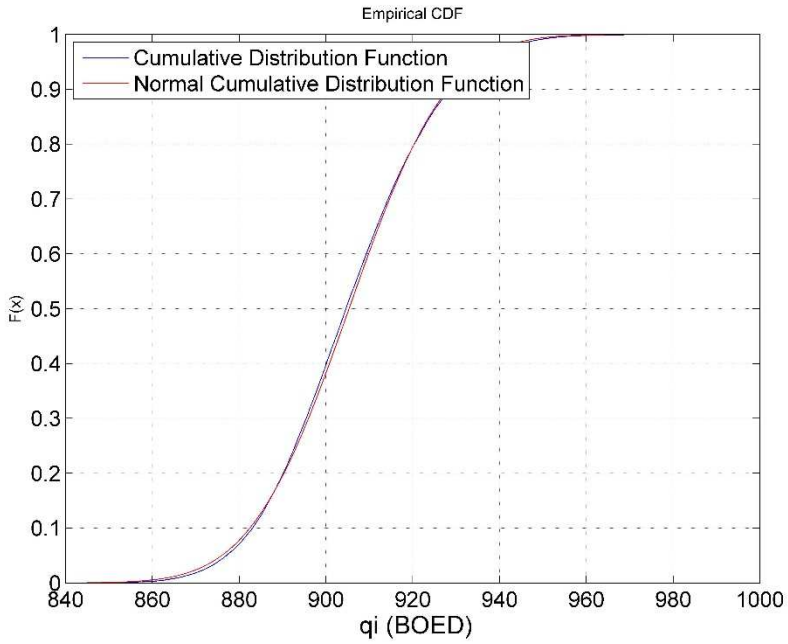

Fig. 392 — Cumulative posterior relative frequency histogram of q_i of Well 67 using the PLE model

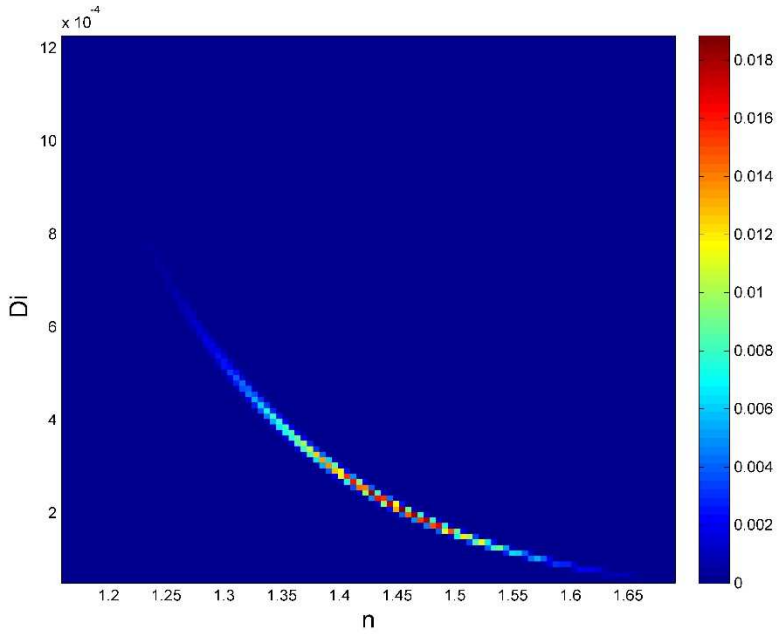

Fig. 393 — Relative frequency diagram between D_i and n of Well 67 using the PLE model

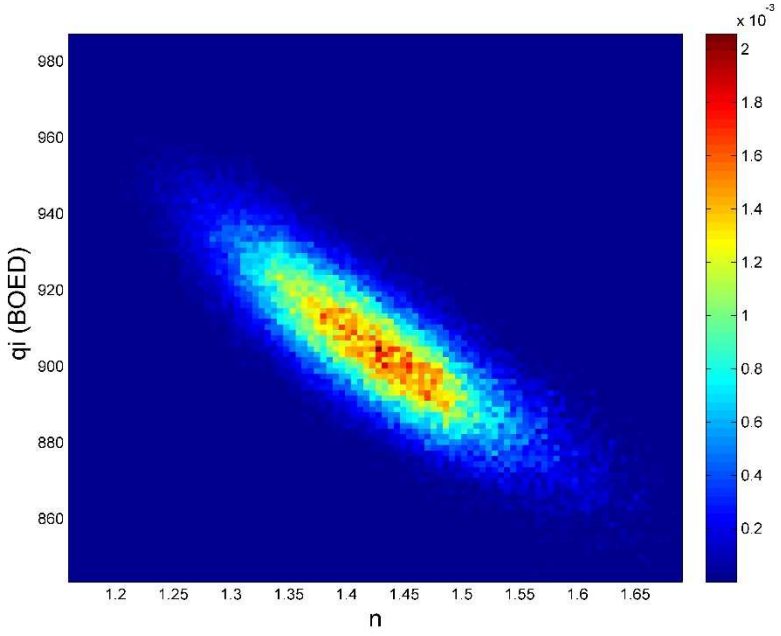

Fig. 394 — Relative frequency diagram between q_i and n of Well 67 using the PLE model

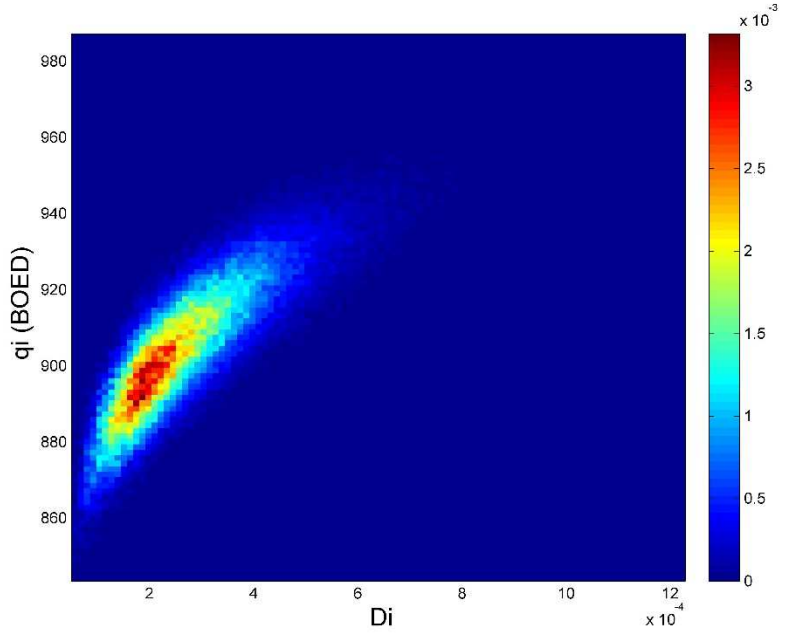

Fig. 395 — Relative frequency diagram between q_i and D_i of Well 67 using the PLE model

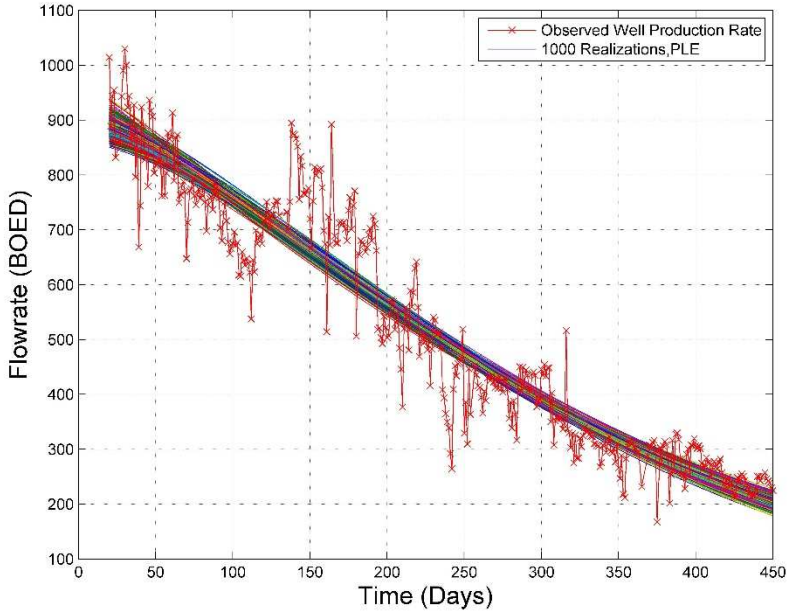

Fig. 396 — The 1,000 realizations of the model predictions using the Bayesian paradigm of Well 67 with the PLE model

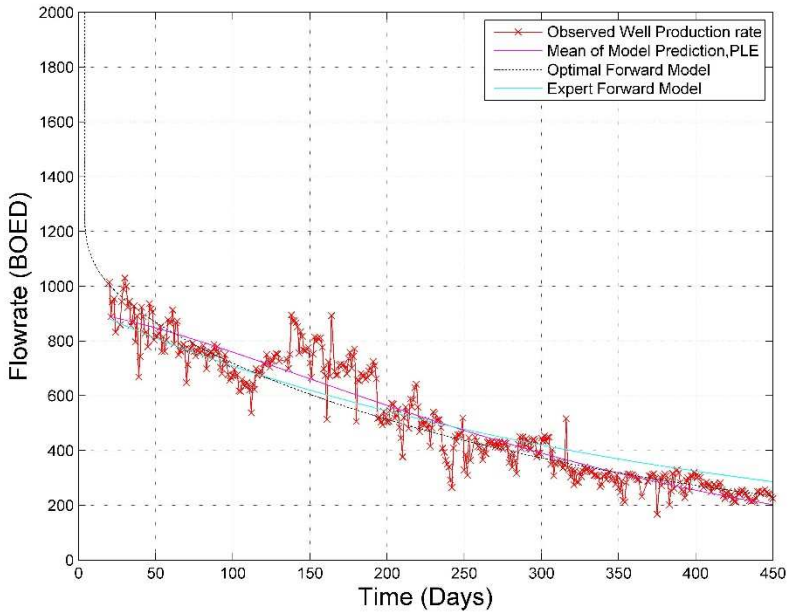

Fig. 397 — The production data with the mean of the realizations, the optimal forward model and the PLE model of Well 67

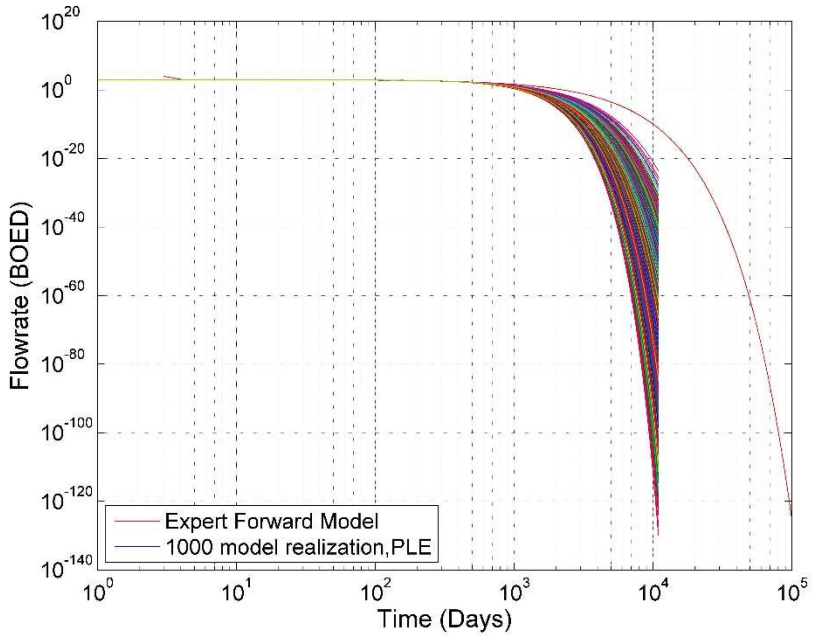

Fig. 398 — The 1,000 realizations of the model predictions using the Bayesian paradigm for 30 years of Well 67

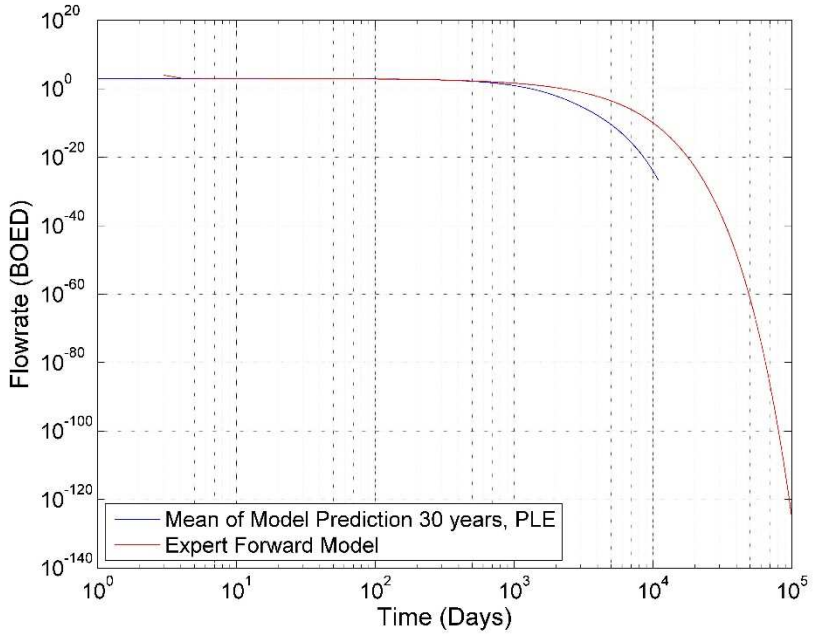

Fig. 399 — The mean of the realizations and the PLE model, plotted for 30 years for Well 67

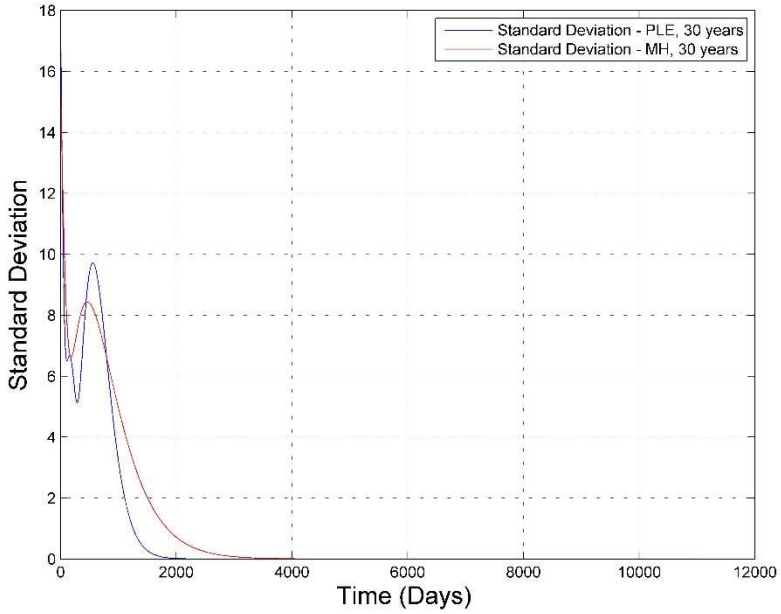

Fig. 400 — Comparison of the Standard Deviation of the two Bayesian models using the MH and PLE models of Well 67

Analysis

Well 67 shows interesting results. The MCMC results do not converge for the *b*-factor, even after 20 million iterations, of the MH model, as seen in **Fig. 358**. However, the D_i and q_i results both converge beautifully, as seen in **Fig. 360** and **362**. Due to the lack of convergence of *b*, the posterior distribution of *b* is meaningless, as seen in **Fig. 364**. However, the posterior distributions of D_i and q_i both show normal distributions, seen in **Fig. 366** and **368**. This is interesting because the trend of the posterior distribution of D_i has been lognormal for all wells. This result is puzzling because there is no reason for it to be different than the previous posterior results of D_i; there is convergence of the MCMC results therefore we expect it to follow the same trend that we have observed until this point.

When we compare these MCMC results with the results produced when applying the PLE model, we notice that that model converges for all three PLE parameters, shown in **Fig. 381**, **383** and **385**. Furthermore, the posterior distributions of these three parameters are as expected; Gaussian for *n* and q_i, as seen in **Fig. 387** and **391**, and lognormal for D_i, seen in **Fig. 389**.

Based on the posterior distributions of the three parameters, we created the relative frequency histograms that show the relationship between two different parameters -- D_i vs. *b*, q_i vs. *b* and q_i vs D_i for the MH model and D_i vs. *n*, q_i vs. *n* and q_i vs D_i for the PLE model. These results can be seen in **Fig. 370, 371** and **372**, respectively, for the MH model and **Fig. 393, 394** and **395**, respectively, for the PLE model. From Fig. 370 and 371, the results are incorrect because of the lack of convergence of the *b*-factor. Most times, we have seen the trend of the relationship between parameters even if there was no convergence, but in this case there is not. Fig. 372 does show a nice relationship between q_i and D_i that follows the same trend that we have seen in the other wells. The results of the PLE model all show the same results that we have seen throughout this study.

Then, we reach the realizations of the Bayesian paradigm using the MH and PLE models. We notice when we plot the mean of the realizations versus the optimal forward model (the results from the LSQ optimization), and the expert forward model (either MH or PLE), the mean of the model prediction and the expert forward model often times have close values for the 700 days plotted. However, when we extend the results to 30 years that there is a divergence between two sets of results. In this case, the MH forward model overestimates the reserves, as seen in **Fig. 376** for the MH model and **Fig. 399** for the PLE model. Both models show that they overestimate the reserves.

Finally, the standard deviation comparison of the two sets of Bayesian results, **Fig. 400**, identifies the uncertainty of the two models. In the case of this well, the standard deviation follow approximately the same trend. The standard deviation of the PLE model peaks higher than that of the MH model, but also drops to 0 before the standard deviation of the MH. From these results, I conclude that the PLE model would be ideal when implementing the Bayesian paradigm.